

STALL PRECURSOR STUDY OF
HIGH FREQUENCY DATA FOR THREE HIGH
SPEED, SWEEP COMPRESSION ROTORS

THESIS

James F. Anderton, Captain, USAF

AFIT/GAE/ENY/94D

This document has been approved
for public release and its
distribution is unlimited.

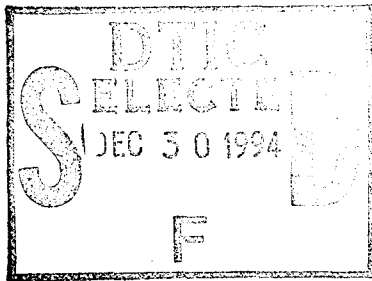
DEPARTMENT OF THE AIR FORCE
AIR UNIVERSITY

AIR FORCE INSTITUTE OF TECHNOLOGY

Wright-Patterson Air Force Base, Ohio

19941228 103

AFIT/GAE/ENY/94D-13



Accession For	
NTIS CRA&I	<input checked="" type="checkbox"/>
DTIC TAB	<input type="checkbox"/>
Unannounced	<input type="checkbox"/>
Justification	
By	
Distribution/	
Availability Codes	
Dist	Availability Codes
A-1	

STALL PRECURSOR STUDY OF
HIGH FREQUENCY DATA FOR THREE HIGH
SPEED, SWEEP COMPRESSION ROTORS

THESIS

James F. Anderton, Captain, USAF

AFIT/GAE/ENY/94D

DTIC QUALITY INSPECTED 2

Approved for public release
Distribution Unlimited

AFIT/GAE/ENY/94D-13

STALL PRECURSOR STUDY OF
HIGH FREQUENCY DATA FOR THREE HIGH
SPEED, SWEPT COMPRESSOR ROTORS

THESIS

Presented to the Faculty of the Graduate School of
Engineering of the Air Force Institute of Technology

Air University

in Partial Fulfillment of the
Requirements for the Degree of
Master of Science in Aeronautical Engineering

James F. Anderton, B.S.

Captain, USAF

December 1994

Approved for public release, Distribution Unlimited

ACKNOWLEDGEMENTS

I would like to thank the many people who have helped me bring this work to its conclusion. I am indebted to my advisor, Dr. Paul King, whose ability to understand what I was thinking rather than what I was writing helped steer me in the right direction on countless occasions. I would also like to acknowledge Dr. Bill Copenhaver and the staff of Wright Laboratories' Compressor Research Group for their assistance in obtaining the experimental data used in this thesis. In particular, Steve Puterbaugh was extremely helpful in answering my many questions about the compressor rotors studied in this report. Thanks also go to Charlotte Coleman of the Scientific and Engineering Applications Section, Communications-Computer Systems Group for her patience in what seemed like endless hours spent in the digitization of analog data.

Of course, no list of acknowledgements would be complete without thanks to my family. To my mother and father, your support during this turbulent time has helped keep me going. Finally, I would like to thank my wife, Cindy, and one year old son Kevin for their love, and their understanding of my need to spend so much time at home hunched over this computer; it is to them that I dedicate this work.

TABLE OF CONTENTS

ACKNOWLEDGEMENTS	i
LIST OF FIGURES	iv
LIST OF TABLES	vii
LIST OF SYMBOLS AND ABBREVIATIONS	viii
ABSTRACT	ix
1.0 INTRODUCTION	1-1
1.1 Motivation	1-1
1.2 Surge	1-2
1.3 Rotating Stall	1-2
1.4 Stall precursors	1-3
1.5 Compressor shock structure research	1-4
1.6 Focus of this work	1-5
2.0 TEST FACILITY AND EQUIPMENT	2-1
2.1 Test Facility	2-1
2.1.1 Compressor Test Rig	2-1
2.1.2 Instrumentation	2-1
2.2 Rotor Design	2-2
2.3 Test Procedure	2-2
2.3.1 Data Recording, Digitizing, and Calibration	2-3
3.0 DATA PROCESSING	3-1
3.1 Fourier Frequency Decomposition of a Signal	3-1
3.2 Frequency Spectrum of Kulite Pressure Data	3-3
3.3 Signal Power	3-5
3.3.1 Expected Behavior of Signal Power	3-6
3.3.1.1 Three dimensional effects	3-8
3.4 Correlation	3-9
4.0 RESULTS	4-1
4.1 Introduction	4-1
4.1.1 Overall Rotor Behavior	4-1
4.1.1.1 TFM Plots and Aliasing	4-2
4.2 Rotor 4	4-3
4.2.1 Rotor 4 at 90% Design Speed	4-4
4.2.2 Rotor 4 at 100% Design Speed	4-6
4.3 Rotor 6	4-9

4.3.1 Rotor 6 at 90% Design Speed	4-9
4.3.2 Rotor 6 at 100% Design Speed	4-10
4.4 Rotor 9	4-11
4.4.1 Rotor 9 at 95% Design Speed	4-11
4.4.2 Rotor 9 at 100% Design Speed	4-13
5.0 DISCUSSION OF RESULTS	5-1
5.1 Introduction	5-1
5.2 Spectral Composition	5-1
5.2.1 Aliasing	5-2
5.3 Modal and Surge Energies	5-3
5.4 Signal Power Techniques	5-4
5.4.1 Total Signal Power - Rotors 4 and 6	5-4
5.5 Summary of Stalling Characteristics: Rotors 4 and 6	5-6
5.6 Stalling Characteristics of Rotor 9	5-6
6.0 CONCLUSIONS AND RECOMMENDATIONS	6-1
6.1 Summary	6-1
6.2 Conclusions	6-1
6.3 Recommendations	6-2
7.0 REFERENCES	7-1
APPENDIX A	A-1
APPENDIX B: Computer Code	B-1

LIST OF FIGURES

Figure 1.1	Planar waves of surge [14]	8-1
Figure 1.2	Blockage inducing rotating stall [14]	8-1
Figure 1.3	Modal waves [14]	8-2
Figure 1.4	Compressor instrumentation for detection of modal waves [14]	8-3
Figure 1.5	Compressor instrumentation for shock structure research [9]	8-4
Figure 1.6	Compressor shock structure, throttle open [9]	8-5
Figure 1.7	Compressor shock structure, mid-range throttle [9]	8-5
Figure 1.8	Compressor shock structure, near stall [9]	8-5
Figure 1.9	Typical compressor pressure signal (Rotor 4, 100%, Kulite #4 digitized at 270 kHz)	8-6
Figure 1.10	Compressor shock wave variations [13]	8-7
Figure 2.1	CARL test facility [14]	8-8
Figure 3.1	Example frequency spectrum	8-9
Figure 3.2	Example Time-Frequency-Magnitude plot	8-9
Figure 3.3	Three dimensional effects on Kulite pressure transducers	8-10
Figure 3.4	Example Cross-Correlation	8-11
Figure 3.5	Cross-Correlation Resulting in Bias	8-12
Figure 3.6	Ramp Bias Correction Multiplier	8-13
Figure 4.1	Rotor 4, 90%, Kulite #4: TFM Plot	8-14
Figure 4.2	Rotor 4, 100%, Kulite #4: TFM Plot	8-15
Figure 4.3	Rotor 6, 90%, Kulite #4: TFM Plot	8-16
Figure 4.4	Rotor 6, 100%, Kulite #4: TFM Plot	8-17
Figure 4.5	Rotor 9, 95%, Kulite #4: TFM Plot	8-18
Figure 4.6	Rotor 9, 100%, Kulite #4: TFM Plot	8-19
Figure 4.7	Rotor 4, 90%, Kulite #1: Total Signal Power (less DC contribution)	8-20
Figure 4.8	Rotor 4, 90%, Kulite #2: Total Signal Power (less DC contribution)	8-21
Figure 4.9	Rotor 4, 90%, Kulite #3: Total Signal Power (less DC contribution)	8-22
Figure 4.10	Rotor 4, 90%, Kulite #4: Total Signal Power (less DC contribution)	8-23
Figure 4.11	Rotor 4, 90%, Kulites #1 through #4: Total Signal Power (less DC contribution)	8-24
Figure 4.12a	Rotor 4, 90%: Comparison of Slope of Signal Power	8-25
Figure 4.12b	Rotor 4, 90%: Comparison of Slope of Signal Power (Kulite #4 scaled by $\delta=0.145$)	8-26
Figure 4.13	Rotor 4, 90%: Power of Blade Passing Frequency Group (6140 Hz to 6380 Hz)	8-27
Figure 4.14	Rotor 4, 90%, Kulite #4: Power of Medium Frequency Group (320 Hz to 6120 Hz)	8-28
Figure 4.15a	Rotor 4, 100%: Cross-Correlation of Kulites #1 and #4 at T=-9.09	8-29
Figure 4.15b	Rotor 4, 100%: Cross-Correlation of Kulites #1 and #4 at T=-1.09	8-30
Figure 4.15c	Rotor 4, 100%: Cross-Correlation of Kulites #1 and #4 at T=-0.49	8-31
Figure 4.15d	Rotor 4, 100%: Cross-Correlation of Kulites #1 and #4 at T=-0.44	8-32
Figure 4.15e	Rotor 4, 100%: Cross-Correlation of Kulites #1 and #4 at T=-0.29	8-33

Figure 4.15f Rotor 4, 100%: Cross-Correlation of Kulites #1 and #4 at $T=-0.04$	8-34
Figure 4.15g Rotor 4, 100%: Cross-Correlation of Kulites #1 and #4 at $T=+0.01$	8-35
Figure 4.15h Rotor 4, 100%: Cross-Correlation of Kulites #1 and #4 at $T=+0.06$	8-36
Figure 4.16 Rotor 4, 100%: Total Signal Power (less DC contribution)	8-37
Figure 4.17 Rotor 4, 100%: Comparison of Slope of Signal Power (Kulite #4 scaled by $\delta=0.0778$)	8-38
Figure 4.18 Rotor 4, 100%: Power of Blade Passing Frequency Group (6880 Hz to 7120 Hz)	8-39
Figure 4.19 Rotor 4, 100%, Kulite #4: Power of Medium Frequency Group (360 Hz to 6860 Hz)	8-40
Figure 4.20 Rotor 4, 100%, Kulite #4: Shock Structure Points on Plot of Signal Power	8-41
Figure 4.21a Rotor 4, 100%: Shock Structure at Point C	8-42
Figure 4.21b Rotor 4, 100%: Shock Structure at Point D	8-43
Figure 4.21c Rotor 4, 100%: Shock Structure at Point E	8-44
Figure 4.21d Rotor 4, 100%: Shock Structure at Point F	8-45
4.22 Rotor 6, 90%: Total Signal Power (less DC contribution)	8-46
Figure 4.23 Rotor 6, 90%: Power of Blade Passing Frequency Group (6200 Hz to 6440 Hz)	8-47
Figure 4.24 Rotor 6, 90%: Comparison of Slope of Signal Power (Kulite #4 scaled by $\delta=0.37$)	8-48
Figure 4.25 Rotor 6, 90%, Kulite #4: Power of Medium Frequency Group (320 Hz to 6180 Hz)	8-49
Figure 4.26 Rotor 6, 100%: Total Signal Power (less DC contribution)	8-50
Figure 4.27 Rotor 6, 100%: Comparison of Slope of Signal Power (Kulite #4 scaled by $\delta=0.086$)	8-51
Figure 4.28 Rotor 6, 100%: Power of Blade Passing Frequency Group (6960 Hz to 7200 Hz)	8-52
Figure 4.29 Rotor 6, 100%, Kulite #4: Power of Medium Frequency Group (360 Hz to 6940 Hz)	8-53
Figure 4.30a Rotor 9, 95%: Cross-Correlation of Kulites #1 and #4 at $T=-4.91$	8-54
Figure 4.30b Rotor 9, 95%: Cross-Correlation of Kulites #1 and #4 at $T=-1.91$	8-55
Figure 4.30c Rotor 9, 95%: Cross-Correlation of Kulites #1 and #4 at $T=-0.91$	8-56
Figure 4.30d Rotor 9, 95%: Cross-Correlation of Kulites #1 and #4 at $T=-0.66$	8-57
Figure 4.30e Rotor 9, 95%: Cross-Correlation of Kulites #1 and #4 at $T=-0.51$	8-58
Figure 4.30f Rotor 9, 95%: Cross-Correlation of Kulites #1 and #4 at $T=-0.16$	8-59
Figure 4.30g Rotor 9, 95%: Cross-Correlation of Kulites #1 and #4 at $T=-0.06$	8-60
Figure 4.30h Rotor 9, 95%: Cross-Correlation of Kulites #1 and #4 at $T=-0.01$	8-61
Figure 4.30i Rotor 9, 95%: Cross-Correlation of Kulites #1 and #4 at $T=+0.04$	8-62
Figure 4.31 Rotor 9, 95%: Total Signal Power (less DC contribution)	8-63
Figure 4.32 Rotor 9, 95%: Comparison of Slope of Power (Kulite #4 scaled by $\delta=0.1935$)	8-64
Figure 4.33 Rotor 9, 95%: Power of Blade Passing Frequency Group (6580 Hz to 6820 Hz)	8-65

Figure 4.34 Rotor 9, 95%, Kulite #4: Power of Medium Frequency Group (340 Hz to 6560 Hz)	8-66
Figure 4.35a Rotor 9, 100%: Cross-Correlation of Kulites #1 and #4 at T=-9.4	8-67
Figure 4.35b Rotor 9, 100%: Cross-Correlation of Kulites #1 and #4 at T=-2.4	8-68
Figure 4.35c Rotor 9, 100%: Cross-Correlation of Kulites #1 and #4 at T=-0.9	8-69
Figure 4.35d Rotor 9, 100%: Cross-Correlation of Kulites #1 and #4 at T=-0.6	8-70
Figure 4.35e Rotor 9, 100%: Cross-Correlation of Kulites #1 and #4 at T=-0.45	8-71
Figure 4.35f Rotor 9, 100%: Cross-Correlation of Kulites #1 and #4 at T=-0.35	8-72
Figure 4.35g Rotor 9, 100%: Cross-Correlation of Kulites #1 and #4 at T=-0.25	8-73
Figure 4.35h Rotor 9, 100%: Cross-Correlation of Kulites #1 and #4 at T=-0.15	8-74
Figure 4.35i Rotor 9, 100%: Cross-Correlation of Kulites #1 and #4 at T=-0.05	8-75
Figure 4.35j Rotor 9, 100%: Cross-Correlation of Kulites #1 and #4 at T=+0.05	8-76
Figure 4.36 Rotor 9, 100%: Total Signal Power (less DC contribution)	8-77
Figure 4.37 Rotor 9, 100%: Comparison of Slope of Power (Kulite #4 scaled by $\delta=0.2815$)	8-78
Figure 4.38 Rotor 9, 100%: Power of Blade Passing Frequency Group (6980 Hz to 7220 Hz)	8-79
Figure 4.39 Rotor 9, 100%, Kulite #4: Power of Medium Frequency Group (360 Hz to 6960 Hz)	8-80
Figure A.1 Example of Fourier transform	A-3
Figure A.2 Fourier resolution of rapidly changing signal	A-4
Figure A.3 Rotor 4, 90%, Kulite #1: TFM Plot	A-5
Figure A.4 Rotor 4, 90%, Kulite #2: TFM Plot	A-6
Figure A.5 Rotor 4, 90%, Kulite #3: TFM Plot	A-7
Figure A.6 Rotor 4, 100%, Kulite #1: TFM Plot	A-8
Figure A.7 Rotor 4, 100%, Kulite #2: TFM Plot	A-9
Figure A.8 Rotor 4, 100%, Kulite #3: TFM Plot	A-10
Figure A.9 Rotor 6, 90%, Kulite #1: TFM Plot	A-11
Figure A.10 Rotor 6, 100%, Kulite #1: TFM Plot	A-12
Figure A.11 Rotor 9, 95%, Kulite #1: TFM Plot	A-13
Figure A.12 Rotor 9, 100%, Kulite #1: TFM Plot	A-14
Figure A.13 Rotor 4, 90%: Cross-Correlation of Kulites #1 and #4 at T = -0.124	A-15
Figure A.14 Rotor 6, 90%: Cross-Correlation of Kulites #1 and #4 at T = -0.15	A-16
Figure A.15 Rotor 6, 100%: Cross-Correlation of Kulites #1 and #4 at T = -0.02	A-17

LIST OF TABLES

Table 5.1 Comparison of Stall Warning Times 5-6

LIST OF SYMBOLS AND ABBREVIATIONS

CARL	- Compressor Aerodynamic Research Laboratory
DC	- Direct Current; corresponds to the zero frequency
DFT	- Digital Fourier Transform
f_n	- Discrete signal value (psig)
F_m	- Discrete Fourier transform coefficient
FFT	- Fast Fourier Transform
j	- Square root of -1
N	- Number of points in a data window
P	- Power (psi^2)
R	- Correlation (unbiased)
R^s	- Correlation (biased)
RMS	- Root Mean Squared
t	- Time at leading edge of data window (seconds before stall)
T	- Time (seconds before stall)
T_s	- Time between data samples (seconds)
TFM	- Time-Frequency-Magnitude
W	- Time window (seconds)

Greek

δ	- Shock decay factor
ω_0	- Fourier fundamental (resolution) frequency, Hz
ψ^2	- Mean squared value
μ	- Mean value
σ	- Standard deviation
τ	- Time shift, seconds

ABSTRACT

The frequency spectra of three single stage, high speed compressor rotors were derived and analyzed from experimental data. The compressor rotors included straight, backward-swept, and forward-swept blade designs. Data was acquired from four pressure transducers located on the compressor casing and arranged axially between locations 40% of blade chord upstream of the rotor face to just over the leading edge of the blades. Each rotor was throttled to stall at two constant speeds between 90% and 100% of design speed. Data digitization at 20 kHz revealed multiples of the rotor frequency up to and beyond a dominant blade passing frequency. Further analyses for characteristics of impending stall included examination of integrated signal power and cross-correlations of transducer signals from the upstream and downstream-most pressure transducers. Results of the integrated signal power approach showed promise as a potential pre-stall warning. This technique detected differences in the signal power at the two transducers in the immediate pre-stall time frame. Pre-stall warning times varied from several seconds to less than 0.5 second, with higher rotor speeds giving less warning time. Results for the forward-swept rotor, however, showed that integrated signal power did not warn of impending stall, and that surge energies played an important role in this rotor's stalling characteristics. An hypothesis for the behavior of the forward swept rotor, based on the possibility of stall development beginning in the near-hub radial region of this compressor, was developed.

1.0 INTRODUCTION

1.1 Motivation

The importance of the compressor stall phenomenon to turbine engine designers, operators and maintainers is readily apparent. To the operator, compressor stall means the loss of engine power, a very serious condition indeed in a single-engine aircraft. Even in a twin engine design, compressor stall typically results in an aborted mission and emergency recovery to the home base. From a maintenance standpoint, compressor stalls lead to extensive engine inspection, tear-down and expensive repairs, with accompanying loss of use of the engine for an extended, unscheduled period. Finally, the engine designer sees compressor stall as a limiting area of operation to be avoided at all costs. Unfortunately, this can place restrictions on engine operation such as reduced acceleration rates and compromise of peak performance. The ability to actively predict impending compressor stall, then, is a highly desirable objective. Should compressor stall be preceded by recognizable warning signs, modern digital engine controls would be able to move the engine operating point away from stall without the input (or even awareness) of the operator.

In order to develop an appreciation for the daunting task posed by compressor stall precursor research, further understanding of the compressor stall phenomena is in order. In essence, a compressor stall is a disruption in the smooth flow of a fluid through the compressor rotor. Compressor stalls, in general, can be divided into two distinct types: surge, and rotating stall.

1.2 Surge

Surge is typified by large amplitude axial pressure and mass flow oscillations in the compressor. These oscillations can be thought of as planar waves of flow (Fig. 1.1). Because of the large amount of energy required to sustain such oscillations, surge typically occurs at high rotor speeds. Although surge results in nearly complete loss of engine performance and the potential for extensive damage due to hot section overheating, full operation can sometimes be recovered by rapidly reducing throttle setting. Whereas surge is a condition affecting the entire face of the compressor, the second form of stall involves limited areas of stalled flow around the compressor face. This phenomenon is known as rotating stall.

1.3 Rotating Stall

The concept of rotating stall was first developed by Emmons et al. [1] in 1955. Rotating stall is a phenomenon in which circumferential sections of compressor blades experience stalled flow, while the rest of the machine continues to operate. An initial perturbation causes the fluid to stall in a passage or passages, reducing flow relative to the rest of the compressor. Fig. 1.2 illustrates how this blockage redirects incoming air to the blades around the stalled section. The change in flow direction tends to reduce the effective angle of attack of the blades preceding the stalled section (relative to rotation direction). At the same time, angle of attack increases in the blades on the opposite side of the stall cell. These changes in angle of attack cause the blades behind the cell to stall, and clear any stall existing in the passages in front of the cell. Through this mechanism, the stall cell rotates in the direction opposite to compressor rotation. Because the stall cell rotation rate is typically slower than the compressor rotation rate, the stall cell, when viewed from a fixed point in

front of the engine, will appear to move in the direction of compressor rotation at a rate less than the engine speed. Various studies ([2], [3]) have shown this rate to be typically 20% to 70% of rotor speed. Rotating stall can be further classified as either abrupt or progressive; an abrupt stall is characterized by a sudden reduction in performance, whereas compressor performance during a progressive stall steadily degrades over a definable period of time. Rotating stall can also co-exist with surge [4]. In fact, surge and rotating stall are sometimes linked in the literature by considering surge to be a rotating stall of order zero [5].

1.4 Stall precursors

Most recent stall precursor research has centered on the theory of modal waves. These waves (Fig. 1.3) can be thought of as sinusoidally distributed, small circumferential variations in the axial flow speed through the compressor [3]. The number of sinusoidal cycles around the face of the compressor determines the mode of the wave. Modal waves may exist in multiple superposed modes at any one time. Detection of the various modes is limited by the small amount of energy in the waves, and the number of pressure sensors located about the face of the compressor (Fig. 1.4). In a highly loaded compressor, these small perturbations will eventually cause the flow to separate in one or more passages. Such a condition would then develop into a rotating stall or surge. Studies by Boyer [6], Frank [7], and Tryfonidis et al. [8] found that stall was sometimes preceded by the formation and rotation of modal waves at rates approximately the same as seen in rotating stalls. Precursor times in these studies varied from several seconds to no warning whatsoever; as a rule, warning time was reduced as rotor speed increased. Because modal wave theory concerns relatively low frequency

phenomena (less than 1 kHz), data for these studies were typically digitized and filtered to provide accurate frequency information below 1 kHz.

1.5 Compressor shock structure research

Studies of transonic compressors such as by Sellin et al. [9], Puterbaugh and Copenhaver [10], and Copenhaver et al. [11] described the changes in shock structure and blade tip vortices of supersonic rotors at various steady-state throttle settings. Because such research requires precise depiction of the pressure distribution in the compressor blade passages, relatively high frequency data is required. Wright Laboratory personnel found that pressure signals contained significant frequency data up to the 9th harmonic of blade passing frequency (the rotation rate of the machine multiplied by the number of blades in the single stage compressor) [9]; at 100% design speed, this equated to 9 times 7 kHz = 63 kHz. Anti-aliasing concerns led to a digitization rate of about 270 kHz. Pressure transducers (Kulites) were arranged in a row over the tip of the compressor blades (Fig. 1.5). Using a once-per-revolution synchronization pulse, the data were analyzed to reveal the pressure distribution in each passage of the compressor. Results of this work showed that the blade shock and vortex structure varied with change in throttle. At open throttle, shock waves existed between the blades at small angles relative to the incoming flow, while the flow field ahead of the blades was relatively quiescent. In Fig. 1.6, these shock waves can be seen as the areas where static pressure contours lie extremely close together. As the throttle was closed, blade shock structures became more oblique to the compressor blades (Fig. 1.7). Finally, at a point near to stall, shock waves detached and extended into the flow ahead of the rotor (Fig. 1.8). Closing the throttle also affected the tip vortex, the rotational flow over the blade tip from the

high pressure side to the low pressure side of the blade. The vortex was found to grow in size, interacting with and weakening the shock waves and partially blocking flow through the blade passages. Although the primary intent of these studies was not to develop a new form of stall precursor, the possibility that shock wave and vortex patterns play a key role in stall development of high speed rotors is evident from the results [9]. Such a connection between stall in the tip region and the shock/vortex interaction was also postulated by Adamczyk et al. [12].

1.6 Focus of this work

The existence of a robust precursor signal in advance of compressor stall or surge has been the subject of numerous recent research efforts. Modal wave theory has shown promise in experiments at medium compressor speeds where warning times have been found to be relatively large, but is less reliable at 100% of transonic rotor design speed as warning times are small or non-existent. Unfortunately, it has been the author's experience as an Air Force pilot with over 2,000 hours of flight time in jet aircraft that most high performance turbine engine stalls occur at or about 100% speed, especially under maneuvering or during modulation of the afterburner.

The quest for increased performance levels has led to higher tip speeds and new blade configurations. The possibility that the stalling characteristics of these rotors is related to their blade shock structure has not yet been widely addressed. Because precise description of shock structure requires high digitization rates and time-consuming analysis techniques, it is doubtful that such methods could be used in active prevention of compressor stall. However, a compromise in data sampling rate between the high frequency shock structure data (digitized

at about 270 kHz) and low frequency modal wave studies (digitized at about 4 kHz) revealed new information. By digitizing at about 20 kHz, it was possible to reveal the blade passing frequency of a high speed rotor. Because a compressor generates a recurring signal whose period is one blade passage (Fig. 1.9), this frequency is dominant in the spectrum of any compressor. The magnitude of this frequency component will be predominantly determined by the amount of the total pressure rise across the blade passage shock wave.

Blade passing frequency for the rotors and speeds considered in this study was in the range of 6 to 7.5 kHz. Because blade passing frequency varies somewhat due to small oscillations in rotor speed, blade passing frequency in this study was defined as the region within ± 120 Hz of the largest frequency component. Visual examination of spectra from the three rotors in this study showed that this 240 Hz bandwidth captured the blade passing frequency peak without intruding on the small peaks at the 19th and 21st harmonics of rotor frequency, which were located about 300 - 350 Hz below and above blade passing frequency. The rest of the spectrum below blade passing frequency was further subdivided into a low frequency group and a medium frequency group. The low frequency group was comprised of frequencies below rotor frequency; this is the range typically studied by modal wave theorists. The remaining frequencies between rotor frequency and blade passing frequency were named "medium" frequencies. When subjected to Fourier frequency analysis, the pressure signal of a supersonic rotor will be found to contain peaks of energy in this range at frequencies corresponding to integer multiples of rotor frequency. These frequencies, as described by Sofrin [13], arise from the non-uniformity of the shock structures in the blade passages around the face of the rotor; small differences in the machining of the rotor blades result in

larger variations in shock structure when the rotor is operated at supersonic tip speeds (Fig. 1.10). In other words, a "perfect" rotor, with no variation in shock patterns from one blade passage to the next, would have no frequency components in this medium range.

The work of researchers such as Sellin et al. [9] has shown that blade shock structure is a strong function of the compressor operating point; shocks intensify in the blade passages as a compressor is throttled towards stall, and shock extension into the flow forward of the compressor rotor begins in the near-stall area of operation (Figs. 1.6 to 1.8). By analyzing the spectrum of a compressor pressure signal at different axial points in front of the compressor face (Fig. 1.5), it was possible to detect the forward movement of the shock waves with far less computational effort than is required to generate the static pressure contours of Figs. 1.6 through 1.8. Additionally, the behavior of the shock system in the extreme near-stall region provided warning of the impending stall. The objective of this thesis, therefore, was to examine compressor pressure signals in the near-stall area of operation in order to characterize their behavior in terms of a robust stall precursor.

2.0 TEST FACILITY AND EQUIPMENT

2.1 Test Facility

The data used in this thesis was obtained by the Compressor Aerodynamic Research Laboratory (CARL), located in Area B of Wright-Patterson Air Force Base, Ohio. This facility, dedicated to the study of new compressor designs, employs a 2000 horsepower, closed loop compressor test machine (Fig. 2.1). For details on the test facility and instrumentation, see Boyer [6] and Sellin [9]. A synopsis of the most pertinent information is as follows:

2.1.1 Compressor Test Rig

Air was brought in through an inlet duct and settling chamber to the compressor. After passing through the compressor (no inlet guide vanes are used), the air was directed to a throttling device and surge valve. The throttling mechanism was used to raise the operating point of the compressor to the desired level; when stall was determined to have occurred (typically via audible indications), a surge valve was opened to clear the stall. The air was passed through a heat exchanger and filter before being returned to the inlet duct.

2.1.2 Instrumentation

For this research, the test rig casing was fitted with ten evenly spaced pressure transducers (Kulites) over the compressor blade path (Fig. 1.5). The forwardmost transducer was 40% of the axial blade chord projection ahead of the blade tip leading edge, while the rearmost Kulite was 80% of chord behind the blade tip leading edge. For this study, only information from Kulites #1 through #4 was considered. These transducers differed from the

radially distributed Kulites used in other studies (Boyer [6], Frank [7], as shown in Fig. 1.4) in that they were arranged along the axial direction of the compressor. The installed Kulites were calibrated by means of a two point (0 and 10 psi) calibration. The operation of the transducers was linear within this range, and each was calibrated so that one volt corresponded to one psi of pressure. Measurement uncertainty analysis for the system (including the Kulites, signal conditioner and amplifier, A/D converter, calibration pressure source, and steady state output measurement device) resulted in an overall uncertainty of ± 0.086 psi with a 95% confidence interval [9].

2.2 Rotor Design

The three rotors in this study were part of the Wright Laboratories Propulsion Directorate Swept Rotor Study, a program begun in 1992 to study the effect of rotor blade sweep on high speed compressor performance. With a design tip speed of 1500 ft/sec, supersonic relative blade speeds occurred over about 60% of blade span [14]. The rotors were designated Rotor 4 (a baseline, straight rotor blade design), Rotor 6 (a backward swept rotor) and Rotor 9 (a forward swept rotor). All three rotors had a tip diameter of 17 inches and were machined from a single forging of 6A1-4V titanium, while the stator was machined from AMS 5616 [14]. Design features of Rotors 4 and 6 are summarized in Boyer [14]; parameters of Rotor 9 have not been approved for public release.

2.3 Test Procedure

Data from the compressor shock structure research was available on analog tape for both steady state (fixed throttle) and continuous-to-stall (closing throttle) conditions. Steady state tests typically were performed at five or six throttle settings and three compressor speeds

(90, 95 and 100% of design speed). Because shock wave phenomena were of primary interest, tests were limited to these relatively high compressor speeds. Continuous-to-stall data was obtained at these three speeds by closing the throttle at a linear rate; due to throttle design, this rate was preset and invariable at approximately -0.3 lbm/sec^2 [14]. For this work, continuous-to-stall data at 90 and 100 percent of design speed were used for Rotors 4 and 6. Because of an error in the setup of the analog-to-digital conversion process, digitization of Rotor 9 at 90 percent speed captured only 4 seconds of pre-stall operation. Therefore, data at 95 and 100 percent of design speed were used for Rotor 9.

2.3.1 Data Recording, Digitizing, and Calibration

Data for each test was provided by the CARL on analog tape. Using the same analog-to-digital conversion process as Boyer [6], and Frank [7], five tracks were digitized: time, and the first four Kulites (as described in section 2.1.2). Digitization sample rate was set at 20 kHz in order to capture frequency information up to blade passing frequency. An 8-pole Butterworth low-pass filter was set at 10 kHz. Although such an approach was necessary to maintain manageable digital file sizes (a 12.5 second test run digitized to 16Mb of data), this procedure will be seen to result in some aliasing of frequencies above 10 kHz. As analog-to-digital converter limitations allowed no more than 250,000 points to be digitized for each data track, only 12.5 seconds of each test run (250,000 divided by 20 kHz sample rate) could be converted. Since each test run lasted from 10 to 30 seconds, with most runs at about 20 to 30 seconds, only part of each run was digitized. By observing analog data on an oscilloscope, it was possible to determine approximately where stall occurred in each test run. After "previewing" analog data, digitization was performed so that about 10 seconds of pre-stall

data would be converted, along with two seconds of stall. This procedure sufficed in all cases except the aforementioned Rotor 9 at 90% of design speed. In addition to test data, a calibration series with a known, 2 volt peak-to-peak sine wave was recorded on each tape track by the test facility. This signal was recorded for each rotor, and was digitized along with test data in order to calibrate the signals of the four Kulites. Digitized data was transferred to a Unix-based Sun Microsystems network, and processed on Sparc-2, -10, and -20 workstations equipped with 32Mb of RAM.

3.0 DATA PROCESSING

3.1 Fourier Frequency Decomposition of a Signal

Fourier analysis is perhaps the most widely used method to obtain frequency information from magnitude vs. time data. The basis for the following discussion was obtained from Stearns and Hush [15] and Bendat and Piersol [16].

Fourier transforms can be subdivided into continuous and discrete forms. A continuous transform is used if the signal of interest is represented by a continuous function, whereas a discrete transform is appropriate for data in the form of a series of values at regular time intervals. The data for this work is of the discrete variety, so Fourier techniques presented here will be limited to the discrete transform approach (digital Fourier transform, or DFT) for signals of finite duration. This method models the data as the sum of sinusoids of a fundamental frequency ω_0 and its harmonics. The fundamental frequency ω_0 is determined by the number of points (samples) used in the analysis, and the sampling rate of the data:

$$\omega_0 = \frac{1}{NT_s} \quad (3.1)$$

where:

T_s = Time between samples (inverse of sample rate, 20 kHz in this study)

N = number of samples in the transform ("window size")

Higher frequencies (harmonics) are obtained from integer multiples of ω_0 , i.e. in general:

$$\omega = \frac{m}{NT_s}; \quad m = 0, 1, \dots, N-1 \quad (3.2)$$

Therefore ω_0 also becomes the frequency resolution of the transform. In other words, if ω_0 were equal to 10 Hz, only frequencies which are multiples of 10 can be precisely resolved. A

frequency of 15 Hz, for example, would be represented as energy at both 10 and 20 Hz. The equation for the DFT is [15]:

$$F_m = \sum_{n=0}^{N-1} f_n e^{-j(2\pi mn/N)}; \quad m = 0, 1, \dots, N-1 \quad (3.3)$$

where:

F_m = discrete Fourier transform component (a complex number)
 f_n = Discrete signal value (i.e. pressure at the Kulite) at time nT
 $j = \sqrt{-1}$

Thus, the Fourier transform of N data points returns N Fourier transform components, each representing an underlying frequency component of the signal. These complex numbers contain information on the frequency they represent. For example, F_1 is a complex number whose absolute value correlates to the magnitude of a sinusoid of frequency $1/NT$ (previously defined as ω_0). Because the discrete data f_n is real (i.e. not complex), only the first $N/2$ values of F_m need be calculated; the remaining values are the mirror image complex conjugates of these components.

Pressure data for this study did not have a constant mean value; mean pressure rose as the throttle was closed. Because DFT analysis is predicated on a constant mean signal value, a windowed approach to data analysis was required. With this approach, small time windows of data are considered separately. Within each of these windows, the mean signal value is approximately constant. Previous studies [17] have used digitization rates of 4 kHz and window sizes of $\frac{1}{8}$ of a second, or 500 data points. All of the data in this study was digitized at the significantly higher rate of 20 kHz, except for a short segment of data from Kulite #4 of Rotor 4 at 100% speed which was sampled at 270 kHz. As a compromise between small

window size and data processing limitations, the frequency decomposition work in this study used a 1/20 second window size except for cross-correlation functions, which used 1/10 second windows for reasons addressed in section 3.4. For the 20 kHz data, 1/20 second equated to 1000 data points; the 270 kHz data used 13,500 data point windows. This 1/20 second window size should better capture the rapidly changing nature of the signals studied here. For further information on Fourier window size and frequency resolution considerations, see Appendix A.

3.2 Frequency Spectrum of Kulite Pressure Data

Frequency decomposition of test data was accomplished via fast Fourier transform (FFT) techniques. MATLAB [18] code (see appendix B) was used to calibrate and Fourier transform the data. A "moving window" approach was used; 1000 data points, beginning with the first data point, were Fourier transformed. Because the Fourier transforms resulted in complex data, the absolute value of each frequency component was taken to determine frequency magnitude. The lower (positive) half of the frequency spectrum was then recorded as a column of a matrix. After the first 1000 points were decomposed and recorded, the window was moved 125 points (1/160 seconds) and the process repeated. For example, column one of the matrix (in the code of Appendix B, this is "fftmatrix") contains frequency data for the signal from 0 to 0.05 seconds; column two, data from 0.00625 to 0.05625 seconds; column three, data from 0.0125 to 0.0625 seconds, etc. A ten second run would therefore be stored as a 500 x 1592 matrix, requiring about 12 Mb of disk space. Note that 1592 columns was 8 fewer than the intuitive 10 seconds divided by 1/160 second steps, or 1600 columns. This was due to the centers of the first and last windows being four steps

removed from the ends of the data stream. This process was performed for Kulites 1, 2, 3 and 4 for Rotor 4, and Kulites 1 and 4 for Rotors 6 and 9.

The matrix next was processed with Mathematica's [19] ListDensityPlot function to provide a two dimensional view of the frequencies as the rotors are throttled into stall.

Figs. 3.1 and 3.2 illustrate this technique. Fig. 3.1 shows the spectral composition of Rotor 4 at 100% speed at time $T=0.05$ seconds (this figure is rotated 90 degrees for ease of comparison with Fig. 3.2). A figure such as this could have been generated for each time window; however, almost 2000 windows of data were available from the maximum 12.5 second data segment, far more than could reasonably be produced and compared. Fig. 3.2, which shall hereafter be referred to as a Time-Frequency-Magnitude (TFM) plot, combined these figures into one plot. Time, as referenced by the abscissa, represented the leading edge of each window. For example, the spectrum generated with data from 0.95 second to 1.0 second was plotted at $T = 160$ (1 unit on the abscissa equals 1/160 second). The magnitude of frequency peaks was indicated by the brightness of the traces across the figure. Note that the frequency peaks of Fig. 3.1 corresponded to the traces on the TFM plot in Fig. 3.2.

While the blade passing frequency was clearly the dominant spectral component on each plot, the width of the blade passing frequency trace on the TFM plot requires explanation. This trace was wide not because of its large magnitude, but because the adjacent frequencies components were also relatively large (i.e., the blade passing frequency was more of a rounded peak than a perfect spike; see Fig. 3.1). In this case, the frequencies within a 200 Hz band of the blade passing frequency were well above average and were displayed in white. Furthermore, any change in the magnitude of the blade passing frequency peak was

impossible to discern; this peak was of such height as to always be displayed as pure white at any time during the experiment. Thus, the main purpose of these plots was to show the important frequencies for each rotor, as well as a display of the changes that occur at stall.

3.3 Signal Power

Interpretation of stall phenomena from visual examination of the spectra of experimental pressure data would be a complex, time consuming task. This job could be greatly simplified if a single quantity describing the spectrum could be calculated and compared at different times (i.e. throttle positions). For example, the Spatial Fourier Coefficient as used by Boyer [6], Frank [7] and others was a single variable which combined data from eight pressure transducers. For this study, signal power represented such a quantity. Using the frequency decomposition data described in the preceding section, signal power was calculated. Power was defined as:

$$P(t) = \psi^2(t) = \frac{1}{N} \sum_{m=0}^{N-1} F_m^2(t) \quad (3.4)$$

where ψ^2 is the *mean squared value* of F_m , and the windowing approach causes F_m to become a function of t , time at the leading edge of the window. Recalling that the second $N/2$ values of F_m were complex conjugates of the first $N/2$ values, equation 3.4 can be rewritten:

$$P(t) = \psi^2(t) = \frac{2}{N} \sum_{n=0}^{\frac{N}{2}-1} F_n^2(t) \quad (3.5)$$

$\psi^2(t)$ is further defined as [16]:

$$\psi^2(t) = \mu^2(t) + \sigma^2(t) \quad (3.6)$$

where $\mu(t)$ is the mean value of $F_m(t)$, and $\sigma(t)$ is the standard deviation of $F_m(t)$.

Calculation of $\psi^2(t)$ was computed with MATLAB's [18] *norm* function. This

function was used to calculate the positive square root of $\psi^2(t)$, a form known as the *Root Mean Squared* (RMS). Squaring this value resulted in the desired quantity of power.

Although this calculation may be performed on raw pressure data, the motivation for the use of the Fourier transform of raw pressure data is described below.

For this study, the goal was to characterize the shock structure on the rotors. Because the passing of a shock wave (such as in Fig. 1.9) creates a sudden rise and drop in pressure, the best way to interpret the strength of the shock is to consider the energy contained in the pressure fluctuations. For a spectral analysis of pressure fluctuations this can be achieved by setting the first (DC) term of the Fourier spectrum to zero, which is tantamount to setting the mean, μ , to zero in the raw data. As a result, total signal power computed in the frequency domain is equivalent to the variance of the original pressure data (all representations of power in this study were derived from Fourier transform data).

MATLAB [18] contains a standard deviation function to calculate total signal power from original pressure data, saving the processing time required to perform FFTs; however, the power for bands or groups of frequencies (such as the previously defined medium and blade passing groups) was also of interest in this study. Power in these frequency bands was derived from the calculation of FFT frequency coefficients (coefficients outside of the frequency range of interest were set to zero). All power plots are obtained from the identical 1000 point (1/20 second) FFT windows used in the generation of TFM spectra (recall the abscissa value of time is for the forward edge of the window).

3.3.1 Expected Behavior of Signal Power

Because signal power was calculated for various axial positions forward of the

compressor face, a correlation among transducer values was desired. Since the small distance between Kulites suggested that spatial variation in signals at adjacent Kulites would be slight, the furthest transducers, Kulites #1 and #4, were selected to obtain a more discernable correlation. Finite wave amplitude theory states that pressure variations due to shock waves decay with distance away from the shock [13]; in the two-dimensional depiction of flow in the tip region such as seen in Figs. 1.6 through 1.8, this decay accounts for differences in the signal generated in the vicinity of Kulite #4 and Kulite #1; as signal strength increases at Kulite #4, proportionately stronger signals should also be seen at Kulite #1. An assumed relationship between power at the two Kulites was:

$$P_1(t) = \delta(t)P_4(t) = \delta(t) \frac{2}{N} \sum_{m=1}^{\frac{N}{2}-1} F_{m_4}^2(t) \quad (3.7)$$

where:

$\delta(t)$ = shock decay factor.

$P_1(t)$ = Power at Kulite 1.

$P_4(t)$ = Power at Kulite 4.

Since the location of Kulites #1 and #4 was fixed, modeling $\delta(t)$ as independent of time results in:

$$P_1(t) = \delta P_4(t) \quad (3.8)$$

A drawback of this model is related to the forward movement of the shocks in the blade passages as the throttle is closed (Figs. 1.6 to 1.8). For example, if a shock wave were located at Kulite #5 (Fig. 1.5), the magnitude of the pressure variations sensed at Kulite #4 would be greater than those seen at Kulite #1. If the shock were to intensify without moving, a proportionately equal increase in the strength of the pressure variations at both Kulite #1 and Kulite #4 would be seen. If, however, the shock were to simply translate infinitely far

downstream, the pressure variations at each of the two Kulites would become the same. Therefore, the value of δ selected in each case was expected to be accurate only over periods of time where shock position was fairly constant. Additional modeling of the data revealed the utility of the addition of a constant to Equation 3.8. This led to:

$$P_1(t) = \delta P_4(t) + C \quad (3.9)$$

$$dP_1(t) = \delta dP_4(t) \quad (3.10)$$

The derivative form (Equation 3.10) was used because of the ease of calculation and interpretability of the results.

3.3.1.1 Three dimensional effects

To more accurately predict results at the various Kulites, the three-dimensional characteristics of the compressor rotor need to be considered; the signal at each Kulite is influenced not only by the tip flow field but in general by the entire compressor rotor. Kulites closer to the rotor are expected to be influenced by conditions at the tip more than Kulites upstream of the rotor. The reason for this effect is illustrated in Fig. 3.3, in which it is seen that although the signal recorded at Kulite #4 includes contributions from points A and B, events at point B are expected to have much less influence on the signal than events at point A. Kulite #1 is also influenced by events at points A and B, but the difference in distances to points A and B is much less dramatic. Thus, the signal at Kulite #1 is expected to be influenced by conditions occurring over a range of radial blade sections on the blade, while Kulite #4 is expected to be mostly influenced by local, tip flow aerodynamics. If the diffusion of the blade passage shocks due to tip vortex growth in the near stall region [9] is

confined to the blade tips, a reduction in power at Kulite #4 relative to power at Kulite #1 should occur.

3.4 Correlation

Results of power techniques did, in fact, point to differences in the signal at the four Kulites studied here when measured over the range of throttle settings. Time-windowed correlation was performed on 2000 point windows of Kulite #1 and Kulite #4 data in an attempt to find a robust, time-independent method to describe these differences. Correlation (R) is a measure of the time-shifted similarity between two windowed signals, and, as calculated in this work, is bounded by the range $-1 \leq R \leq 1$ (these bounds are achieved by dividing each windowed signal by its norm before cross correlation, where the norm is defined as the square root of the sum of the squares of the data points in the window). For example, Fig. 3.4 depicts two sine waves and their corresponding correlation function. The two sinusoids are separated by a phase angle of 50 points. The correlation of these two waves is also a sinusoid with a value of 1 at $x = 50$. This shows that, if one of the sinusoids were shifted 50 points in phase, the two signals would line up (correlate) perfectly. At $x = 550$, $R = -1$; shifting the signal 550 points results in perfect negative correlation, where each value on one sinusoid is complemented by an identical negative value on the other sinusoid. Thus, a correlation function contains two pieces of information: time shift on the x axis, and correlation at that time shift on the y axis. The correlation process is performed by MATLAB's [18] *xcorr* function. The mathematical representation of correlation is [16]:

$$R_{xy}(\tau) = \frac{1}{W - \tau} \int_0^{W - \tau} x(t)y(t + \tau) dt \quad (3.11)$$

where:

R_{xy} = Cross-correlation of signals x and y

τ = time shift

W = time window

Because the signals examined in this study were of finite length, results of correlation were subject to ramp bias error [16]. This error resulted in too small values of R at the correlation window endpoints. Fig. 3.5 illustrates this problem: the two signals of Fig. 3.5a were sinusoids of finite duration whose correlation should have been another sinusoid, as was the case with Fig. 3.4. However, Fig. 3-5b showed that the output of the correlation function underestimated true values of R at each end of the window. Correcting ramp bias error required multiplying the correlation function by [16]:

$$R(\tau) = \frac{W}{W - \tau} R^s(\tau) \quad (3.12)$$

where R^s was the uncorrected correlation with ramp bias error. Fig. 3.6 is an example of the ramp bias correction multiplier. Even with this correction, results at the extreme endpoints were nearly singular; therefore, figures in this study were confined to the middle 50% of the correlation time window. In other words, although correlation was conducted with 2000 point (0.10 second) windows in this study, correlation plots displayed only the middle ± 0.05 seconds of time shift. The 50% reduction in data displayed suggested the choice of the 2000 point window size, so that maximum displayed time shift corresponded to the same 1/20 second window size used in the power plots.

For this work, a correlation between Kulites 1 and 4 was calculated for all rotor and speed combinations. Additionally, cross-spectral density functions were calculated which identified the power in frequencies common to the two correlated signals. These latter plots

were derived by point-by-point multiplication of frequency magnitudes of the Fourier transform data for the two pressure signals. For example, if the 100 Hz component of signal 1 was 100, and the 100 Hz component of signal 2 was 0, the cross-spectral density plot would display a value of 0 at 100 Hz. If signals 1 and 2 had a 100 Hz magnitude of 10, cross-spectral density at 100 Hz would be 100. Cross-spectral density techniques are actually an adjunct to correlation, as the inverse FFT of the cross-spectral density plot will result in a (biased) correlation curve.

4.0 RESULTS

4.1 Introduction

The techniques of Chapter 3 were applied to Rotors 4, 6 and 9 of the Compressor Aerodynamic Research Laboratory's Swept Rotor Study series. Rotor 4 was examined in the most detail; all four available Kulites were used in analysis of this rotor. Based on trends identified for Rotor 4, analysis was limited to Kulites 1 and 4 for the remainder of the study.

4.1.1 Overall Rotor Behavior

With one exception, all rotor and speed combinations resulted in abrupt stalls; Rotor 6 at 90% of design speed stalled in a progressive fashion. Approximately 8 to 10 seconds of data preceding stall were available for each of the six cases studied here. Spectral analysis of each case was accomplished by preparing TFM plots as an overview, and cross-correlation studies for a more detailed examination. Because of the difficulty in interpreting the TFM plots (Section 3.2), only figures for Kulite #4 were included to demonstrate the technique; the remainder of the TFM plots were placed in Appendix A. Additionally, correlation results are limited to Rotor 4 at 100% speed and Rotor 9 at 95% and 100% speed. Correlation for the other cases did not reveal any new information; representative plots were also placed in Appendix A.

Power analysis was subdivided into total signal power, and the two frequency groups previously identified as medium and blade passing. For example, blade passing frequency for Rotor 4 at 90% speed was 6260 Hz; the blade passing frequency group was set at 6140 Hz to 6380 Hz, and medium frequencies ranged from rotor frequency (320 Hz) to just below the

lower limit of the blade passing frequency group (6120 Hz). In every case, as stated in Section 3, calculated power excluded the typically large DC component. Thus, total signal power as presented here represents the power of signal deviation from the mean. In general, the time at which stall occurred was determined by reference to the total signal power. With two exceptions, total signal power at Kulite #4 dropped abruptly at stall entry; stall ($T = 0$) was determined to occur at the bottom of this abrupt power drop. The two exceptions, Rotor 6 at 90% and Rotor 9 at 100% will be addressed in the appropriate sub-sections.

With the exception of the discussion in the next section of the TFM plots for all the rotors and speeds, the remainder of this chapter will address each rotor and speed combination individually.

4.1.1.1 TFM Plots and Aliasing

Fig. 4.1 is the TFM plot of Rotor 4 at Kulite #4 for 90% design speed. This plot shows a regular series of important frequencies rising above the noise level. There were twenty frequency peak traces up to and including blade passing frequency (6.26 kHz), a quantity which corresponded to the number of blades in the rotor. Such behavior was consistent with the spectra of supersonic compressors as studied by Sofrin [13]. Above blade passing frequency were additional small peaks at multiples of rotor frequency; additionally, there was a large peak at approximately 7.5 kHz, believed to be an aliased component.

Aliasing occurs according to the following relationship:

$$f_{alias} = f_{sample} - f_{signal} \quad (4.1)$$

The frequency of the second harmonic of blade passing frequency is twice 6.26 kHz, or 12.52 kHz. The alias of this frequency occurs at $20 \text{ kHz} - 12.52 \text{ kHz} = 7.48 \text{ kHz}$, suggesting

that the peak at about 7.5 kHz in Fig. 4.1 is the aliased second harmonic of blade passing frequency. Confirmation of aliasing was accomplished using Rotor 4 at 100% speed (Fig. 4.2) by noting that the energy at about 6.01 kHz visible in Fig. 4.2 was not present in the Rotor 4 at 100% speed data sampled at 270 kHz by Sellin et al. [9].

Eight-pole Butterworth filtering at 10 kHz during the analog-to-digital conversion process was insufficient to prevent aliasing. Although this filter attenuated the 12.5 kHz harmonic of Rotor 4 at 90% speed by 12 dB, the magnitude of the unattenuated energy (seen to be on the order of magnitude of the blade passing frequency in the 270 kHz, 100% speed data) was great enough to ensure that the frequency presence would be strong at the aliased position. Aliased frequencies also were easily discerned by the behavior of time-evolved frequency components in the stall and post stall recovery region of the plots: as seen in Figs. 4.1 and 4.2, aliased frequencies drop slightly during stall and rose during recovery, a mirror image of the slight rise and drop of true frequencies. Aliasing was also evident in TFM plots for the other rotor and speed combinations (Figs. 4.3 to 4.6) except for Rotor 9 at 95% (Fig. 4.5), where it was obscured by the blade passing frequency. For the moment, the implications of aliasing will be ignored, although they will be addressed again in section 5.0, Discussion of Results.

4.2 Rotor 4

Of the three compressors studied here, this straight-bladed rotor was most like those currently in use in actual propulsion systems. In the results of Boyer [14] and Frank [17], this rotor gave the least amount of warning time prior to stall, ranging from 0.35 seconds [14] and 0.086 seconds [17] at 90% speed, to 0.1 second [14] and 0.0 seconds [17] at 100% speed.

4.2.1 Rotor 4 at 90% Design Speed

Figs. 4.7 through 4.10 show the power of the total signal deviation from the mean at each Kulite plotted versus time. At Kulite #1 (Fig. 4.7), power increased steadily as the throttle was closed; stall formation was indicated by an abrupt increase in power between $T = 0$ and $T = 0.1$. Between $T = 0.1$ and $T = 0.6$, stall intensifies, as indicated by another increase in power. From $T = 0$ to $T = 0.6$, the widely oscillating power readings are consistent with the unsteady nature of stalled flow. Next, at $T = 0.6$, the surge valve was opened by lab personnel, and power dropped very rapidly. Finally, a brief post-stall recovery period was seen just before the end of the data stream. At Kulite #2 (Fig. 4.8), results were quite similar up to the point of stall. At $T = 0$ to $T = 0.1$, however, power did not increase as it did at Kulite #1, although oscillations in power were similar to those at Kulite #1. Power did increase from $T = 0.1$ to $T = 0.6$, and behaved in a manner similar to Kulite #1 during the surge valve opening and post stall recovery. At Kulite #3 (Fig. 4.9), response was again similar up to the point of stall. In this case, power diminished at a rapid, fairly constant rate from $T = 0$ to $T = 0.6$. Finally, power measured at Kulite #4 (Fig. 4.10) was substantially different from the results of the first three pressure transducers. Power again increased fairly steadily as the throttle was closed; however, at about $T = -4$ seconds, the slope of the power curve was seen to decline. By -1.5 seconds, power had entered a period of steady decay, which dropped rather precipitously at stall.

Fig. 4.11 shows power at all four Kulites overlaid on one plot. As expected (Section 3.3.1), power at any time before stall was highest at Kulite #4; finite amplitude wave effects caused the pressure signal to decay as it propagated forward to Kulites #3, #2, and #1.

However, in the immediate pre-stall time frame ($T = -1.5$ to $T = 0$) a drop in power measured at Kulite #4 occurred while power at the other three Kulites continued to increase. This was in accordance with the model of Section 3.3.1.1, in which shock-vortex interaction was expected to cause a decrease in power at Kulite #4 as compared to Kulite #1. Note that, during stall, power at each Kulite tended to converge upon a common value near 150 psi (Kulite #1 was somewhat less); the unsteady flow during stall was distributed more evenly in the axial range between the Kulites.

Next, an attempt was made to bring out the difference in the slopes of the four power curves. Because data from the 1000 point windows was too oscillatory for meaningful analysis of slope, the following process was used:

Mean power from 25 time windows was calculated. For example, mean power for windows 1 through 25 was calculated, followed by mean power for windows 2 through 26, etc. Although this is tantamount to re-calculating power using a larger window, this technique was faster as it used existing data for power of the 1/160 second windows. The use of these larger windows smoothed the data, and slope was calculated from the difference in power at points 5/16 of a second apart. Finally, a trial-and-error process was used to find the best value of δ , the shock decay factor of Equation 3.10. Because movement of shocks was expected to undermine the assumption that δ was constant (Section 3.3.1), δ was chosen to give the longest overlay of the slope plots as close to stall as possible.

Fig. 4.12a shows the results of this process before the δ scaling was applied (Kulite #2 results largely overlaid Kulite #3 and were omitted for clarity). This plot shows that Kulite #3 was

also seeing some change in slope in the near stall time period ($T = -1$ to $T = 0$). Fig. 4.12b shows the results for Kulites #1 and #4 when a δ of 0.145 was applied to Kulite #4 slope. Although good overlay was achieved from $T = -8$ to $T = -5.5$, the declining nature of Kulite #4 slope after $T = -5.5$ made it impossible to find a δ which kept the slope plots together for more than a fraction of a second after this point. As explained in Section 3.3.1.1, this was an indication that shock strength was lessening at the blade tip from $T = -5.5$ to $T = 0$ due to shock-vortex interaction, while blade sections closer to the hub continued to produce strong shocks.

The importance of the different frequency ranges was also considered. Comparing power of the blade passing frequency group (Fig. 4.13), to total signal power (Fig. 4.11) revealed that blade passing frequency accounted for most of the total signal power for this rotor and speed combination. This was the expected result, given the tremendous dominance of the blade passing frequency spike in the spectrum of the rotor.

The unusual behavior of total signal power at Kulite #4 prompted a study of medium frequency power for this Kulite. As discussed in Section 1.6, this frequency group is a measure of the differences in the shock structures of the blade passages around the face of the rotor. Medium frequency power was found to increase steadily throughout the greater portion of the test run (Fig. 4.14). Thus, although mean shock strength at this Kulite was declining in the 1.5 seconds preceding stall (Fig. 4.10), the global variation in shocks continued to increase.

4.2.2 Rotor 4 at 100% Design Speed

Contrary to results for this rotor at 90% speed, cross-correlation and cross spectral

density plots provided an interesting view of a transient, self-clearing stall in the 100% speed test run. Fig. 4.15a was typical of cross-correlation results for times well removed from stall. In Fig. 4.15b, energy at about 190 Hz was in the range where mode 1 energy would occur (20% - 70% of rotor frequency, or 70 Hz - 245 Hz). Figs. 4.15c and 4.15d showed the large amount of surge energy at about 35 Hz and the uneven appearance of cross-correlation during transient stall. Energy in the modal range is still present in these plots, but appears less due to the increased scale of the y-axis in Fig. 4.15d. In Fig. 4.15e the uneven pattern of cross-correlation disappears along with most of the surge energy; this figure is similar in appearance to Fig. 4.15a even though stall is only 0.3 seconds in the future. Finally, Figs. 4.15f through 4.15h show the abrupt formation of stall in the form of large surge energies and low cross-correlation values. As explained in Section 3.4, the time at which stall is apparent from cross-correlation lags the time determined from the power plots by about 0.1 second.

Total signal power (Fig. 4.16) exhibits some of the same characteristics as were seen at 90% speed: power rose until stall, at which point power at Kulite #1 increased abruptly, while Kulite #4 saw a drop in power as power at all Kulites converged to a median range. In this figure, the transient stall of the cross-correlation results (Figs. 4.15c and d) appears as a peak of power in the same time range (about $T = -0.4$). Unlike the 90% case, only a very brief period of changed slope of the power plot was seen at Kulite #4 from $T = -1$ to $T = 0$ (Fig. 4.17). Fig. 4.18 shows blade passing frequency power versus time. Comparison with total signal power (Fig. 4.16) shows that, as for 90% speed, the blade passing frequency band accounted for most of the total signal power.

Fig. 4.19 shows medium frequency power; note the large increase at $T = -0.5$. As was

seen in the cross-correlation study (Figs. 4-15c and d), this appeared to be the result of a short burst of self-clearing stall. In general, medium frequency power increased throughout the pre-stall time frame; this was similar to the behavior of this frequency group at 90% speed (Fig. 4.14).

Total signal power results for Rotor 4 at 100% speed were compared to results of the tip shock structure study of section 1.4. Because the data examined by Sellin et al. [9] was taken at a series of fixed throttle settings, some method was required to determine throttle setting at any point in the stream of continuously closing throttle data used in this report. By assuming linear closure rate between test start and stall (throttle position was recorded for both of these points, and the valve is designed to close at a continuous rate), an approximate correlation of throttle position with time was achieved. The points labeled C, D, E, and F by Sellin et al. [9] were visible in the results of this study (Fig. 4-20). While Point C (Fig. 4.21a) was an intermediate throttle setting, Point D (Fig. 4.21b) corresponded to the peak efficiency of the blade tip region and points E (Fig. 4.21c) and F (Fig. 4.21d) were described as "near stall". At points C and D, the shock wave was contained between the blades. At points E and F, the shock wave began to detach and extend into the flow field in front of the blades. Note that, at the extreme left side of Fig. 4.20, there appeared to be a region of fairly flat slope. This suggested that, as long as the shock remains within the blade passage, the amount of signal oscillation about the mean was relatively constant as measured by the four Kulites. As the rotor was throttled, the shock wave extended forward until it reached the Kulites. The effect of the shock passing over the Kulite was to induce a large increase in deviation from mean pressure, recorded here as an increase in power.

4.3 Rotor 6

This rotor, with backward-swept blades, was the only one to experience a period of progressive stall. Also studied by Boyer [14] and Frank [17], pre-stall warning times were >2.0 seconds [14] and 3.81 seconds [17] at 90% speed. At 100% speed, stall warning times were determined to be 0.2 seconds [14] and no warning [17]. These warnings represented an improvement over the times found by these researchers for Rotor 4.

4.3.1 Rotor 6 at 90% Design Speed

This was the only rotor and speed combination which resulted in a progressive stall. As no abrupt drop in power at Kulite #4 was recorded, stall time was subjectively determined as the time at which total signal power at Kulite #4 began to oscillate widely. Indeed, since the TFM plot of Fig. 4.3 lacks the characteristicly widespread low to medium frequency energy which accompanied stall in the other rotor and speed combinations (Fig. 4.1, for example), it seems likely that a completely stalled state was not reached in the recorded data stream.

Figs. 4.22 shows total signal power versus time. In this figure, power at Kulite #4 began to drop several seconds before stall, while power at Kulite #1 rose for nearly the entire test run. As for Rotor 4 at 100% speed (Fig. 4.16), power at Kulite #1 was steady at a low value for several seconds at the beginning of the data ($T = -8.5$ to $T = -6$), then rose until the progressive stall was encountered. This pattern, also as for Rotor 4, was probably due to the extension of the shock into the flow field at Kulite #1. On the other hand, power at Kulite #4 does not rise significantly and begins to drop at $T = -4$. By the model of Section 3.3.1.1, this meant that blade tip shock-vortex interaction occurred well before stall. Fig. 4.23 shows the

power of the blade passing frequency band. As for Rotor 4, a comparison of Fig. 4.23 and Fig. 4.22 shows that the blade passing frequency band contributed most of the power in the total signal plot. Fig. 4.24, a comparison of slopes of total signal power, shows that the slopes of the two signals diverge at about $T = -4.5$.

Fig. 4.25 shows medium frequency power for Kulite #4; medium frequency power for Rotor 6 at 90% speed tended to increase throughout the pre-stall time frame.

4.3.2 Rotor 6 at 100% Design Speed

Results for this rotor and speed combination were quite similar to those for Rotor 4 at 100% speed. In Fig. 4.26, total signal power versus time is displayed. This case contradicted the expectations of Section 3.3.1, in that power at Kulite #1 initially exceeded power at Kulite #4 ($T = -9$ to $T = -5.5$). It is possible that this was caused by three-dimensional effects as described in Section 3.3.1.1, if blade sections away from the tip were producing a stronger signal in the $T = -9$ to $T = -5.5$ time span than was the case at the blade tip. An additional factor was the rearward sweep of the rotor blades, which placed Kulite #1 closer to the blade sections away from the tip of the rotor. A brief period of no increased power seen at the beginning of the data stream ($T = -9$ to $T = -7$) presumably coincided with the confinement of shocks within the blade passages. A period of steady increase in power followed at both Kulites, and stall occurred abruptly. As with Rotor 4 at 90% and 100% speed, stall was denoted by an increase in power at Kulite #1, while power at Kulite #4 dropped. Fig. 4.27 shows the slope of the power curves at the two Kulites. Here, only a brief period of decrease in Kulite #4 was seen, starting at $T = -0.6$ seconds. Fig. 4.28 shows the power of the blade passing frequency group. The similarity between blade passing frequency power and total

signal power (Fig. 4.26) demonstrated that, as with Rotor 4, the blade passing frequency dominated the power spectrum. Curiously, power rose abruptly at stall at Kulite #1 before dropping to a lower, sustained value.

Fig. 4.29 shows medium frequency power. Power rise here was less smooth throughout the test run than was typical of the previous cases. However, the trend of this figure is the same as was seen in Rotor 4 at 90% and 100% speed, and Rotor 6 at 90% speed: medium frequency power generally increased up until stall.

4.4 Rotor 9

Whereas many similarities were seen in the behavior of Rotors 4 and 6, results for Rotor 9 with its forward-swept blades were markedly different from the preceding two rotors. Rotor 9 was also studied by Frank [17]; stall warning times were determined to be 2.5 seconds at 90% speed, and 0.14 seconds at 100% speed.

4.4.1 Rotor 9 at 95% Design Speed

Figs. 4.30a through 4.30i are the cross-correlation results for this case. Fig. 4.30a is typical of results from $T = -11$ to $T = -0.91$. If the cross-correlation curve of Fig. 4.30a were enlarged, it would be possible to see a signal whose period corresponded to the blade passing frequency for this rotor speed. However, the relatively large time scale of the plot (0.10 seconds, or about 670 cycles at blade passing frequency) causes the dense, black appearance of the cross-correlation plot. Note that the wavy appearance of the correlation curve of Fig. 4.30a was very different from the results for Rotor 4 (Figs. 4.15). The peaks of the waves ranged from about 0.06 seconds apart at low values of T (Fig. 4.30a) to 0.03 seconds apart at $T = -0.01$ (Fig. 4.30h), corresponding to a frequency range of about 17 to 35 Hz.

Thus, cross-correlation results for Rotor 9 at 95% speed were typified by a blade passing frequency component superposed with a 17 to 35 Hz frequency component. Although energy at 17 to 35 Hz was visible in the cross-spectral density results of Figs. 4.30a, b, and c, the magnitude of this energy was still relatively small. However, 0.25 seconds after the results of Fig. 4.30c, Fig. 4.30d shows that power at about 35 Hz had increased tenfold and was second only to blade passing frequency power. Figs. 4.30e through 4.30h show that 35 Hz power continued to dominate the spectrum below blade passing frequency as stall was approached. Power at 35 Hz before time $T = -0.91$ (Fig. 4.30c) was generally in the range of 30 to 120 psi^2 ; from $T = -0.91$ to stall, 35 Hz power grew from 60 psi^2 to over 1000 psi^2 (Figs. 4.30d to h). During this time, the shape of the correlation curve remained essentially unchanged. In Fig. 4.30i ($T = +0.04$), stall is seen to have occurred abruptly, as evidenced by generally low correlation and large, low frequency cross-spectral energy. The large amount of 35 Hz energy present in the immediate pre-stall time frame for this rotor and speed combination suggested that stall was linked to the appearance of this low-frequency, surge-like energy.

Fig. 4-31 is a plot of total signal power versus time. Note the relatively long period of little or no increase in power at Kulite #1 ($T = -11$ to $T = -4.5$) as compared to Rotors 4 and 6 (Figs. 4.7, 4.16, 4.22, 4.26). The inference here was that the shock waves did not propagate outward toward Kulite #1 in this time span. Shock wave movement toward the blade leading edges, as evidenced by an increase in slope of power at Kulite #1 in Fig. 4.31, occurred just 4 seconds before stall. Power at Kulite #4 showed an unusually coherent sinusoidal behavior from $T = -11$ to $T = -5$. The frequency of this sinusoid increased from an initial 13 Hz to 15 Hz when it disappeared at around $T = -5$. This frequency range was close to the estimated 17

Hz frequency at $T = -4.91$ seen in an early cross-correlation plot (Fig. 4.30a). The source of this energy, and the cause for its loss of coherency at $T = -5$, were uncertain. Fig. 4.32 shows that the slope of the power curves at Kulites #1 and #4 did not compare as well as in Rotors 4 and 6. In fact, in the last 0.8 seconds before stall, Kulite #1 slope appeared to decay; this was diametrically opposed to the decline of slope at Kulite #4 as seen in Rotors 4 and 6.

Blade passing frequency power is given in Fig. 4.33. Once again, blade passing frequency was found to account for most of the energy in the total signal power plot (Fig. 4.31).

Fig. 4.34 shows medium frequency power for Kulite #4. Medium frequency power increased fairly regularly except for a leveling and slight decline in the 1 second immediately preceding stall.

4.4.2 Rotor 9 at 100% Design Speed

This rotor / speed combination provided the most unusual results of any of the cases studied here. Instead of total signal power dropping at stall, power rose abruptly. Therefore, stall was determined to have occurred at the peak of the abrupt rise in power at Kulite #4 (Fig. 4.36).

Figs. 4.35a through 4.35j show the results of cross-correlation. Maximum correlation, initially close to 1.0 as in Fig. 4.35a ($T = -9.4$), dropped to a low of about 0.25 in Fig. 4.35b ($T = -2.3$). In Fig. 4.35c ($T = -0.9$), correlation increased and began to develop an uneven appearance. Also in Fig. 4.35c, surge-like energy at about 40 Hz had increased to 300 psi^2 . In Fig. 4.35d ($T = -0.6$), the growth in surge-like energy continued, and the uneven

appearance of correlation is greater than in Fig. 4.35c. The distance between peaks of the correlation curve of Fig. 4.35d corresponds to a frequency of 40 Hz, the same as the energy peak in the low frequency detail of this figure. By $T = -0.45$ (Fig. 4.35e), the difference between positive and negative correlation varied greatly over the displayed span of time shift. For example, for a time shift of about -0.04, positive correlation was about 0.35 and negative correlation was about -0.45; positive correlation minus negative correlation was 0.8. At a time shift of about -0.03, positive correlation was about 0.6 and negative correlation was about -0.5; the difference between positive and negative at this time shift was 1.1. Thus, signals from Kulites #1 and #4 were alternately becoming similar (high correlation) and dissimilar (low correlation) at a 40 Hz rate. Surge power had increased to almost 3000 psi^2 , up from just 36 psi^2 at $T = -2.4$ (Fig. 4.35b). This trend of increasing surge power continued in Fig. 4.35f ($T = -0.35$). By $T = -0.35$, surge power was far above all other frequencies except blade passing frequency. In Figs. 4.35g through 4.35i ($T = -0.25$ to $T = -0.05$), surge power grew until stall. Just prior to stall (Fig. 4.35i), surge power was about 11,500 psi^2 . In Fig. 4.35j, stall occurs abruptly.

Fig. 4.36 is the total signal power plot for Kulites 1 and 4. As with Rotor 6 at 100% speed (Fig. 4.26), the model of Section 3.3.1 does not hold from $T = -9$ to $T = -5$, where power at Kulite #1 exceeds power at Kulite #4. Also, the forward sweep of this rotor would cause Kulite #1 to be farther from blade sections away from the rotor tip. A possible explanation for the relatively high power at Kulite #1 will be offered in the discussion of blade passing frequency band power for this rotor. Note that power at Kulite #1 generally remained steady or decreased from $T = -9.5$ to $T = -0.7$. Again, the implication was that

shock waves were not detaching and moving forward towards Kulite #1. Power at Kulite #4 behaved more in the fashion of Rotors 4 and 6; a steady (actually slightly decreasing) power level from $T = -9.5$ to $T = -6.5$, followed by a steady increase from $T = -6.5$ to $T = -0.7$. The period preceding stall ($T = -0.7$ to $T = 0$) for this rotor and speed combination was markedly different from any of the other rotors or speeds. Here, power at both Kulites increased rapidly, and stall power levels were higher than any pre-stall value (i.e. no drop in power at Kulite #4 during stall as was seen in the other rotor and speed combinations). Since the rapid increase in power between $T = -0.7$ and $T = 0$ occurred with the development of high surge energies (Figs. 4.35c to i, $T = -0.8$ to $T = +0.05$), it seems likely that surge pressures contributed to the movement of shocks from inside the blade passages to the blade leading edges. Analysis of the slope of the power curves (Fig. 4.37) showed that there was little difference between the two Kulites in the immediate pre-stall time range.

Even more interesting was the behavior of the blade passing frequency group. Fig. 4.38 shows the blade passing frequency power versus time. Starting at $T = -7$, power at Kulite #1 dropped to a near-zero value at $T = -2.5$ before rising rapidly to the stall point. This near-zero point occurred at the same time as the low correlation of Fig. 4-35b, indicating that the signals from Kulites #1 and #4 were dissimilar. While the rise in power at Kulite #4 ($T = -6.5$) occurred at approximately the same time as the beginning of the fall in power at Kulite #1 ($T = -7$), no change in the trend of increasing power at Kulite #4 accompanied the rising of power at Kulite #1 at $T = -2.5$. These results led to the following scenario as a possible explanation of the unique performance of this rotor:

From $T = -9$ to $T = -7$, shocks in blade passages nearer the hub of the rotor were

strong bow shocks similar to those in Fig. 1.8; shocks at the tip were weaker and contained within the blade passages, as in Fig. 1.7. Because Kulite #1 saw pressures from a radial range of blade sections as in Fig. 3.3, this shock distribution resulted in higher power at Kulite #1 than at Kulite #4 (Figs. 4.36, 4.38). At about $T = -7$, the near-hub blade sections with bow shocks began to stall, causing the reduction in blade passing frequency band power as calculated from Kulite #1 data (Fig. 4.38). At the same time, reduced flow in the stalled near-hub region redirected incoming air to the blade tips, causing the shocks there to move forward, seen in Fig. 4.38 as increased power at Kulite #4. Power at Kulite #1, affected by both the increase in pressure variations from shock waves at the blade tips and the decreased pressure variations from the stalled blade sections away from the tips, remained approximately constant. By about $T = -3$, however, shocks at the tips had moved forward far enough to begin to be registered as increased power at Kulite #1 (Figs. 4.36, 4.38). Shortly thereafter, stall progressed to the blade tips as evidenced by the increased surge energies in the $T = -0.8$ to $T = +0.15$ time frame of Figs. 4.35.

A plot of medium frequency power at Kulite #4 (Fig. 4.39) showed that medium frequency power increased in a fairly linear fashion until $T = -0.8$, where it increased rapidly in the same manner as total signal power. This behavior was unlike that seen for the other rotor and speed combinations.

5.0 DISCUSSION OF RESULTS

5.1 Introduction

The six cases studied here (three rotors, two speeds each), and the two techniques used in the analysis (spectral / cross-spectral analysis and power of signal frequency groups), provided a seemingly limitless opportunity for contrast and comparison. However, of primary importance were the underlying causes for rotor behavior in the near stall time span, and the effectiveness of the analysis techniques in detecting this behavior so that impending stall can be avoided. To this end, a summary of analysis techniques with an assessment of their usefulness follows. Since Rotors 4 and 6 performed in a similar manner, conclusions about their performance were made based on results of the analytical methods used. Although comments on Rotor 9's behavior were included as appropriate, conclusions about this rotor's unusual performance were relegated to a separate section.

5.2 Spectral Composition

The spectral composition of pressure data examined in this study contained a great deal of information about the near stall and stalled aerodynamics of these rotors. However, visual interpretation of frequency spectra did not lead to the identification of a stall precursor. The two outputs which focused on spectral composition were the TFM plots and the cross-spectral plots. Each of the rotors had frequency peaks at most multiples of the rotor frequency, even at times well in advance of stall (Figs. 4.1 to 4.6). These peaks were also noted in studies by Boyer [14], Frank [17] and Tryfonidis et al. [8]. The size of the individual peaks below blade passing frequency was dependent upon the nature of each rotor,

and was not consistent from one rotor to another or even one speed to another in the same rotor. However, the existence of these peaks, which are not seen at subsonic tip speeds [13], indicated that there was a substantial difference in flow patterns around the rotor. In short, the presence of shock waves amplified the small variations inherent in the machine.

Since these frequency peaks were an indication of a variation in flow around the rotor, in a sense they represented a fundamental unsteadiness of the rotor. Examining any of the TFM plots (Figs. 4.1 to 4.6) helps make this point: in the pre-stall, steady operating region, relatively little energy was found in the range below blade passing frequency. At the highly unsteady stall, energy was spread over the lower frequencies, and blade passing frequency energy was greatly reduced. The pre-existing variations around the rotor are due to different degrees of loading in each blade passage; when exacerbated by surge (global variation in loading) and modal (local variation in loading) energies, the most highly loaded blade passage will likely stall before its neighbors. If conditions are favorable, this stall will rapidly (abruptly) propagate around the compressor. On the other hand, as seen in Rotor 4 at 100% speed (Fig. 4.20), the stall may be self-clearing. Prediction of stall propagation or clearing was not possible by spectral analysis alone.

5.2.1 Aliasing

Aliasing was present in every data set examined, as evidenced by TFM plots. The effect of aliasing was minimal in most cases, as the power of the entire signal deviation from the mean was the most common tool for analysis. Because the aliased frequencies were a legitimate part of the signal, albeit at a somewhat attenuated strength, they did not corrupt the results of analysis techniques which focussed on the total signal. When frequency ranges

were examined, however, aliasing posed a problem. For example, in Rotor 4 at 100% speed (Fig. 4.2), the second harmonic of blade passing frequency aliased to near the 17th harmonic of rotor frequency, and was included in the previously defined medium frequency group. Since this frequency was clearly not part of the medium frequency group, blade passing frequency aliasing influenced the power of medium frequencies at 100% of design speed (Figs. 4.20, 4.29, 4.39). This was not the case for 90% speed where the second harmonic aliased above blade passing frequency, and for the 95% speed where aliasing occurred at blade passing frequency.

5.3 Modal and Surge Energies

To date, studies of compressor rotor stall warning have focused on modal wave theory. Studies by Boyer [6], Frank [7] and Tryfonidis et al. [8] have found modal energy in the near-stall pressure data of rotors, including those rotors examined here. However, their test instrumentation was quite different; each of these studies used a ring of pressure transducers arranged around the face of the compressor. With such an arrangement, it was possible to track the rotation rate of modal waves as they moved around the compressor face. This rotation rate is critical; it defines the difference between modal energy and surge energy. Transducers arranged axially in front of the compressor, as was the case in this study, were not conducive to the detection of modal rotation. Energy at frequencies in the frequency range of modal waves, then, could not be conclusively proven to be due to modal waves. At any rate, as was seen by Boyer [14], transient modal energies appeared well before stall. The presence of these energies alone was determined by Boyer to be insufficient to signal an imminent stall; sustained periods of rotation at the rate of 20% - 70% of rotor frequency of

Greitzer [2] and Day [3] were required to confirm the presence of modal waves.

Surge, however, is a planar energy form in which modal rotation rate is not important. Results for Rotor 9 showed that its stall mechanism is closely tied to surge; this rotor was able to continue operating while extremely large amounts of surge energy were building. In this sense, Rotor 9 stalled in a manner different from the other two rotors. In summary, no inferences could be made regarding modal waves of order one or higher; although energy was noted in the correct frequency range, no confirmation of modal rotation was possible. For this reason, the modal energy stall precursor techniques of Boyer [6], Frank [7], and others could not be applied to the cross-correlation results of this study.

5.4 Signal Power Techniques

The most important tool in this analysis was the signal power calculation. In every case for Rotors 4 and 6, some change in the form of signal power immediately preceded stall. As was the case in previous studies, lower rotor speeds gave longer warning times.

5.4.1 Total Signal Power - Rotors 4 and 6

The most significant result of this study was the finding that total signal power, when measured at two different axial locations, revealed stall warning information. Key to this technique was a comparison of signal power at Kulite #4 (located at the leading edge of the blade tips) with Kulite #1 (located 40% of axial chord in front of the rotor). Because Kulite #4 was the closest of all sensors in this study to the source of the pressure variations, it was expected to always have a higher value of signal power than Kulites #1, #2, and #3. However, in Rotors 4 and 6 (Figs. 4.12b, 4.17, 4.24, 4.27), the slope of the total power curve at Kulite #4 (scaled by δ , the shock decay factor) declined in the immediate pre-stall time

frame when compared to the slope of power at Kulite #1. In other words, the value of power at Kulite #4 increased less rapidly as stall approached than the value of power calculated for Kulite #1. Furthermore, the 90% speed results for both Rotors 4 and 6 (Figs. 4.10, 4.22) showed that the value of power at Kulite #4 actually decreased as stall was approached. This meant that shock decay effects alone were insufficient to explain the differences in pressure sensed at the two Kulites. The underlying cause of this phenomenon involved the three-dimensional effects of Section 3.3.1.1. Whereas changes in shock patterns confined to the blade tips dominated the readings at Kulite #4, the three dimensional nature of the flow field caused Kulite #1 to see an average of signals originating from a larger radial section of blading (Fig. 3.3) - the blade sections away from the tip were presumably still functioning normally while shock-vortex interactions diffused shock strength at the blade tip.

Figures 4.12b, 4.17, 4.24, and 4.27 are the basis for Table 5.1, a summary of stall warning times as compared to Boyer [14] and Frank [17]. Although determination of stall warning was subjective at best, the standard used was $\frac{1}{4}$ second of generally steady or decreasing slope at Kulite #4 while slope at Kulite #1 increased.

5.4.2 Medium Frequency Power - Rotors 4 and 6

Medium frequency power behavior was fairly consistent over all six test cases. In Rotors 4 and 6, the power of this frequency group increased at a relatively steady rate as the throttle was closed (Figs. 4.14, 4.20, 4.25, 4.29). The lack of any definitive changes in the trend of rising medium frequency power as the throttle was closed made the power of this portion of the frequency spectrum a poor stall precursor for Rotors 4 and 6.

Table 5.1 Comparison of Stall Warning Times

		Stall Warning Time (seconds)			Shock decay factor
		Researcher			
Rotor	Speed	Boyer [14]	Frank [17]	Anderton	δ
4	90	0.35	0.086	>3	0.145
	100	0.1	0.0	0.5	0.0778
6	90	>2	3.81	4	0.37
	100	0.2	0.0	0.3	0.086
9	95	(a)	2.5 ^b	(c)	0.1935
	100	(a)	0.14	(c)	0.2815

Notes:

a: Rotor 9 was not included in this study.

b: 95% speed was not studied; this value is from the results for 90% speed.

c: Slope comparison technique not effective.

5.5 Summary of Stalling Characteristics: Rotors 4 and 6

Rotors 4 and 6, as analyzed with by their total signal power, seemed to stall in the same fashion. Prior to stall, both rotors experienced an operating range where total signal power increased at all measuring points (Figs. 4.11, 4.16, 4.22, 4.26). This range probably coincided with extension of the shock into the flow in front of the compressor. Just prior to stall, power calculated from pressure variations at Kulite #4 either receded (both rotors at 90% speed) or increased less rapidly (both rotors at 100% speed). This was possibly due to the tip vortex diffusing the shock structure in the blade tip region. For this reason, the stall event is hypothesized to originate at the blade tip. Power at Kulite #1 continued to increase in the near-stall time span, as this Kulite was not so greatly affected by the tip region as Kulite #4.

5.6 Stalling Characteristics of Rotor 9

Rotor 9 behaved in a manner quite different from the other two rotors. At both 95% and 100% speed, cross-correlation plots (Figs. 4.30, 4.35) had an uneven appearance unlike Rotor 4 (Fig. 4.15). The 100% speed results were easily explained; the extent of the uneven correlation behavior corresponded to the amount of surge energy present (Figs. 4.35). At 95% speed, however, Fig. 4-30a had an uneven form (periodic in the surge frequency range at 17 - 35 Hz) with relatively low surge energy. For the 95% speed, the difference between positive and negative correlation remained relatively constant, even as surge energy became quite large just before stall. This had the same effect as superposing a correlation curve of constant magnitude with a 17 - 35 Hz sinusoid. The strict interpretation of the cross-correlation results for this case is that the signals alternately became very similar and very dissimilar at a 17 - 35 Hz rate; the source of this phenomenon was not, however, apparent.

Behavior of the blade passing frequency was another distinguishing characteristic of this rotor. Results at 95% speed were generally similar to Rotors 4 and 6, in which the blade passing frequency band accounted for most of the power in the signal. At 100% speed, however, the behavior of blade passing frequency at Kulite #1 is entirely different than in any other rotor and speed combination; rather than contributing most of the energy in the total signal power calculation, blade passing frequency energy virtually disappears at $T = -2.5$ (Fig. 4.38). The hypothesis of Section 4.4.2 attributes this decline in blade passing frequency energy to stalled flow in the blade sections located radially away from the rotor tip (i.e. closer to the hub). This hypothesis could also explain the behavior of this rotor at 95% speed; in Fig. 4.32, slope at Kulite #1 is seen to decline slightly relative to Kulite #4 from $T = -0.8$ to

$T = 0$, about the same time as the appearance of the surge energies of Figs. 4.30c to 4.30g. Because Kulite #1 is affected by a larger radial span of blade sections than Kulite #4, this decline in slope may be linked to an attenuation of blade passing frequency energy in blade sections located away from the rotor tip as these sections begin to stall. For this rotor at 100% speed, a drop in power at Kulite #1 was thought to be caused by the early appearance of stalled flow in the near-hub region (Fig. 4.36, $T = -7$) due to high blade section loading away from the rotor tip. If the blade section loading at 95% speed was more evenly distributed over the radial length of the blades, stalling of the near-hub blade sections would occur when blade tip loading was also near stall. This would lead to complete stall much more quickly than at 100% speed, since blade tip sections would be quickly overloaded by airflow diverted from the hub region. Thus, the decline in slope of power at Kulite #1 (Fig. 4.32) and the appearance of surge energies (Figs. 4.30) may be a symptom of the same mechanism which caused stall at 100% speed: high aerodynamic loading in blade sections away from the rotor tip.

Examination of medium frequency power results shows that power generally increased as the throttle was closed at both 95% and 100% speeds for Rotor 9 (Figs. 4.34 and 4.39); however, power dropped slightly from $T = -1.0$ to $T = 0$ at 95% speed, and rose abruptly from $T = -0.5$ to $T = 0$ at 100% speed. This inconsistent behavior made medium frequency power a poor indicator of impending stall for this rotor.

6.0 CONCLUSIONS AND RECOMMENDATIONS

6.1 Summary

The three rotors in this study (straight-bladed, backward-swept blades, and forward-swept blades) were found to behave differently in the time span immediately preceding stall. The straight- and backward-swept designs (Rotors 4 and 6, respectively) behaved in a similar manner; the relationship between total signal power at a transducer located at the blade leading edge and a transducer located 40% of axial blade chord upstream of the blade leading edge provided a basis for a stall precursor. The forward-swept compressor (Rotor 9), however, appeared to have a different stall mechanism and a good stall precursor was not determined.

6.2 Conclusions

(1) The frequency spectra of the supersonic compressors were made up of relatively small peaks of energy at multiples of rotor frequency, and a large peak of energy at blade passing frequency. Peaks at multiples of rotor frequency persisted at frequencies above blade passing frequency.

(2) Visual interpretation of spectral data did not identify any single frequency component as containing stall warning information. However, calculating the power of the entire spectrum (less the DC contribution) as a function of time led to the development of a possible stall precursor.

(3) The power of the blade passing frequency group generally accounted for the majority of total signal power. However, Rotor 9 provided an exception to this observation in

that, at 100% speed, power of the blade passing frequency group was found to drop to a near-zero level at the forwardmost transducer. Because of its relative ease of calculation, total signal power was superior to blade passing frequency power as a stall precursor for Rotors 4 and 6.

(4) The power of the medium frequency group was not useful as a stall precursor.

(5) Cross-correlation plots and cross-spectral density plots revealed a transient, self-clearing stall in Rotor 4 at 100% speed and illustrated the large surge energies in Rotor 9. Although cross-correlation results provided a graphical means to view a developed stall, cross-correlation techniques did not predict impending stall.

(6) Stall in Rotors 4 and 6 originated at the tip of the rotor blade. This was supported by a comparison of the power of the pressure signal at the forwardmost transducer to power at the blade leading edge transducer. Power at the forwardmost transducer was influenced by blade sections away from the blade tips, while power calculated from the signal at the blade leading edge transducer was affected mostly by local, blade tip flow patterns. Stall formation in the blade tip region was characterized by a decline in power at the blade leading edge transducer relative to power calculated from the signal at the forwardmost transducer.

(7) The cause of stall in Rotor 9 was unclear. However, it was linked to the appearance of large amounts of surge energy and unusual behavior of the blade passing frequency band power. This led to the conclusion that stall may have originated in the near-hub blade sections of this rotor.

6.3 Recommendations

(1) Although aliasing was found to have limited impact on the results, recreation of these results with higher digitization rates would eliminate aliasing altogether. Higher digitization rates would require a reduction in the number of seconds of data digitized, or the division of the data into separate files, if processing were to be accomplished on SPARC stations.

(2) Examination of the Kulites aft of Kulite #4 may be of value (recall that data from six Kulites behind Kulite #4 exists but were not digitized for this study).

(3) In the past, high data digitization rates (up to 300 kHz) have been used to generate detailed depictions of shock and vortex structures such as those published by Sellin et al [9]. Although such studies have been accomplished for fixed throttle settings, analysis of continuously closing throttle tests are needed to better understand these phenomena as they relate to stall.

(4) The hypothesis that Rotor 9 initially stalls in the region away from the blade tips needs to be investigated. This may be possible by instrumenting inlet guide vanes so that characteristics of flow away from the blade tips can be observed.

(5) An explanation for the uneven appearance of the cross-correlation results for Rotor 9 at 95% speed is required.

(6) Conducting these tests at lower compressor speeds (70%, 80%) is necessary in order to examine the entire range of operation of the rotors.

7.0 REFERENCES

1. Emmons, H.W., C.E. Pearson, H.P. Grant, "Compressor Surge and Stall Propagation," *Transactions of the ASME*, Vol 77, May 1955, pp. 455-469.
2. Greitzer, E.M., "Surge and Rotating Stall in Axial Flow Compressors," Parts I & II, *Transactions of the ASME, Journal of Engineering for Power*, Volume 98, April 1976, pp. 190-217.
3. Day, I.J., "Stall Inception in Axial Flow Compressors," ASME Paper 91-GT-86, June 1991.
4. Stenning, A.H., "Rotating Stall and Surge," *Transactions of the ASME, Journal of Fluids Engineering*, Vol 102, March 1980, pp. 14-20.
5. Paduano, J, A.H.Epstein, L. Valavani, J.P. Longley, E.M. Greitzer, G.R. Guenette, "Active Control of Rotating Stall in a Low Speed Axial Compressor," as submitted to the 1991 ASME Gas Turbine Conference.
6. Boyer, K.M., P.I. King, W.W. Copenhaver, "Stall Inception in Single Stage, High-Speed Compressors with Straight and Swept Leading Edges," AIAA 93-1870, 29th Joint Propulsion Conference, June 28-30 1993, Monterey, CA.
7. Frank, B.J., P.I. King, W.W. Copenhaver, "Effects of Leading Edge Sweep on Stall Inception in a High-Speed Single Stage Compressor," AIAA 94-2696, 30th Joint Propulsion Conference, 27-29 June 1994, Indianapolis, IA.
8. Tryfonidis, M., O. Etchevers, J.D. Paduano, A.H. Epstein, "Pre-Stall Behavior of Several High-Speed Compressors," as submitted for presentation at 1994 ASME Turbo Expo, The Hague, Netherlands, June 1994.
9. Sellin, M.D., S.L. Puterbaugh, W.W. Copenhaver, "Tip Shock Structures in Transonic Compressor Rotors," AIAA Paper 93-1869, June 1993.
10. Puterbaugh, S.L., W.W. Copenhaver, "Flow Field Unsteadiness in the Tip Region of a Transonic Compressor Rotor," proceedings of Unsteady Flow in Aerodynamic Propulsion; Recent Advances in Experimental and Computational Methods, ASME Winter annual meeting, November 1994.
11. Copenhaver, W.W., E.R. Mayhew, C. Hah, "The Effect of Tip Clearance on a Swept Transonic Compressor Rotor," as submitted for presentation at the 1994 ASME Turbo Expo, The Hague, Netherlands, June 1994.

12. Adamczyk, J.J, M. L. Celestina, E.M. Greitzer, "The Role of Tip Clearance in High Speed Fan Stall," ASME Journal of Turbomachinery, Vol. 115, January 1993, pp. 28 - 39.
13. Sofrin, T.G., "Aircraft Turbomachinery Noise, Fan Noise," *Advanced Topics in Turbomachinery Technology*, Principle Lecture Series #2, Name, Ed: Japiska, D., Concepts ETI, Inc., Norwich, VT.
14. Boyer, K.M., "Characterization of Stall Inception in High-Speed Single Stage Compressors," Masters thesis, AFIT/GAE/ENY/92D-21, Air Force Institute of Technology, Dec 1992.
15. Stearns, S.D., D.R. Hush, "Digital Signal Analysis," Prentice-Hall, Inc., Englewood Cliffs, NJ, 1990.
16. Bendat, J.S., A.G. Piersol, "Engineering Applications of Correlation and Spectral Analysis," John Wiley & Sons, Inc., New York, NY, 1993.
17. Frank, B.J., "Analysis and Characterization of Compressor Stall Precursor Signals in Forward and Aft Swept High Speed Compressors," Masters thesis, AFIT/GAE/ENY/93D-14, Air Force Institute of Technology, Dec 1993.
18. "PRO-MATLAB for Sun Workstations, User's Guide," The MathWorks, Inc., 21 Eliot Street, South Natick, MA 01760, Jan 1990.
19. Wolfram, S., "Mathematica," Addison-Wesley Publishing Company, Inc., Redwood City, CA, 1991.

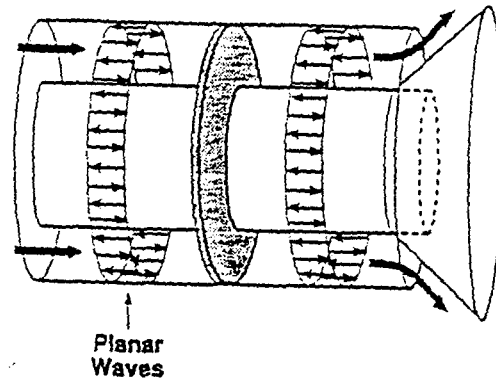


Figure 1.1 Planar waves of surge [14]

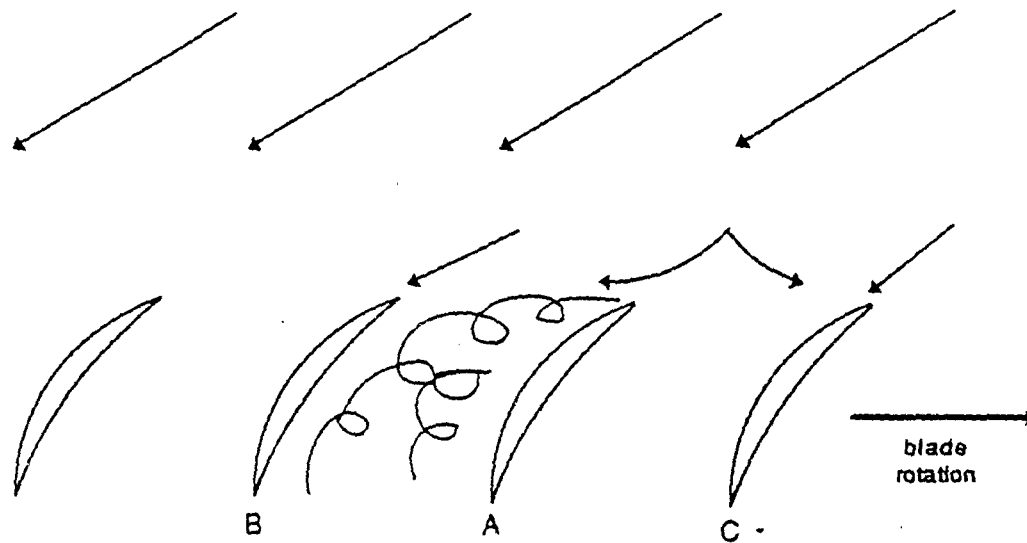


Figure 1.2 Blockage inducing rotating stall [14]

Axial velocity field

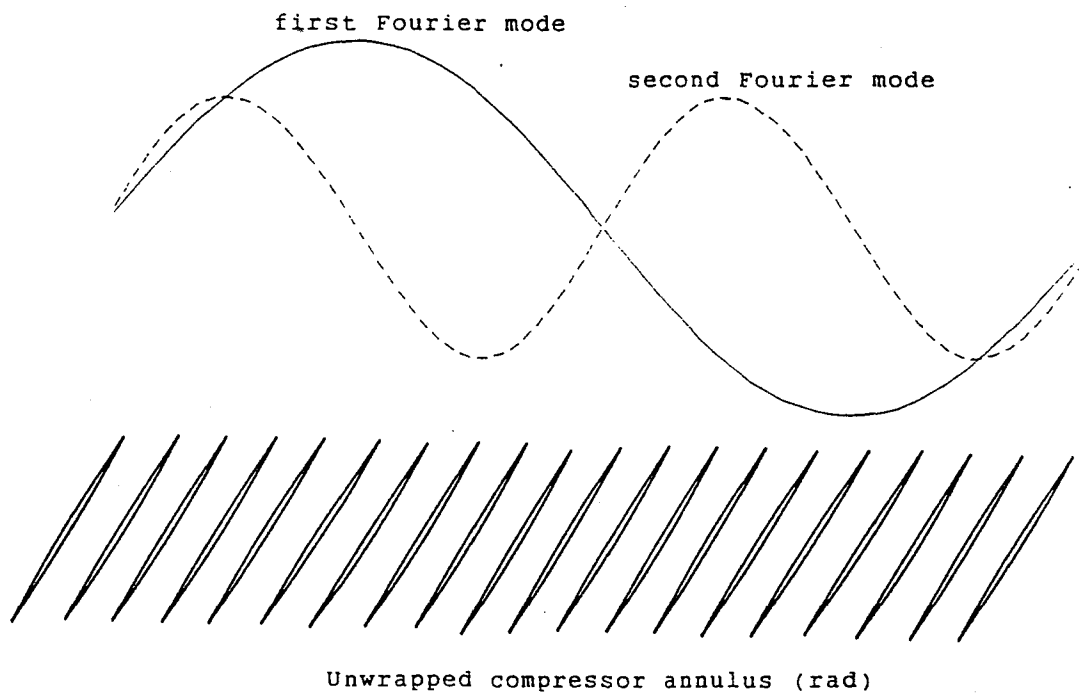


Figure 1.3 Modal waves [14]

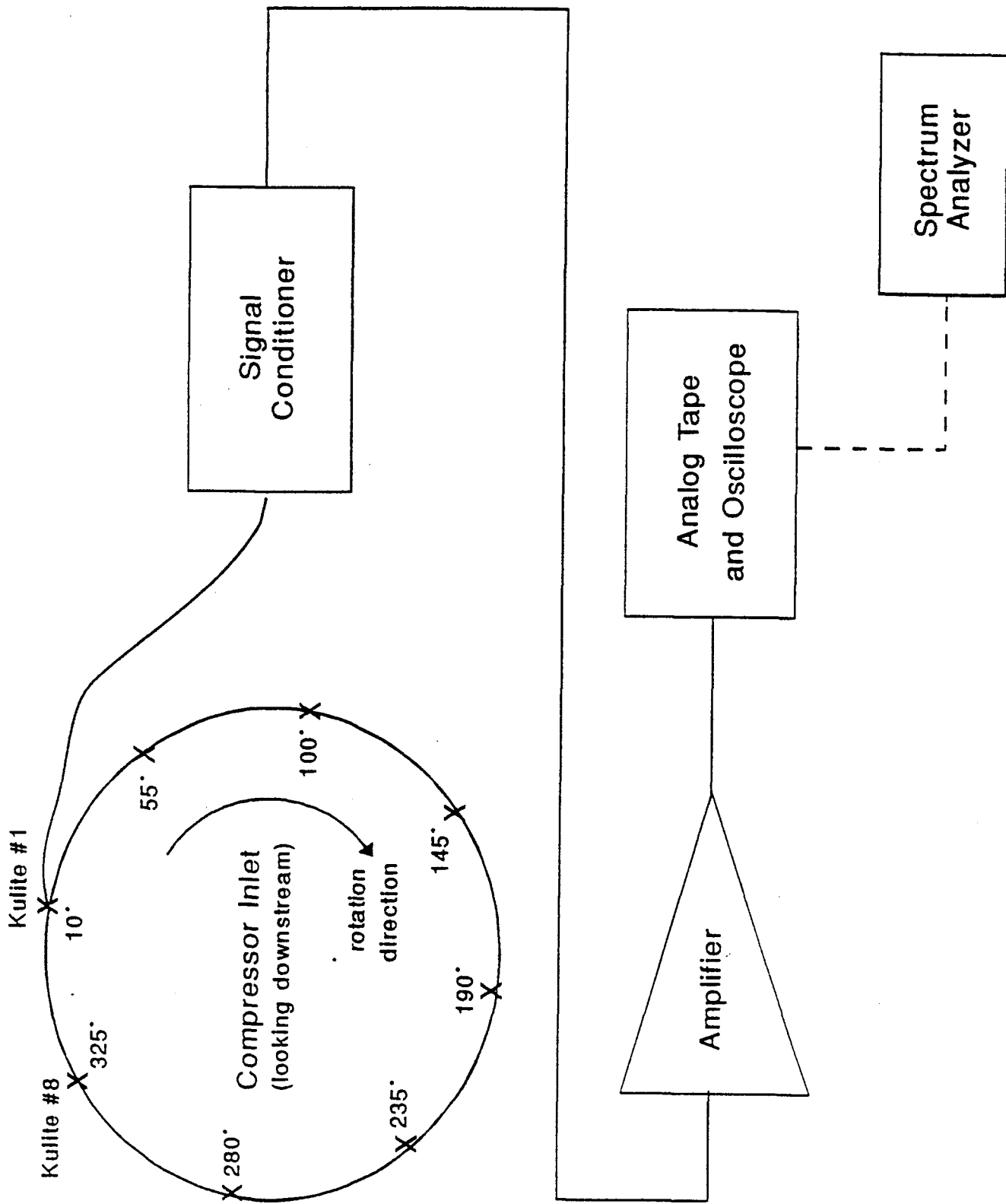


Figure 1.4 Compressor instrumentation for detection of modal waves [14]

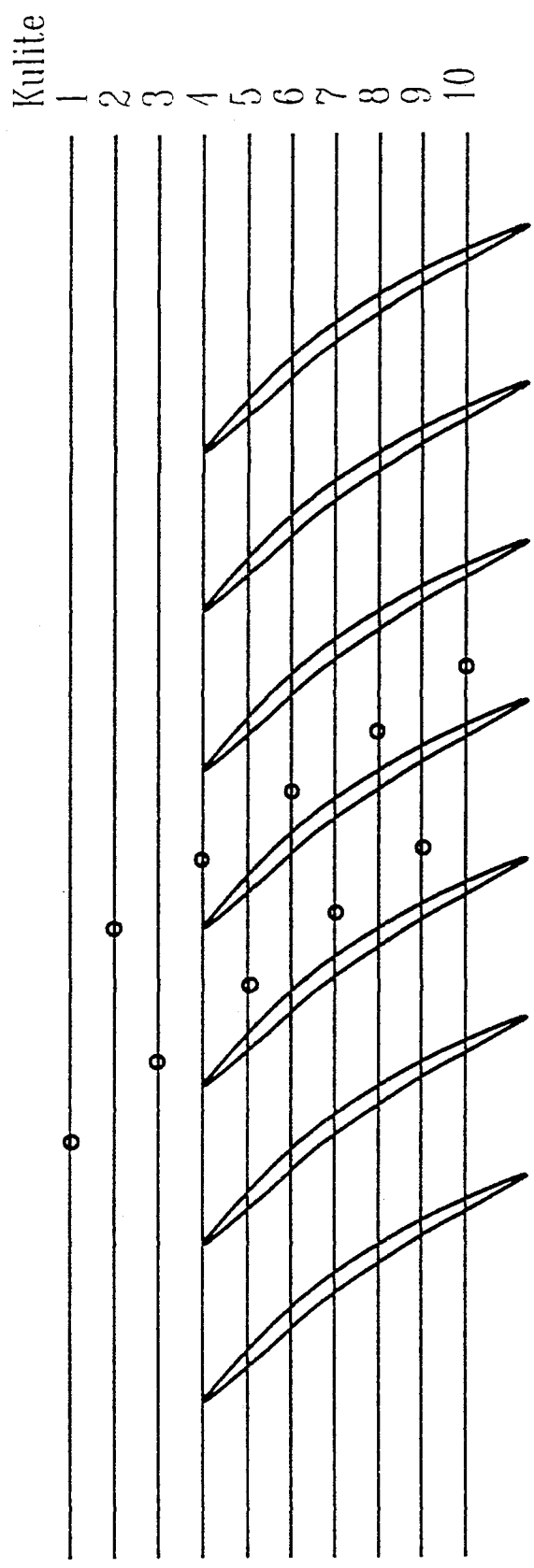


Figure 1.5 Compressor instrumentation for shock structure research [9]

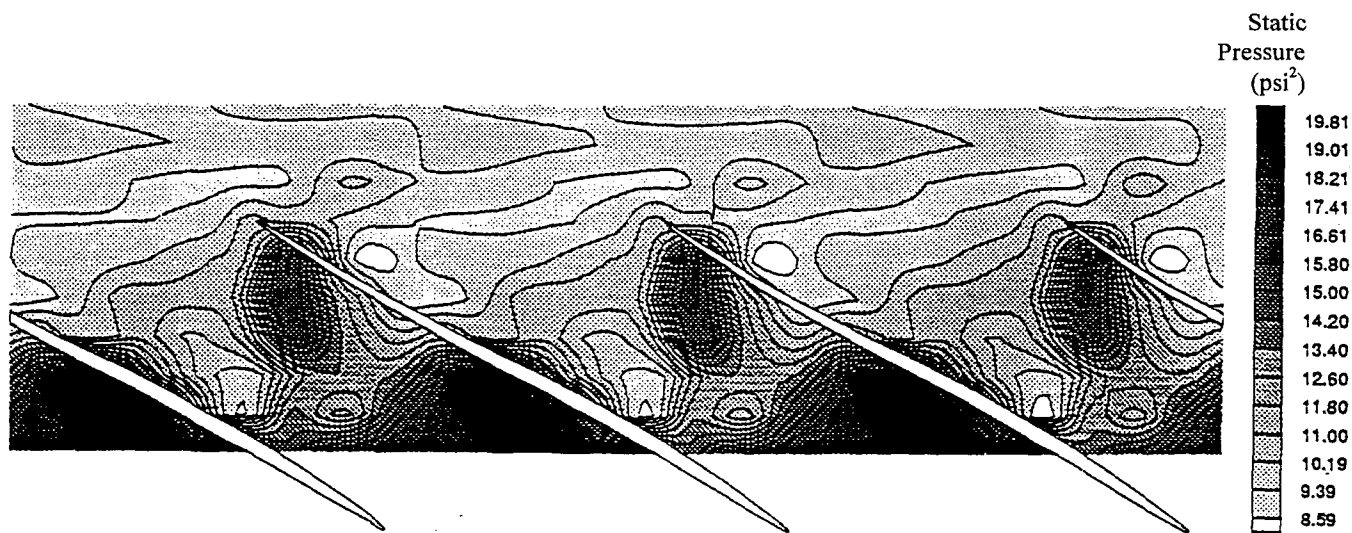


Figure 1.6 Compressor shock structure, throttle open [9]

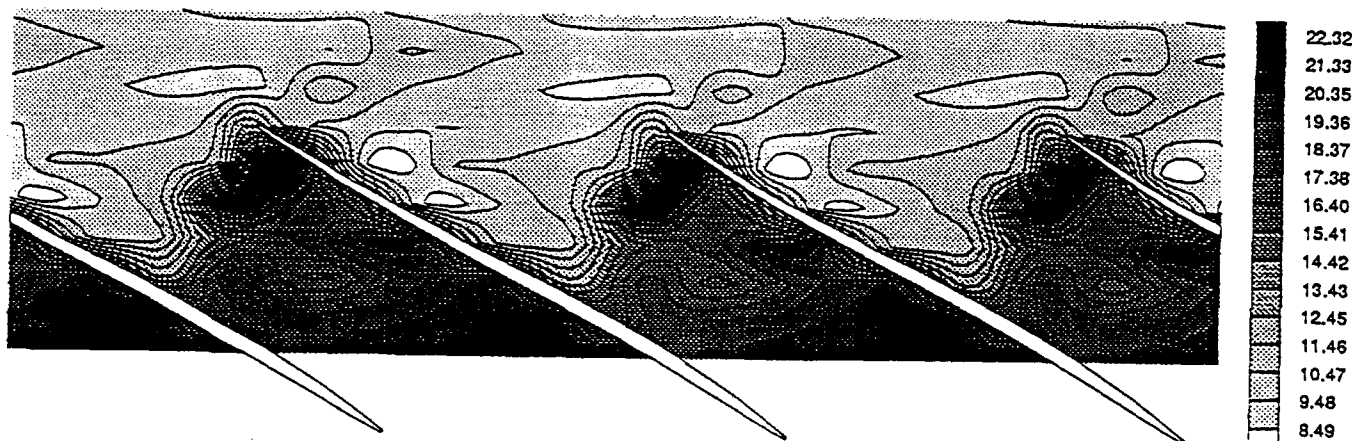


Figure 1.7 Compressor shock structure, mid-range throttle [9]

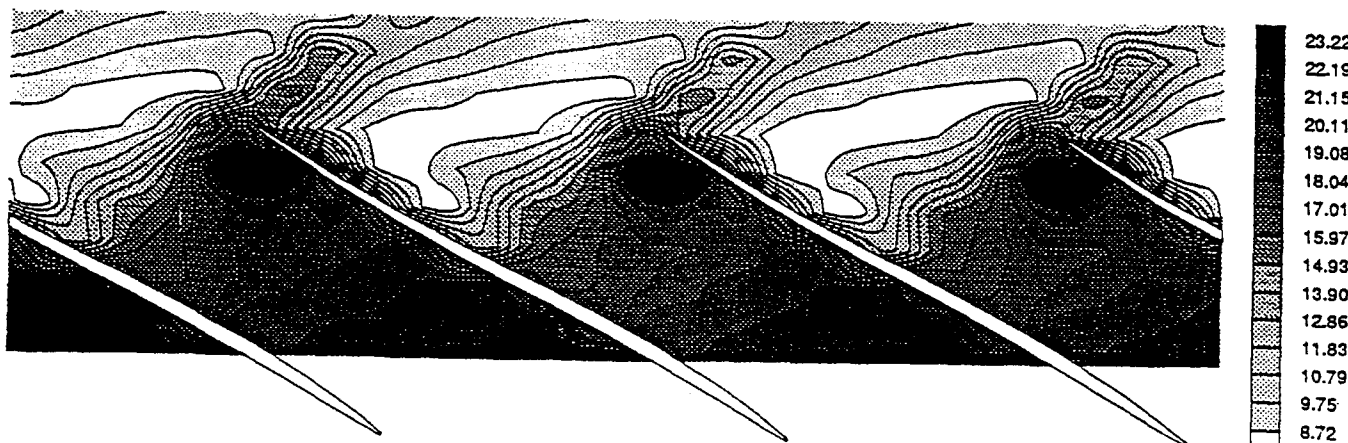


Figure 1.8 Compressor shock structure, near stall [9]

Example Correlation

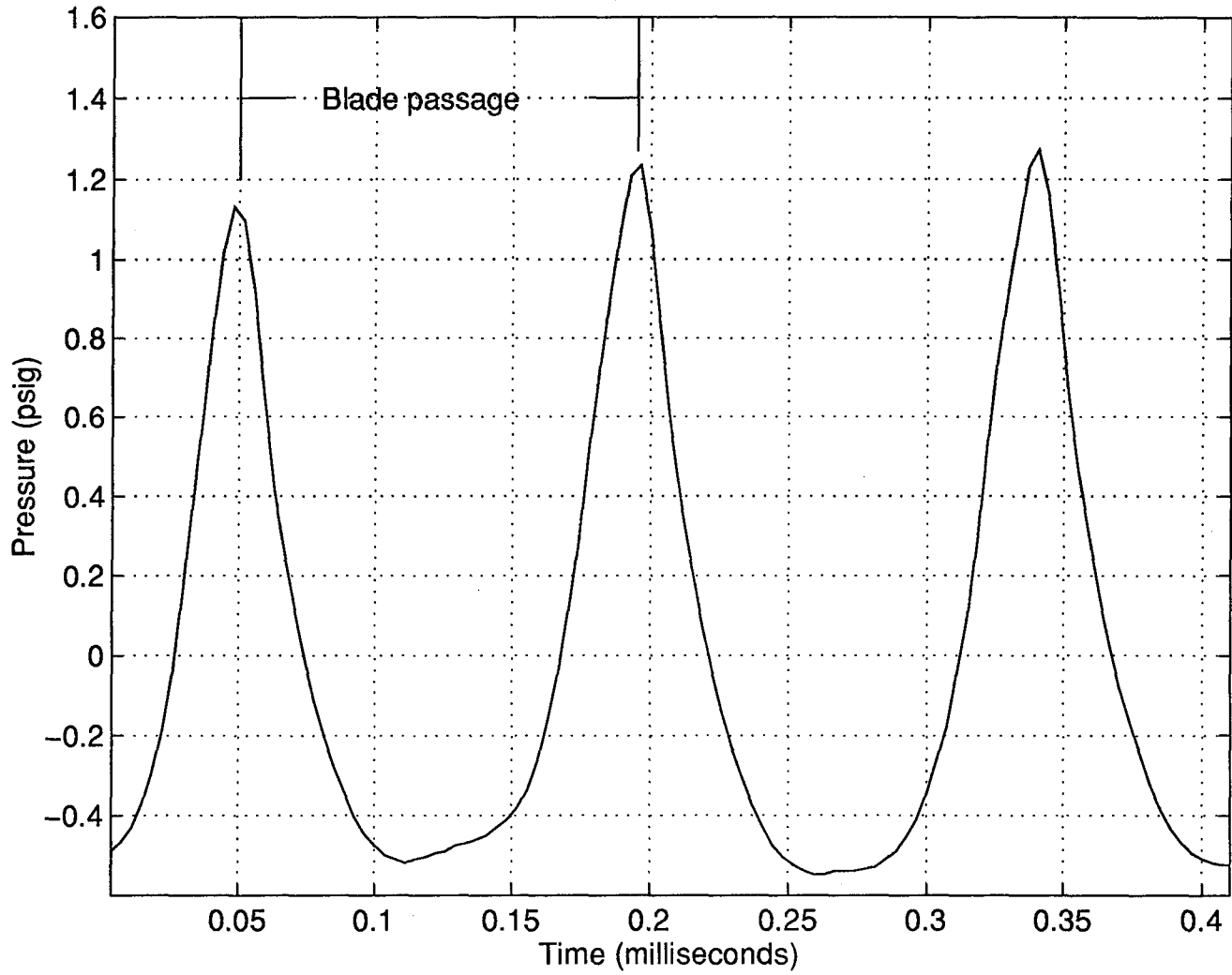


Figure 1.9 Typical compressor pressure signal (Rotor 4, 100%, Kulite #4 digitized at 270 kHz)

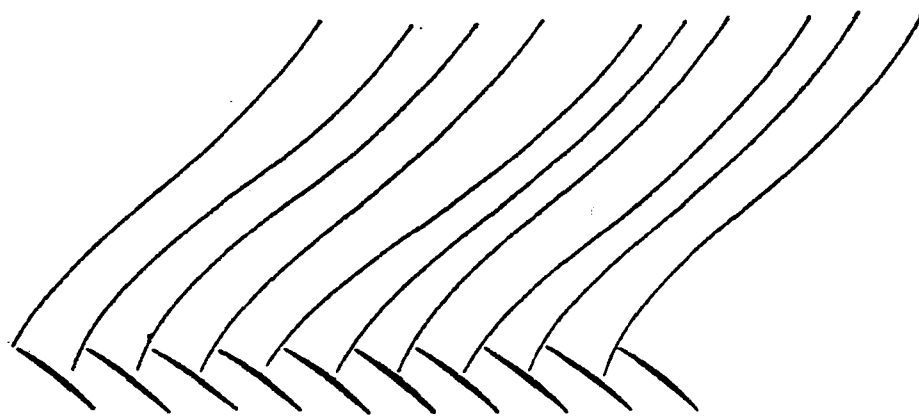


Figure 1.10 Compressor shock wave variations [13]

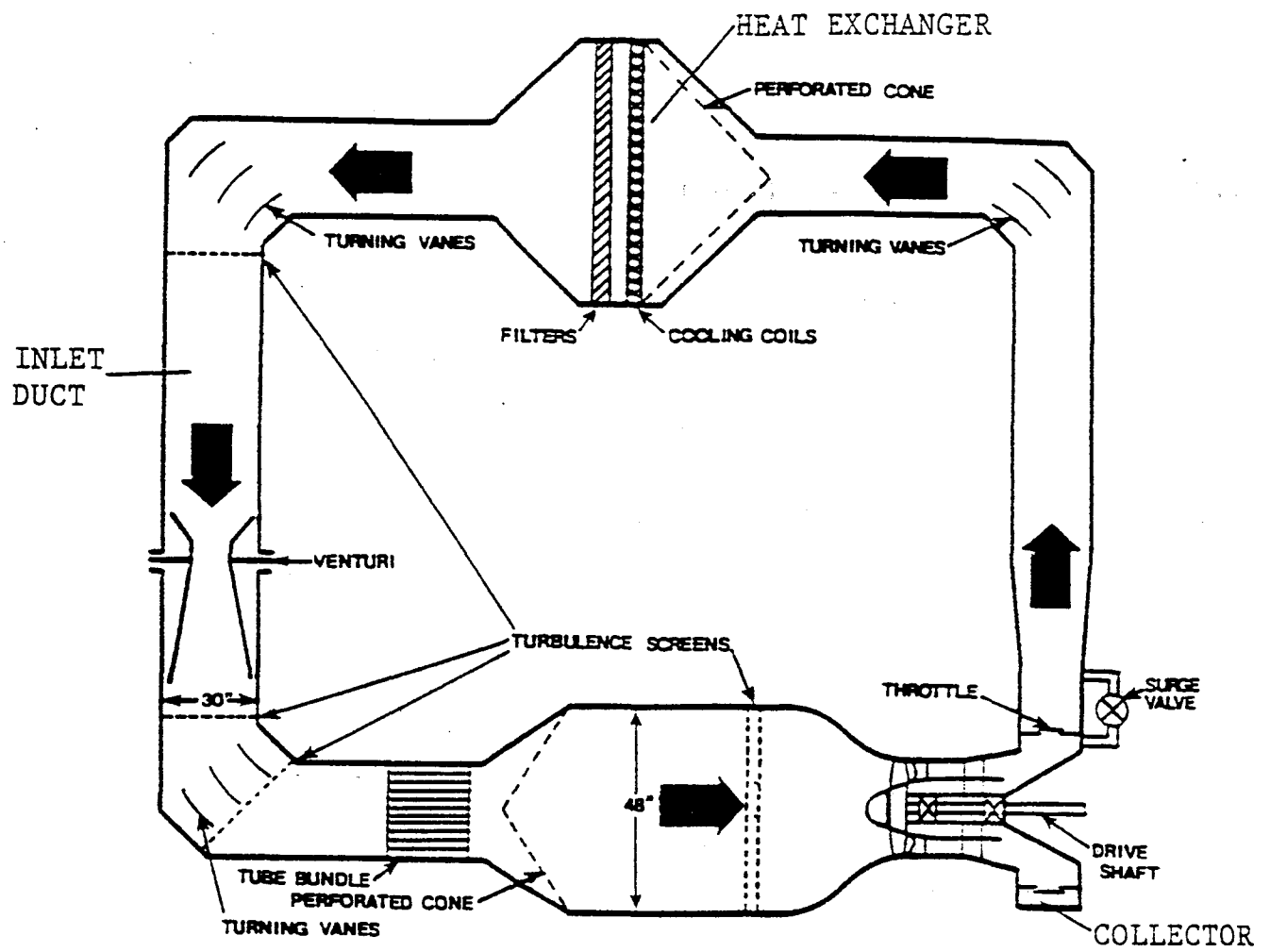


Figure 2.1 CARL test facility [14]

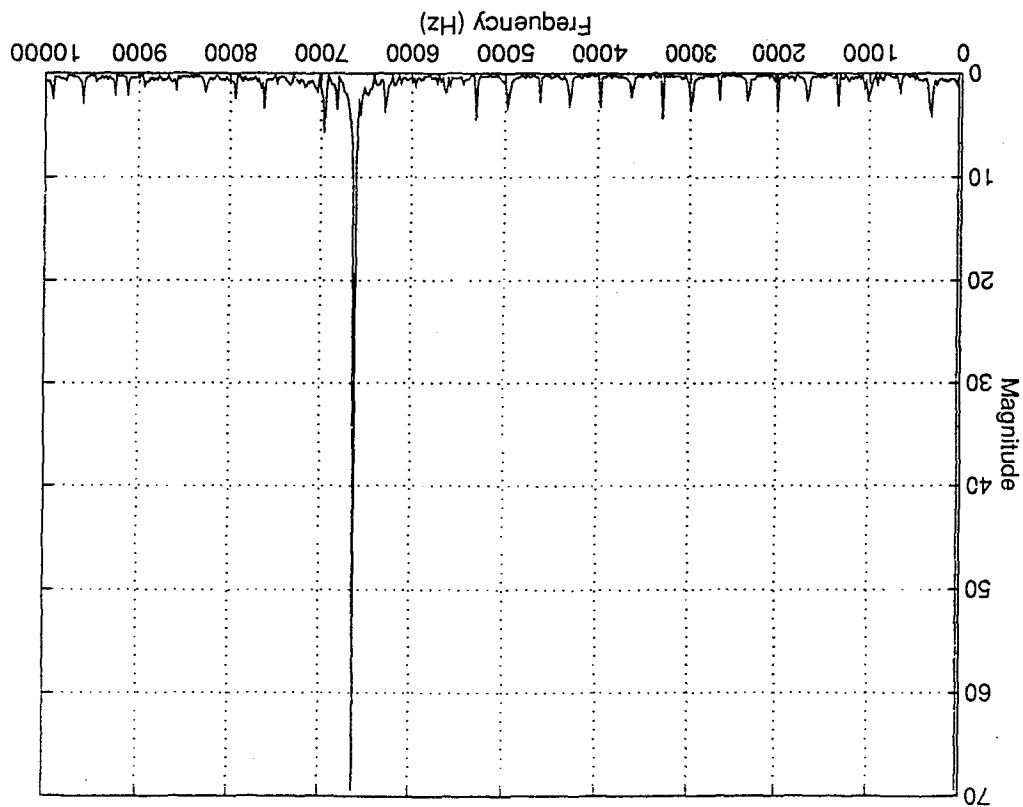


Figure 3.1 Example frequency spectrum
(Rotated 90 degrees for comparison)

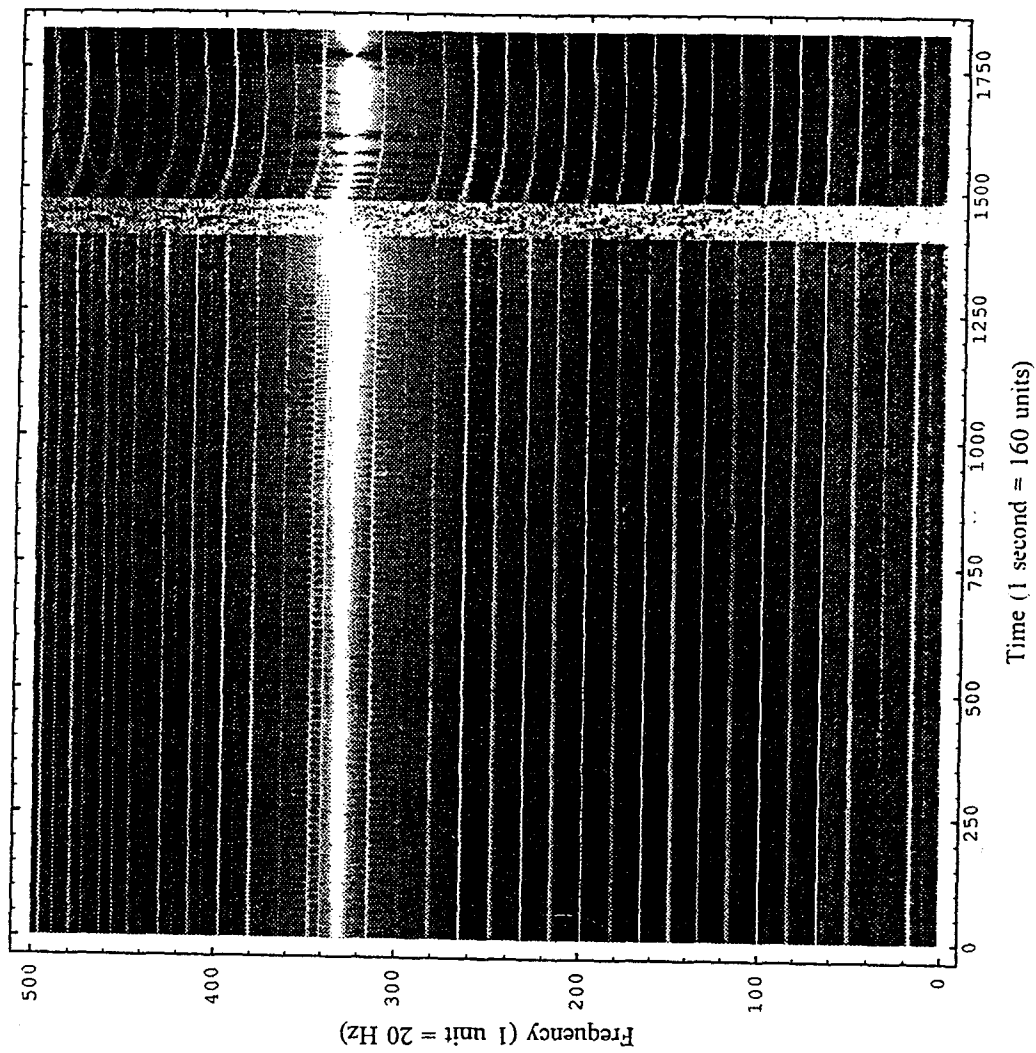


Figure 3.2 Example Time-Frequency-Magnitude plot

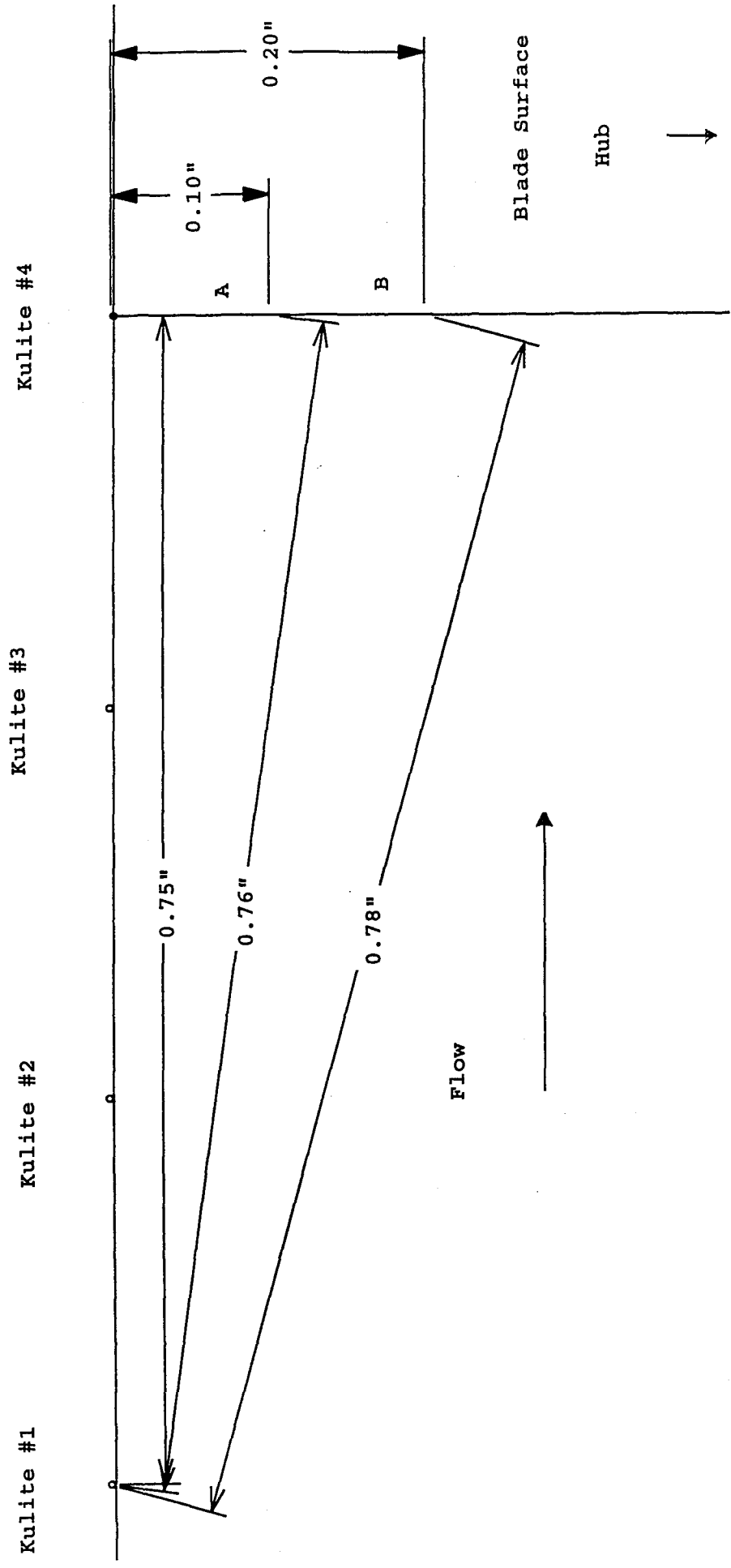


Figure 3.3 Three dimensional effects on Kulite pressure transducers

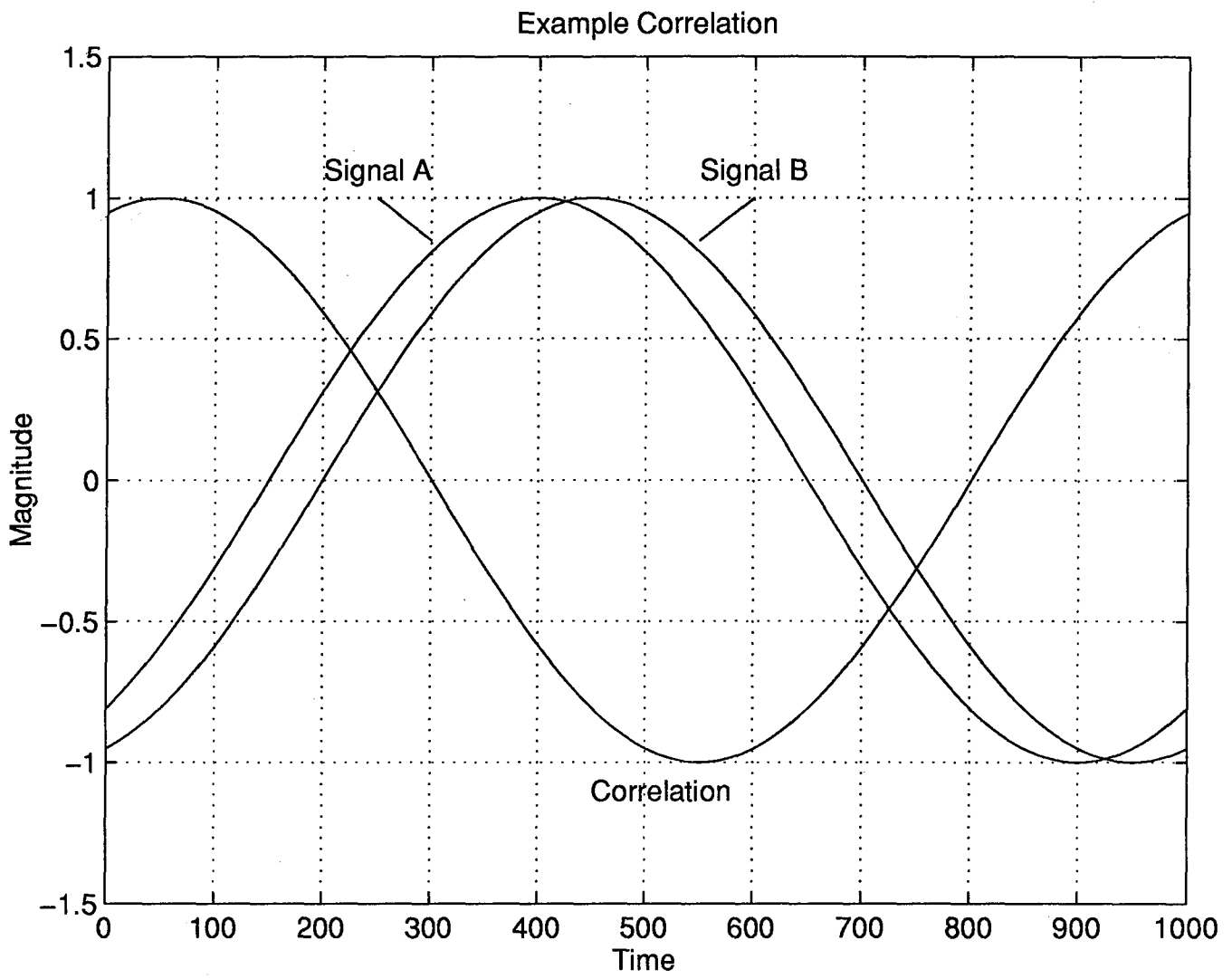


Figure 3.4 Example Cross-Correlation

Fig 3-5a: Sine and Cosine Waves

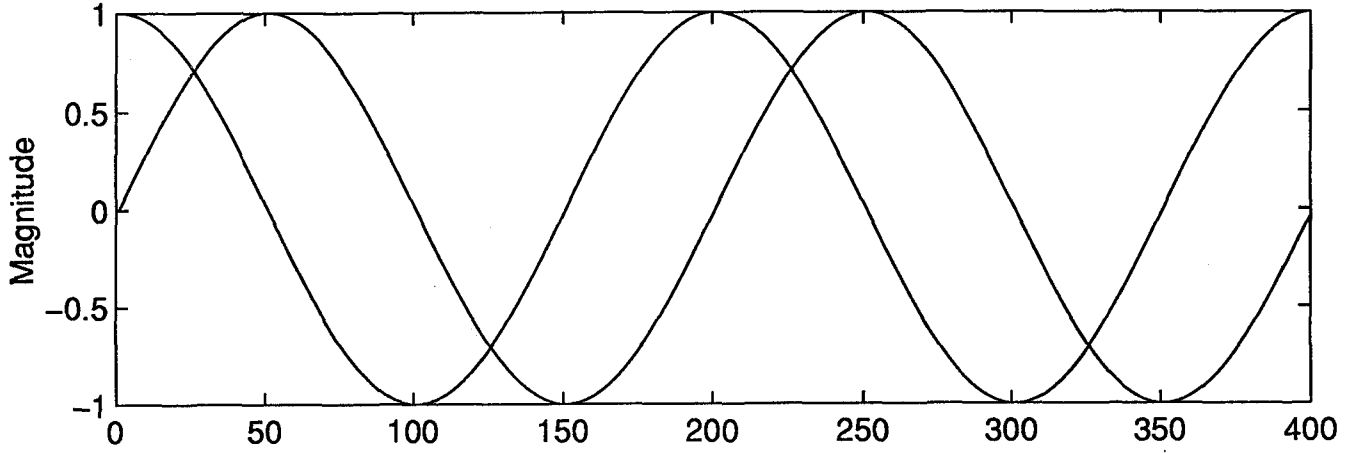


Fig 3-5b: Biased Correlation of Sine and Cosine Waves

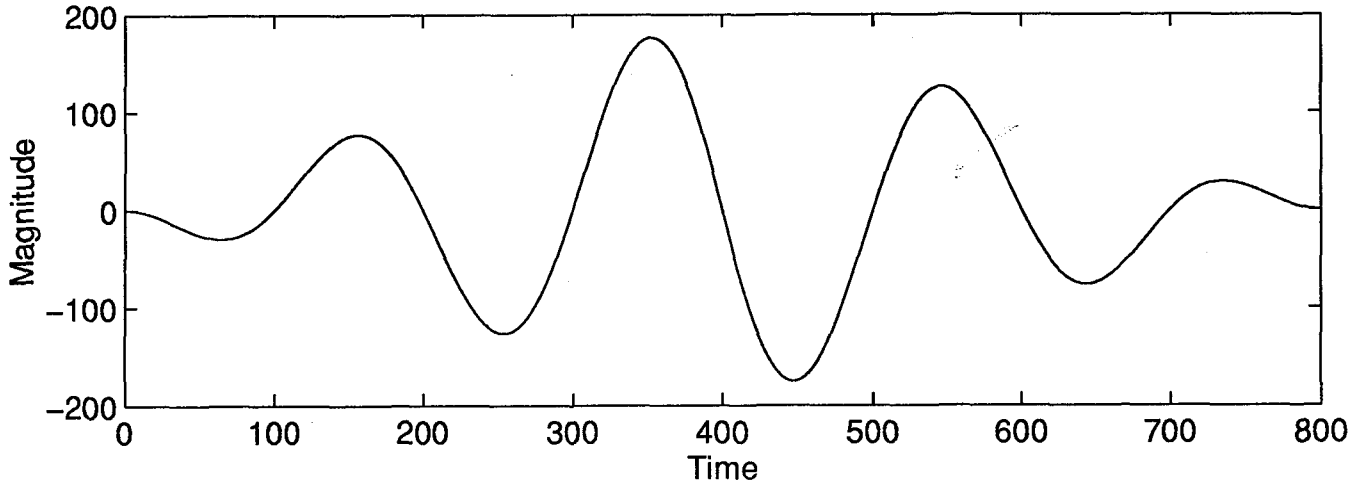


Figure 3.5 Cross-Correlation Resulting in Bias

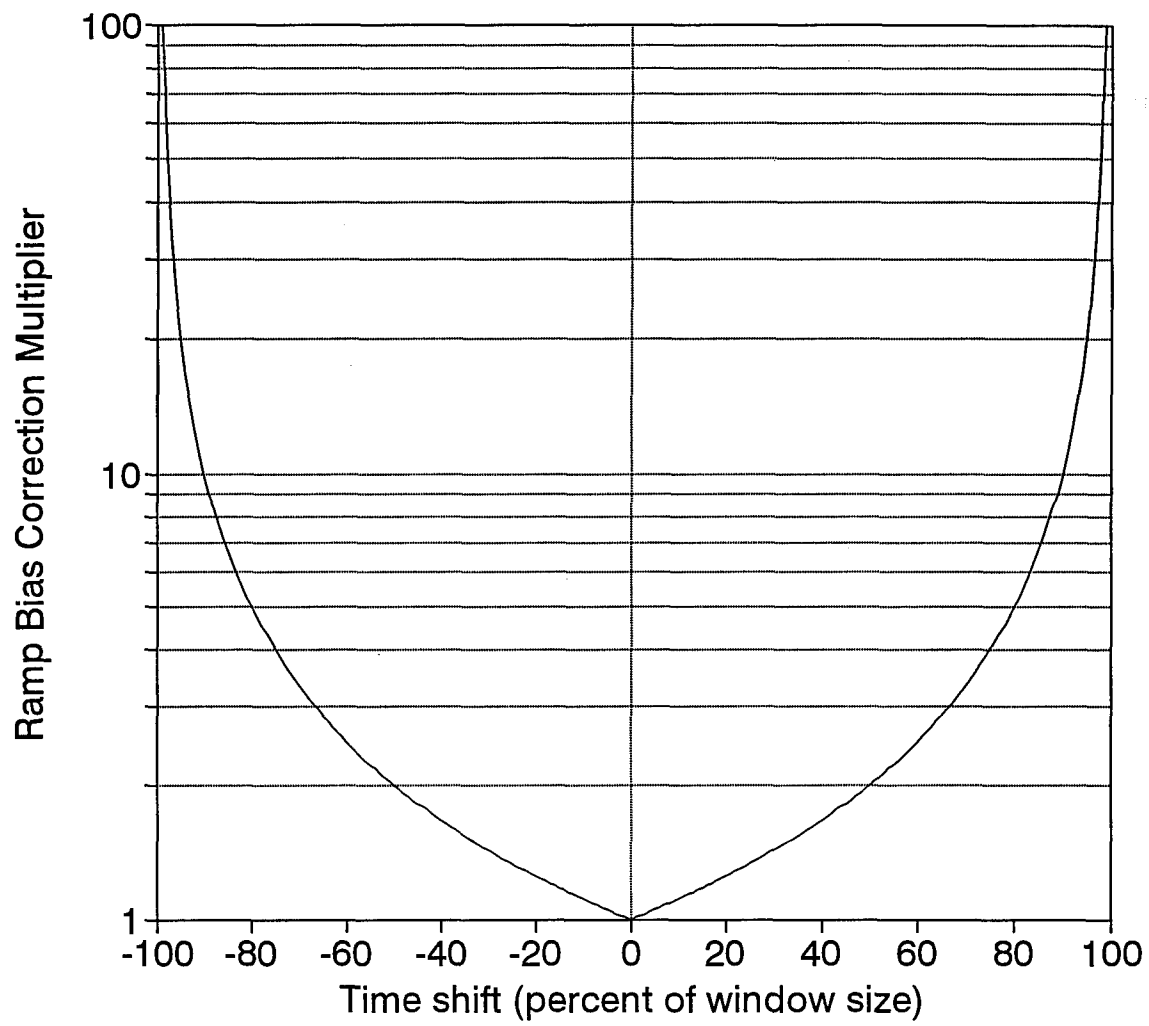


Figure 3.6 Ramp Bias Correction Multiplier

Rotor 4: 90%, Kulite #4

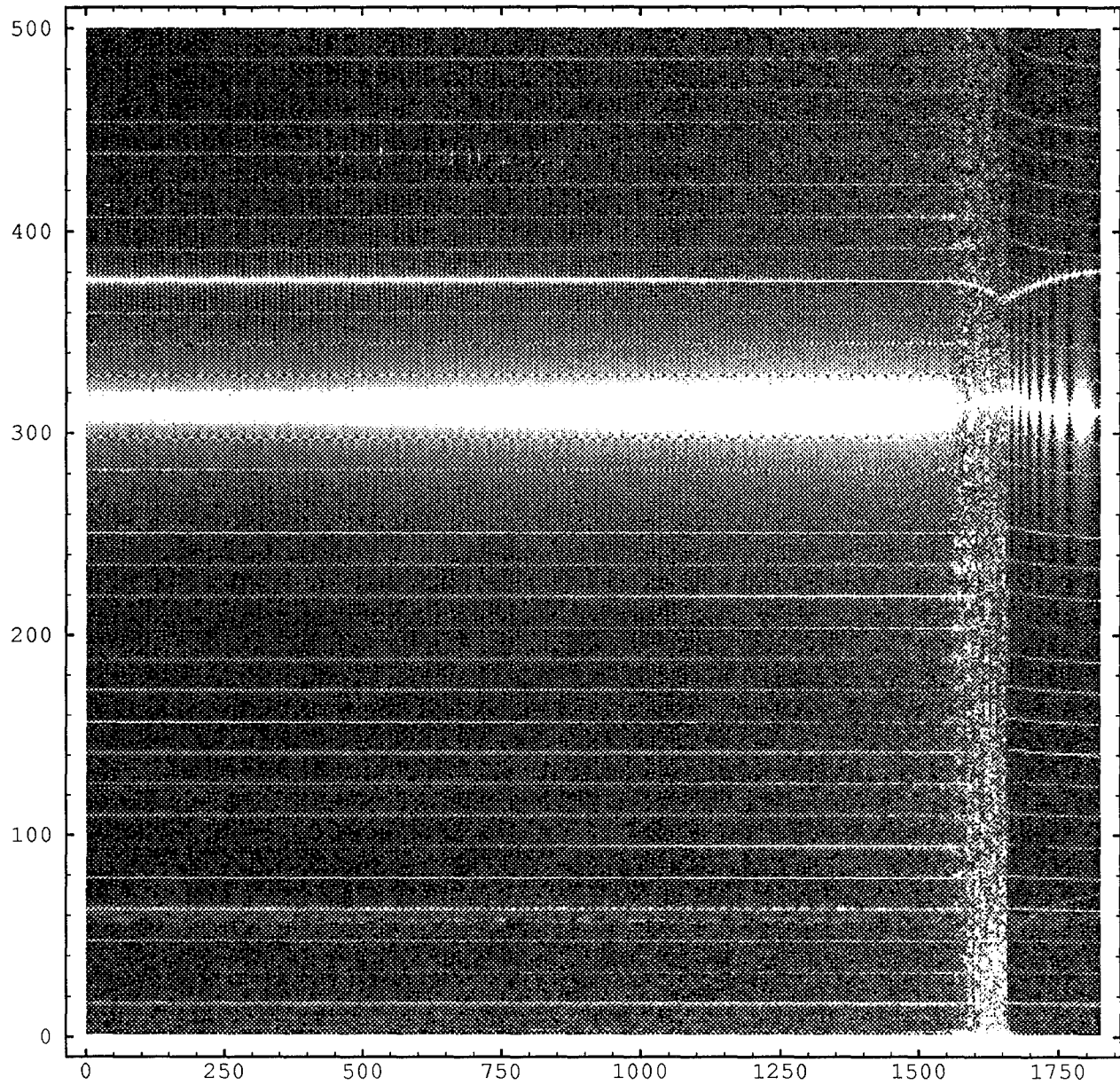


Figure 4.1 Rotor 4, 90%, Kulite #4: TFM Plot

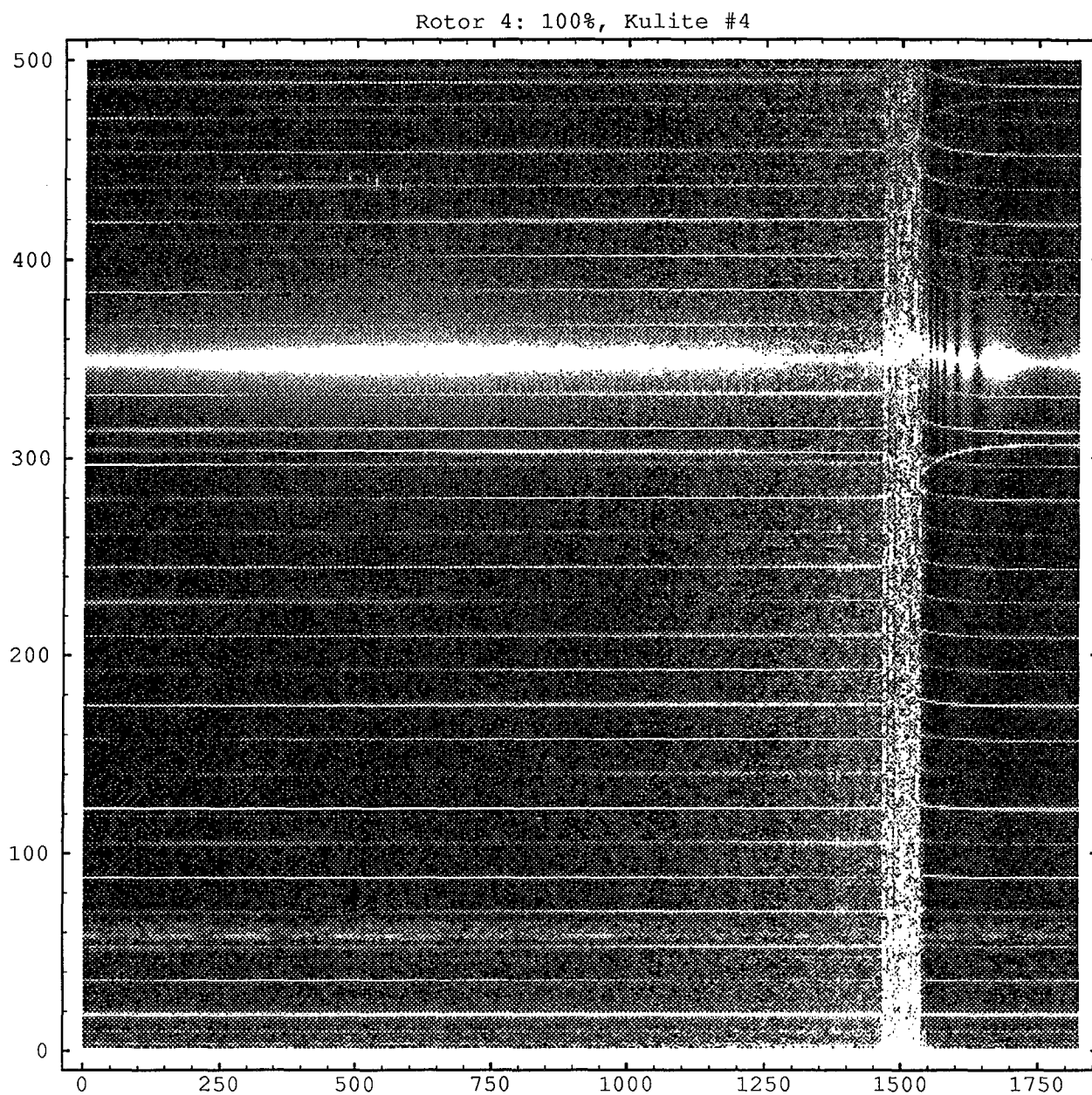


Figure 4.2 Rotor 4, 100%, Kulite #4: TFM Plot

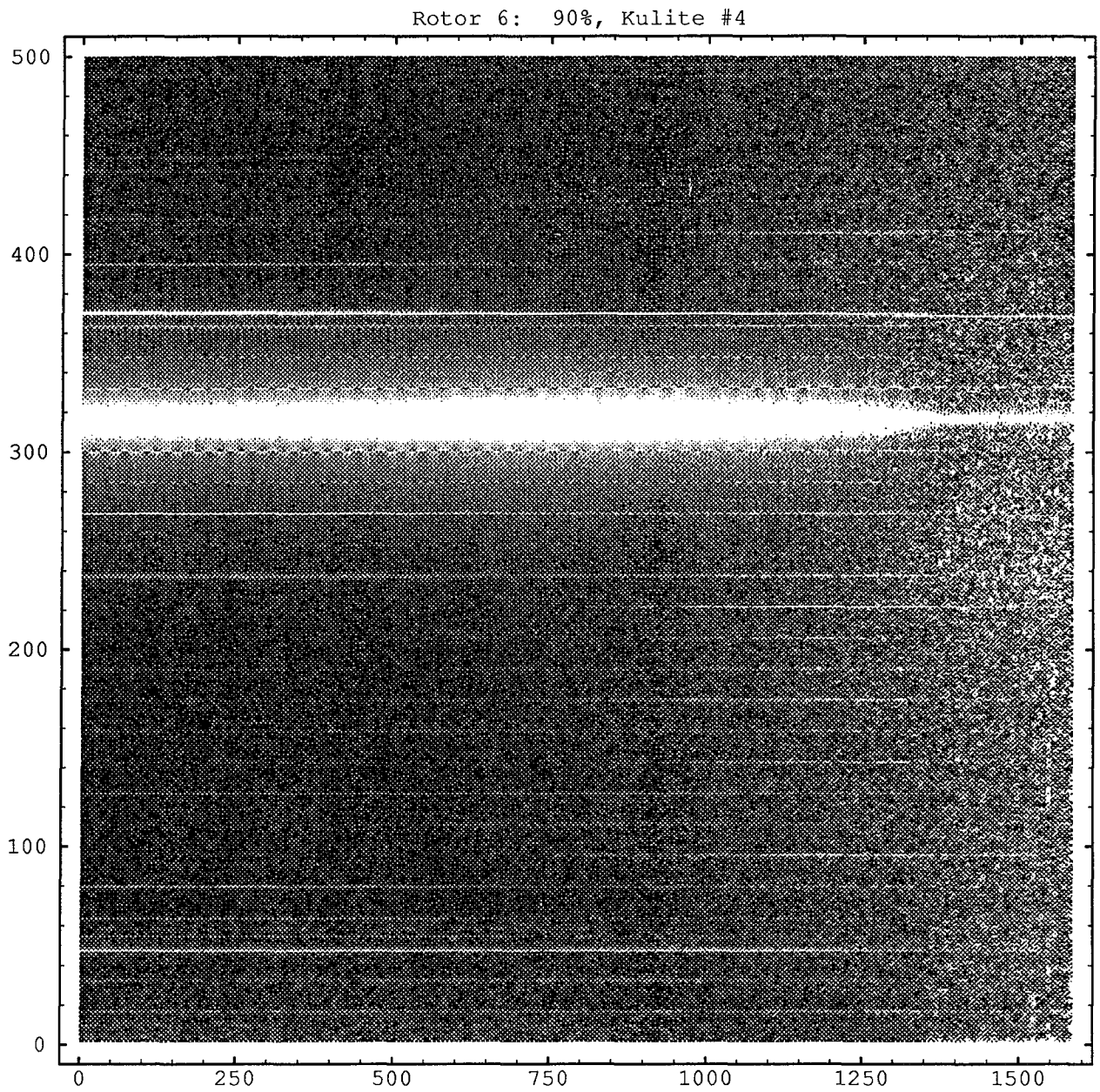


Figure 4.3 Rotor 6, 90%, Kulite #4: TFM Plot

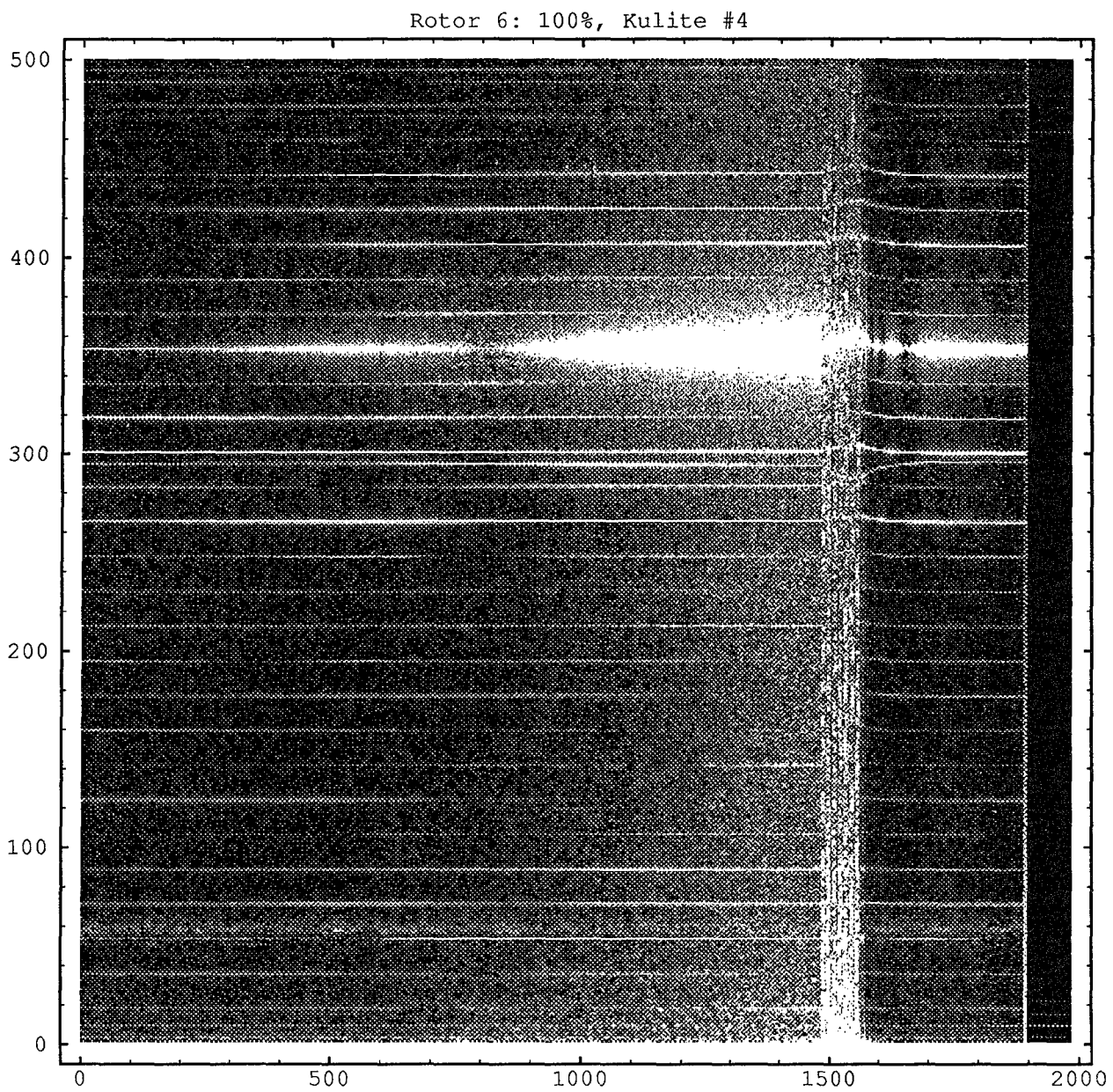


Figure 4.4 Rotor 6, 100%, Kulite #4: TFM Plot

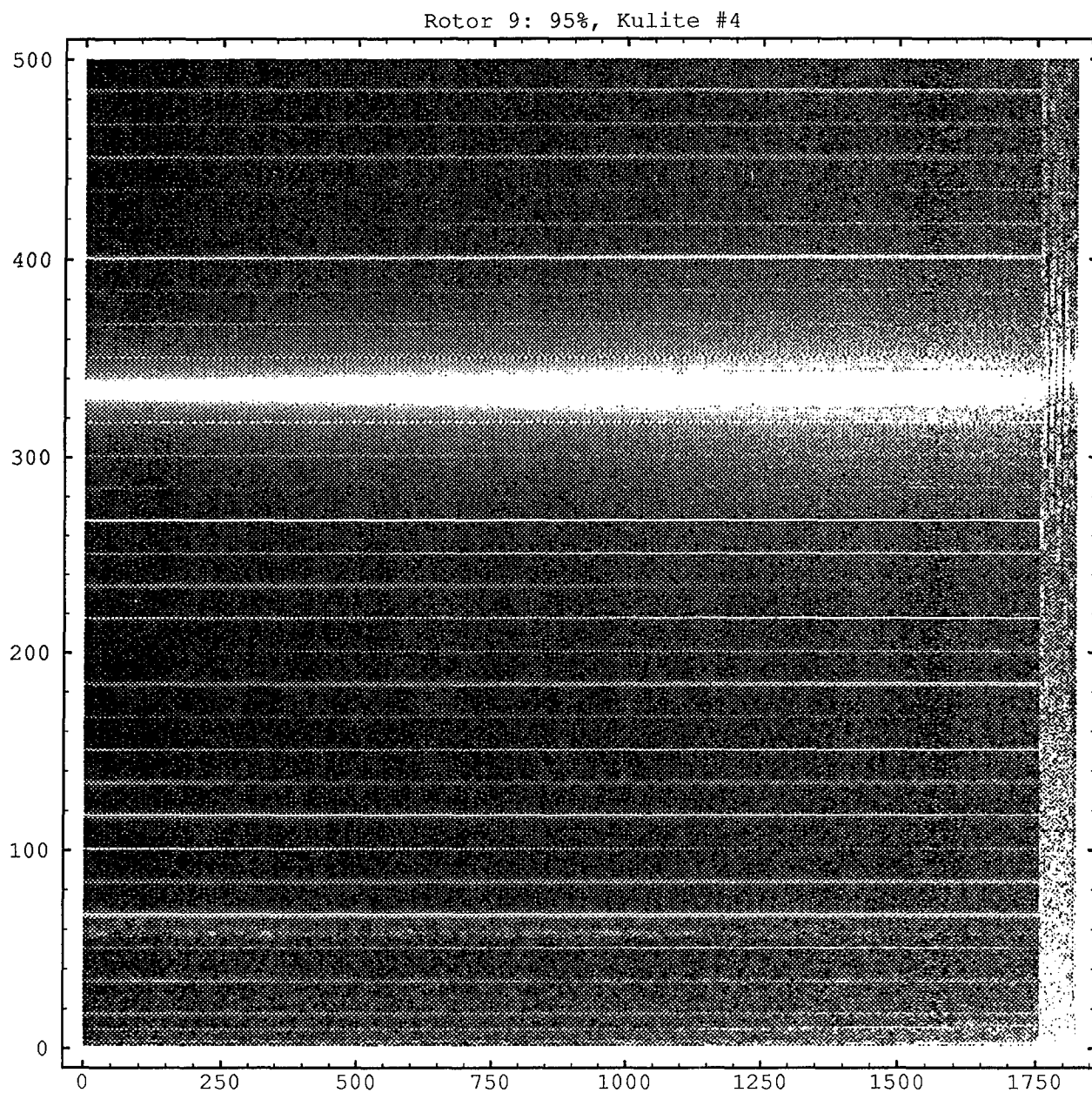


Figure 4.5 Rotor 9, 95%, Kulite #4: TFM Plot

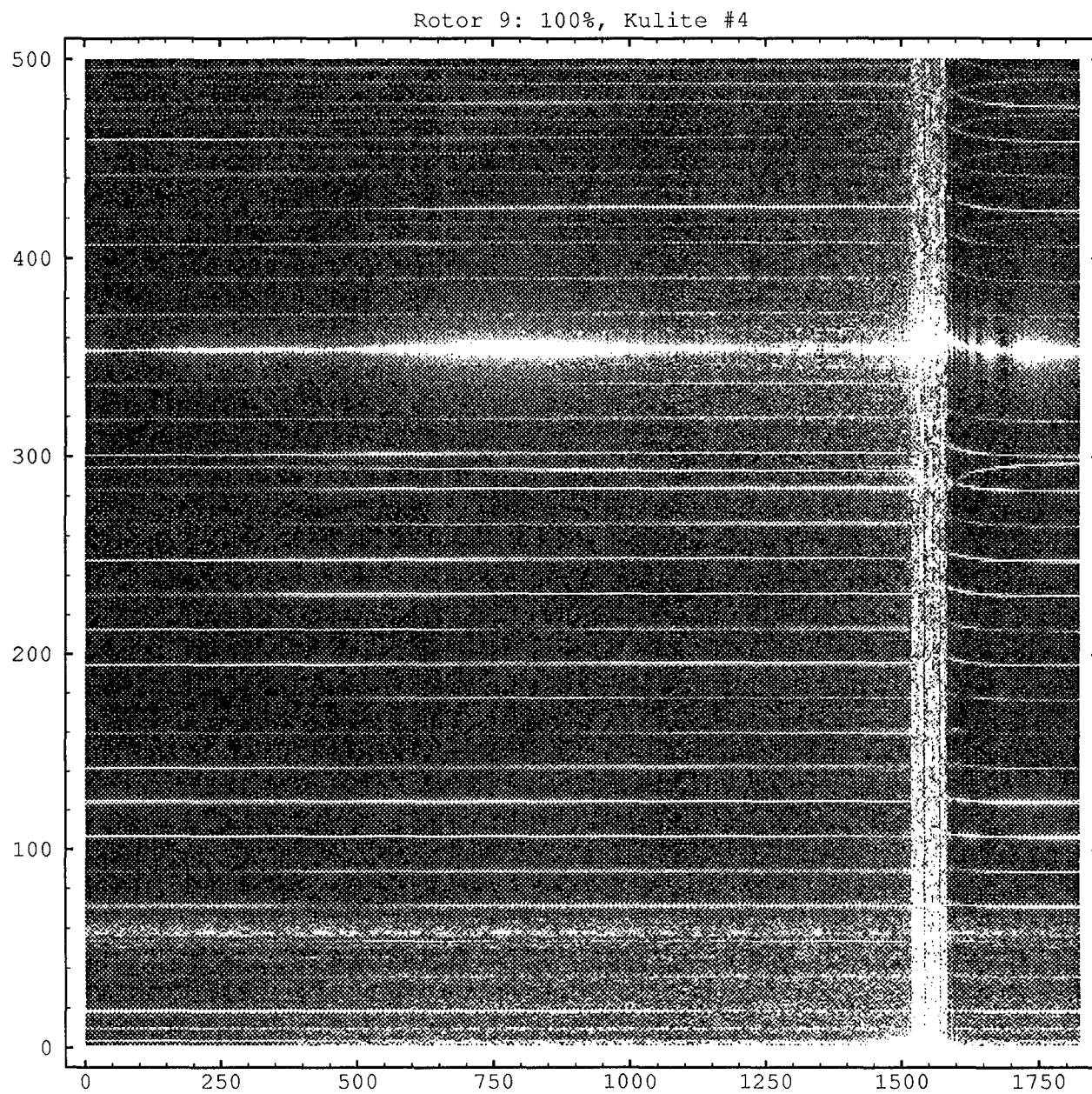


Figure 4.6 Rotor 9, 100%, Kulite #4: TFM Plot

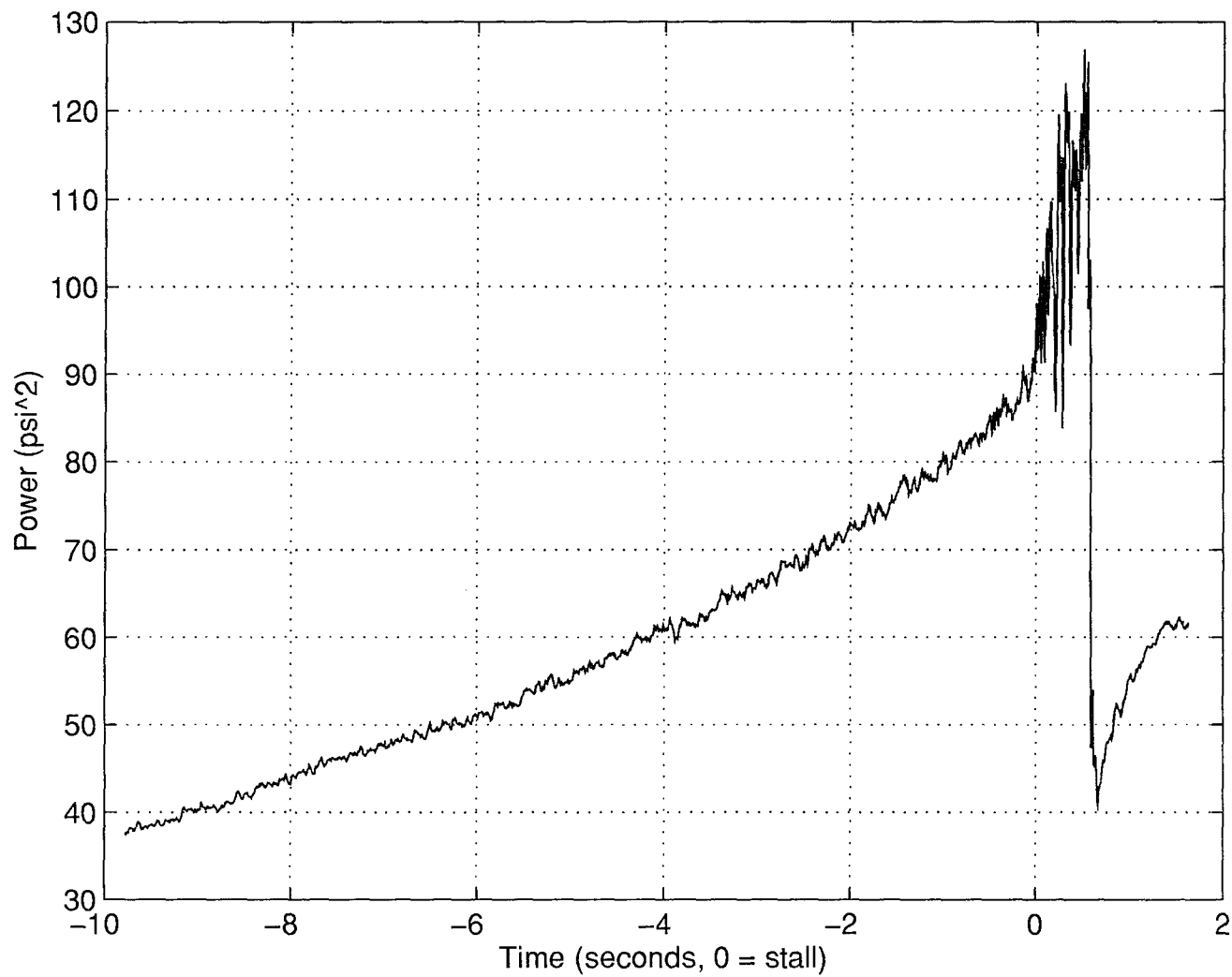


Figure 4.7 Rotor 4, 90%, Kulite #1: Total Signal Power (less DC contribution)

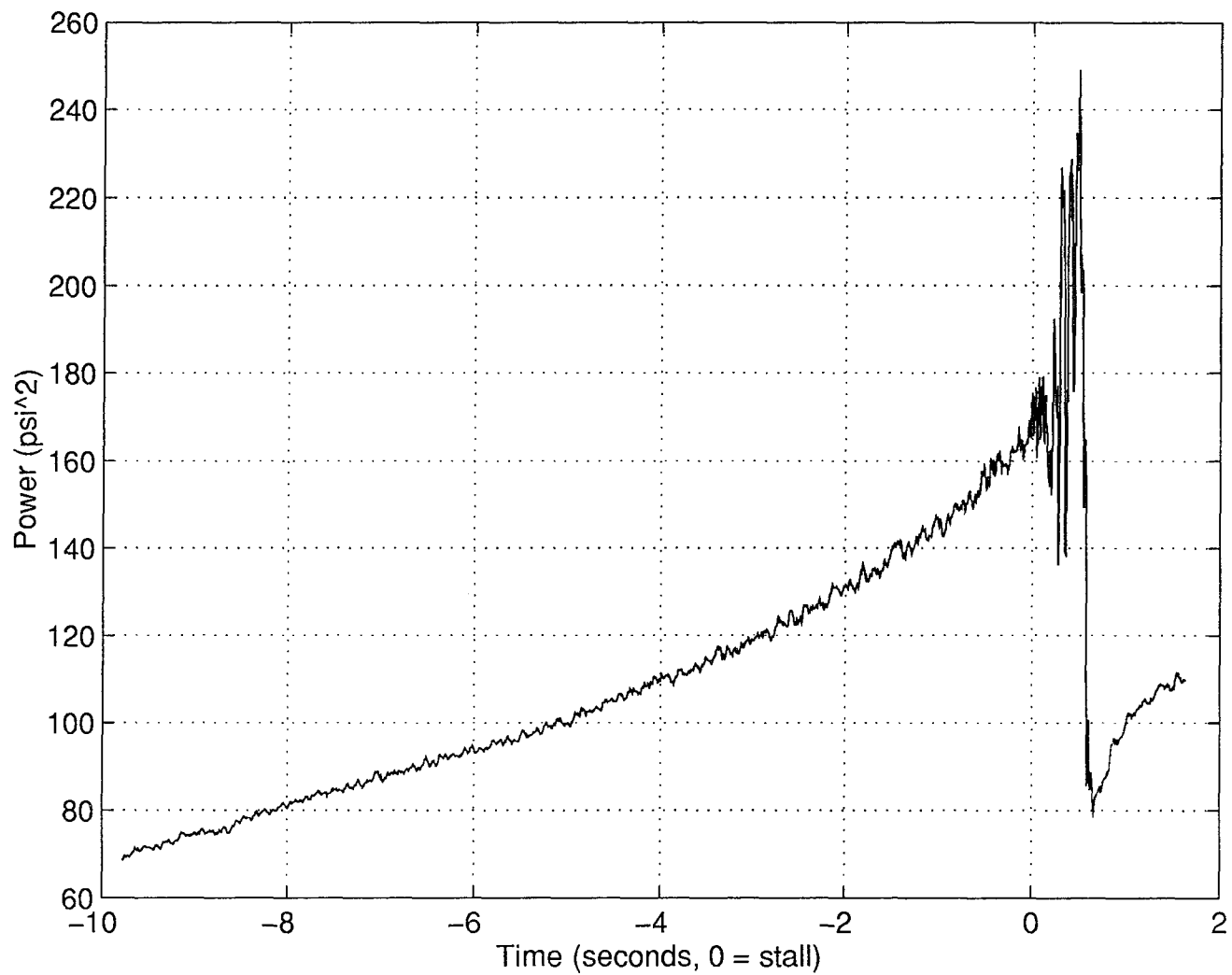


Figure 4.8 Rotor 4, 90%, Kulite #2: Total Signal Power (less DC contribution)

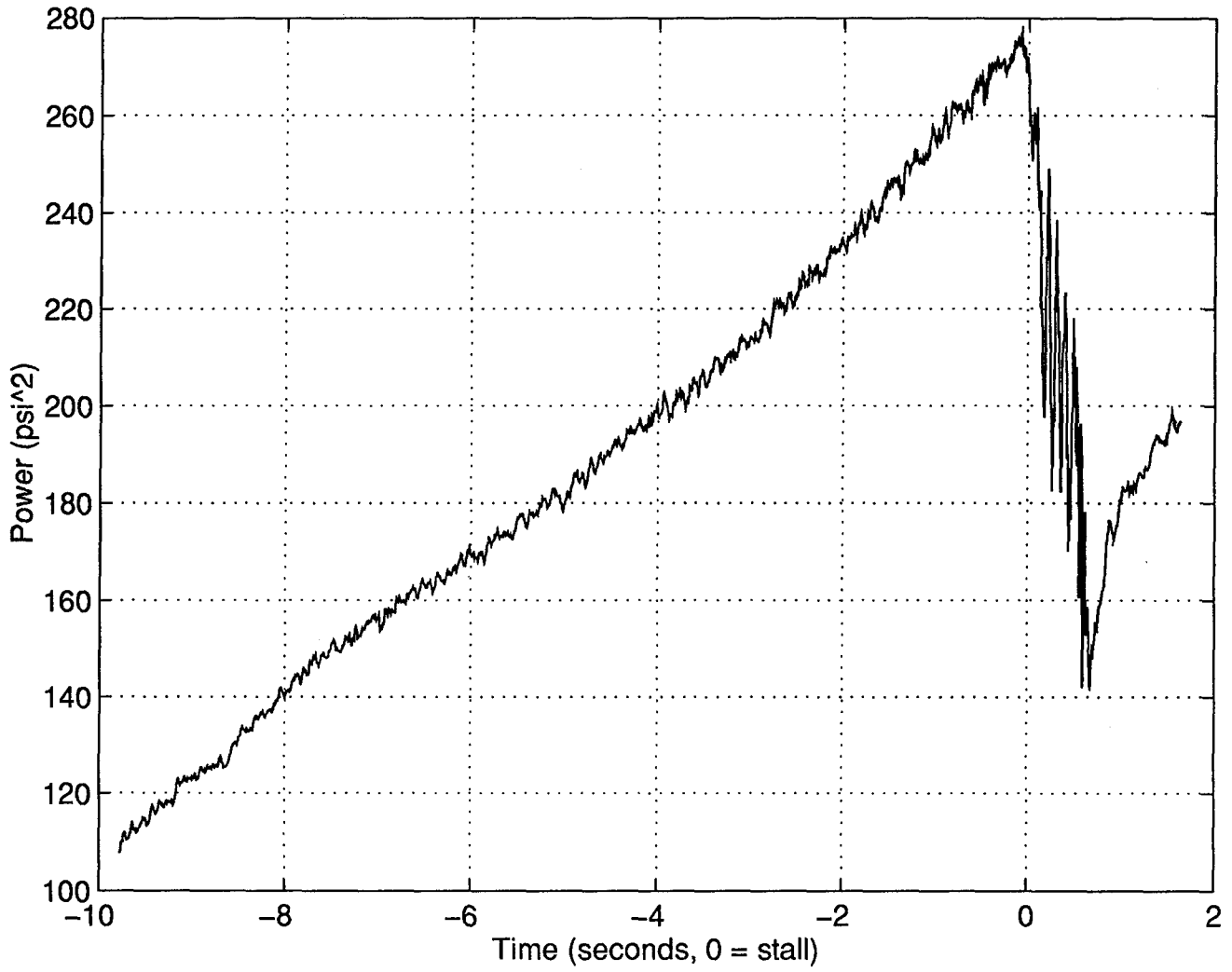


Figure 4.9 Rotor 4, 90%, Kulite #3: Total Signal Power (less DC contribution)

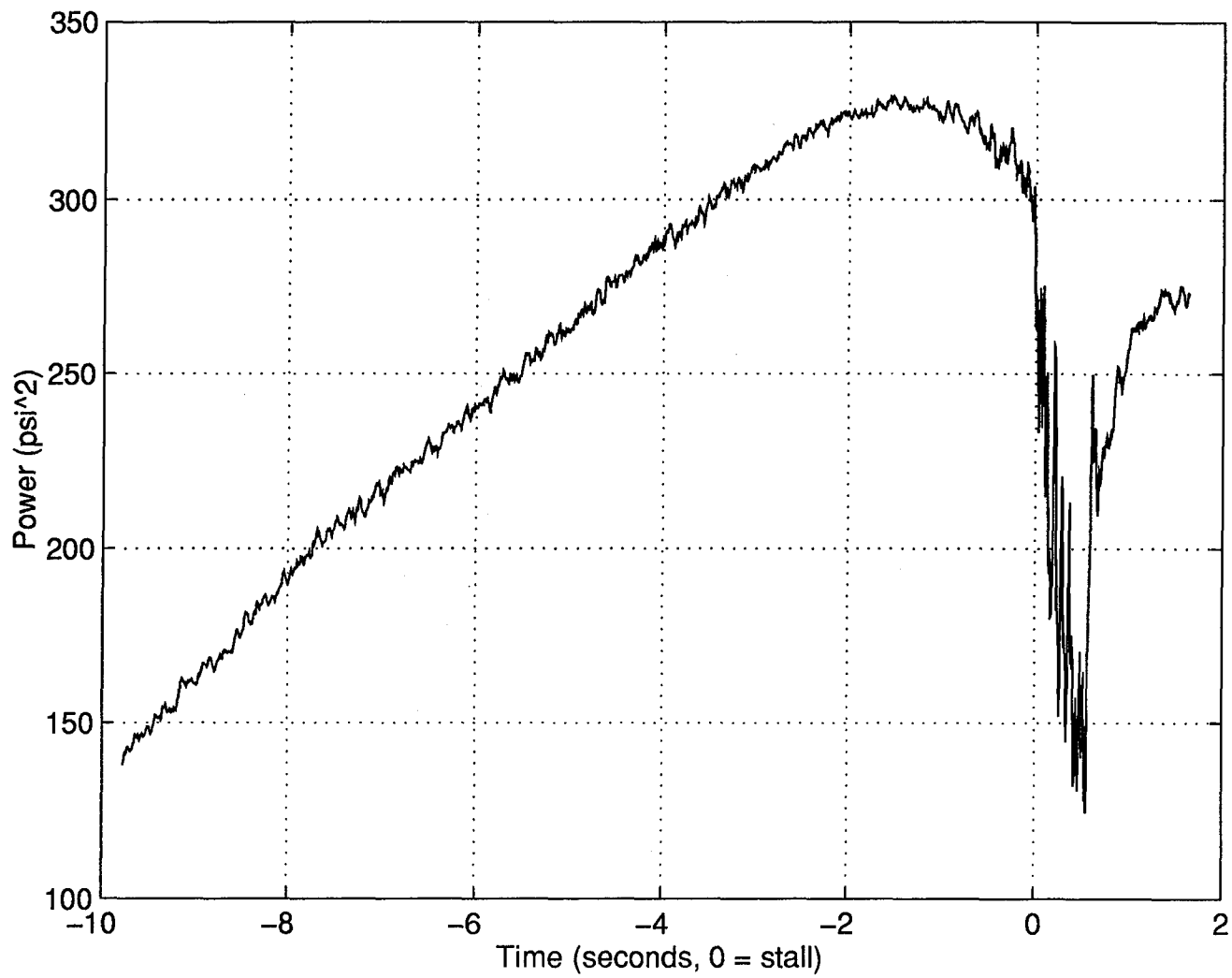


Figure 4.10 Rotor 4, 90%, Kulite #4: Total Signal Power (less DC contribution)

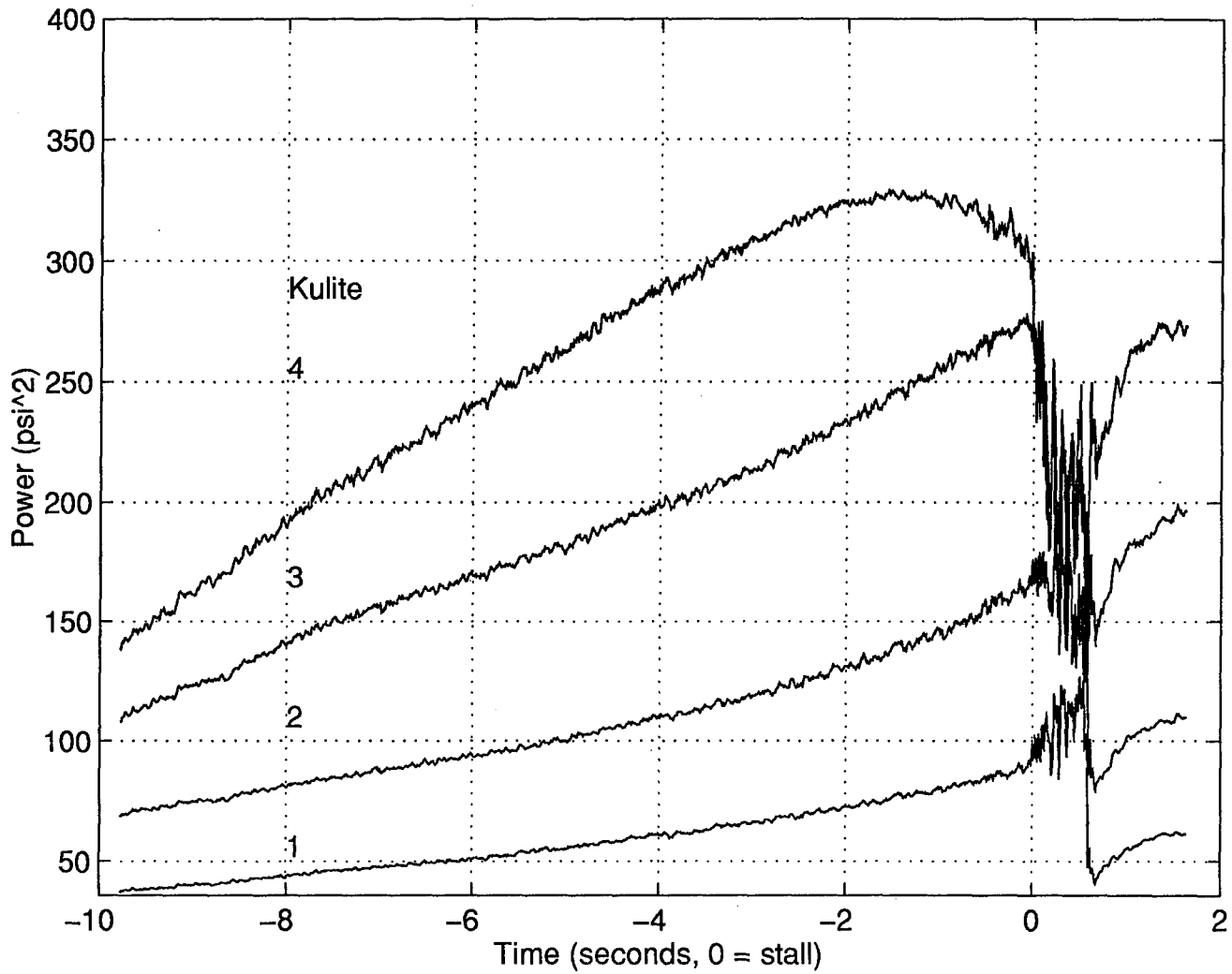


Figure 4.11 Rotor 4, 90%, Kulites #1 through #4: Total Signal Power (less DC contribution)

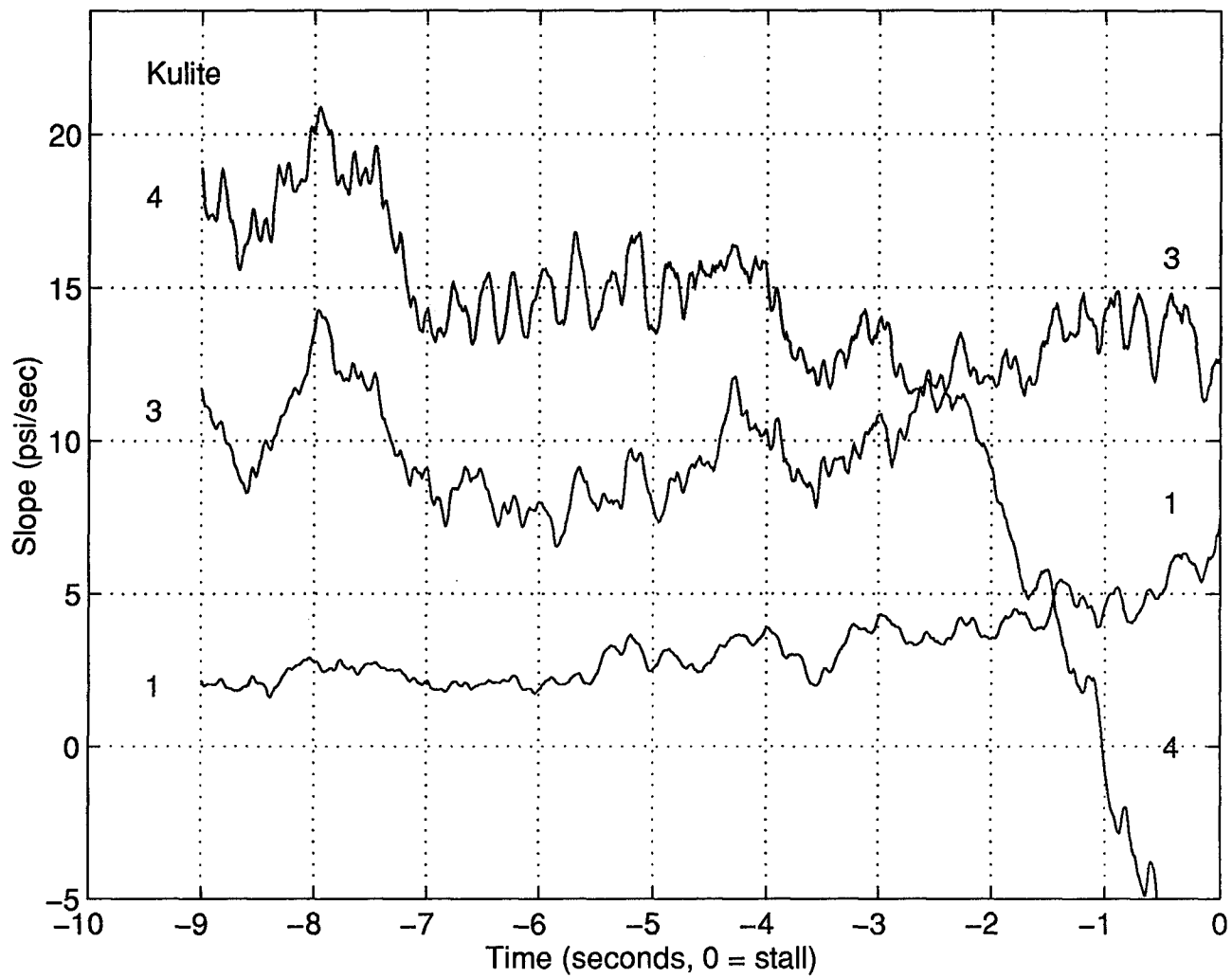


Figure 4.12a Rotor 4, 90%: Comparison of Slope of Signal Power

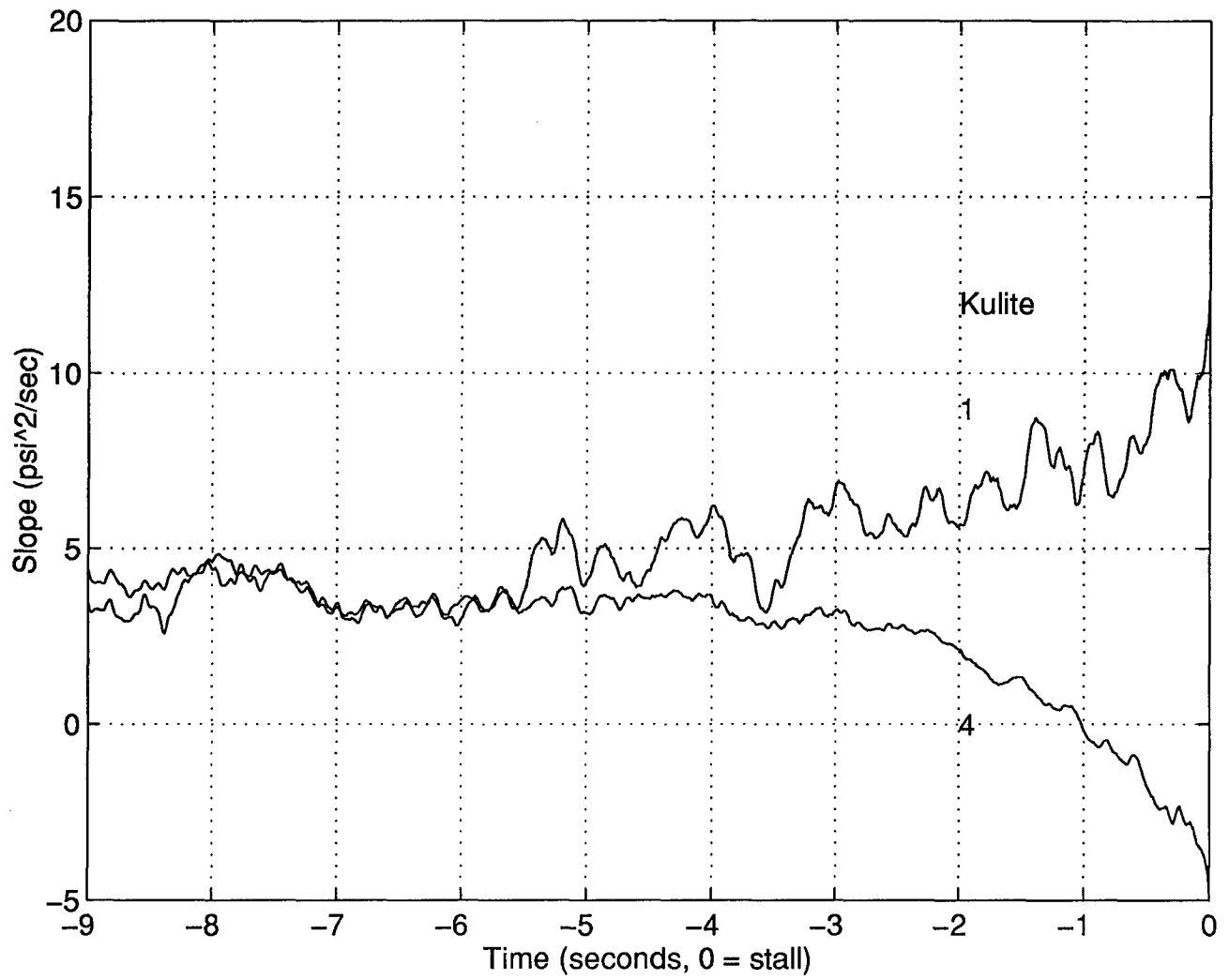


Figure 4.12b Rotor 4, 90%: Comparison of Slope of Signal Power (Kulite #4 scaled by $\delta=0.145$)

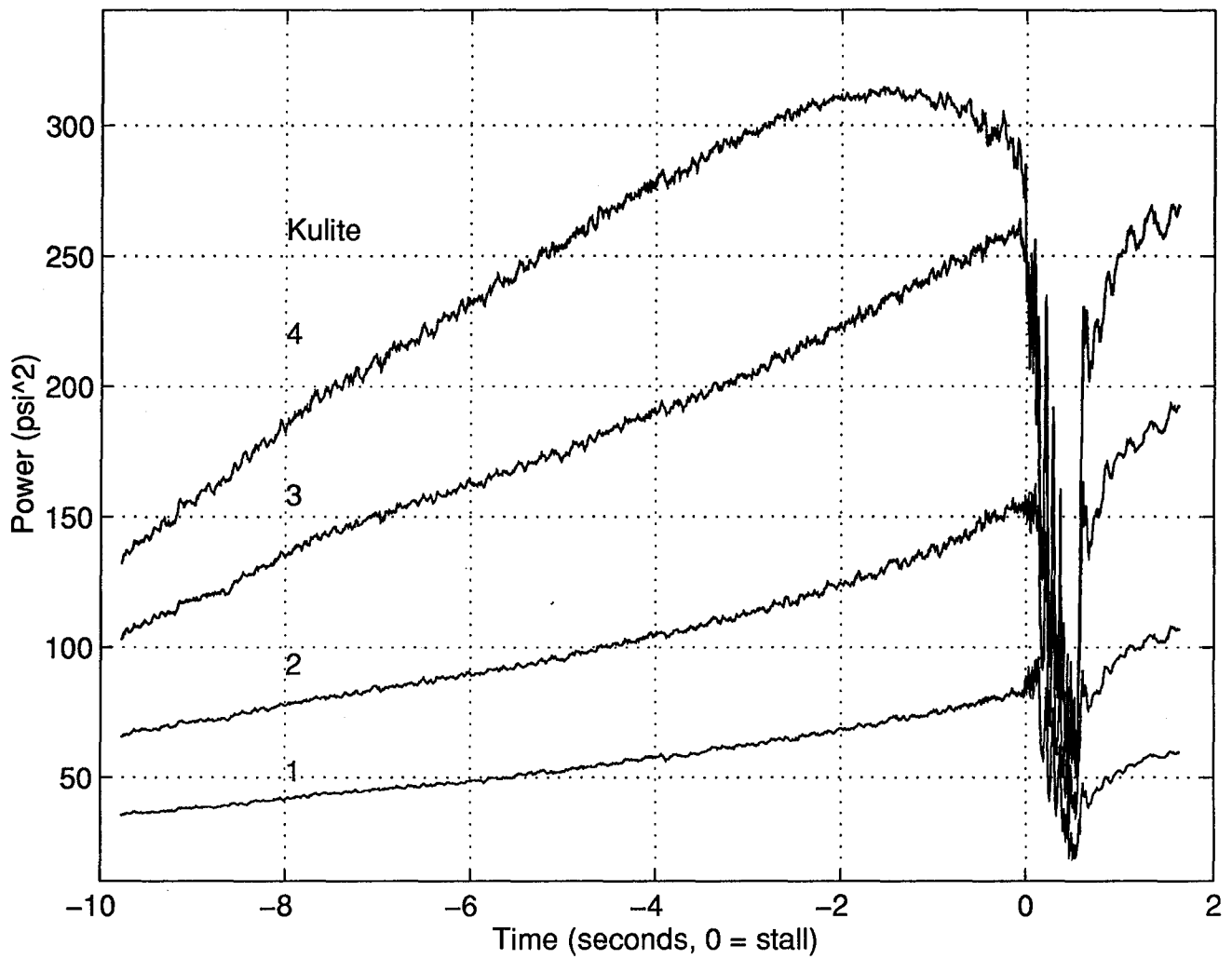


Figure 4.13 Rotor 4, 90%: Power of Blade Passing Frequency Group (6140 Hz to 6380 Hz)

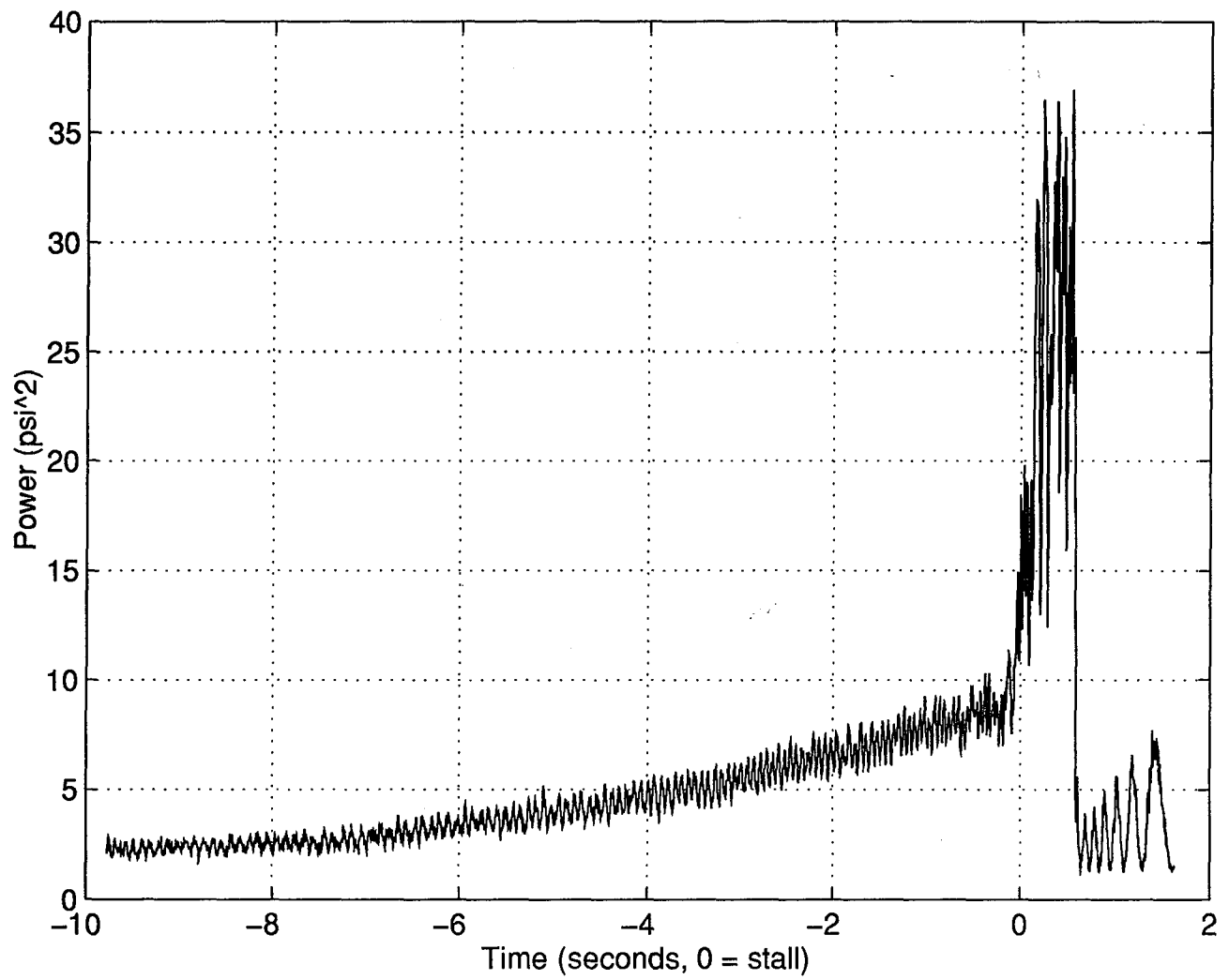


Figure 4.14 Rotor 4, 90%, Kulite #4: Power of Medium Frequency Group
(320 Hz to 6120 Hz)

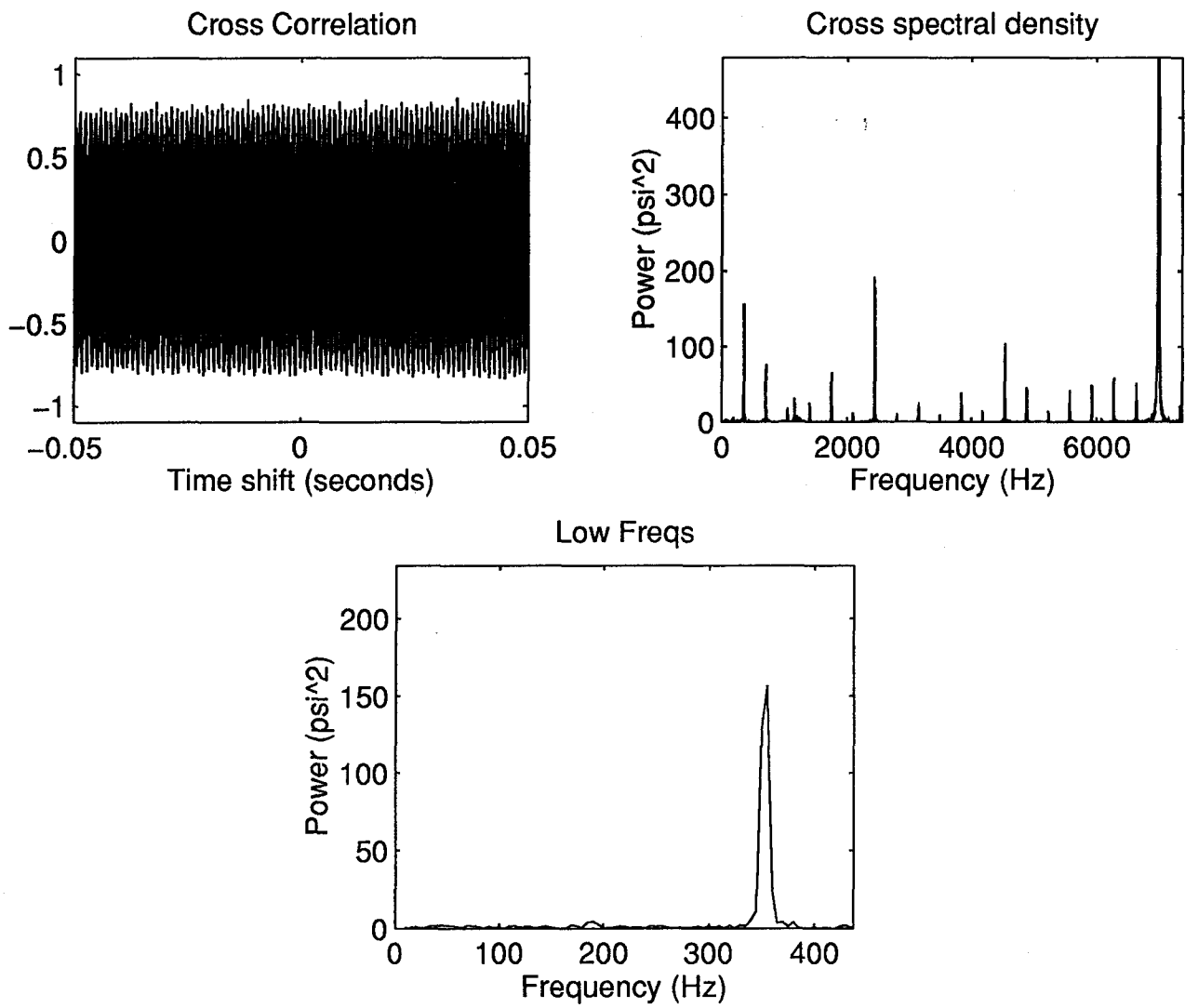


Figure 4.15a Rotor 4, 100%: Cross-Correlation of Kulites #1 and #4 at $T = -9.09$

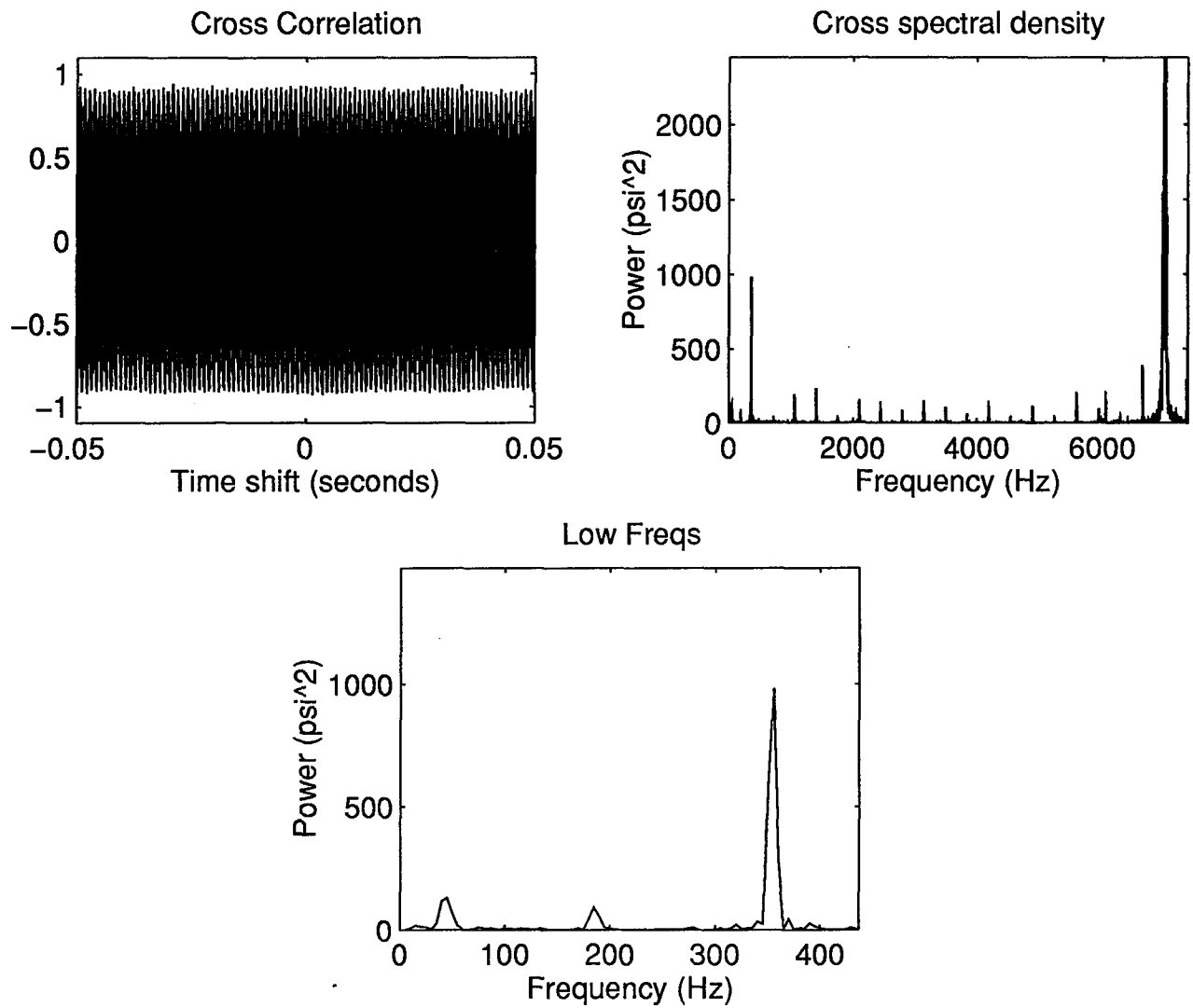


Figure 4.15b Rotor 4, 100%: Cross-Correlation of Kulites #1 and #4 at T=-1.09

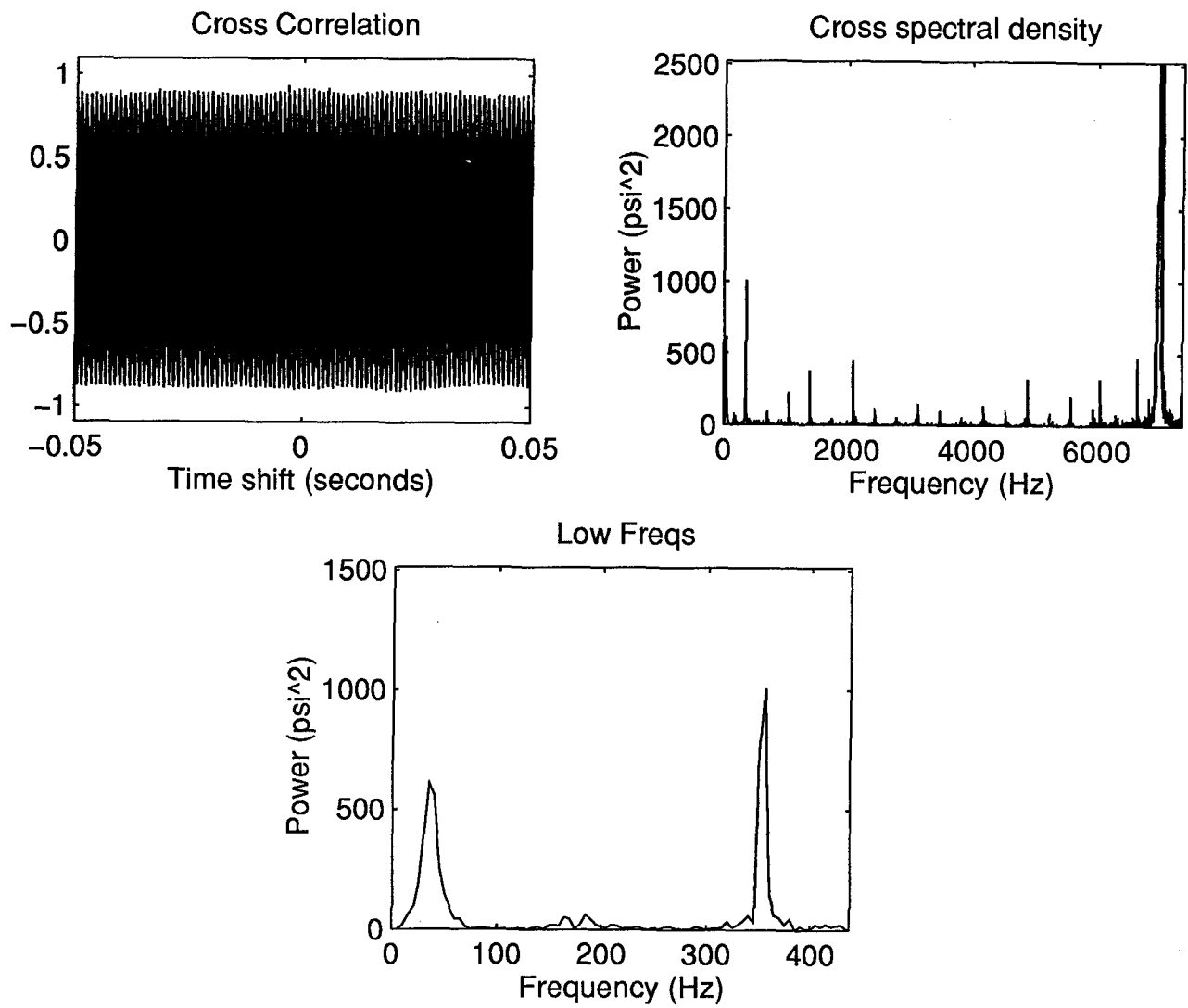


Figure 4.15c Rotor 4, 100%: Cross-Correlation of Kulites #1 and #4 at T=-0.49

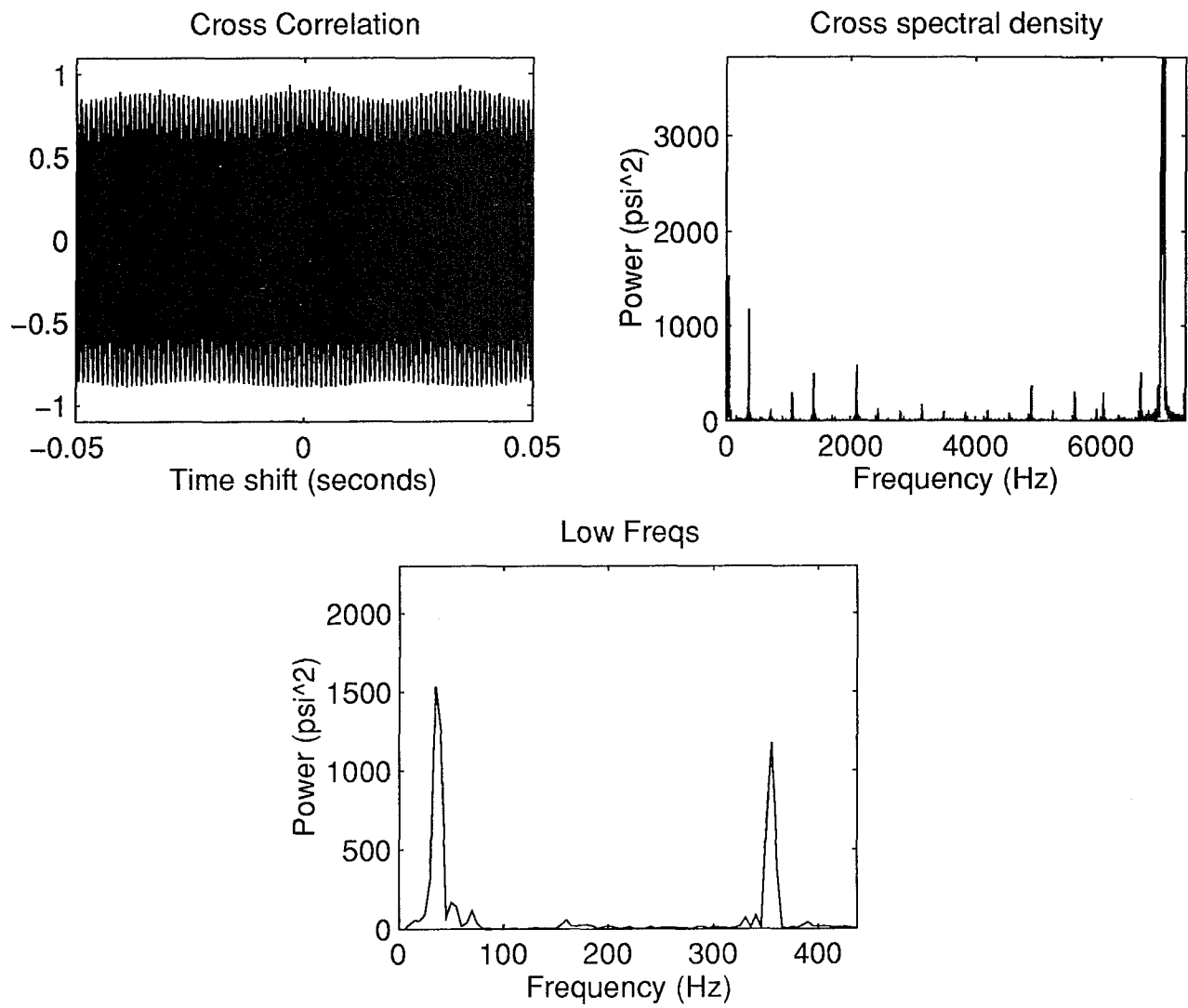


Figure 4.15d Rotor 4, 100%: Cross-Correlation of Kulites #1 and #4 at $T = -0.44$

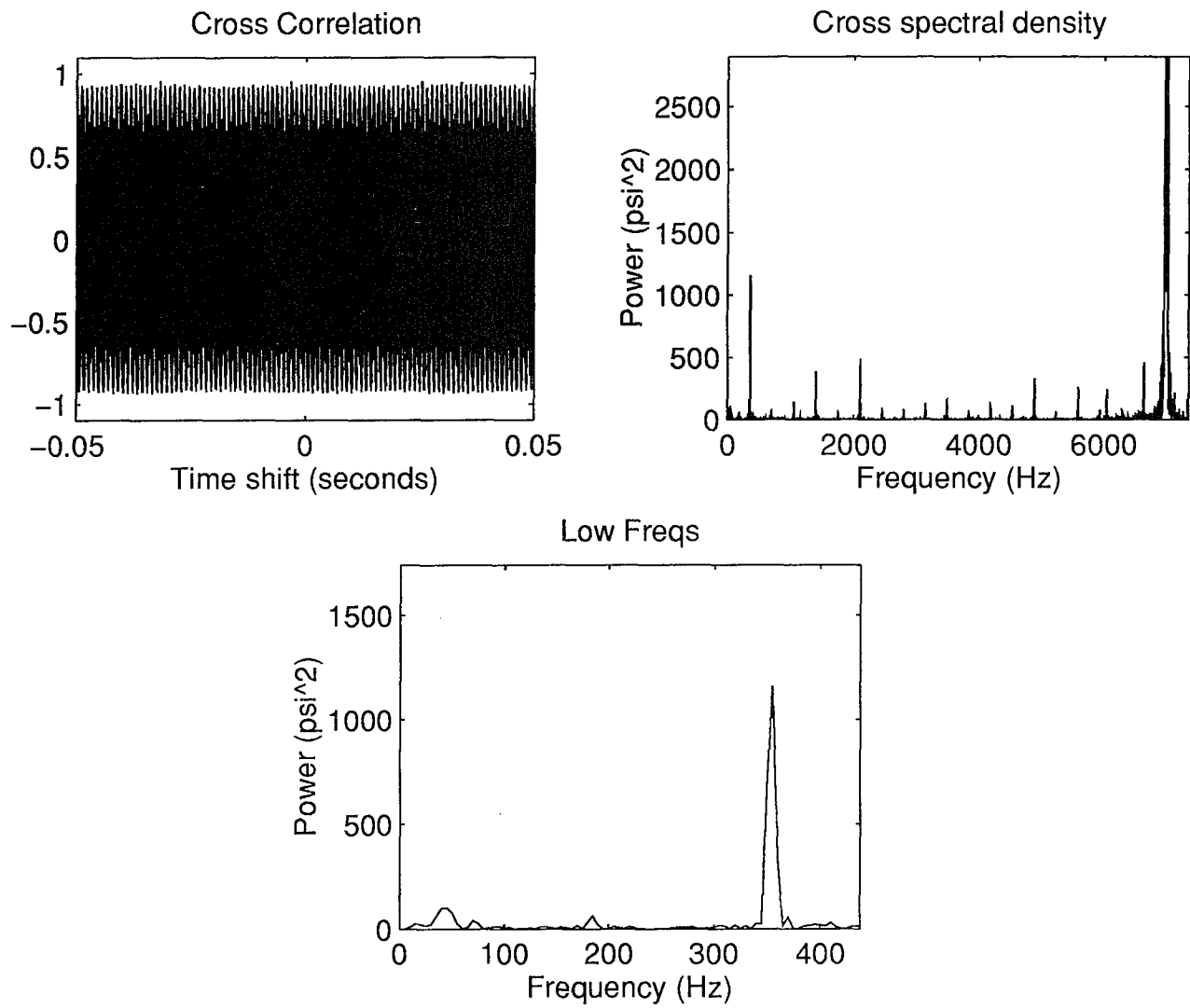


Figure 4.15e Rotor 4, 100%: Cross-Correlation of Kulites #1 and #4 at T=-0.29

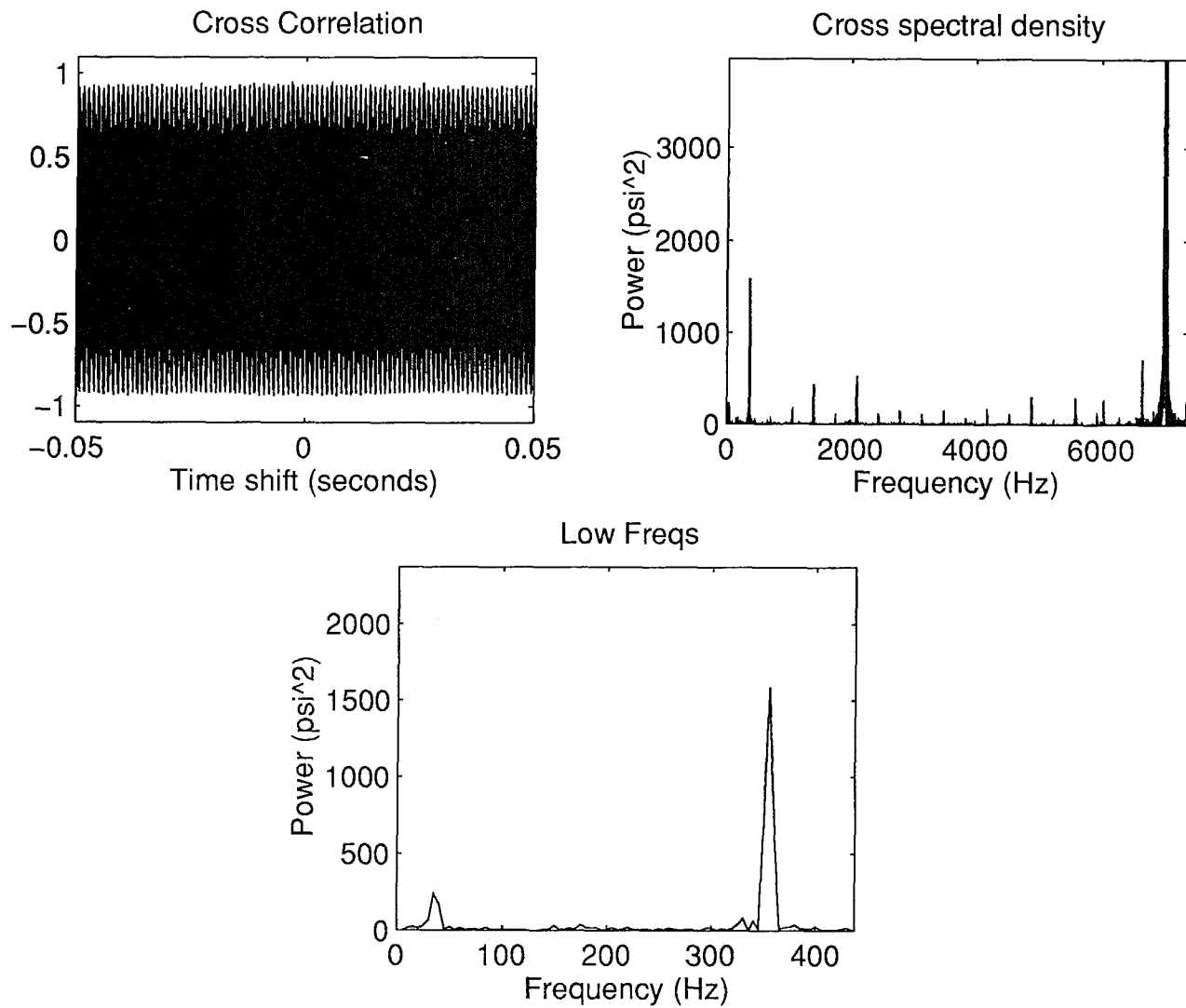


Figure 4.15f Rotor 4, 100%: Cross-Correlation of Kulites #1 and #4 at $T=-0.04$

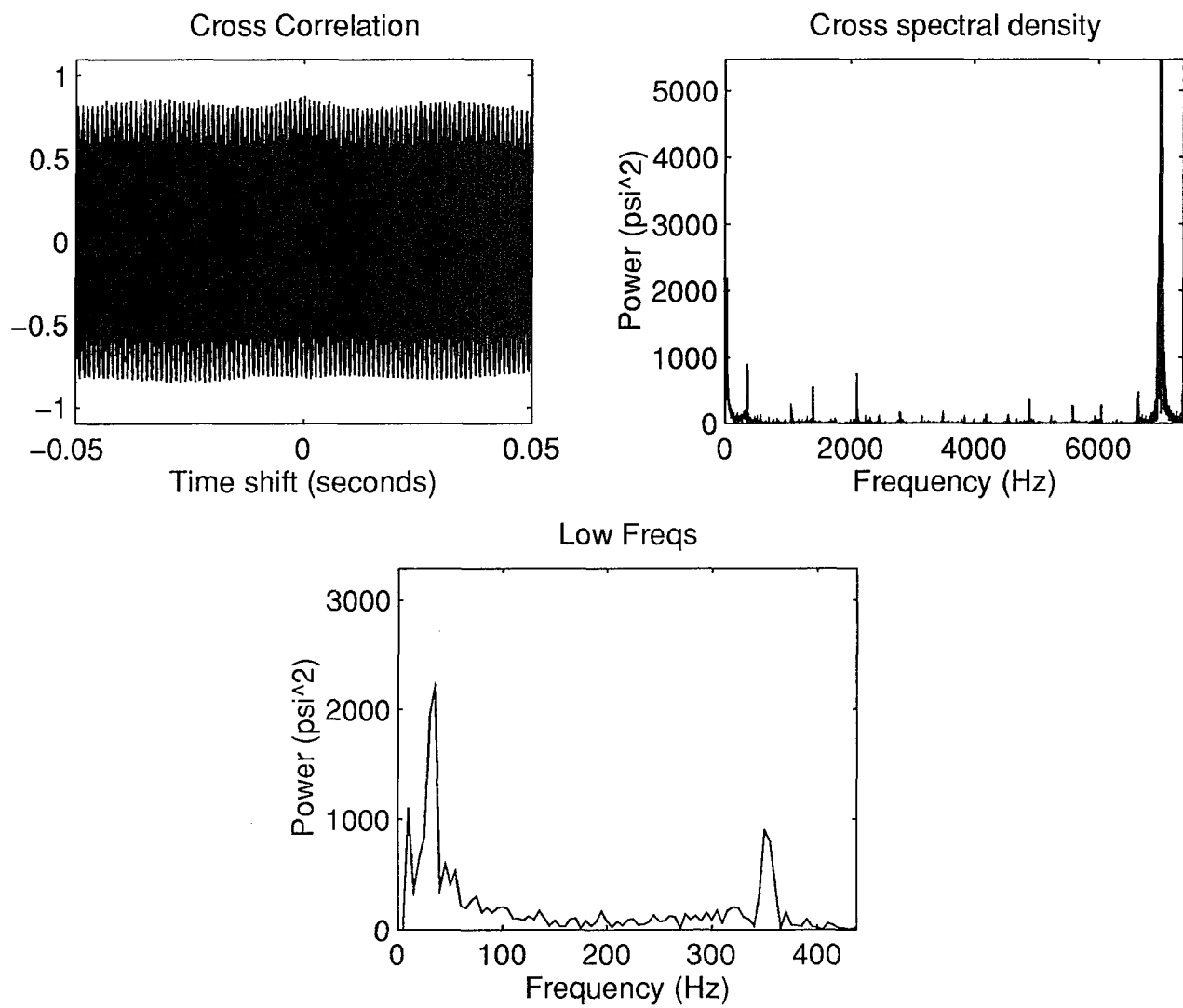


Figure 4.15g Rotor 4, 100%: Cross-Correlation of Kulites #1 and #4 at $T=+0.01$

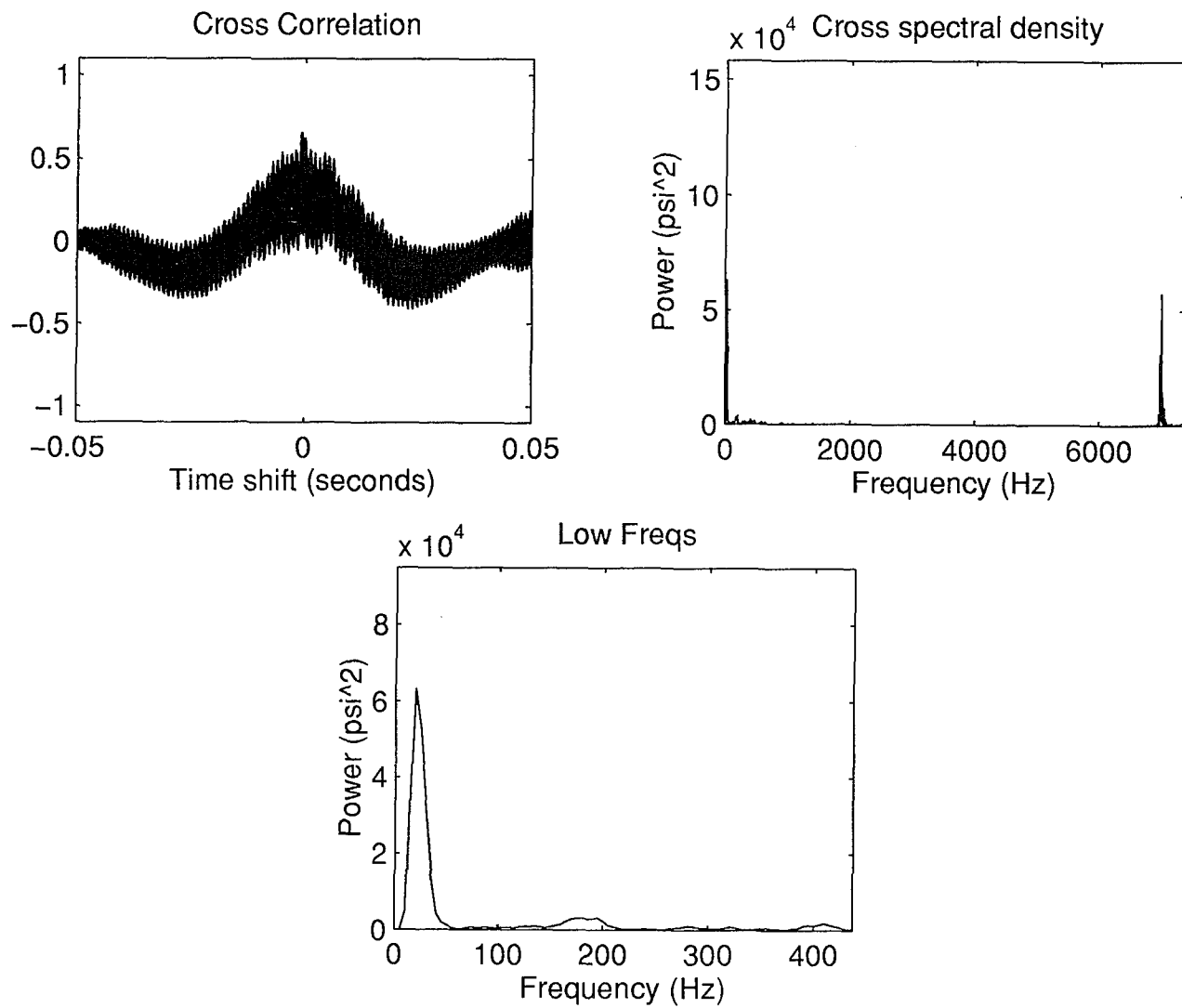


Figure 4.15h Rotor 4, 100%: Cross-Correlation of Kulites #1 and #4 at $T=+0.06$

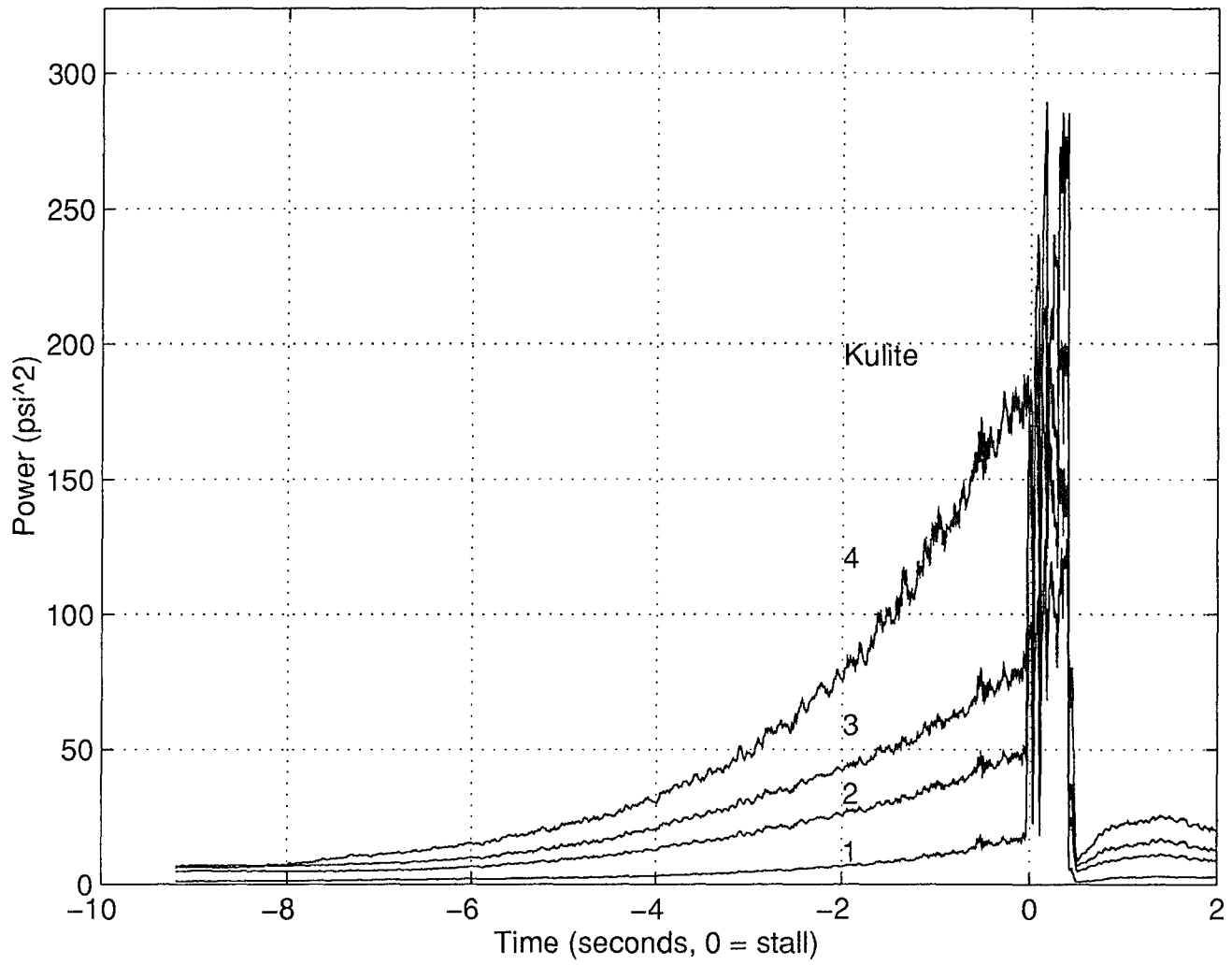


Figure 4.16 Rotor 4, 100%: Total Signal Power (less DC contribution)

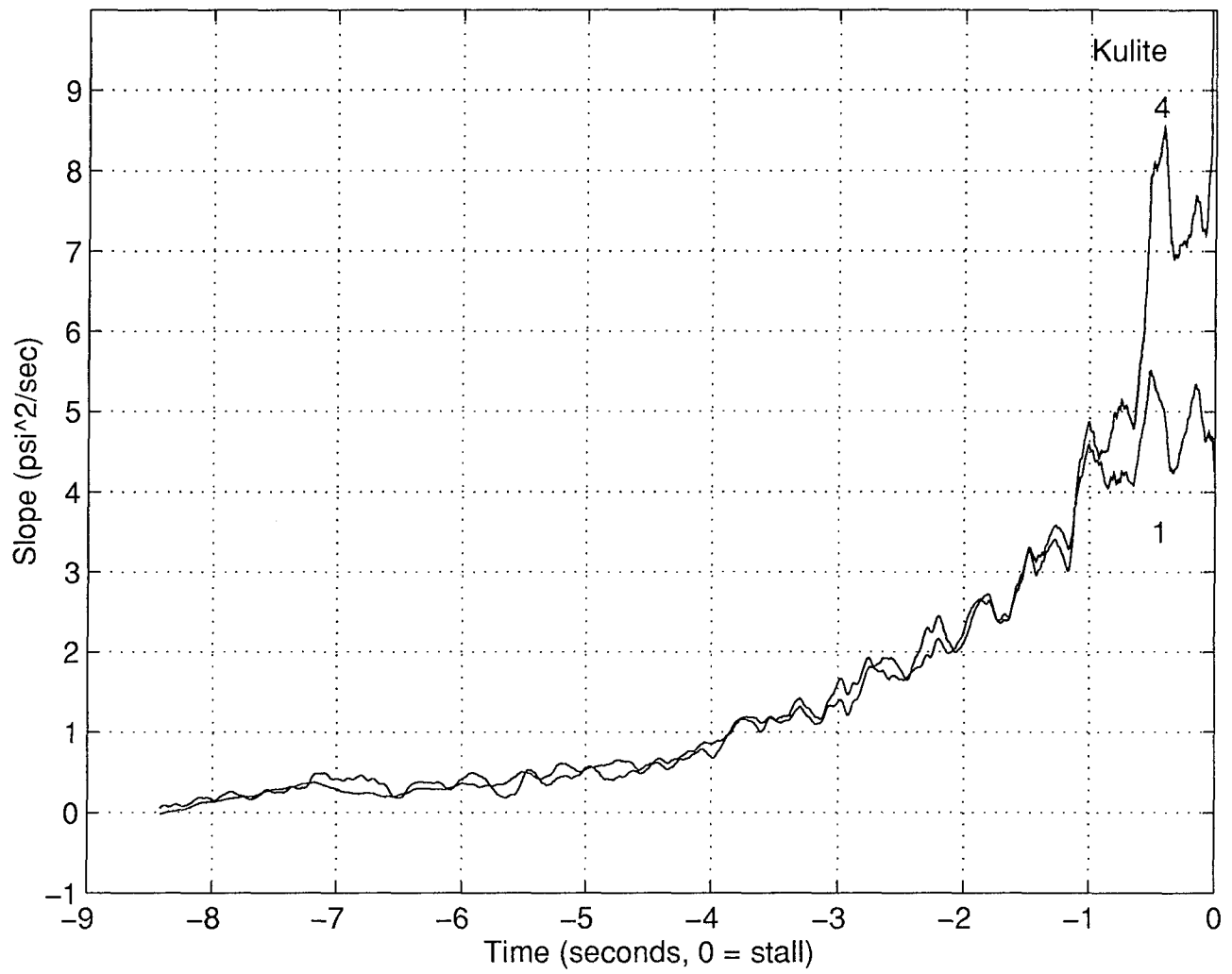


Figure 4.17 Rotor 4, 100%: Comparison of Slope of Signal Power (Kulite #4 scaled by $\delta=0.0778$)

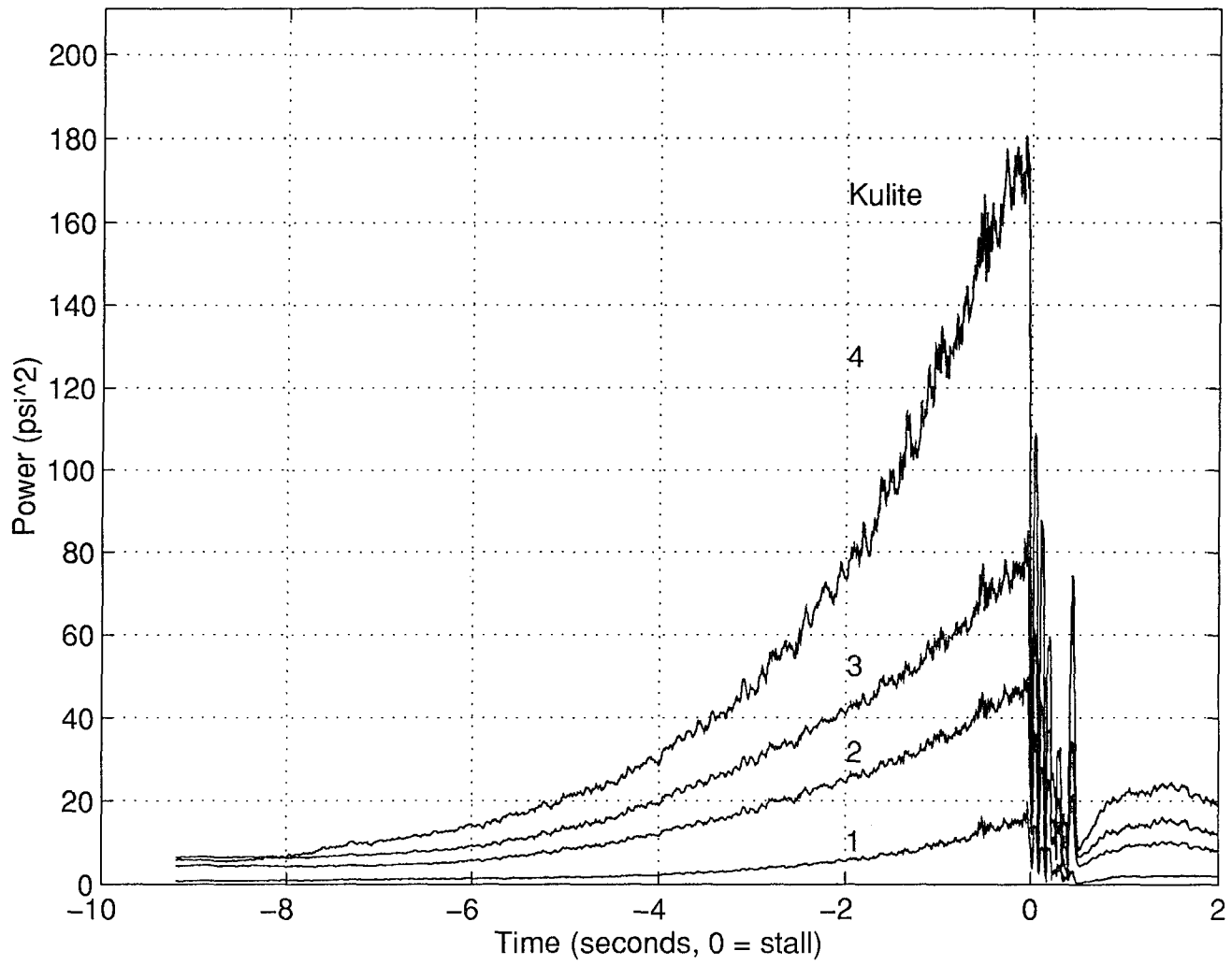


Figure 4.18 Rotor 4, 100%: Power of Blade Passing Frequency Group (6880 Hz to 7120 Hz)

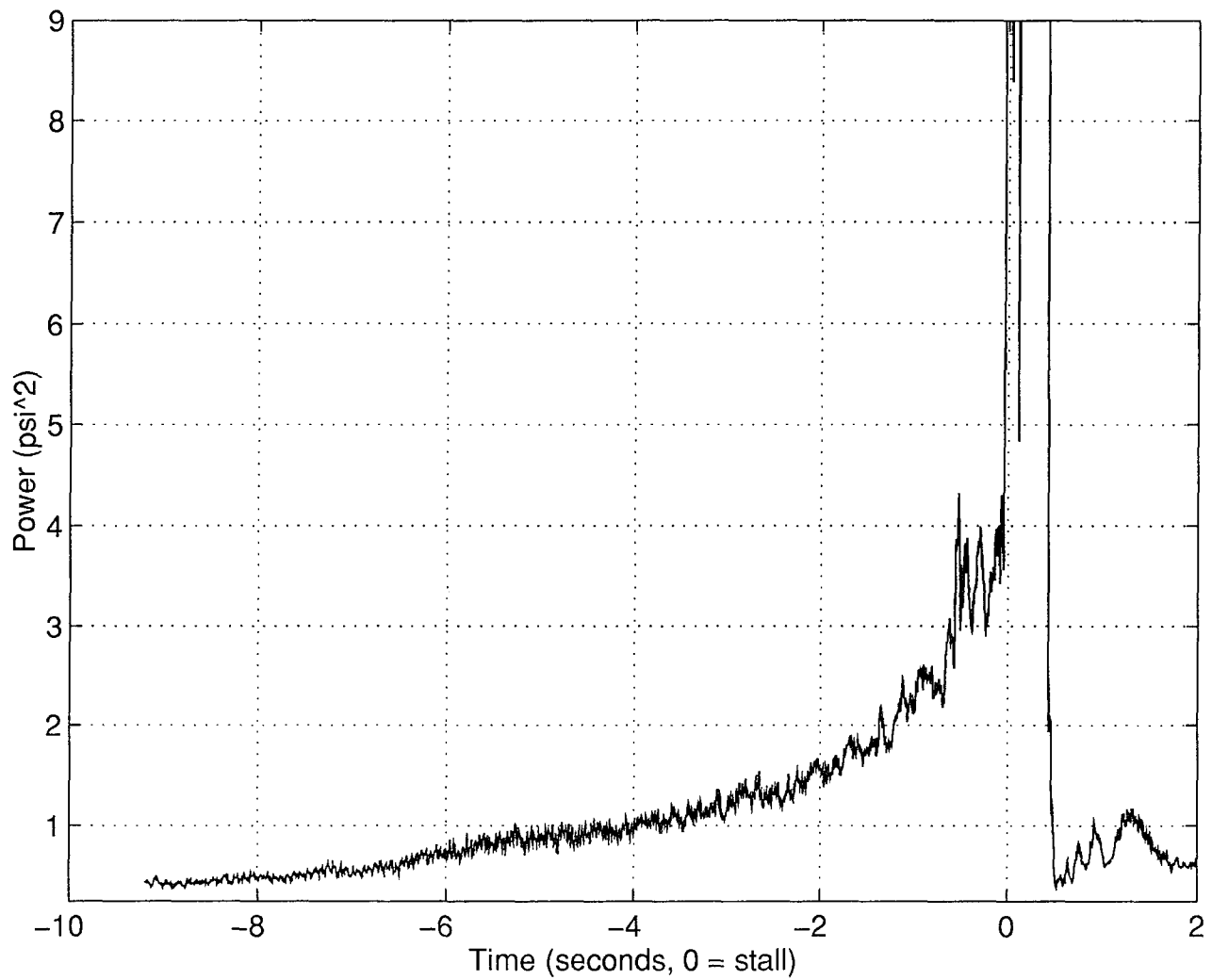


Figure 4.19 Rotor 4, 100%, Kulite #4: Power of Medium Frequency Group (360 Hz to 6860 Hz)

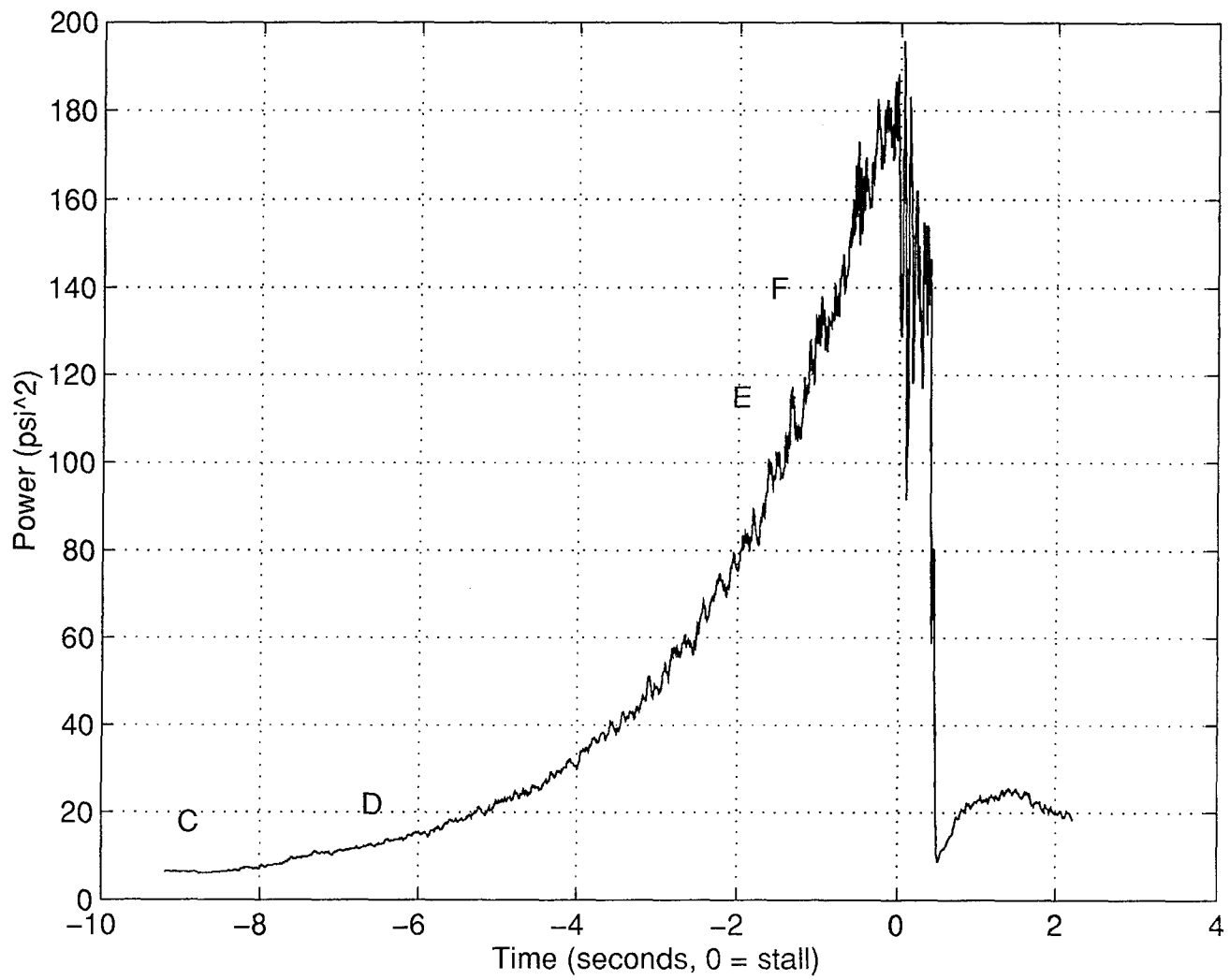


Figure 4.20 Rotor 4, 100%, Kulite #4: Shock Structure Points on Plot of Signal Power

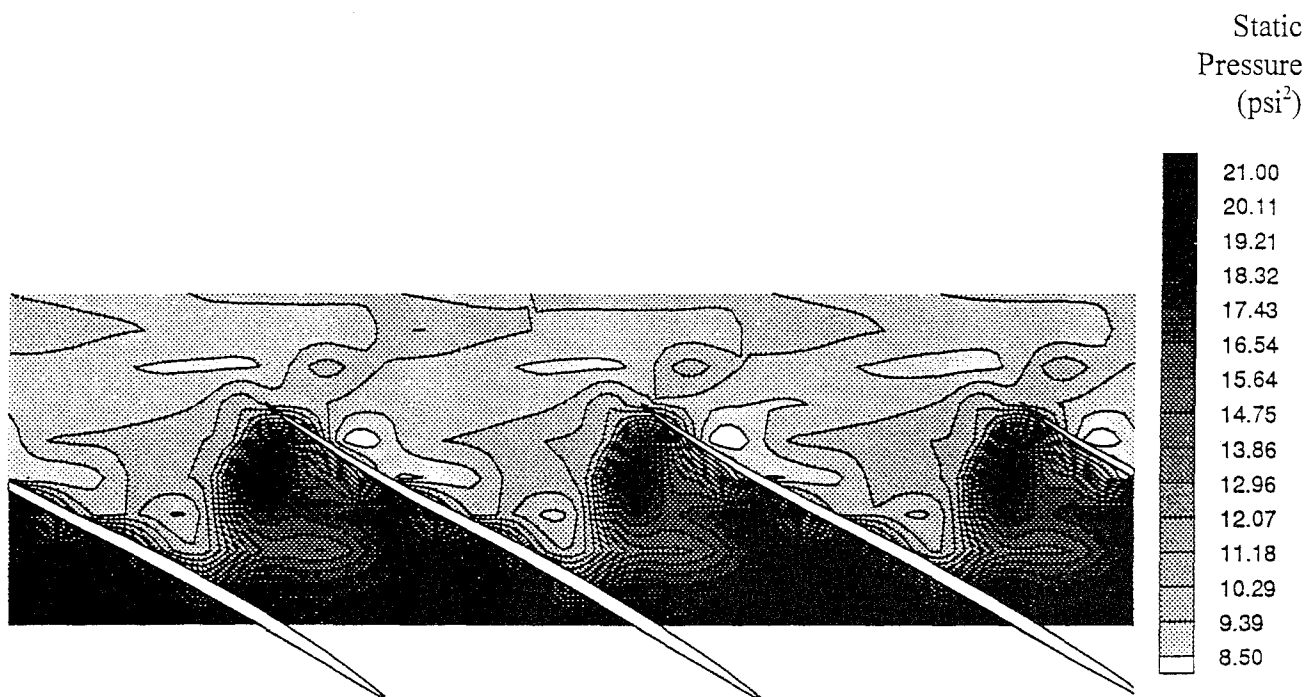


Figure 4.21a Rotor 4, 100%: Shock Structure at Point C

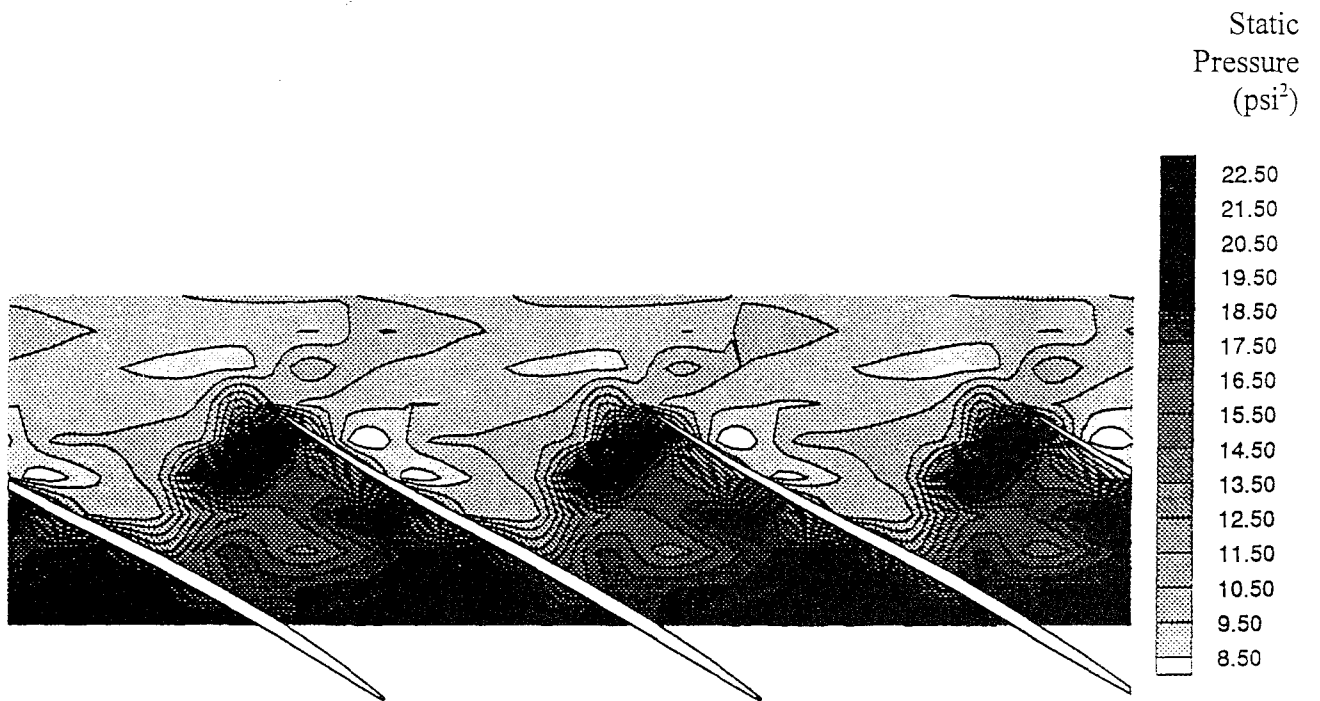


Figure 4.21b Rotor 4, 100%: Shock Structure at Point D

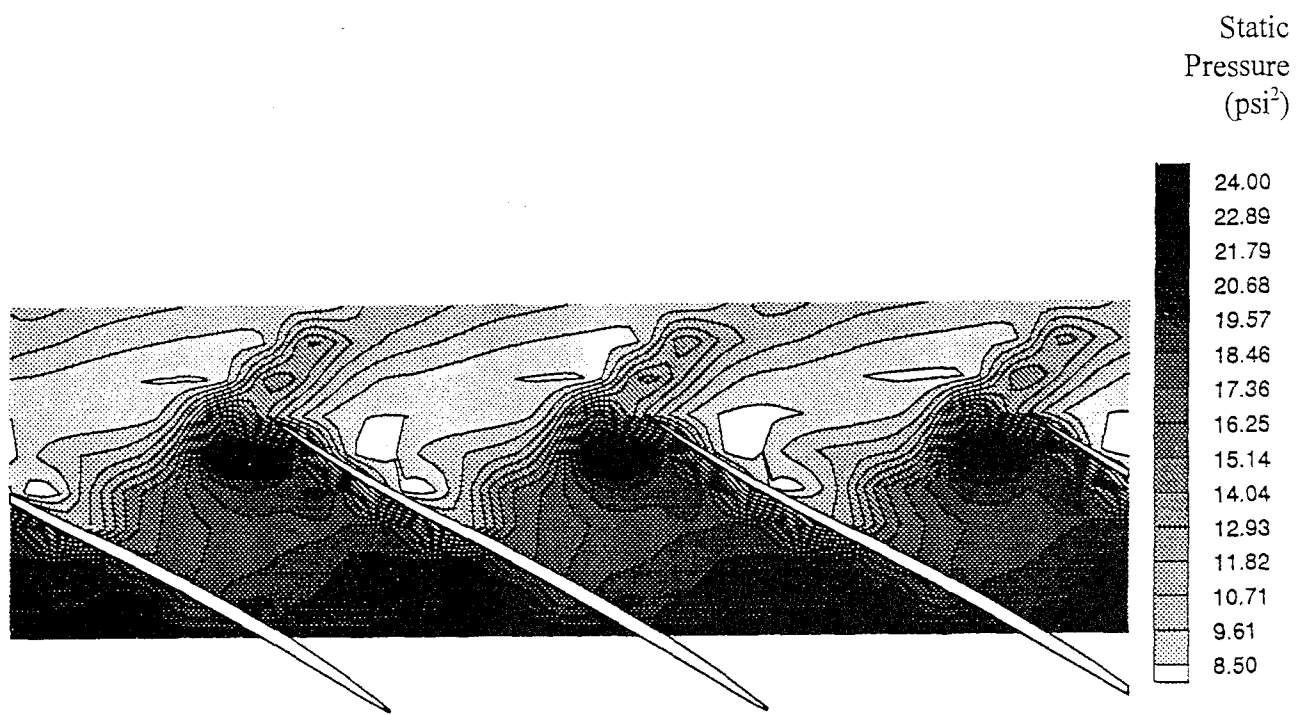


Figure 4.21c Rotor 4, 100%: Shock Structure at Point E

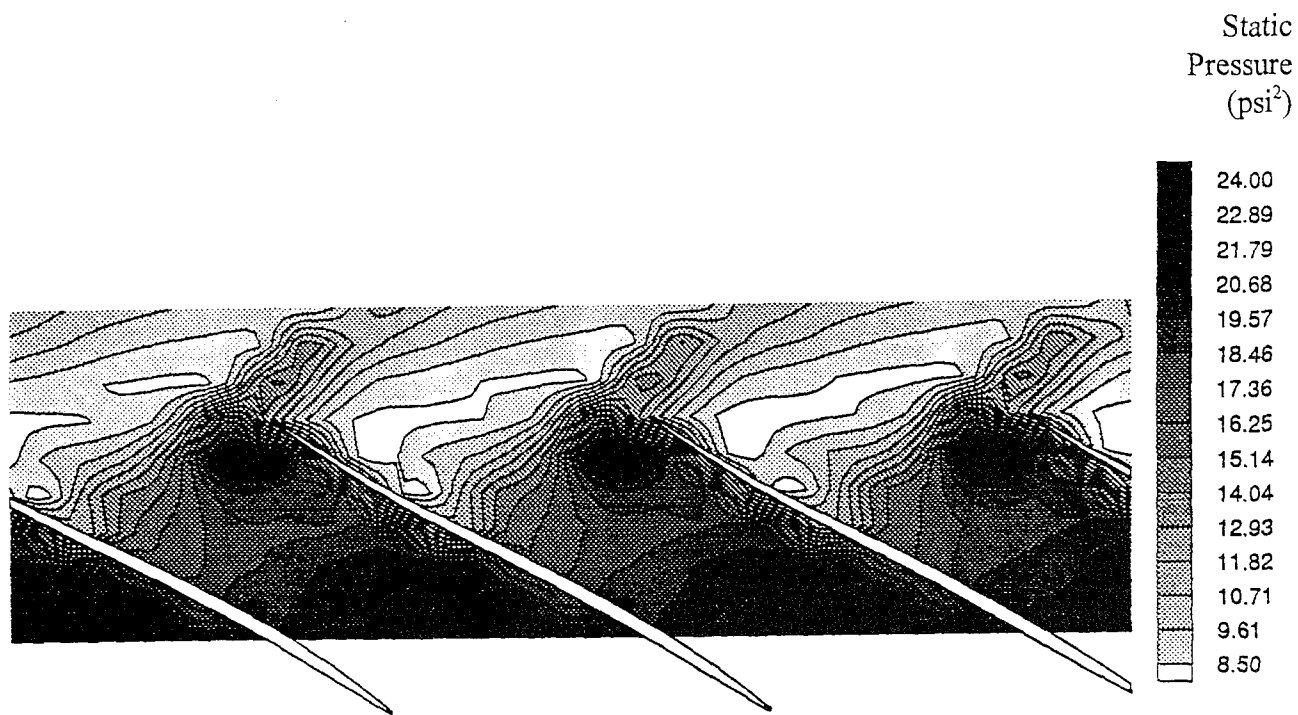
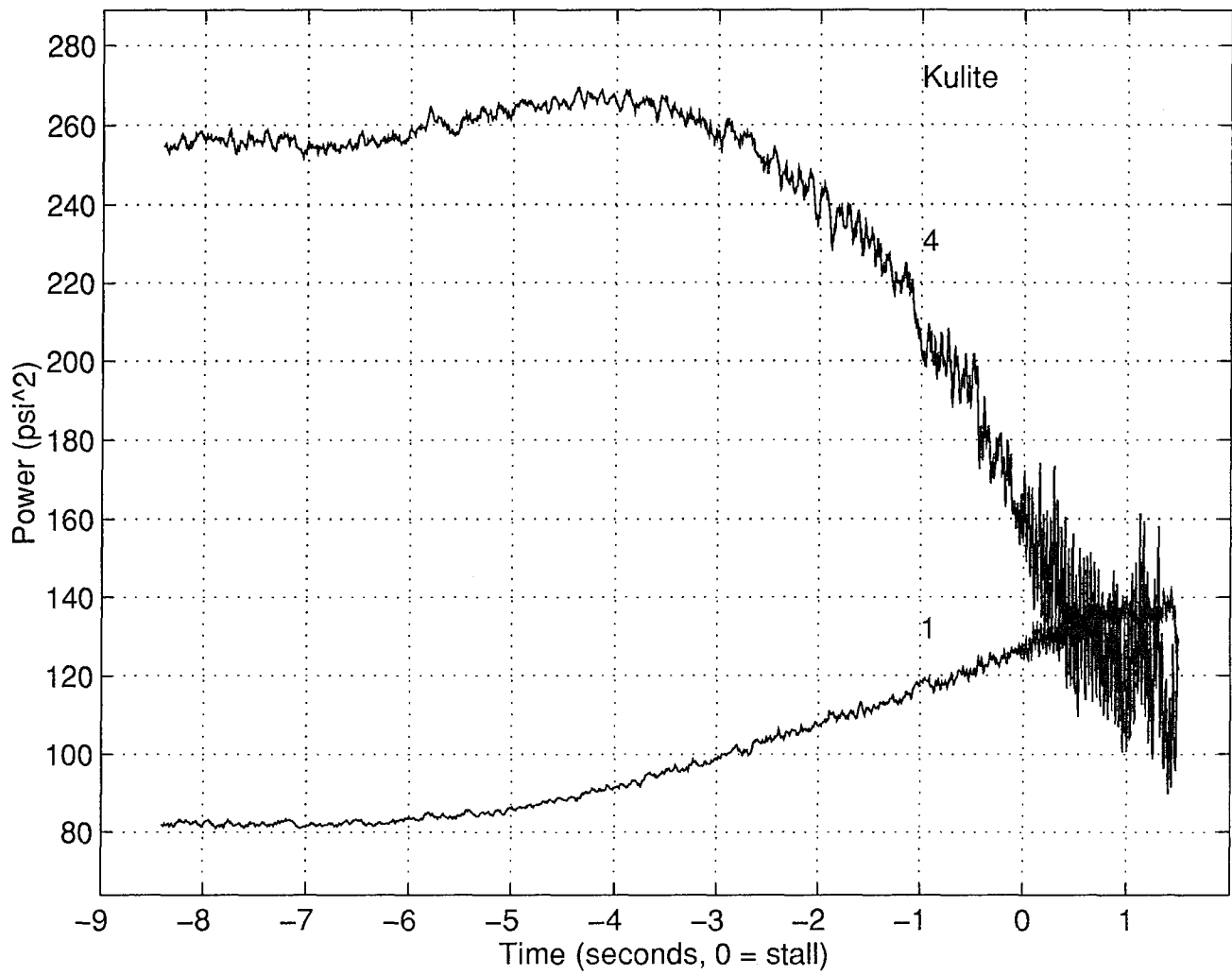


Figure 4.21d Rotor 4, 100%: Shock Structure at Point F



4.22 Rotor 6, 90%: Total Signal Power (less DC contribution)

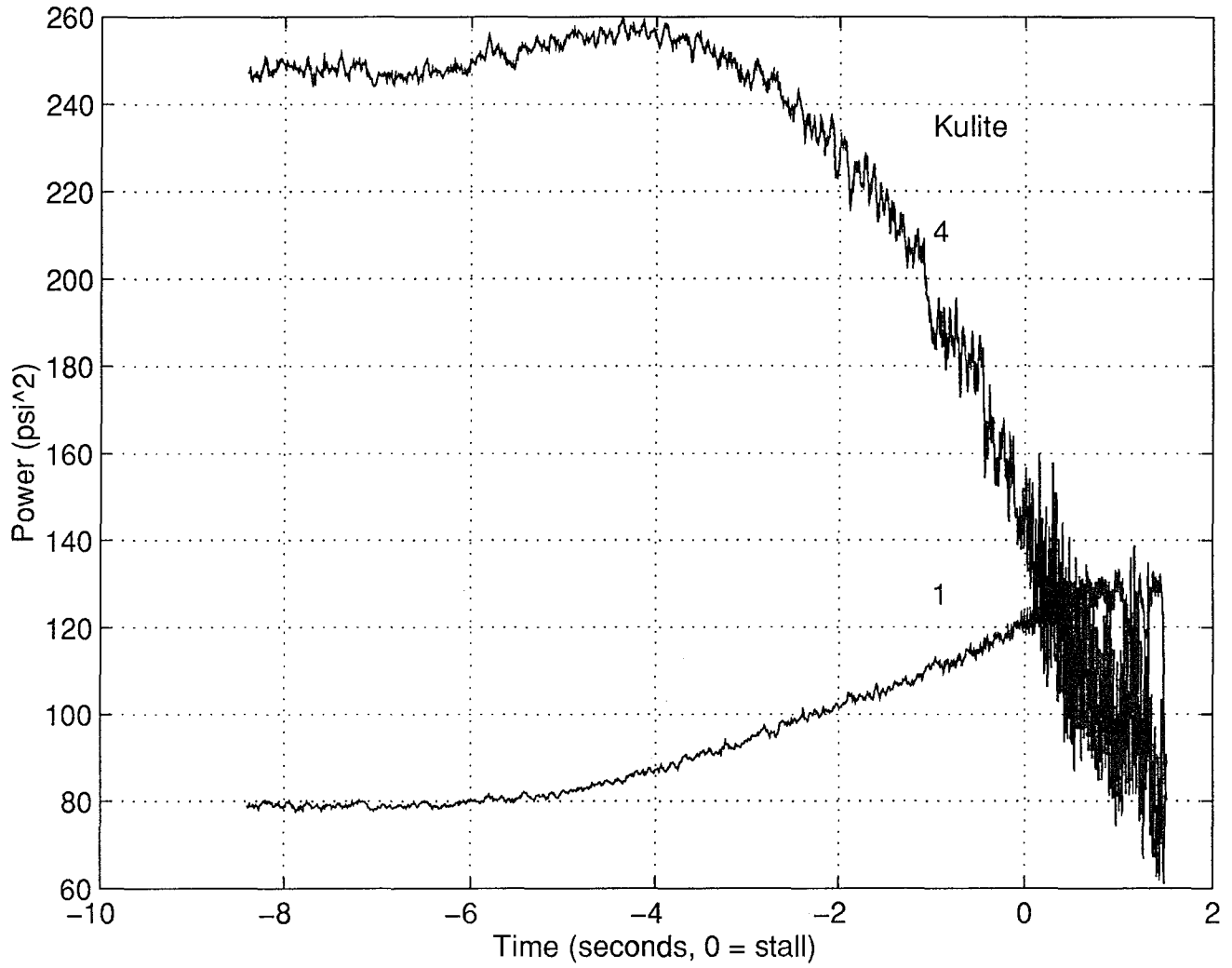


Figure 4.23 Rotor 6, 90%: Power of Blade Passing Frequency Group (6200 Hz to 6440 Hz)

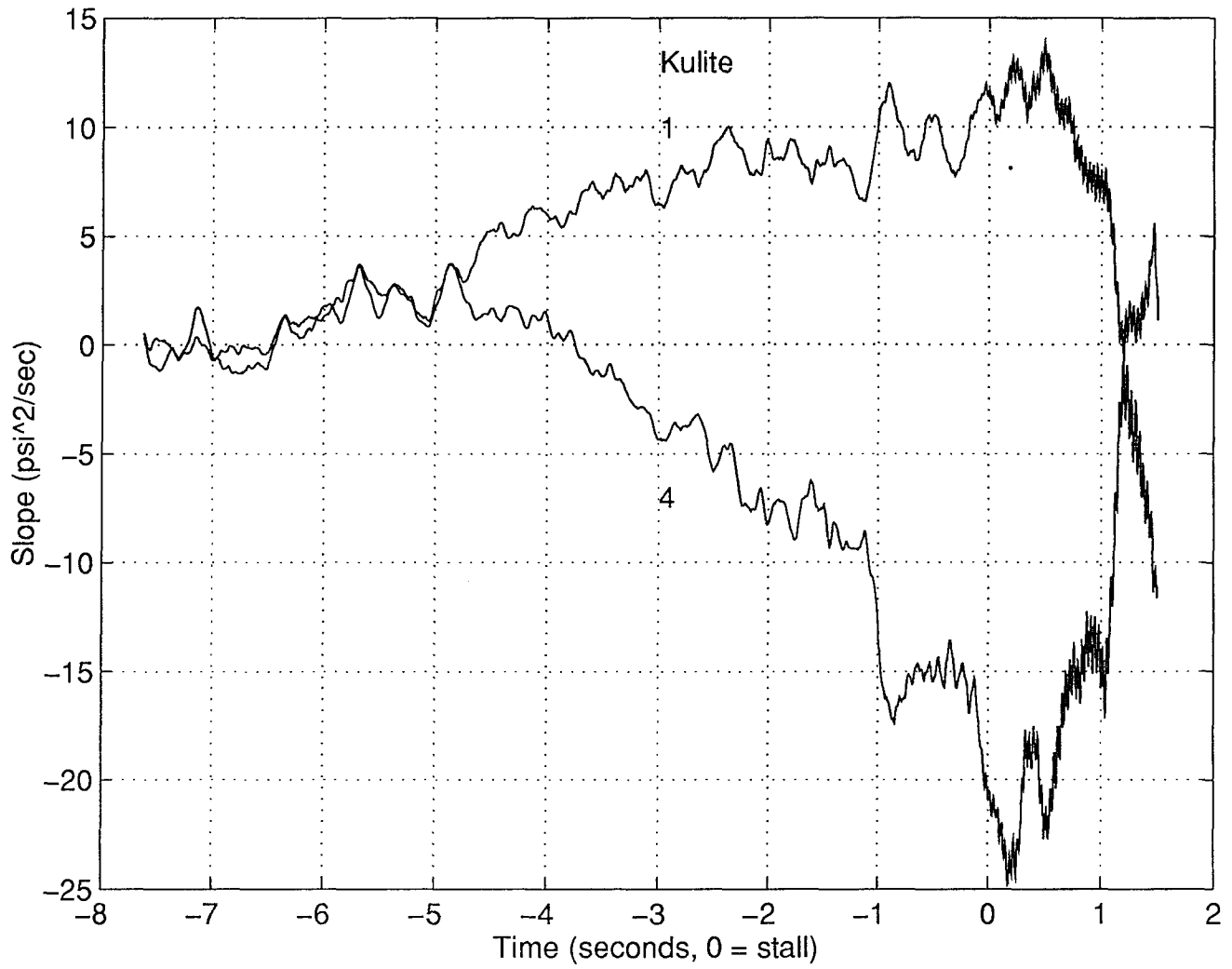


Figure 4.24 Rotor 6, 90%: Comparison of Slope of Signal Power (Kulite #4 scaled by $\delta=0.37$)

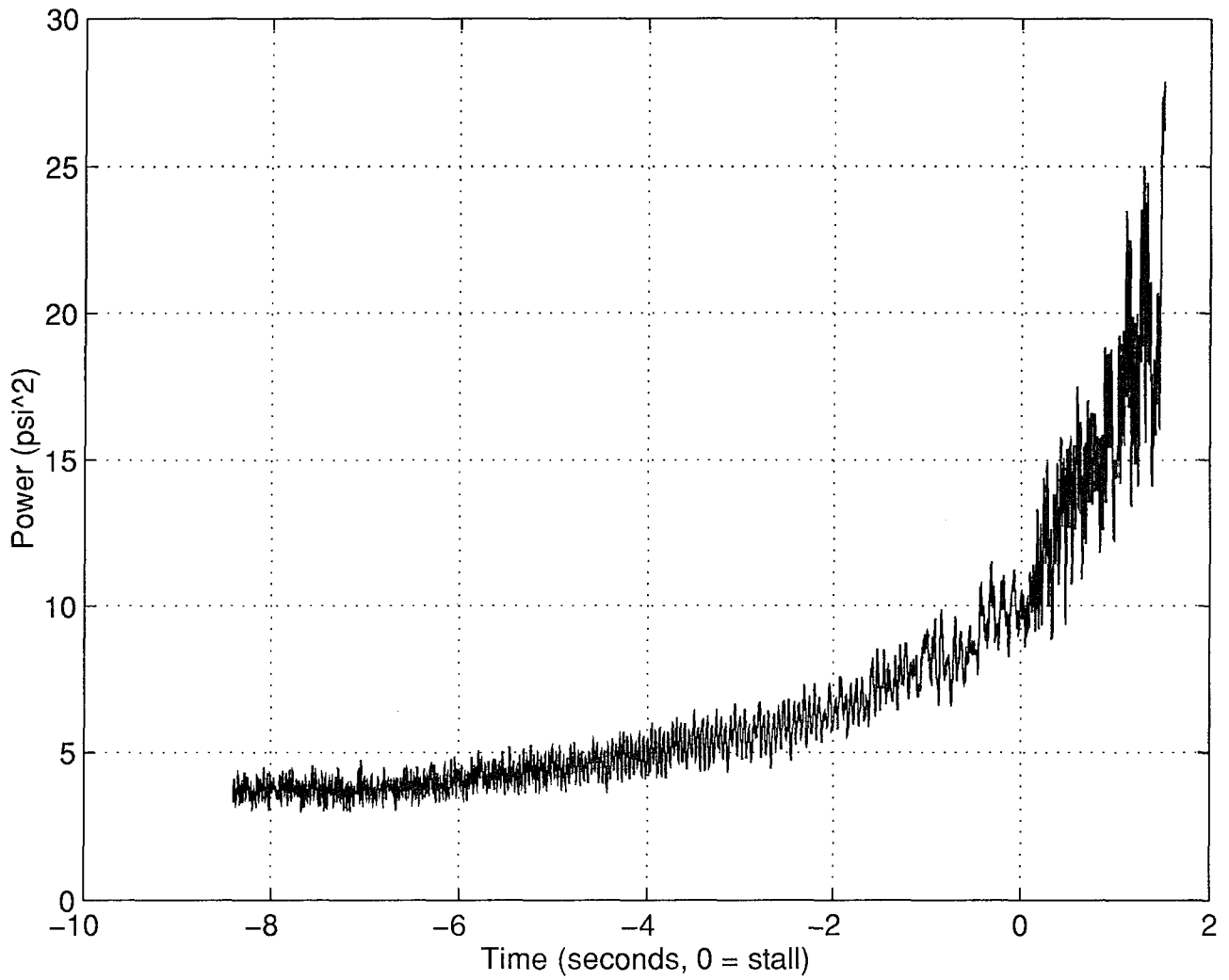


Figure 4.25 Rotor 6, 90%, Kulite #4: Power of Medium Frequency Group (320 Hz to 6180 Hz)

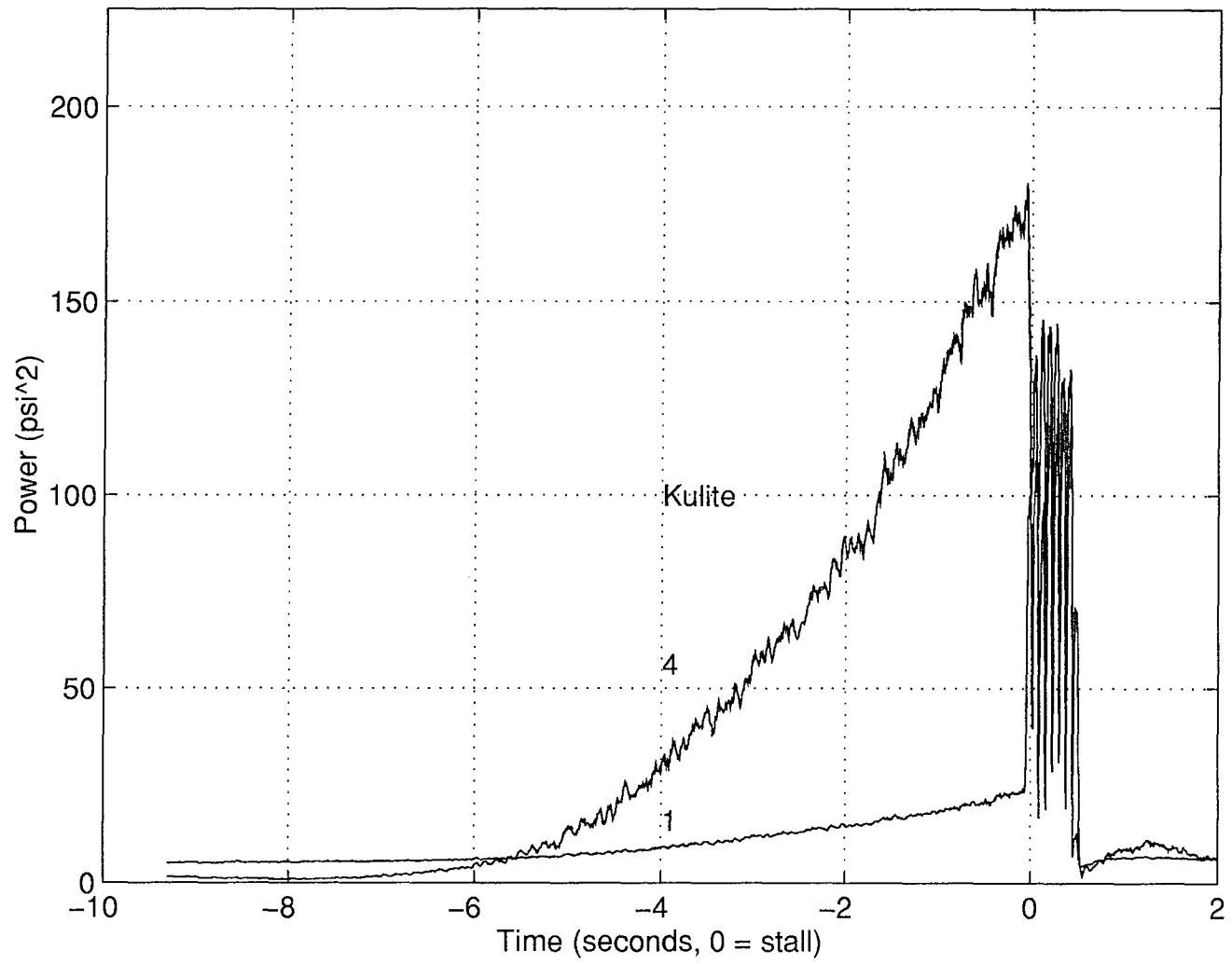


Figure 4.26 Rotor 6, 100%: Total Signal Power (less DC contribution)

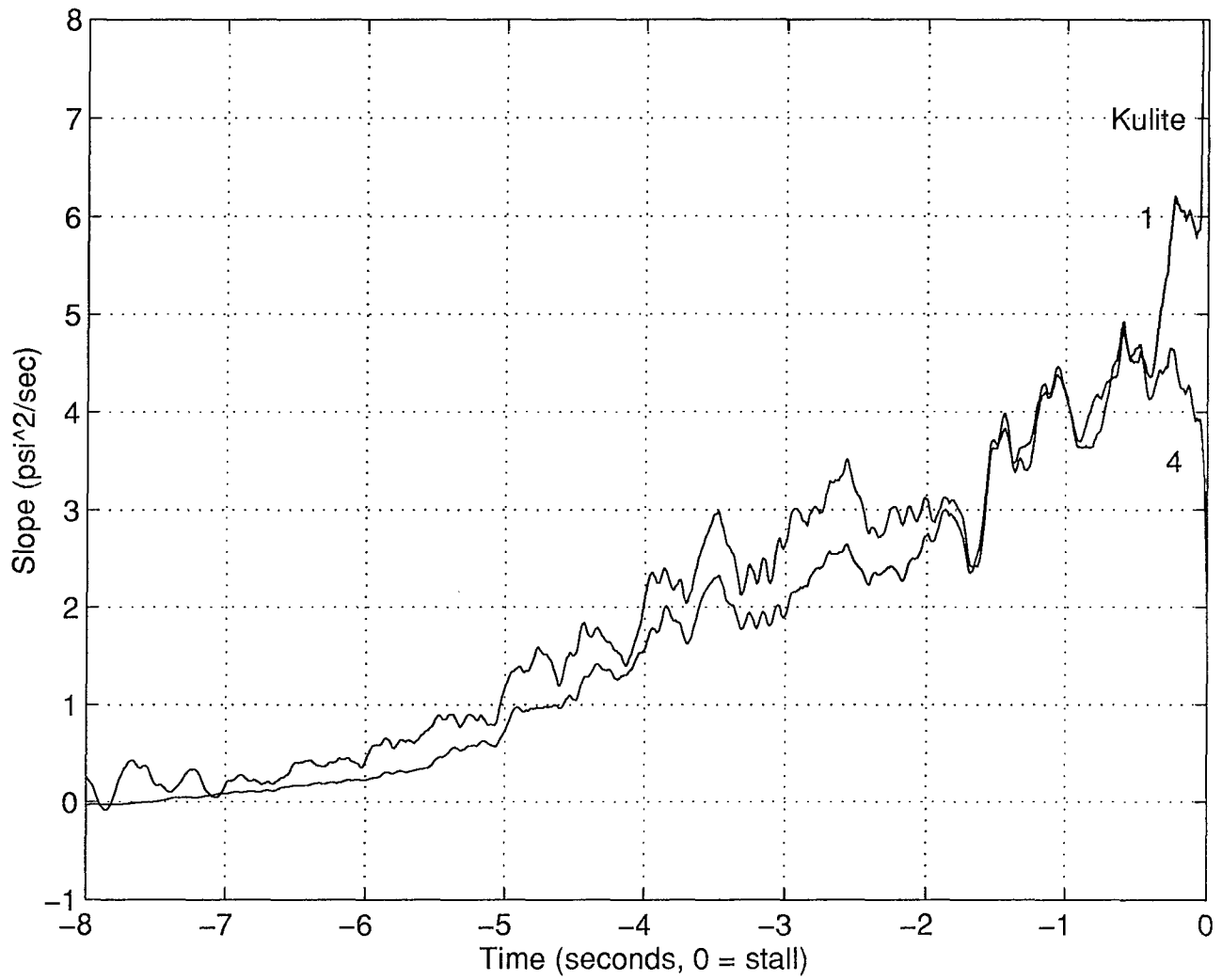


Figure 4.27 Rotor 6, 100%: Comparison of Slope of Signal Power (Kulite #4 scaled by $\delta=0.086$)

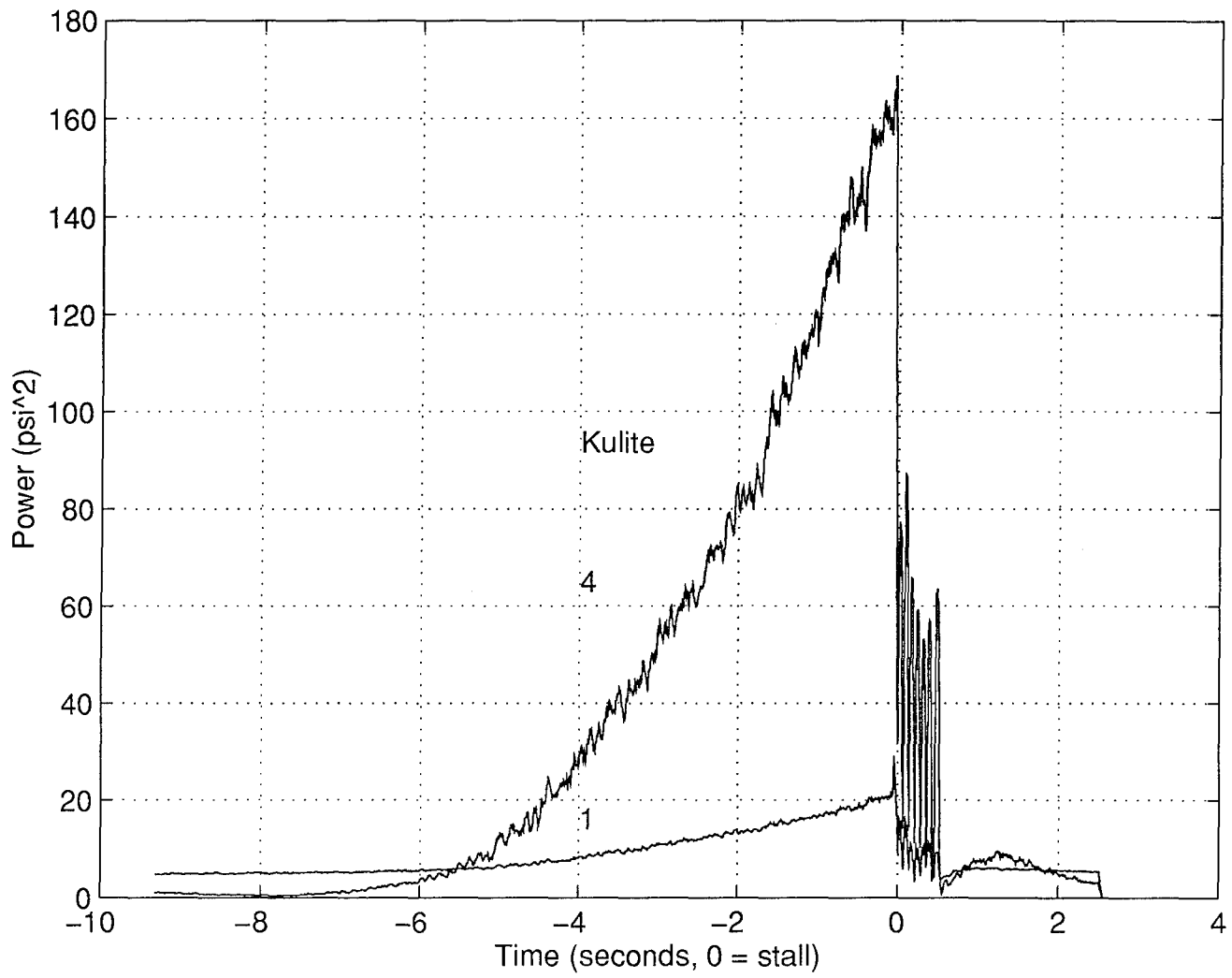


Figure 4.28 Rotor 6, 100%: Power of Blade Passing Frequency Group (6960 Hz to 7200 Hz)

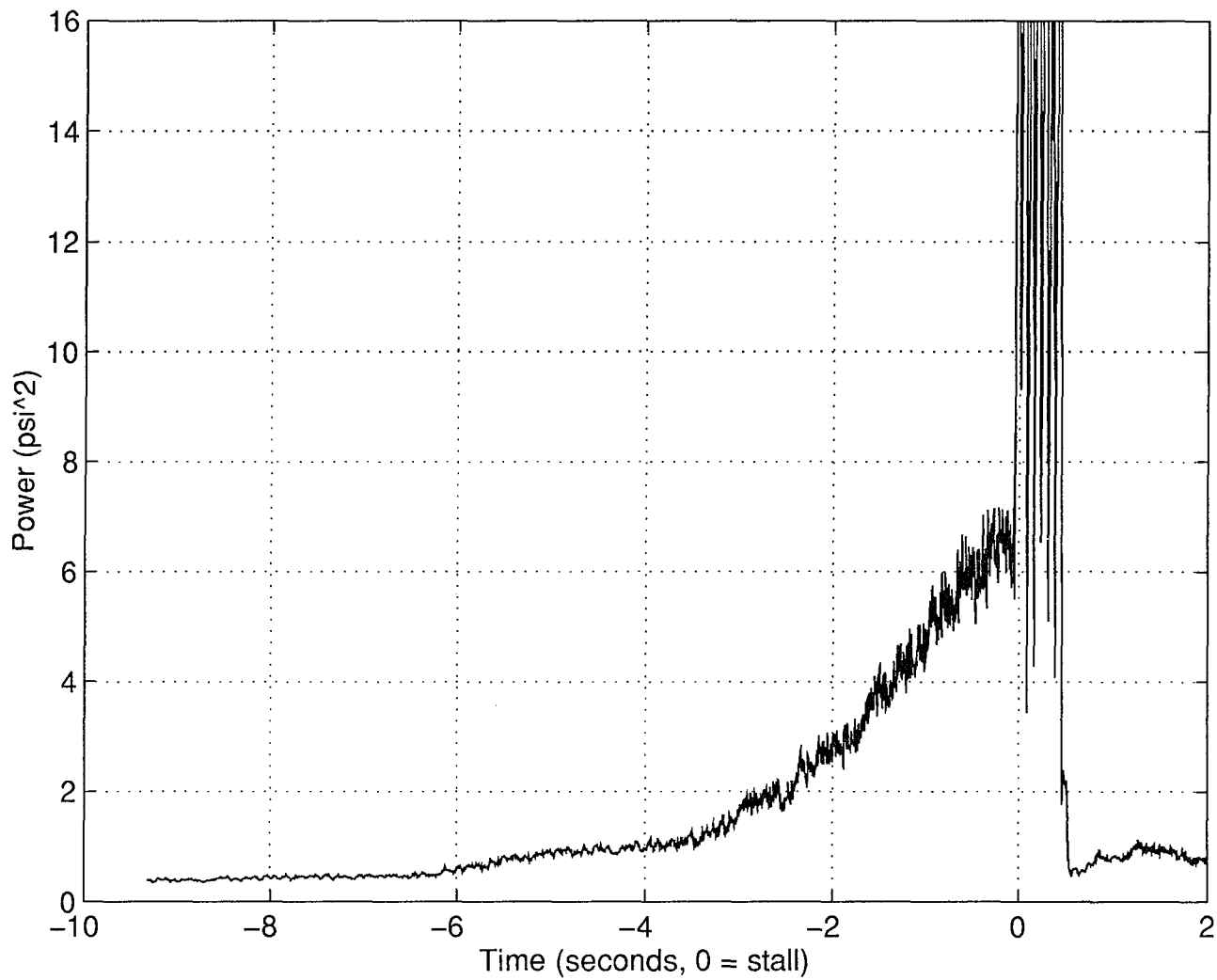


Figure 4.29 Rotor 6, 100%, Kulite #4: Power of Medium Frequency Group (360 Hz to 6940 Hz)

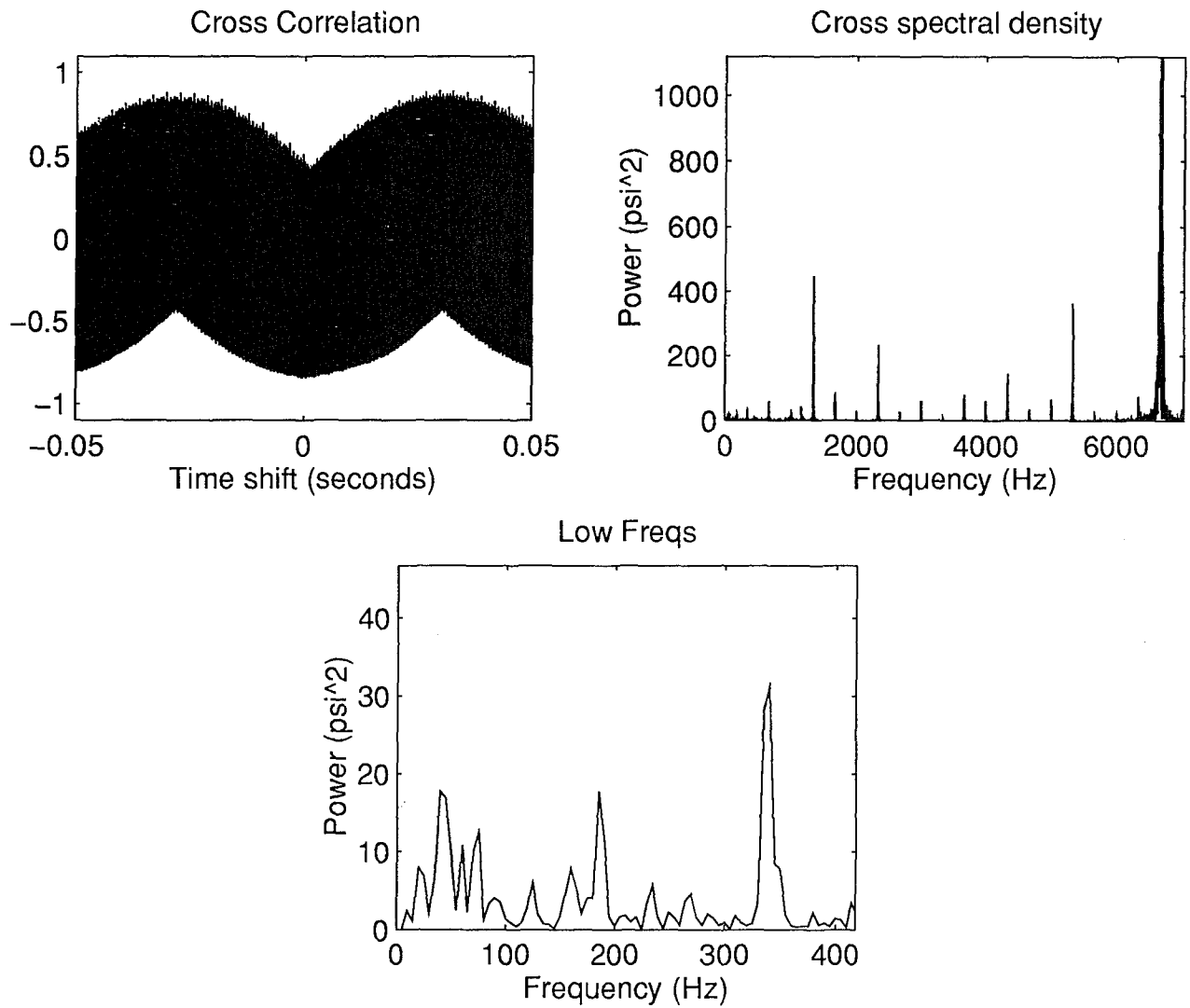


Figure 4.30a Rotor 9, 95%: Cross-Correlation of Kulites #1 and #4 at T=-4.91

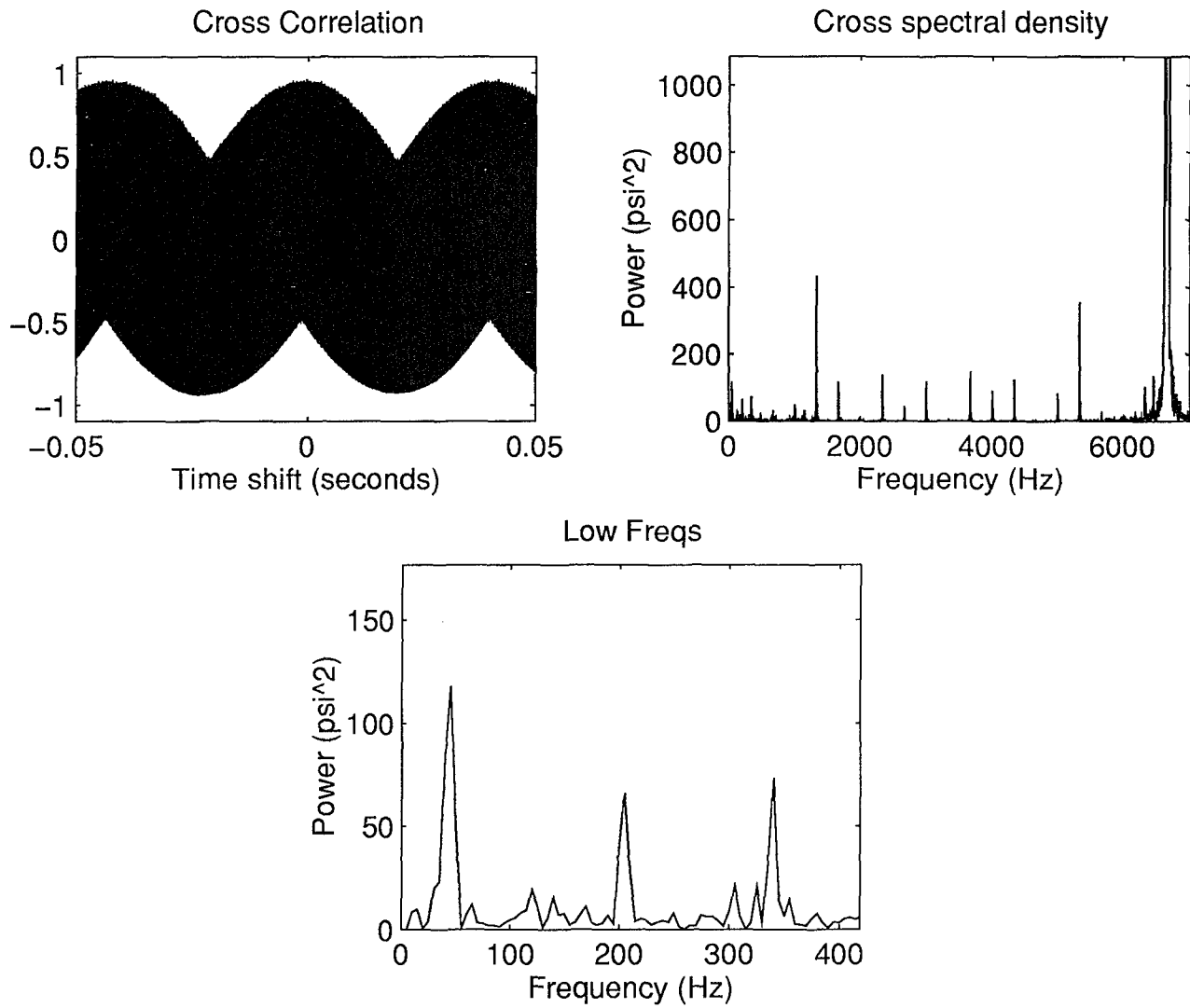


Figure 4.30b Rotor 9, 95%: Cross-Correlation of Kulites #1 and #4 at T=-1.91

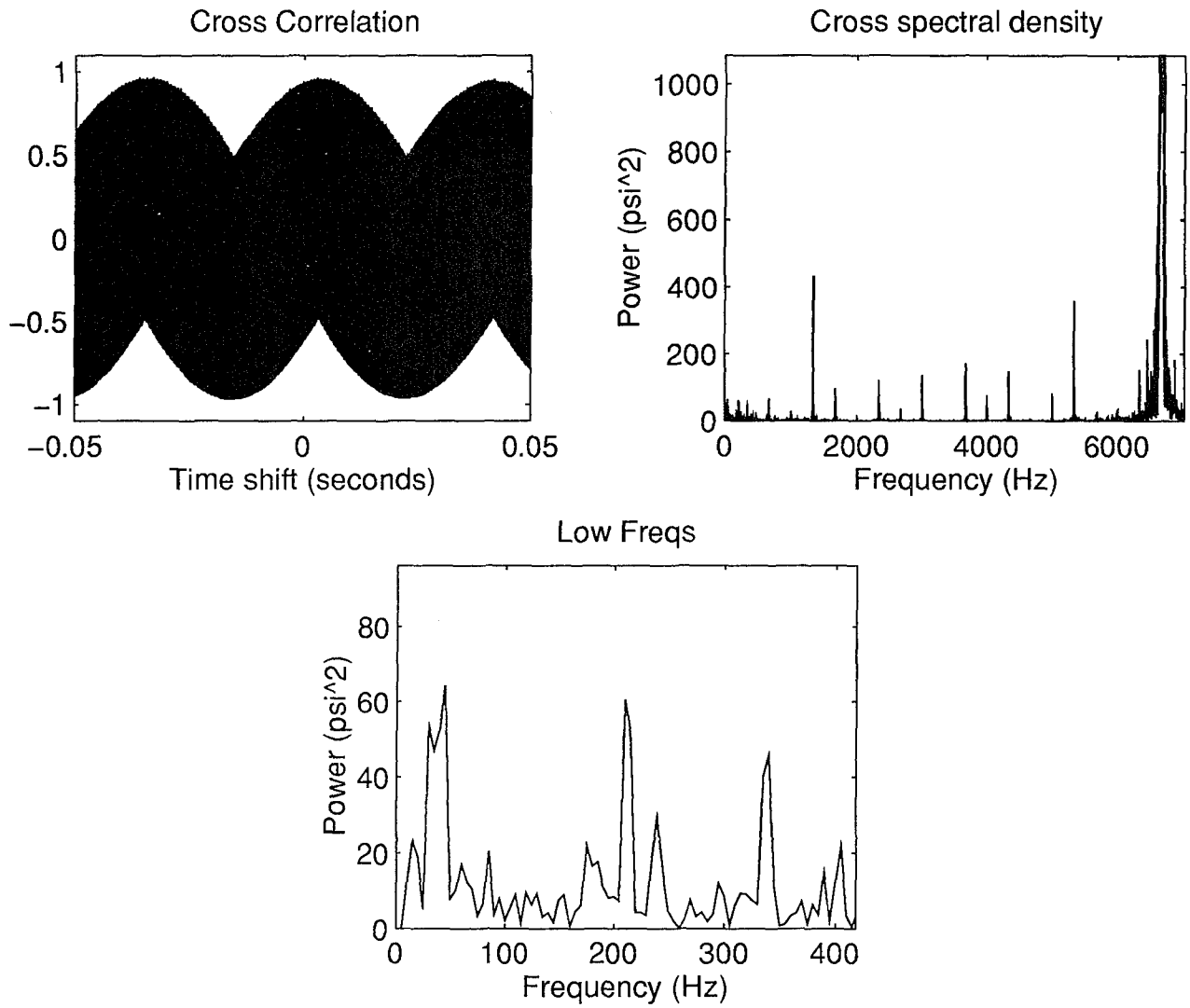


Figure 4.30c Rotor 9, 95%: Cross-Correlation of Kulites #1 and #4 at T=-0.91

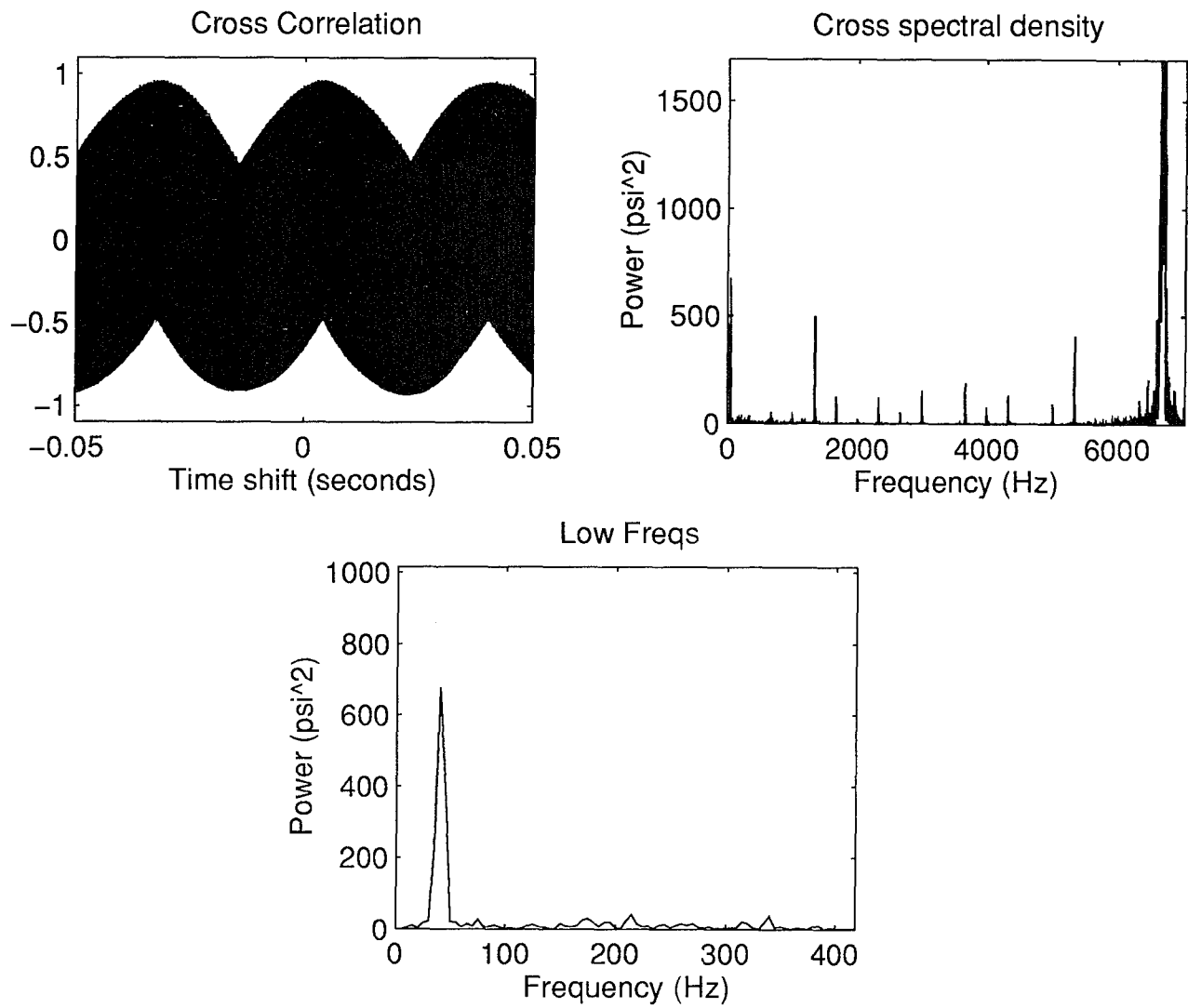


Figure 4.30d Rotor 9, 95%: Cross-Correlation of Kulites #1 and #4 at T=-0.66

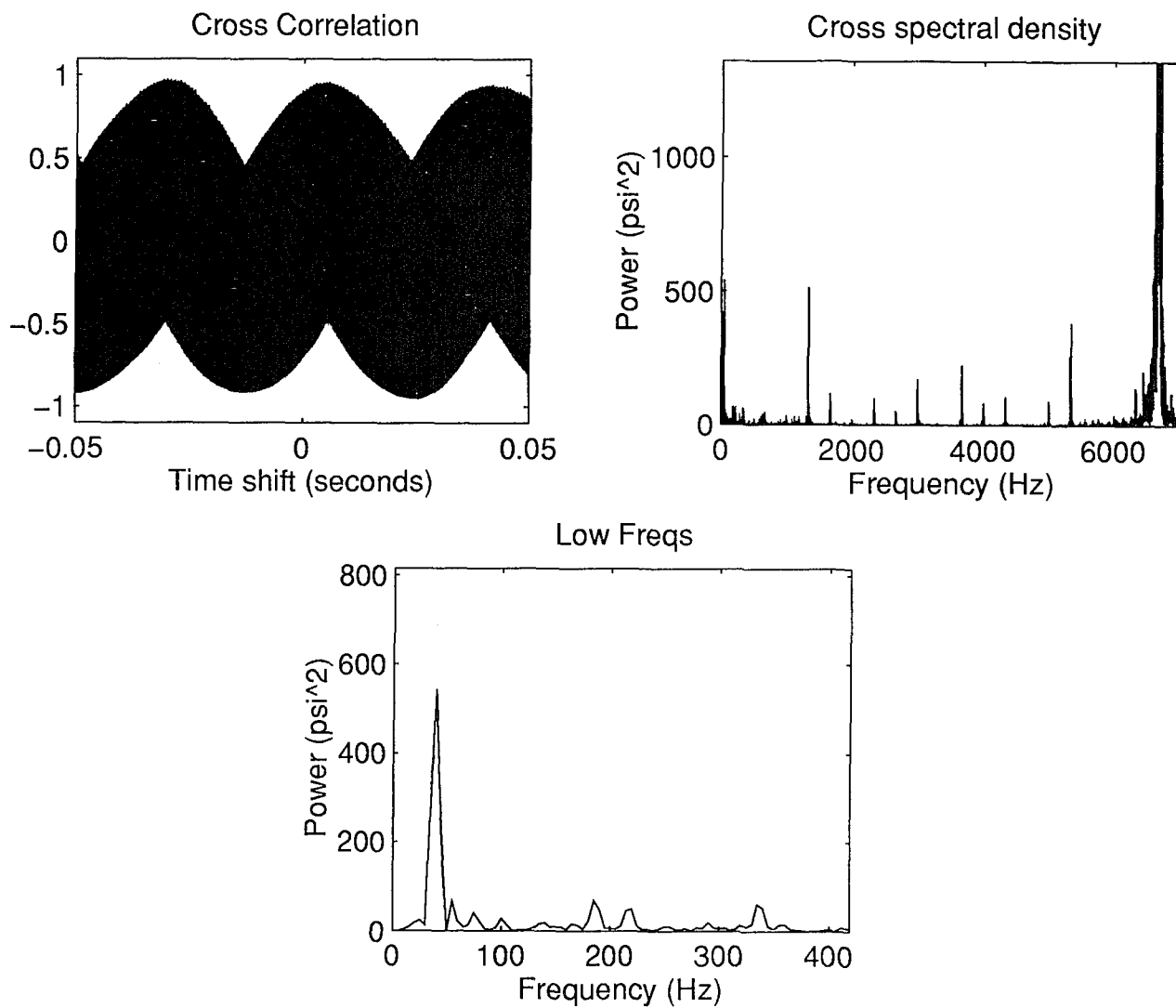


Figure 4.30e Rotor 9, 95%: Cross-Correlation of Kulites #1 and #4 at T=-0.51

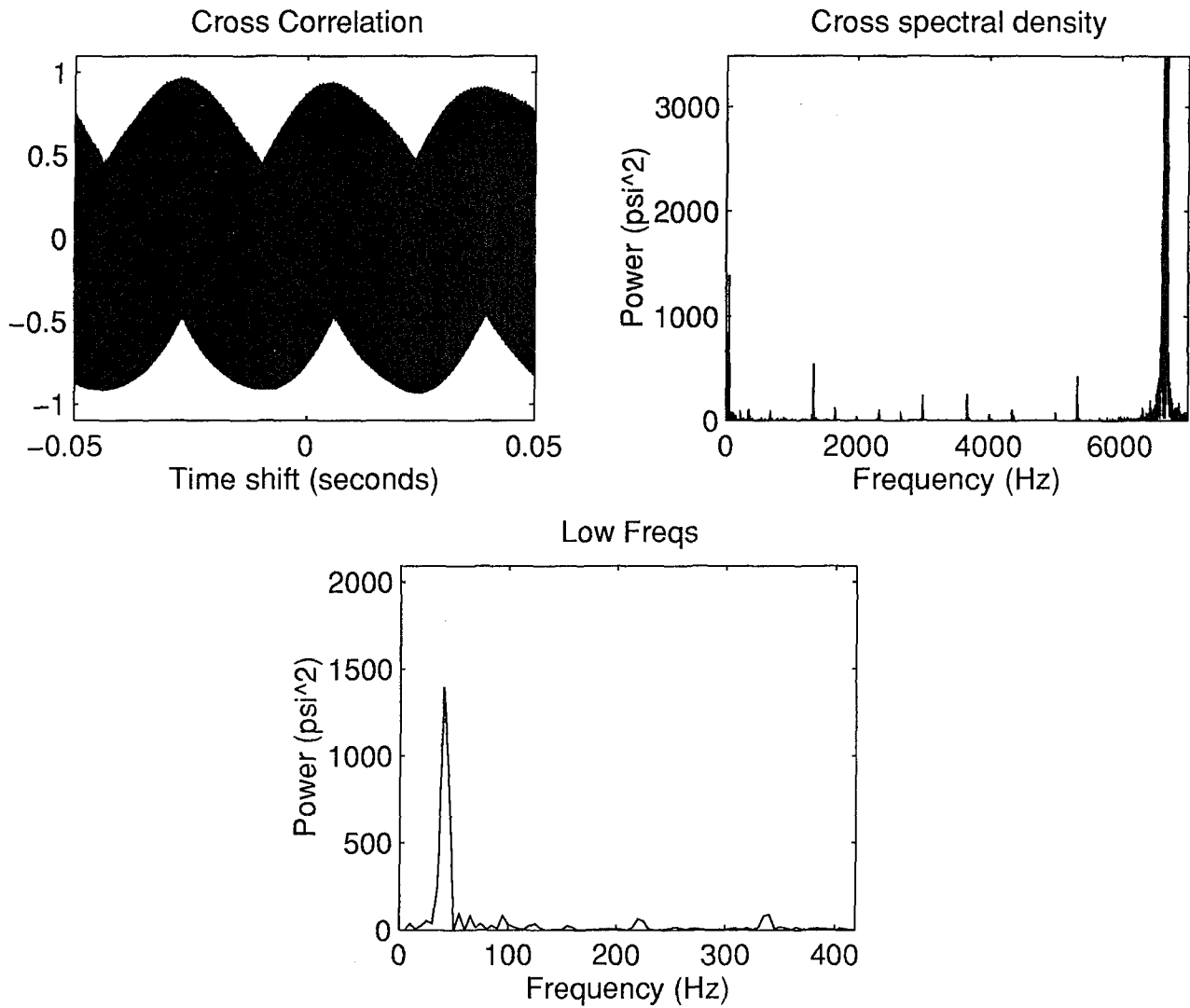


Figure 4.30f Rotor 9, 95%: Cross-Correlation of Kulites #1 and #4 at T=-0.16

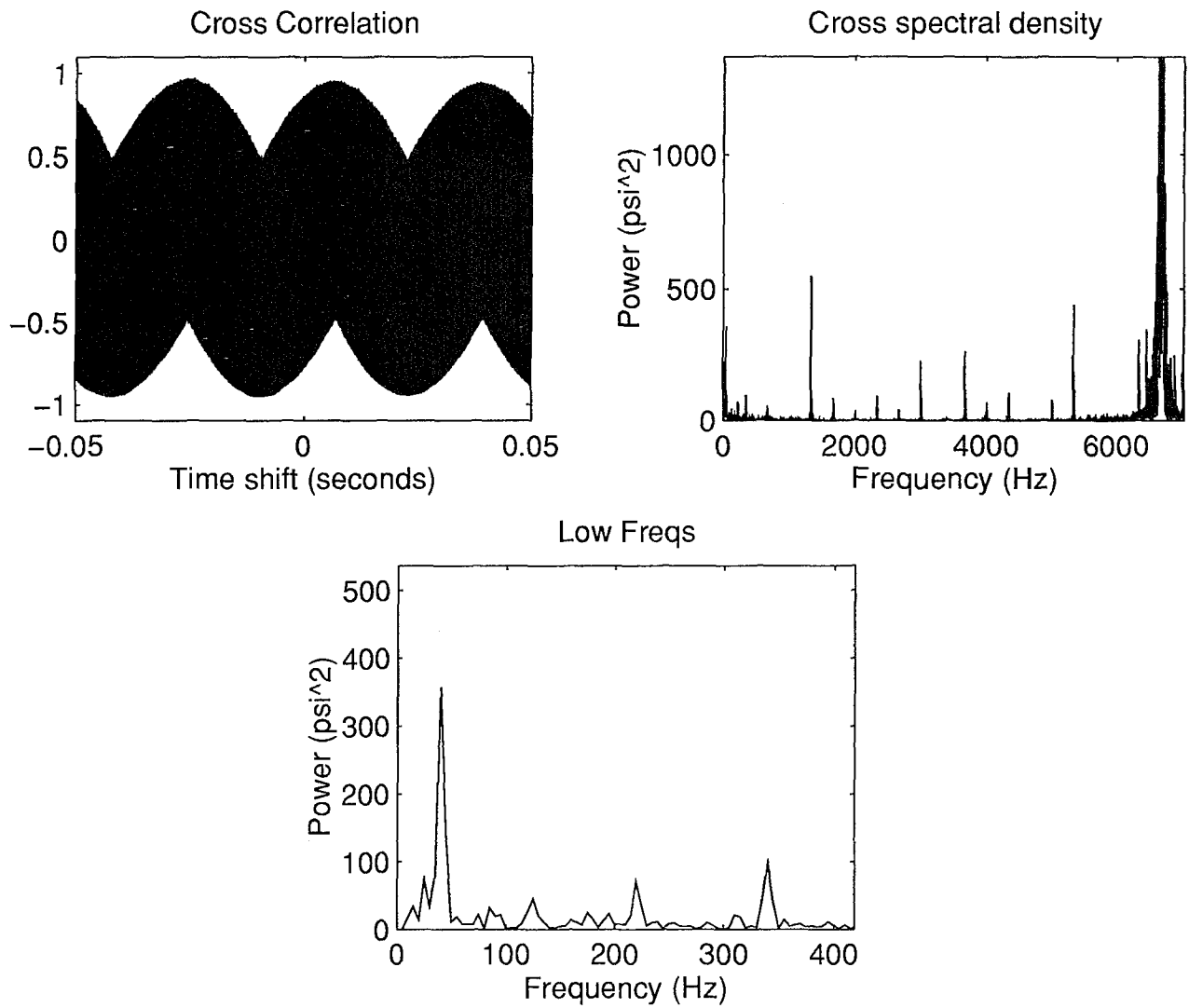


Figure 4.30g Rotor 9, 95%: Cross-Correlation of Kulites #1 and #4 at T=-0.06

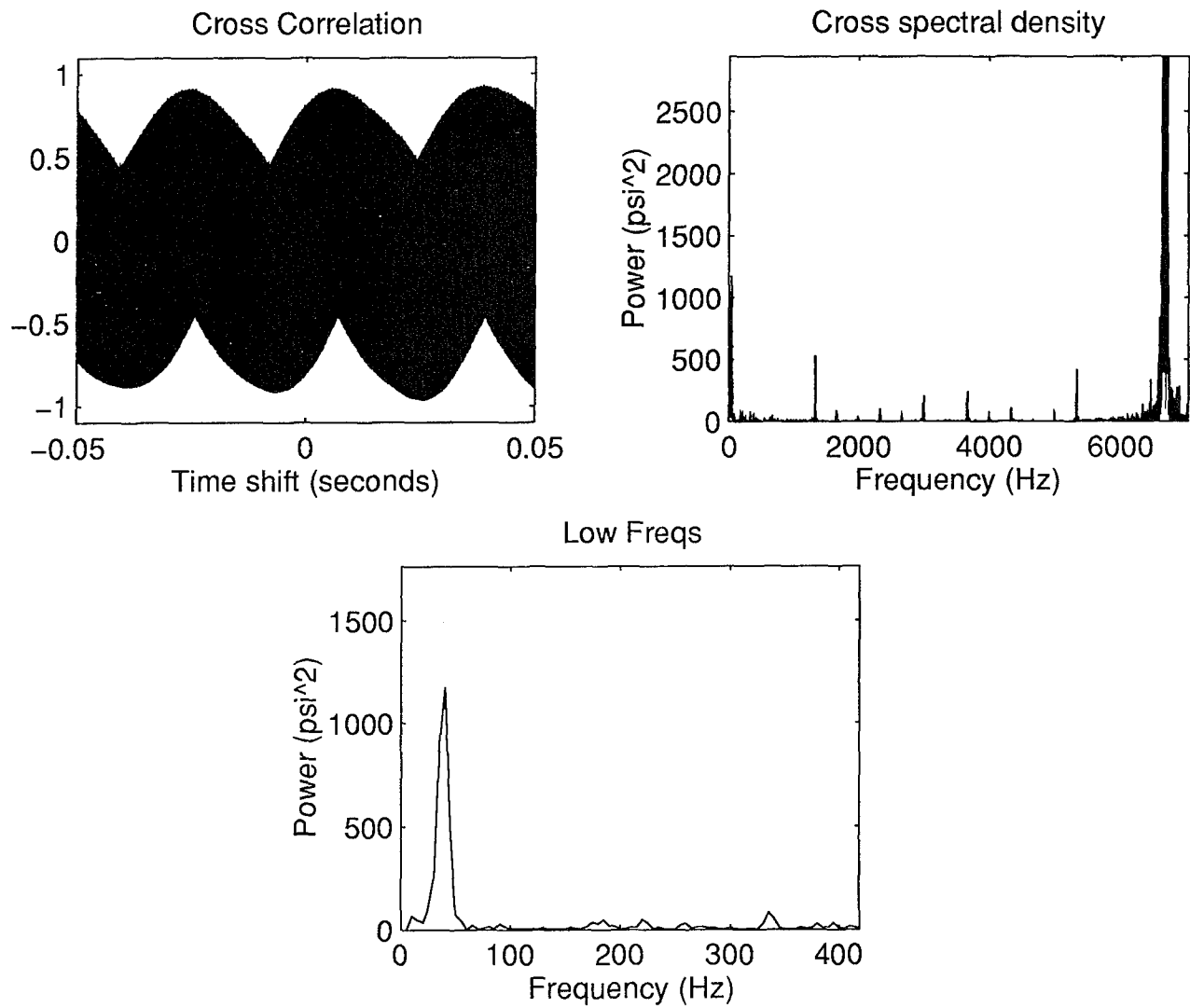


Figure 4.30h Rotor 9, 95%: Cross-Correlation of Kulites #1 and #4 at $T = -0.01$

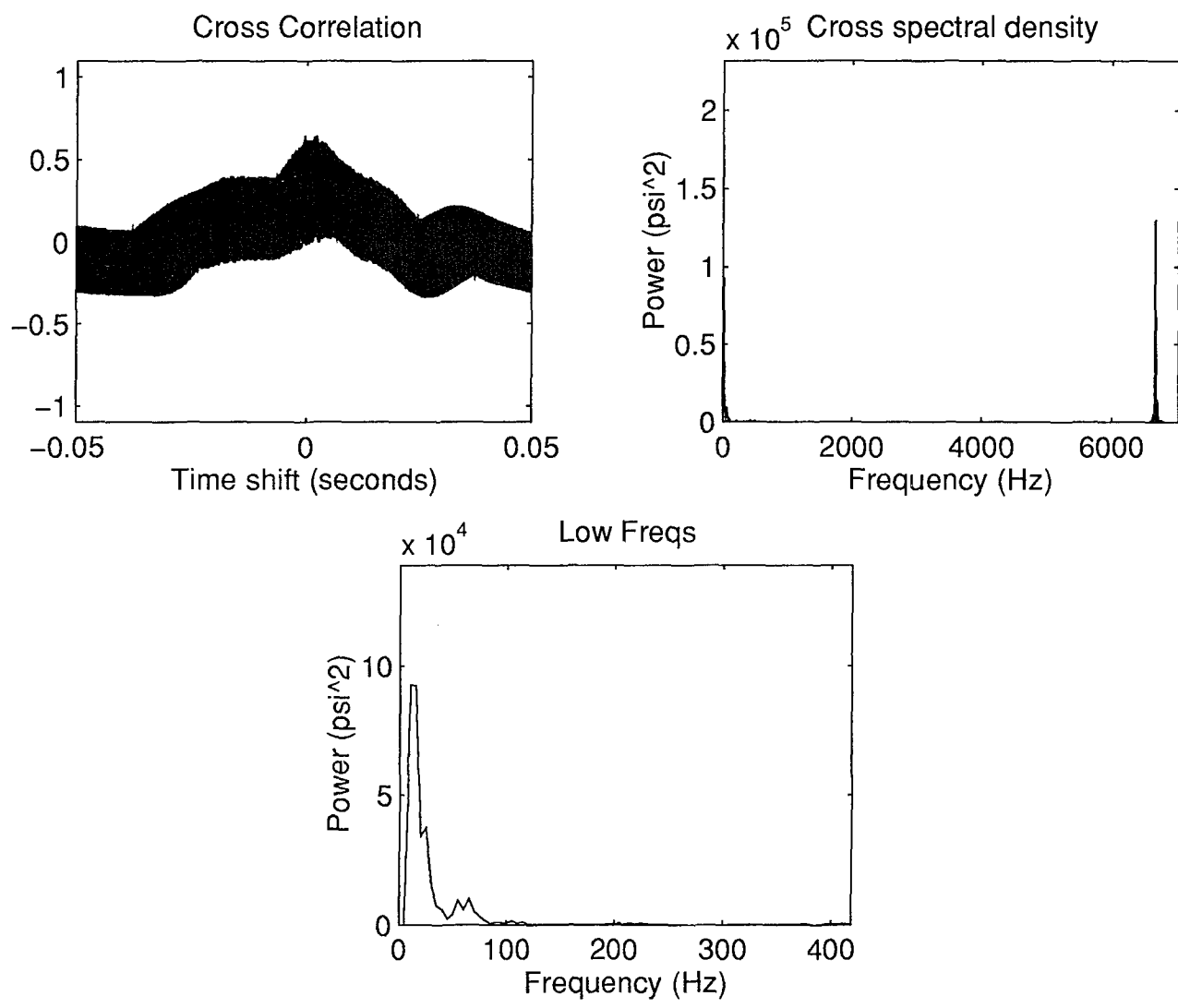


Figure 4.30i Rotor 9, 95%: Cross-Correlation of Kulites #1 and #4 at T=+0.04

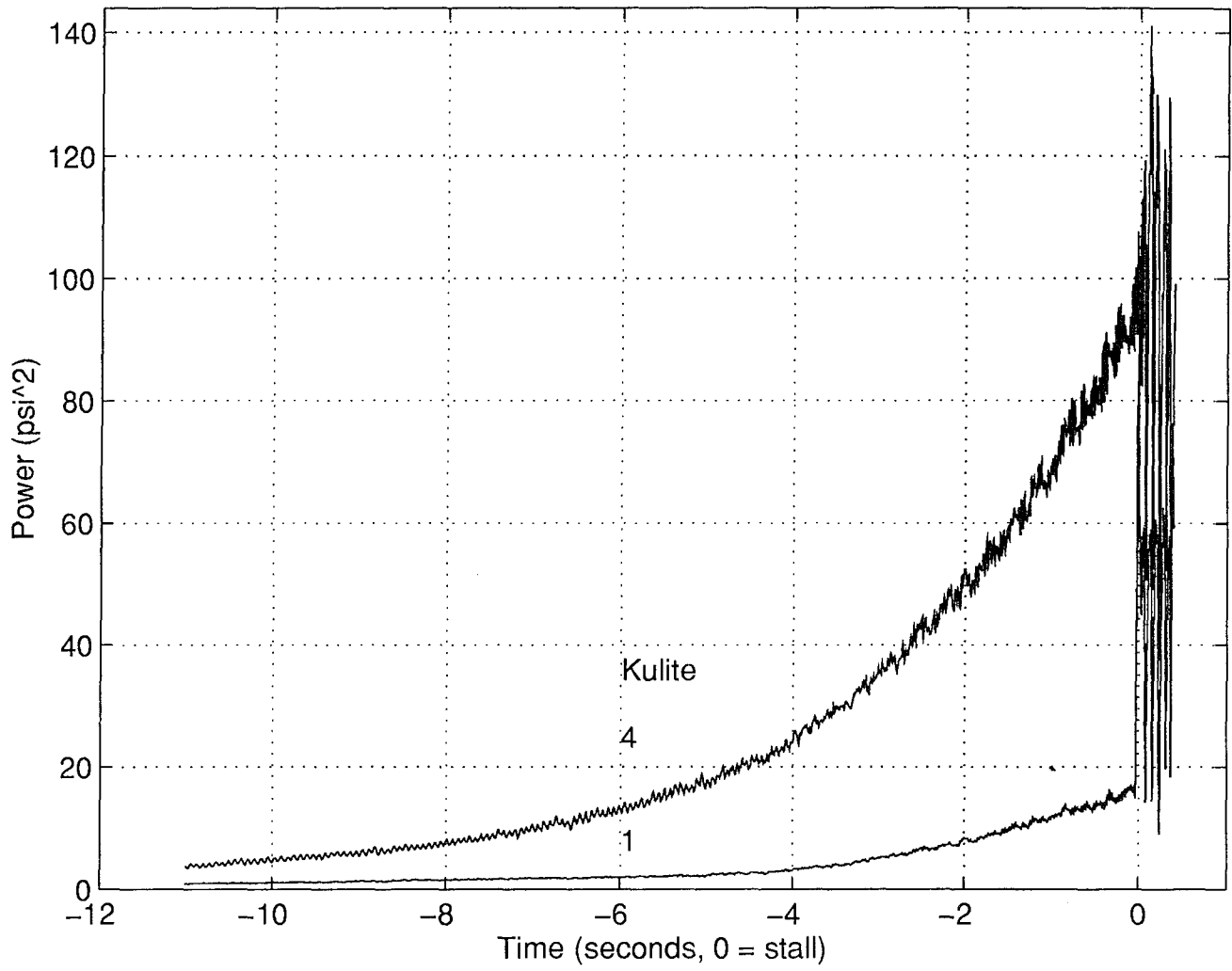


Figure 4.31 Rotor 9, 95%: Total Signal Power (less DC contribution)

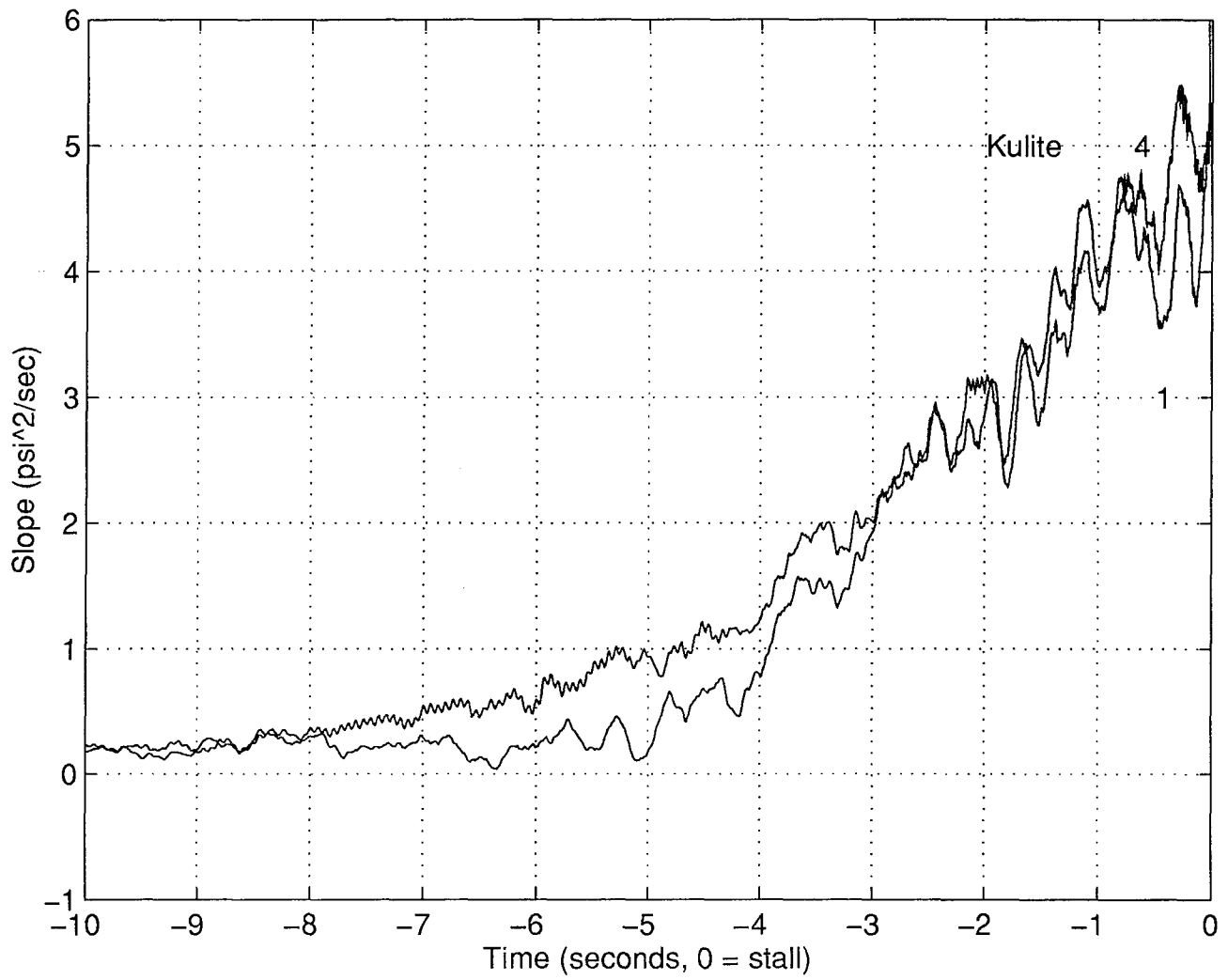


Figure 4.32 Rotor 9, 95%: Comparison of Slope of Power (Kulite #4 scaled by $\delta=0.1935$)

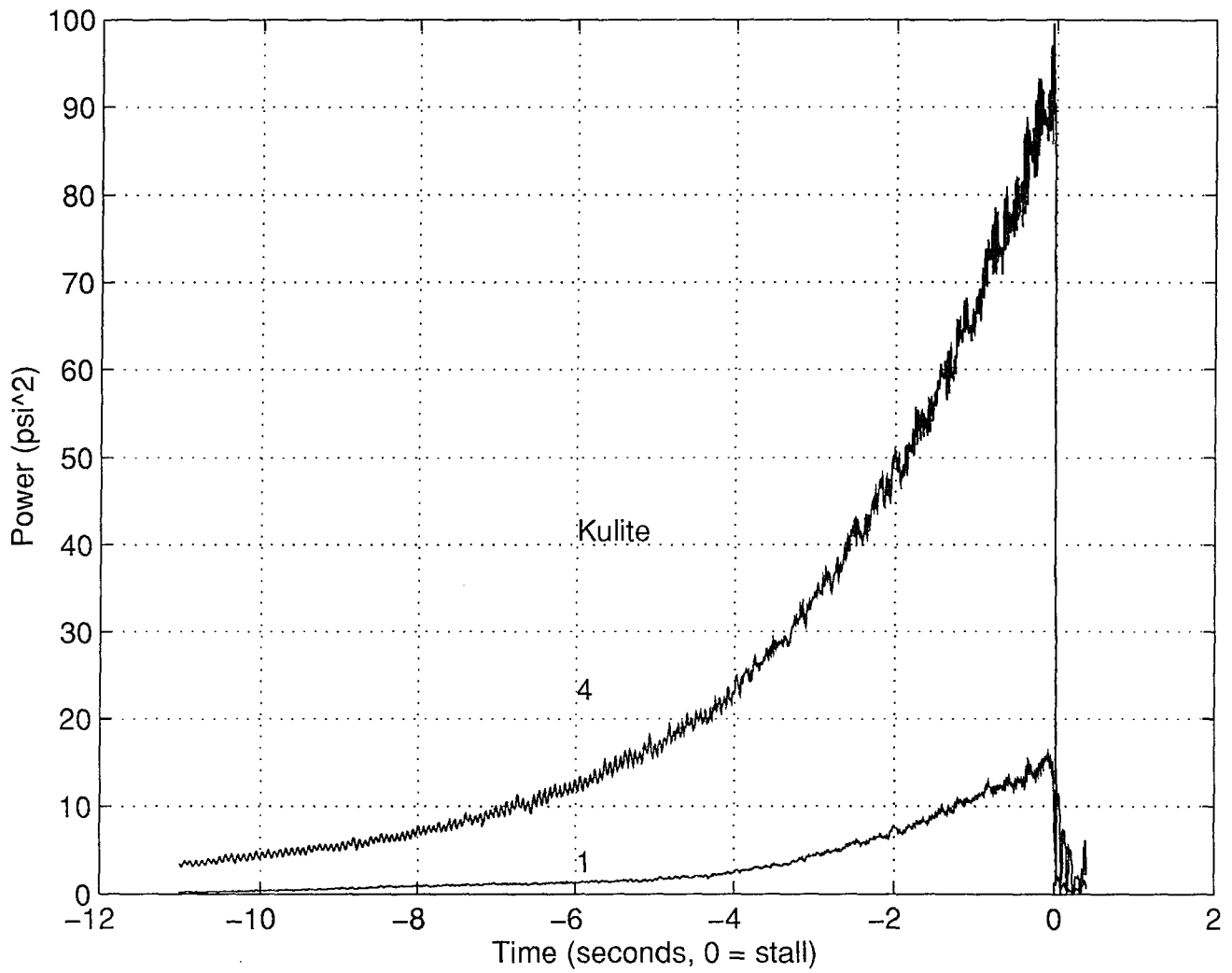


Figure 4.33 Rotor 9, 95%: Power of Blade Passing Frequency Group (6580 Hz to 6820 Hz)

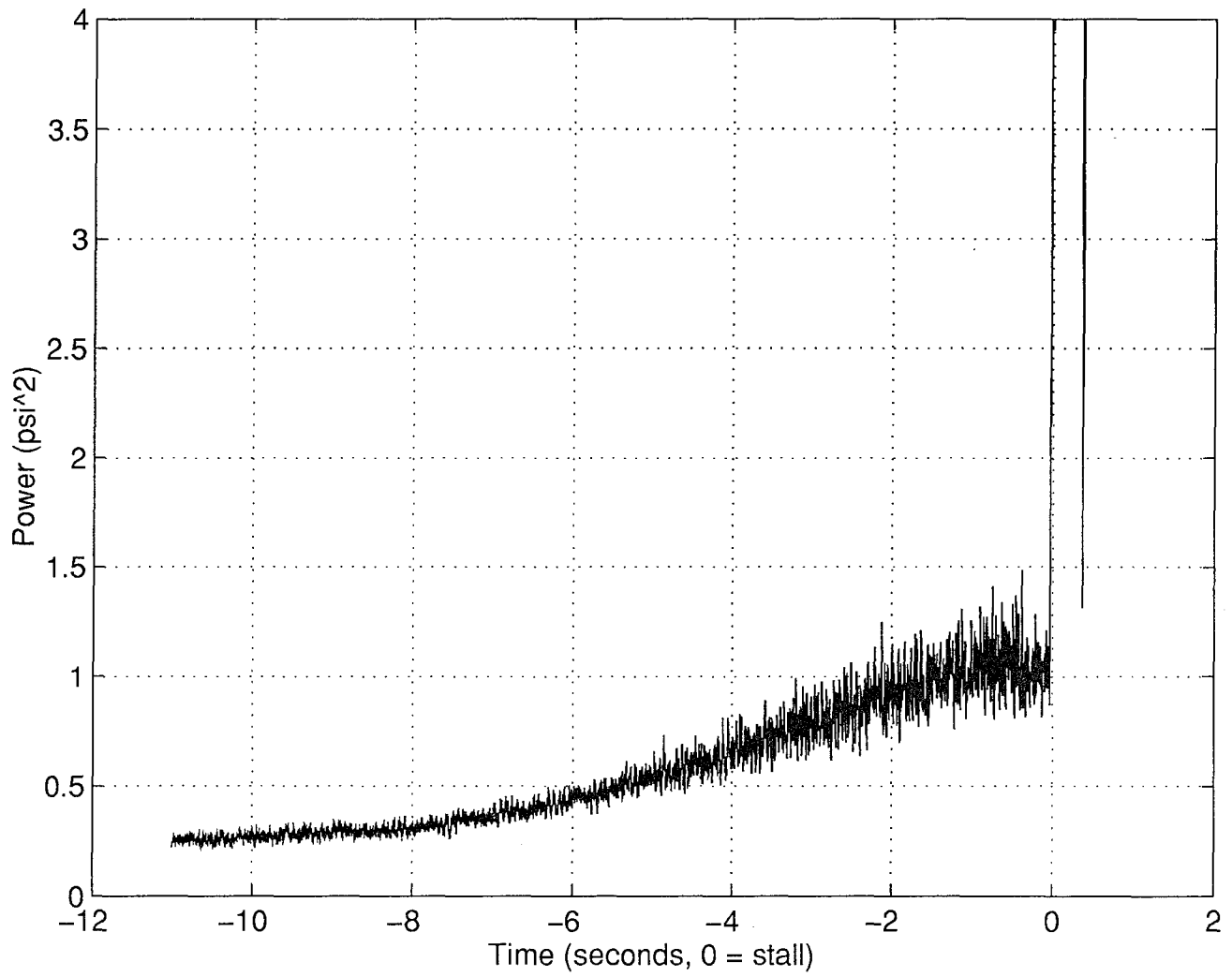


Figure 4.34 Rotor 9, 95%, Kulite #4: Power of Medium Frequency Group (340 Hz to 6560 Hz)

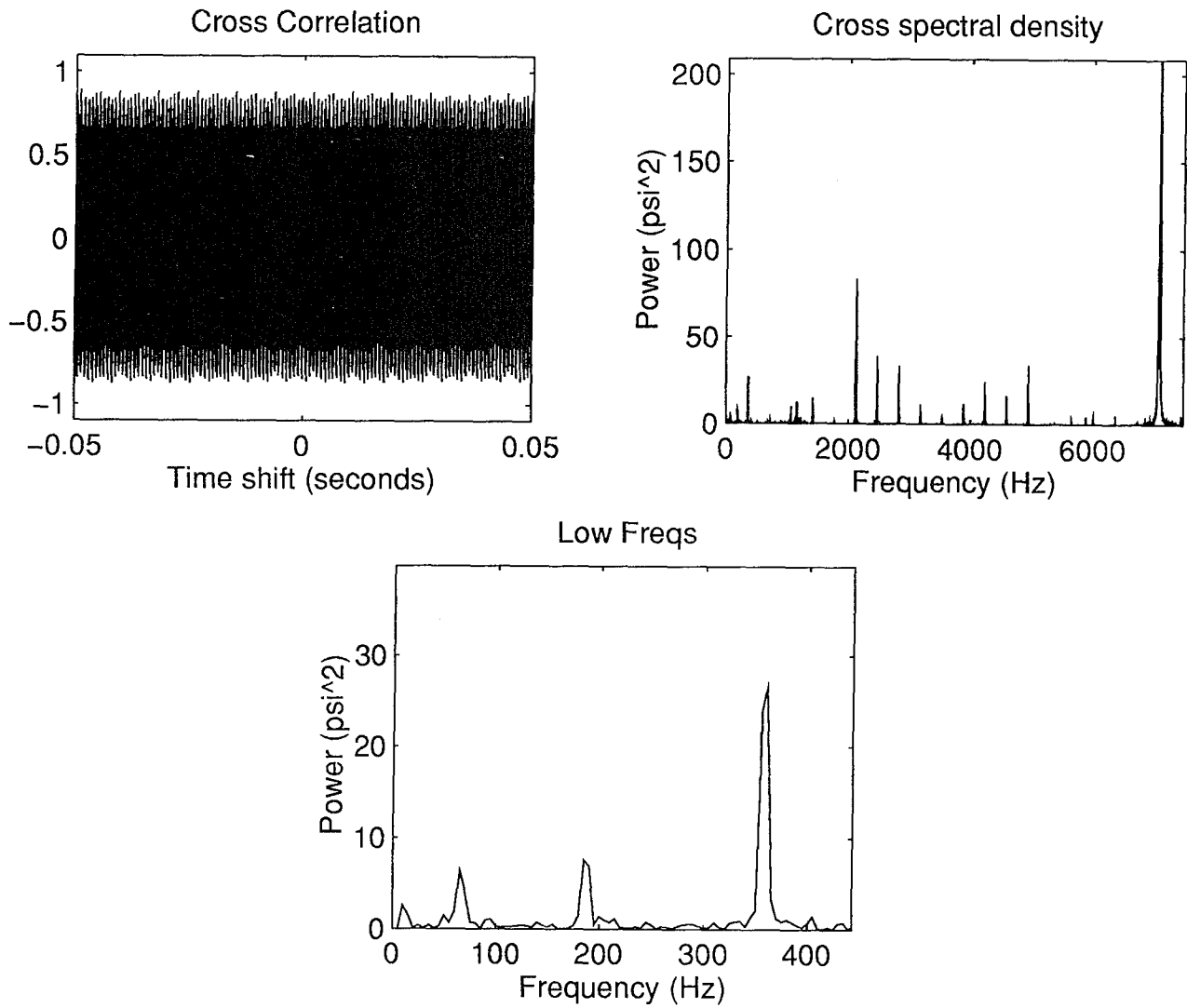


Figure 4.35a Rotor 9, 100%: Cross-Correlation of Kulites #1 and #4 at $T=-9.4$

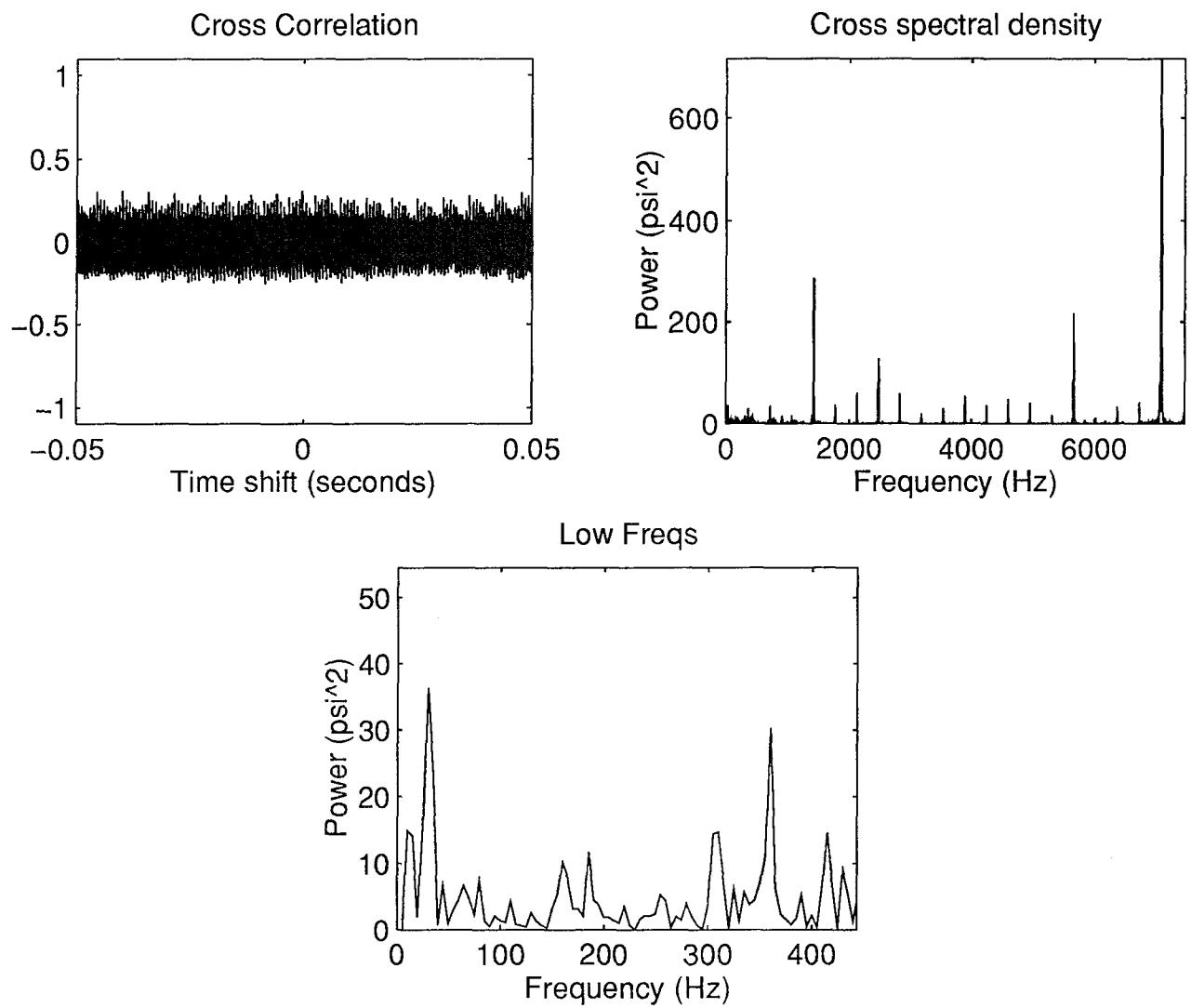


Figure 4.35b Rotor 9, 100%: Cross-Correlation of Kulites #1 and #4 at T=-2.4

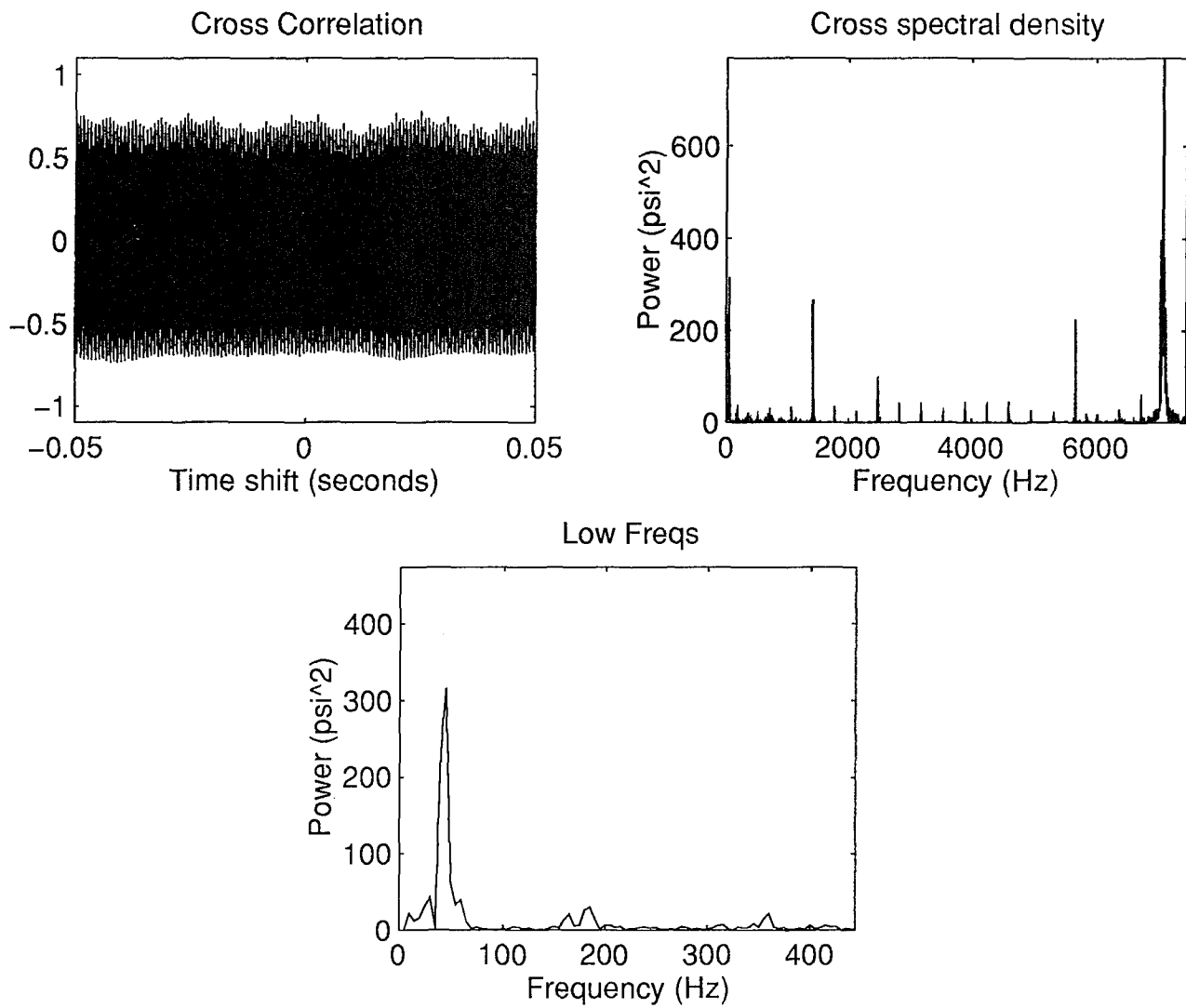


Figure 4.35c Rotor 9, 100%: Cross-Correlation of Kulites #1 and #4 at T=-0.9

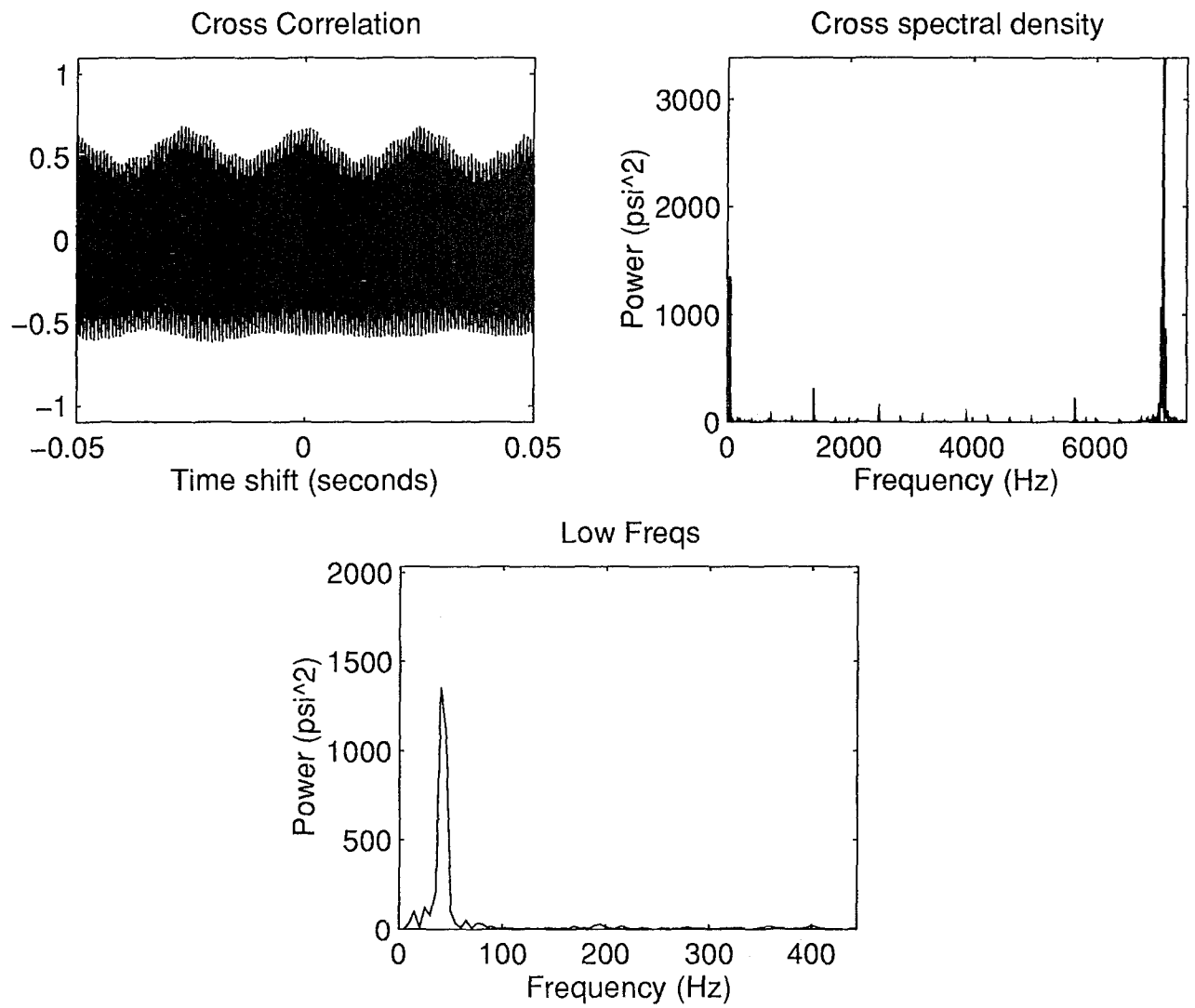


Figure 4.35d Rotor 9, 100%: Cross-Correlation of Kulites #1 and #4 at $T = -0.6$

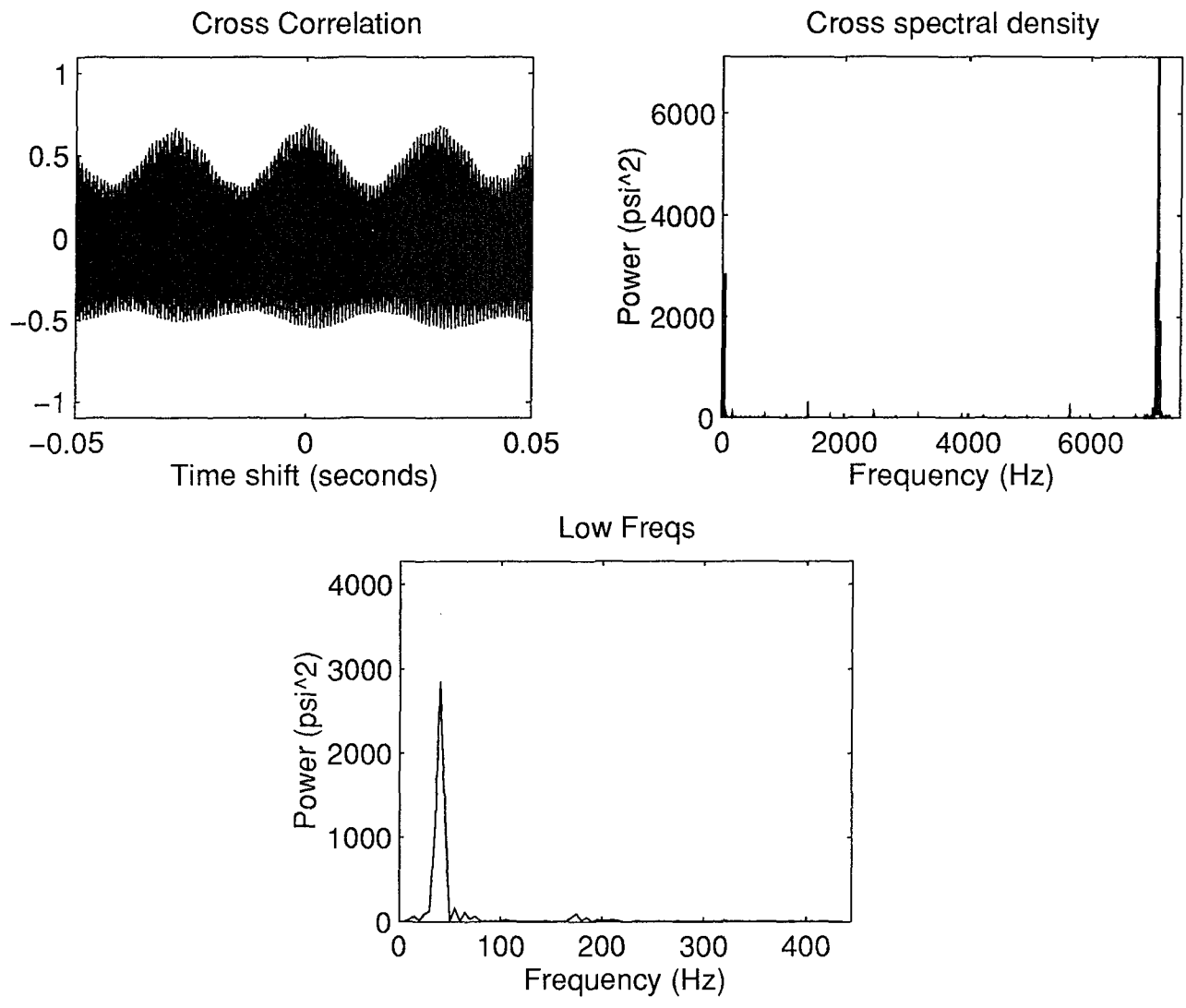


Figure 4.35e Rotor 9, 100%: Cross-Correlation of Kulites #1 and #4 at $T = -0.45$

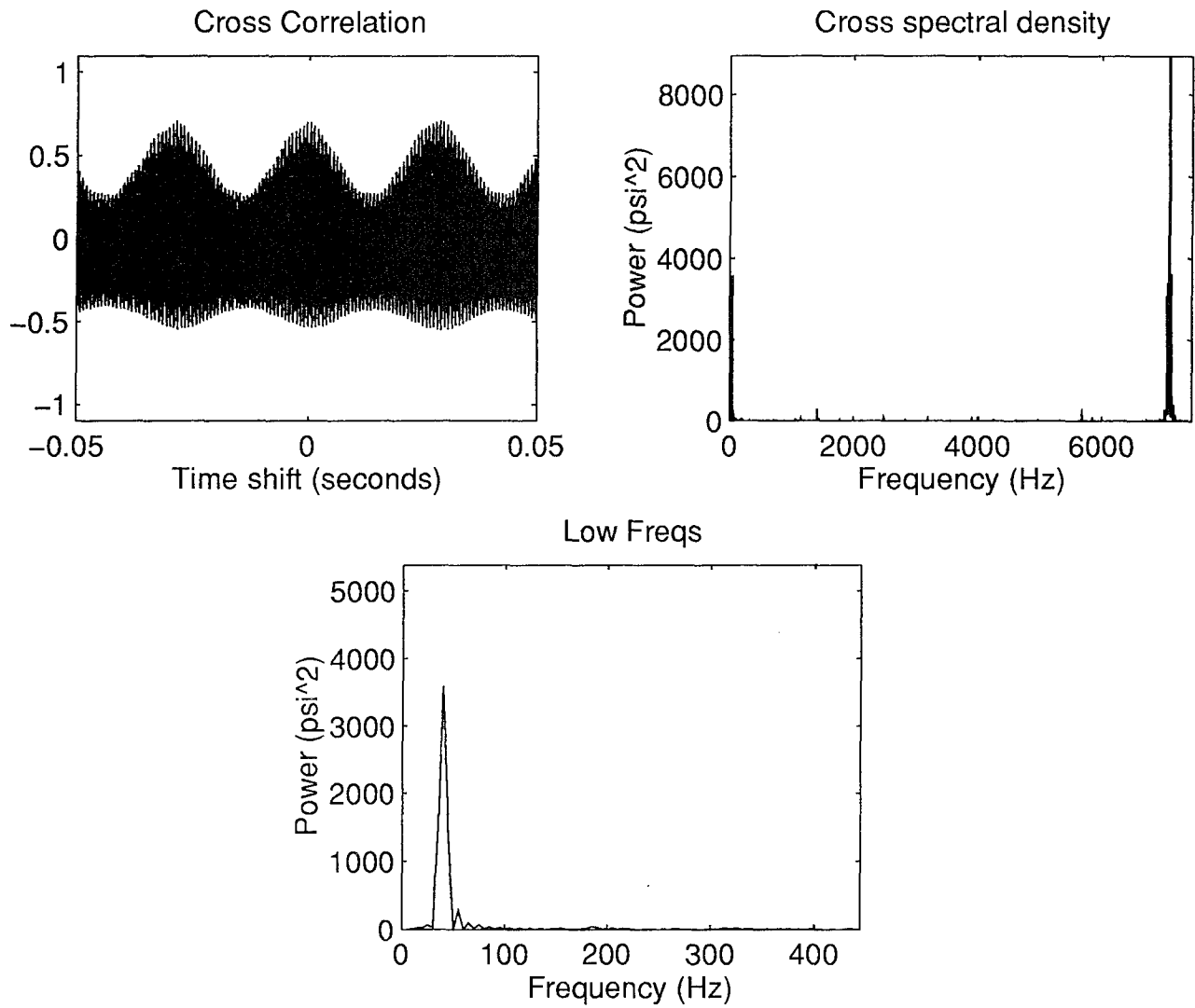


Figure 4.35f Rotor 9, 100%: Cross-Correlation of Kulites #1 and #4 at T=-0.35

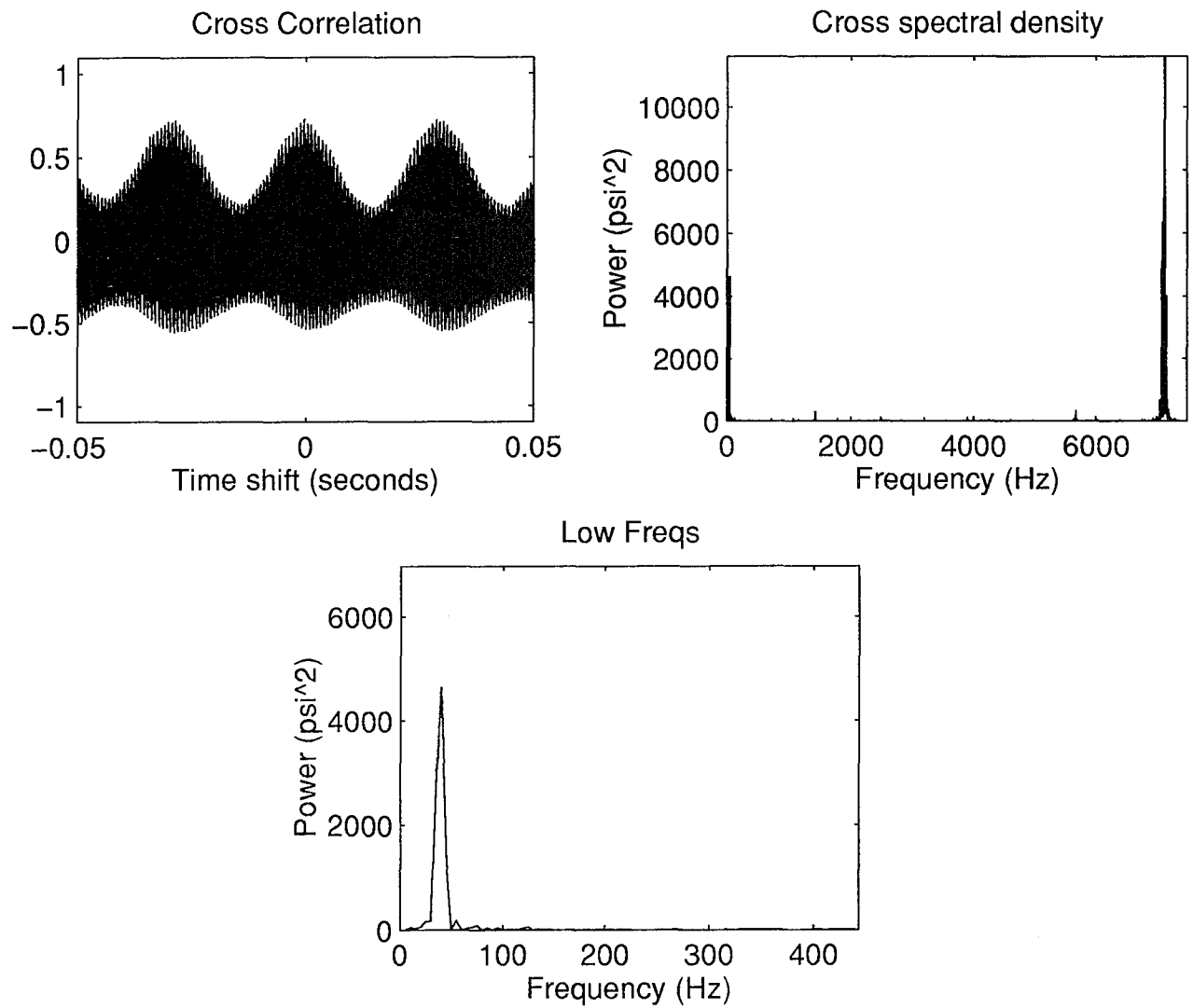


Figure 4.35g Rotor 9, 100%: Cross-Correlation of Kulites #1 and #4 at T=-0.25

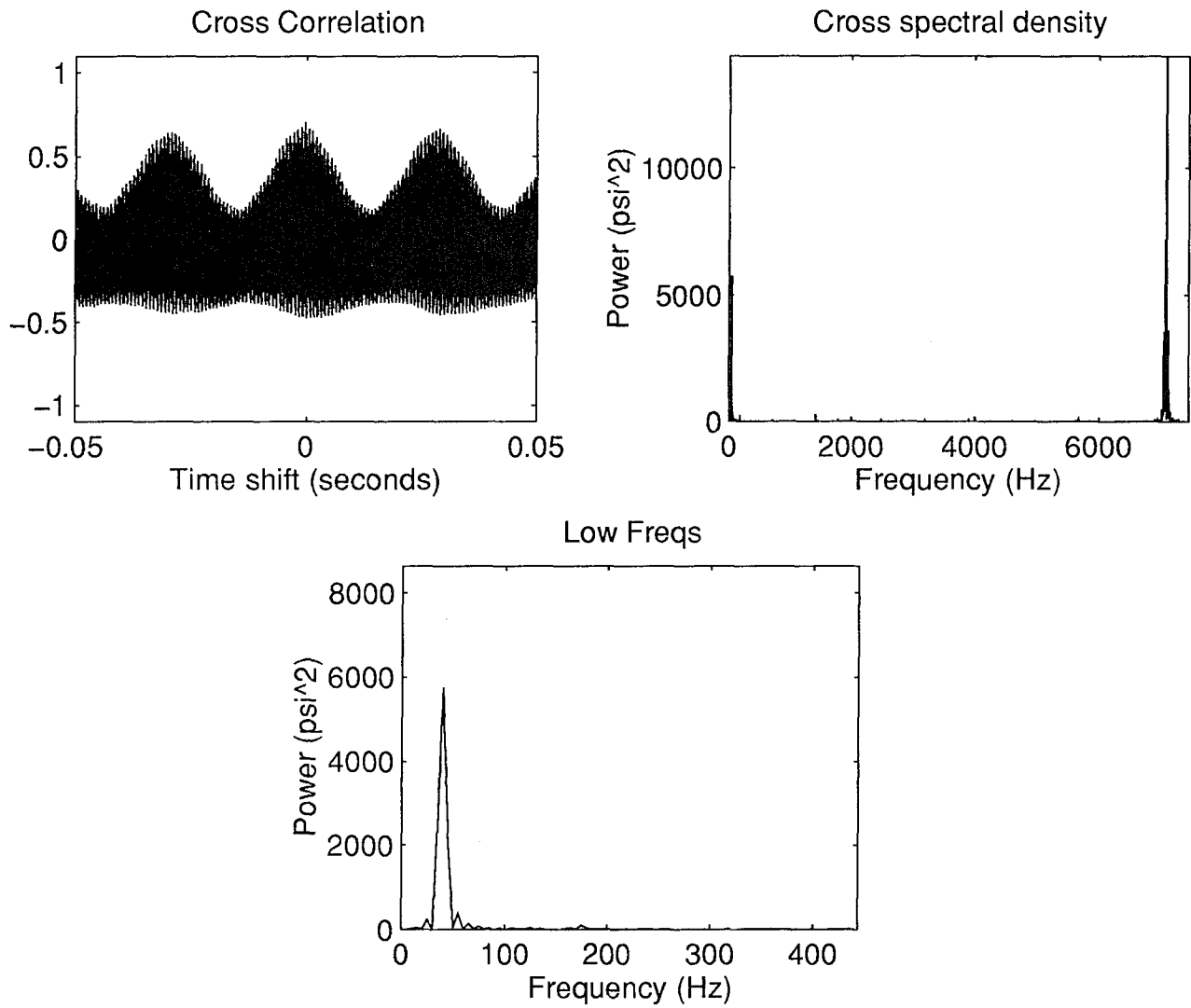


Figure 4.35h Rotor 9, 100%: Cross-Correlation of Kulites #1 and #4 at T=-0.15

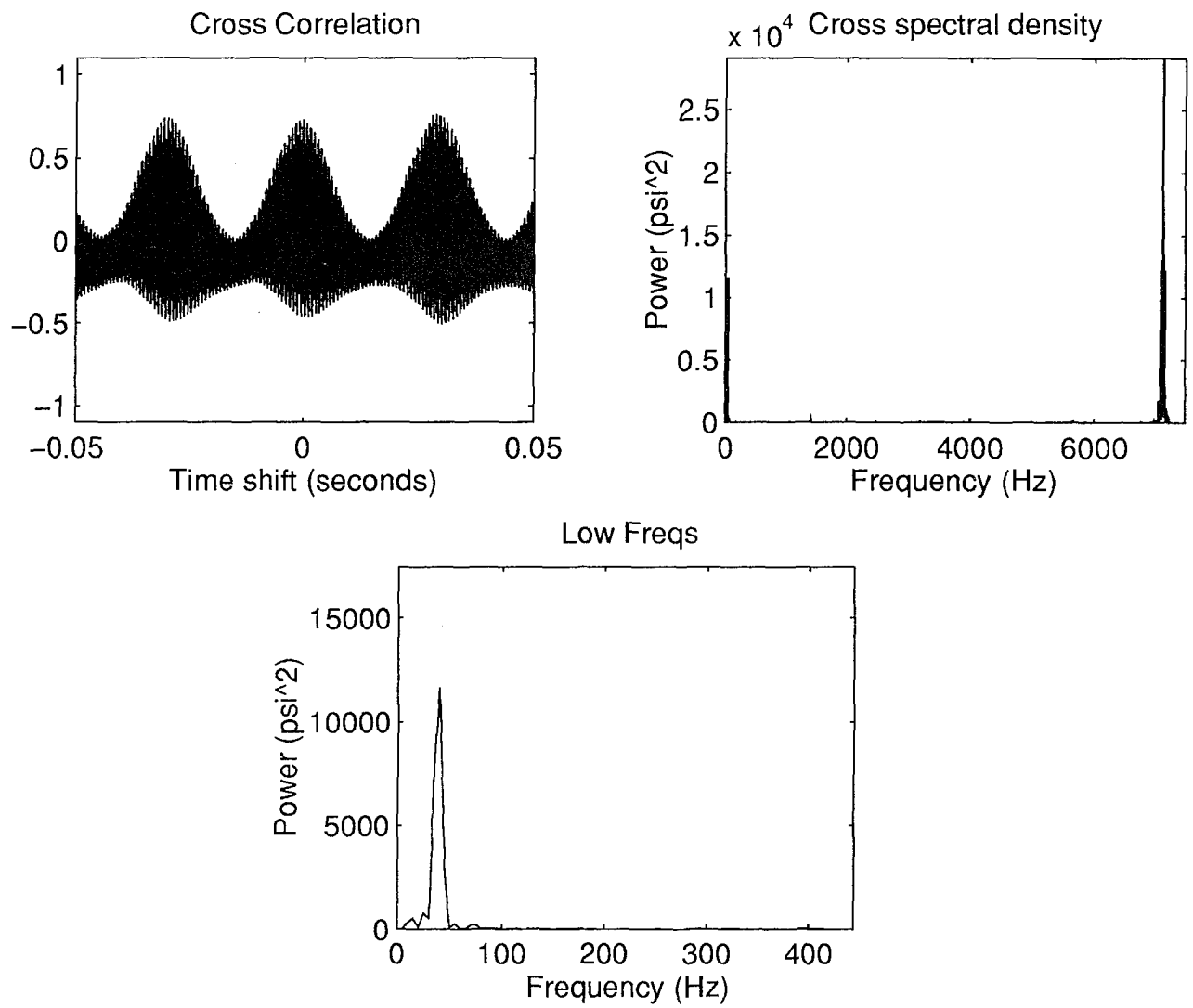


Figure 4.35i Rotor 9, 100%: Cross-Correlation of Kulites #1 and #4 at $T = -0.05$

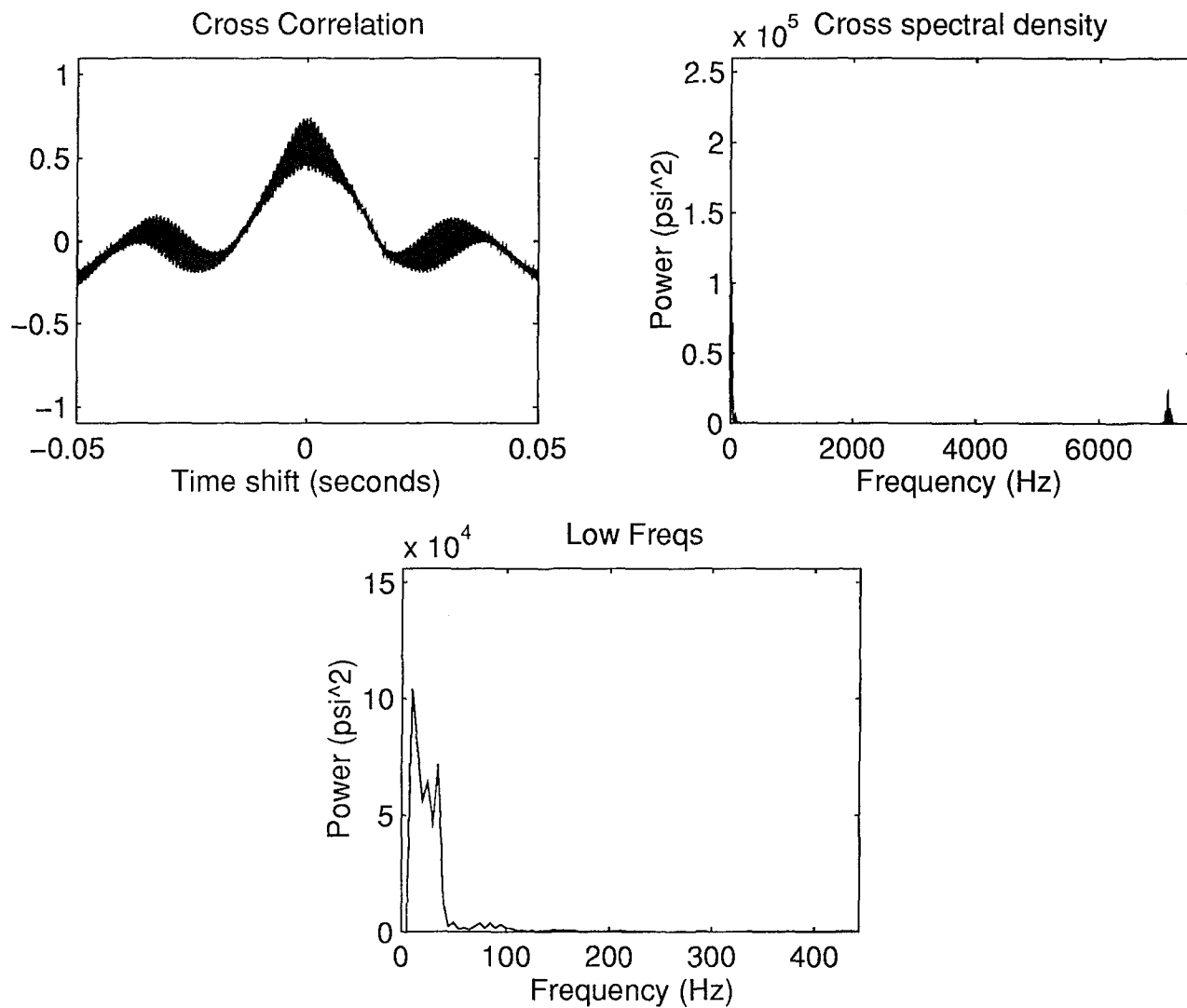


Figure 4.35j Rotor 9, 100%: Cross-Correlation of Kulites #1 and #4 at T=+0.05

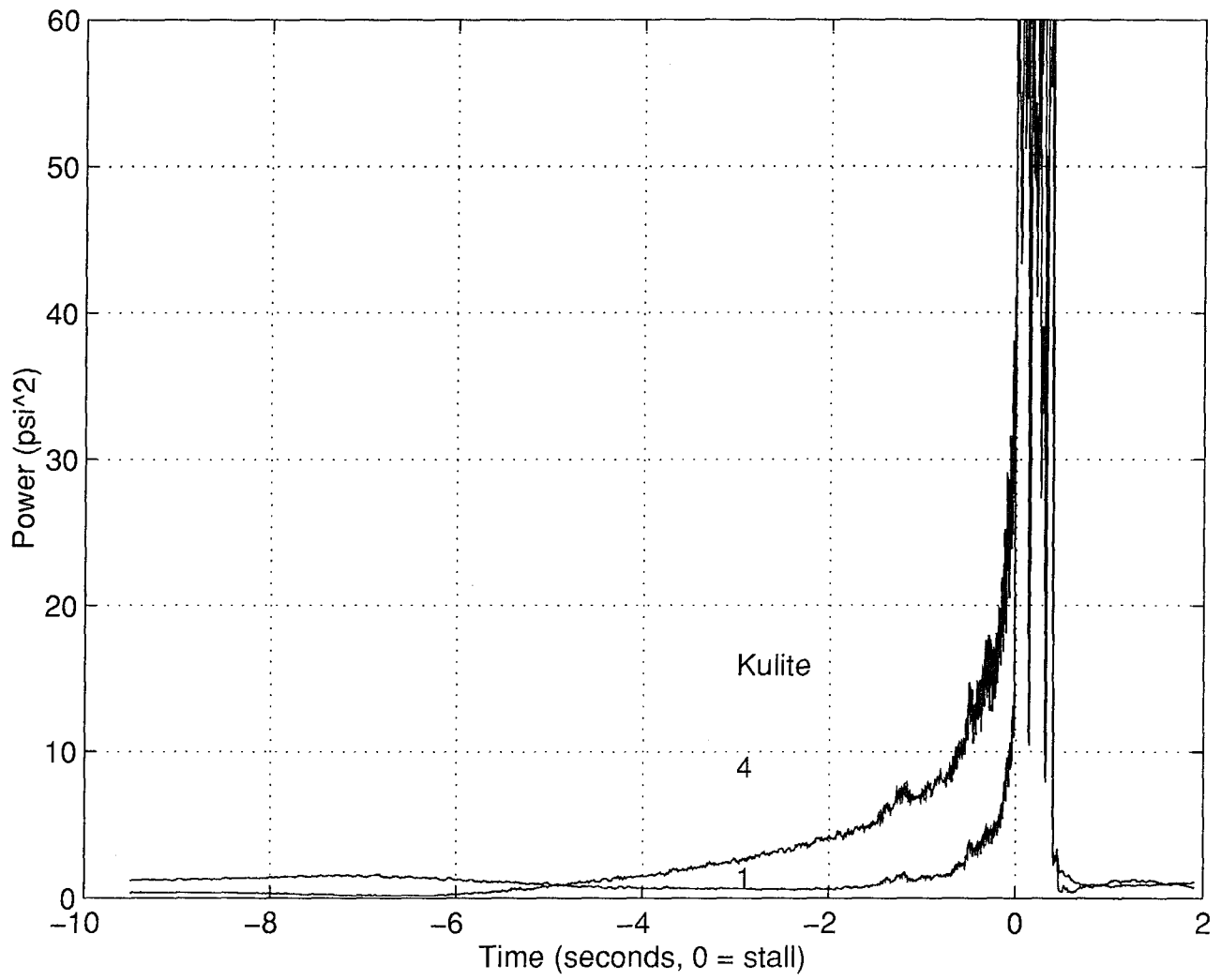


Figure 4.36 Rotor 9, 100%: Total Signal Power (less DC contribution)

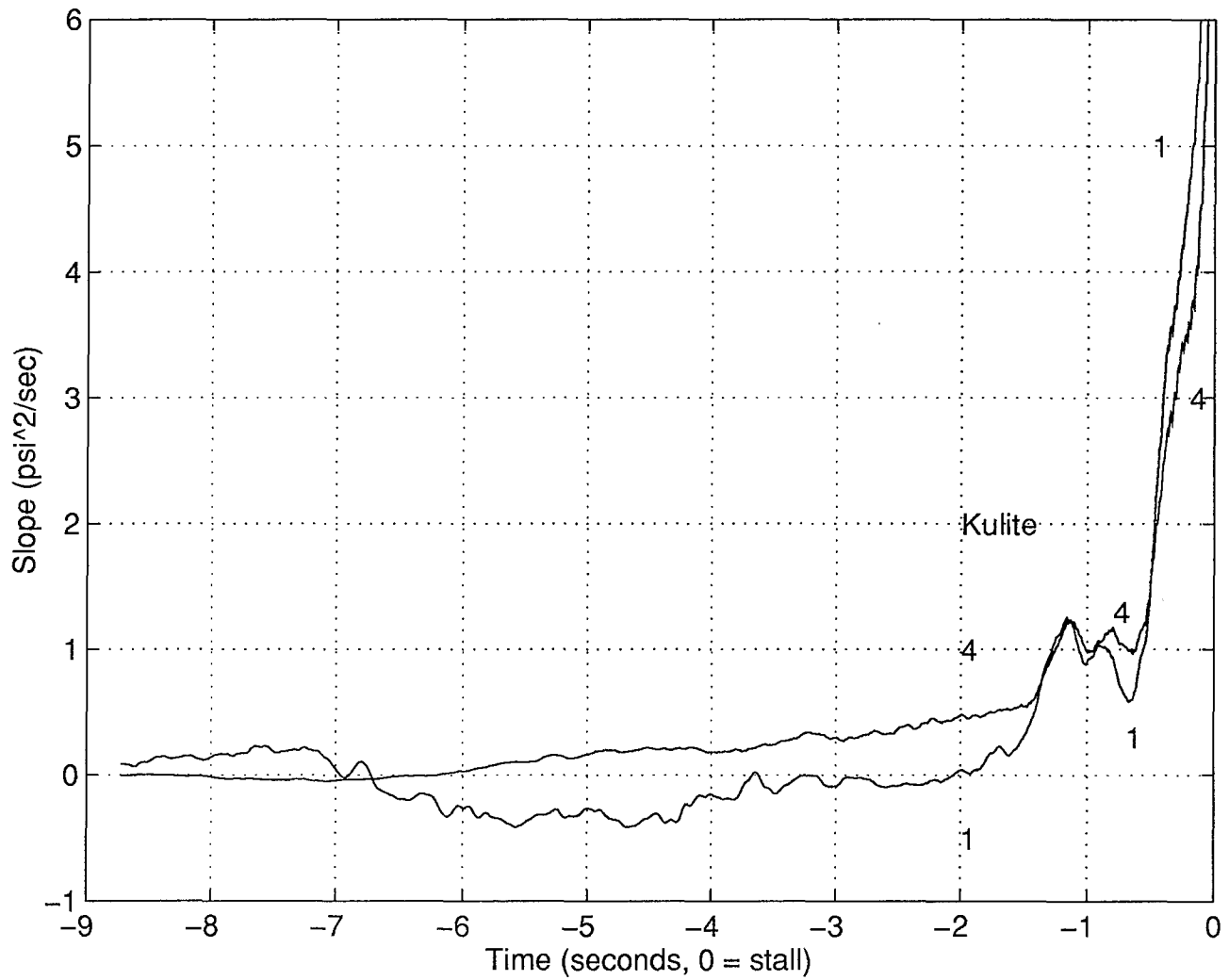


Figure 4.37 Rotor 9, 100%: Comparison of Slope of Power (Kulite #4 scaled by $\delta=0.2815$)

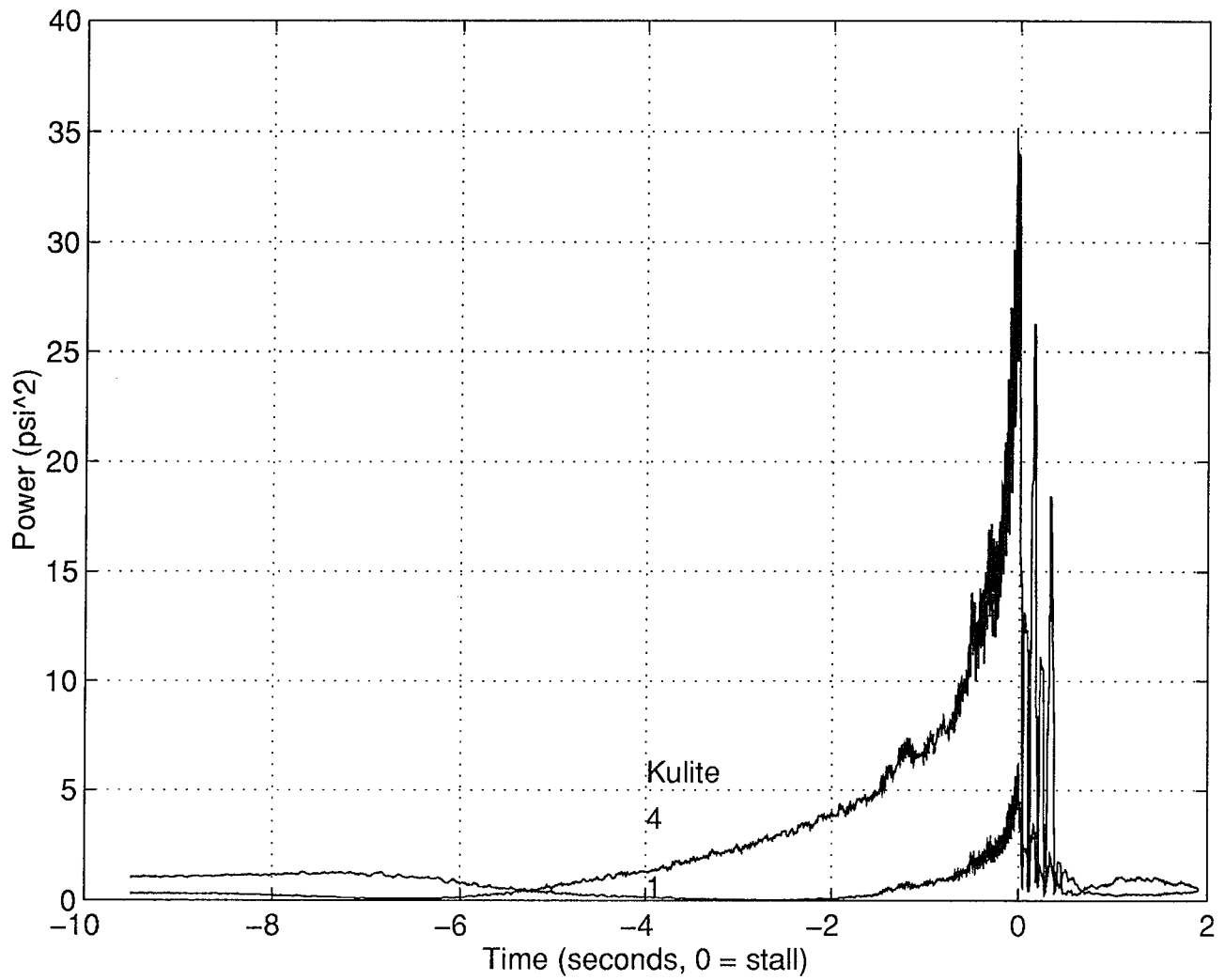


Figure 4.38 Rotor 9, 100%: Power of Blade Passing Frequency Group (6980 Hz to 7220 Hz)

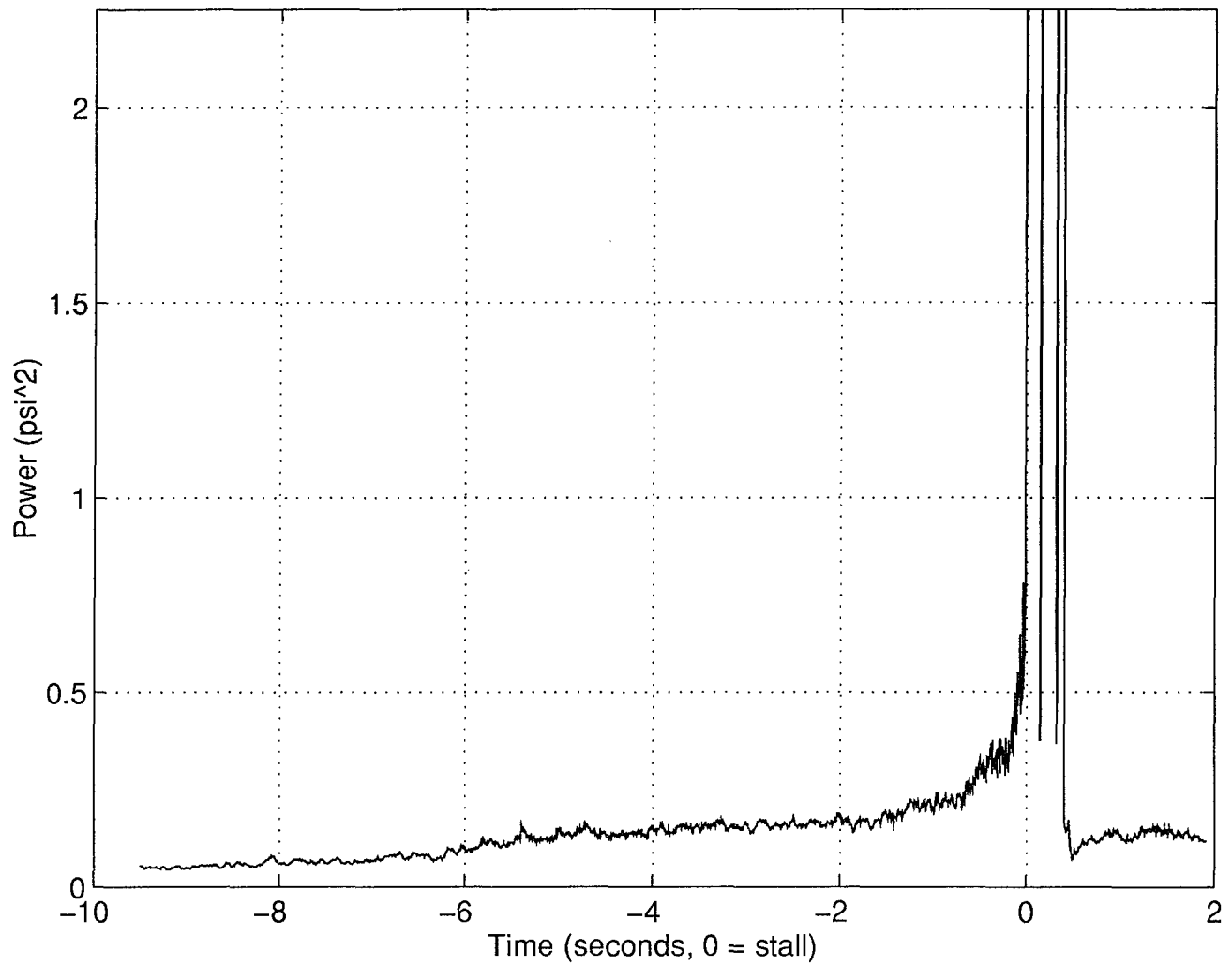


Figure 4.39 Rotor 9, 100%, Kulite #4: Power of Medium Frequency Group (360 Hz to 6960 Hz)

APPENDIX A

A.1 Fourier Window Size and Frequency Resolution

A completely accurate Fourier transform would be able to represent any frequency which might be present in the signal of interest. However, the lowest (fundamental) frequency ω_0 , the maximum frequency $(N/2)\omega_0$ and the number of frequencies available between these extremes is proportional to the number of data points in the window (N) and sample rate (T). Using the Fourier transform to decompose a signal into its frequency components, then, is exact only if an infinite amount of data is available. Since this is obviously never the case when using results obtained by experiment, frequency decomposition of data represents an approximation whose accuracy improves with the number of data points available. For example, Fig. A.1 shows two identical sinusoids, one sampled at a window size of 1 second while the other is sampled with a window of 10 seconds. The Fourier transform of these data streams should ideally result in a single spike at the sinusoid frequency. While neither transform achieves this fidelity, the 10 second transform is much more accurate. Thus, using the largest possible window of time gives the best results. While this is true of a periodic signal, the experimental data examined here is random; window size for a random signal must be chosen with care.

A universal disadvantage of selecting a large T is the increased amount of data which must be processed. Also, if a constant value of frequency resolution is desired, N must be increased in equal proportion; this further compounds data processing problems. While increasing N alone is a reasonable approach for a periodic signal, data containing rapidly shifting frequencies must use as small a window as possible. Consider Fig. A.2: the 6000 data point signal in Fig. A.2a is comprised of 5900 points of a 1 Hz sinusoid with 100 points of a 10 Hz sinusoid buried in the middle of the window. The FFT of the entire 6000 points

is shown in Fig. A.2b; note that, while the 1 Hz signal is easily visible, the 10 Hz signal is difficult to see.

A.2 Other Signal Processing Techniques

Only those processing techniques which produced consistent results are included in the main body of this report. Other techniques which were tried and found inconsistent or uninformative included:

1. Power of the low frequency group normalized by total signal power.
2. Power of surge frequencies normalized by total signal power. This will obviously work for Rotor 9, but was not useful for the other rotors.
3. Power of the frequencies around 1/2 of rotor frequencies. This group includes typical first mode frequencies.
4. Variance of power signals as measured by the technique: $(f(t)-f(t-1))/f(t)$ where t is one time step (1/160 second for this study).

Wavelet techniques were suggested, but consultation with the Math department revealed that this would be a lot of work to learn and apply with little hope for improvement in analysis. This still might be a good approach for someone who already knew about wavelets and could obtain software to apply them.

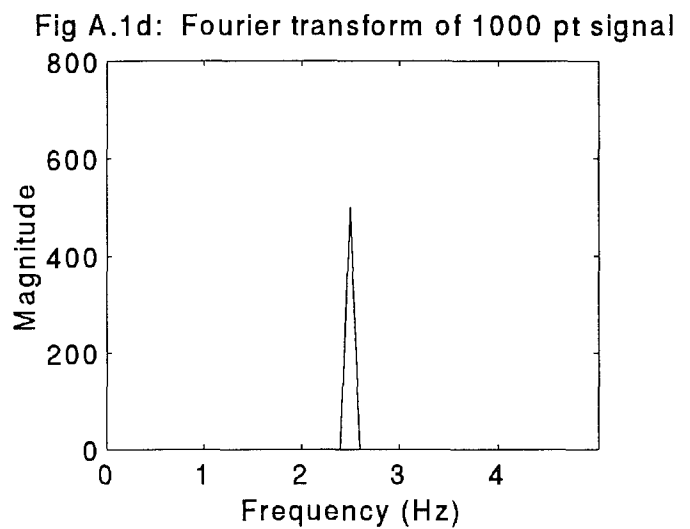
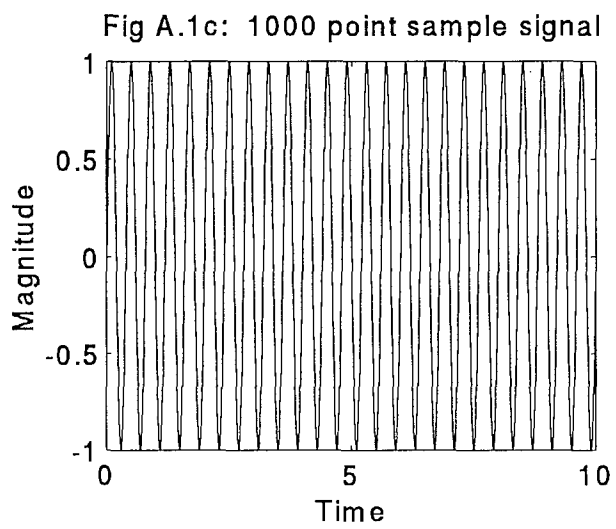
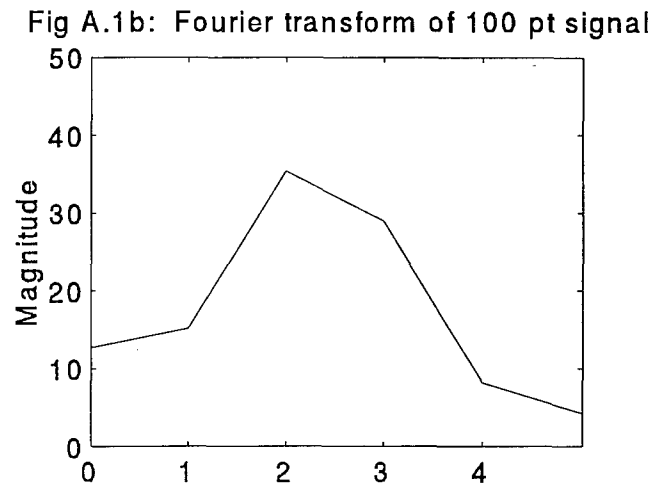
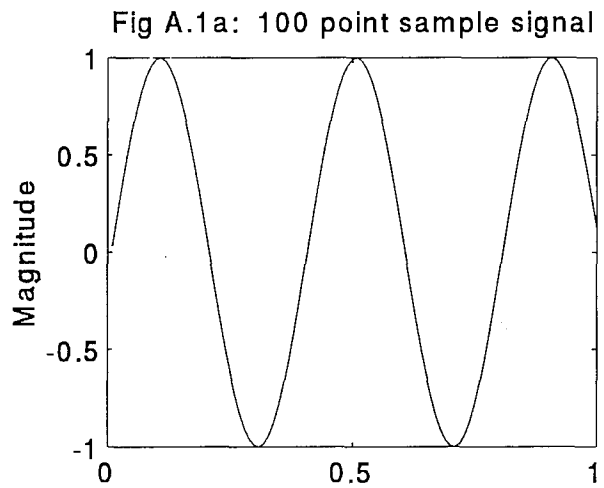


Figure A.1 Example of Fourier transform

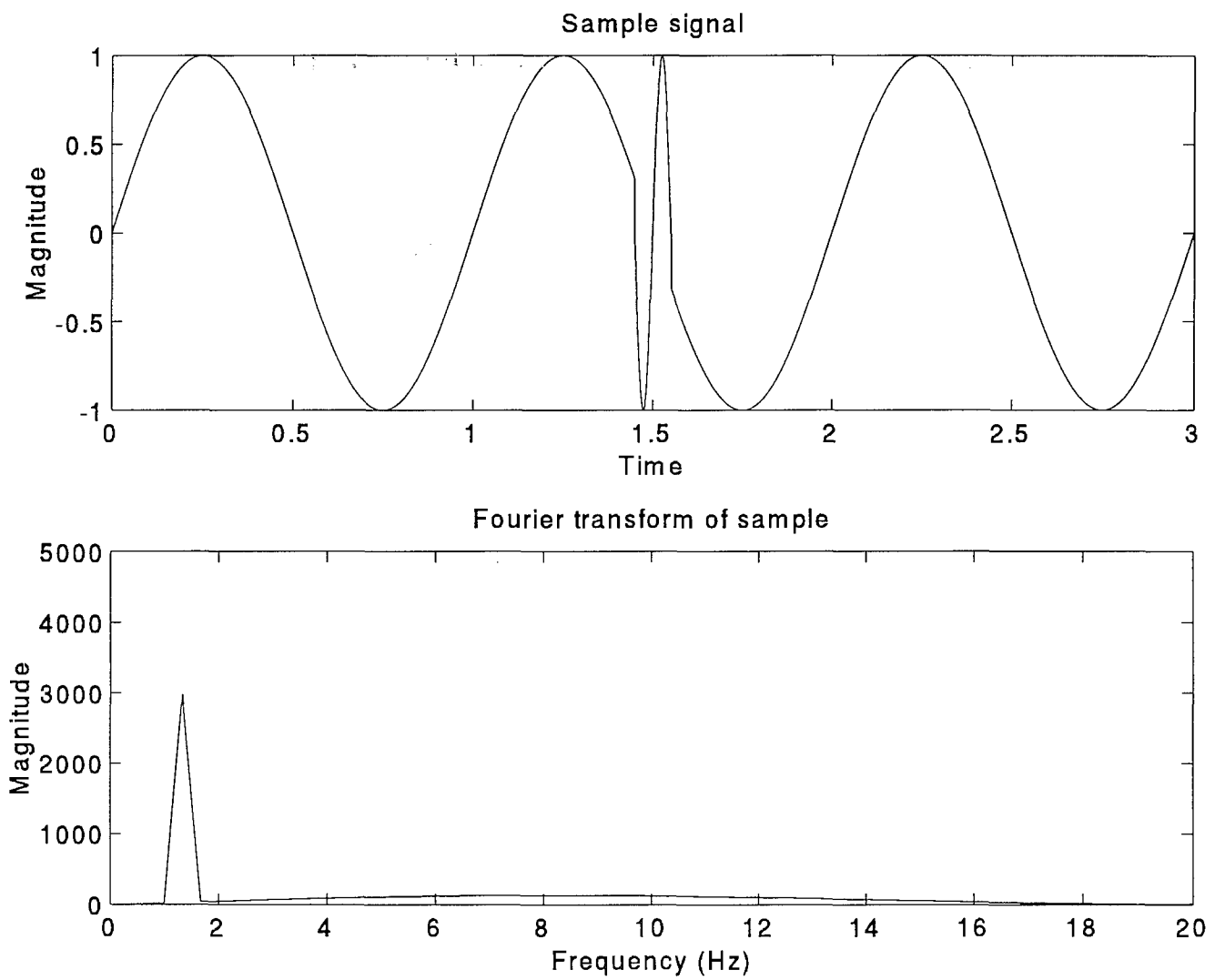


Figure A.2 Fourier resolution of rapidly changing signal

Rotor 4: 90%, Kulite #1

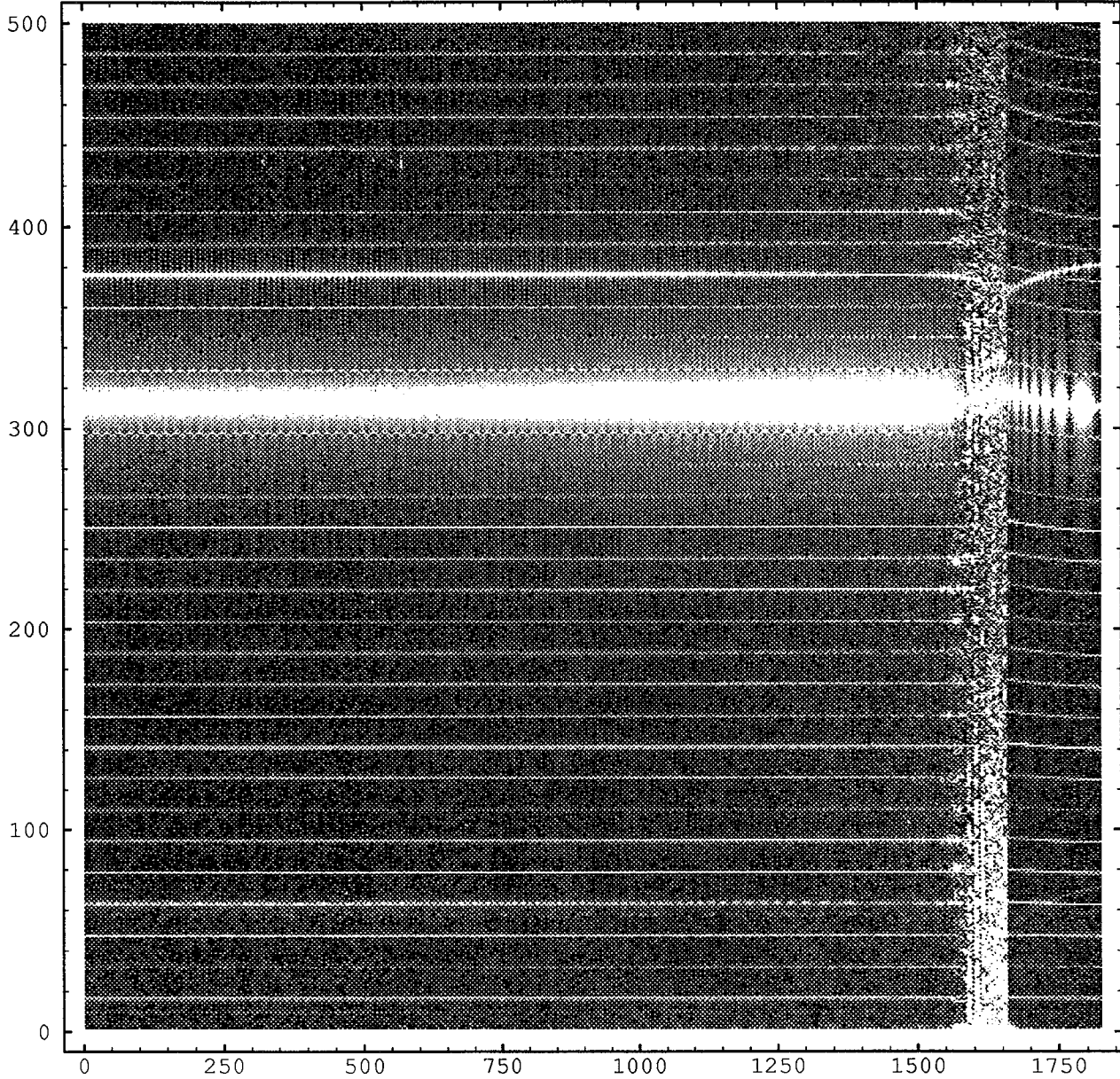


Figure A.3 Rotor 4, 90%, Kulite #1: TFM Plot

Rotor 4: 90%, Kulite #2

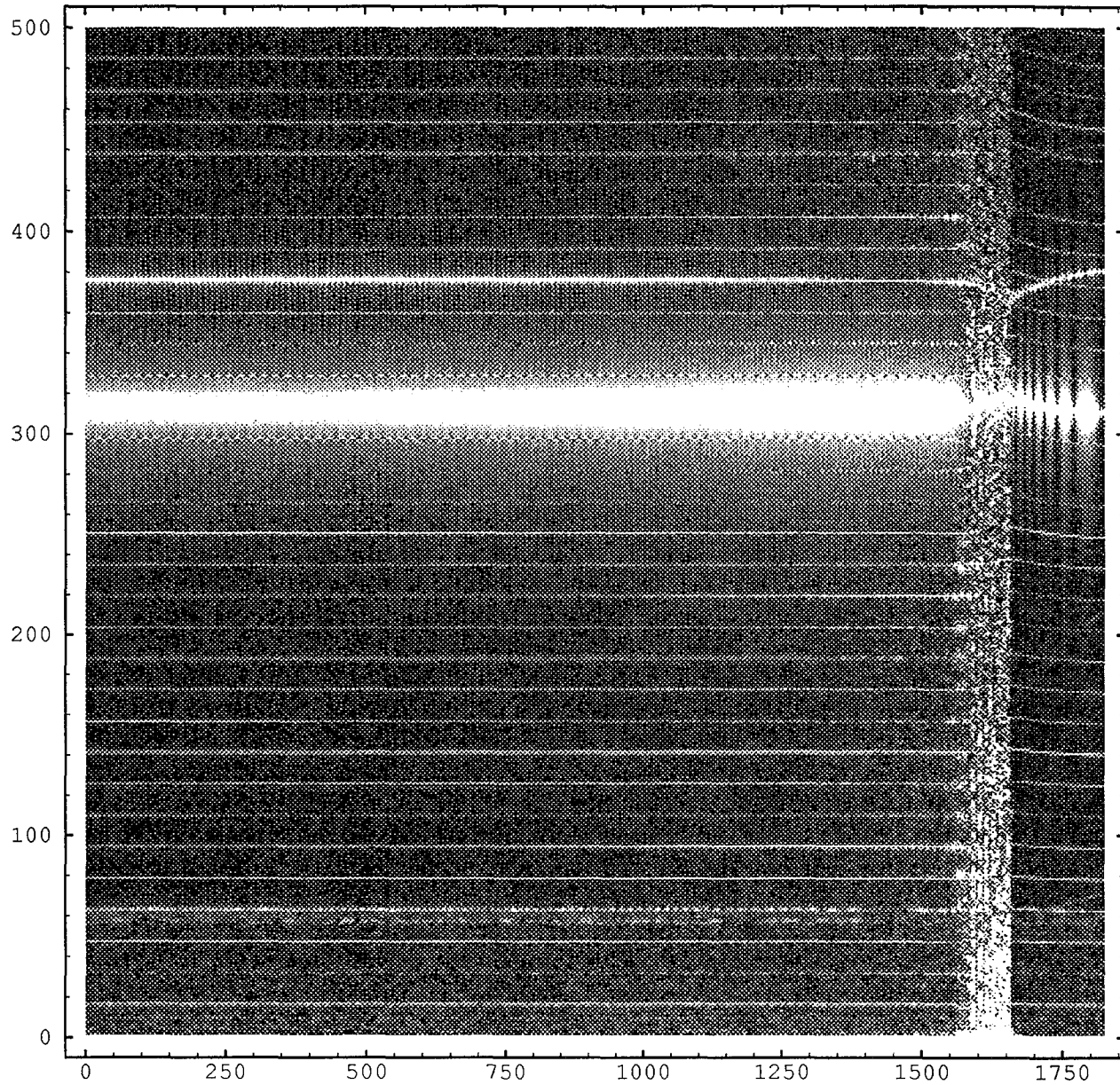


Figure A.4 Rotor 4, 90%, Kulite #2: TFM Plot

Rotor 4: 90%, Kulite #3

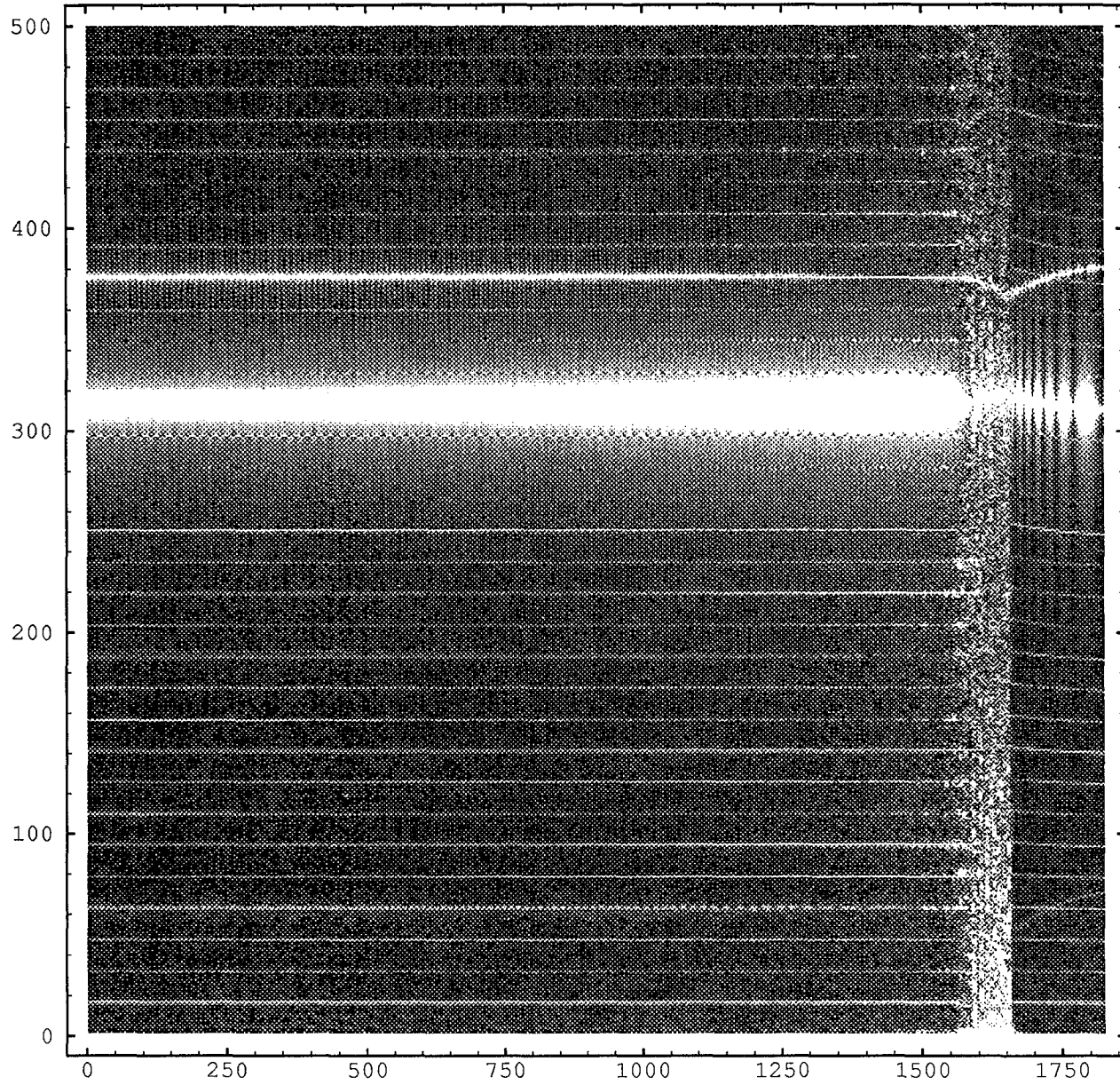


Figure A.5 Rotor 4, 90%, Kulite #3: TFM Plot

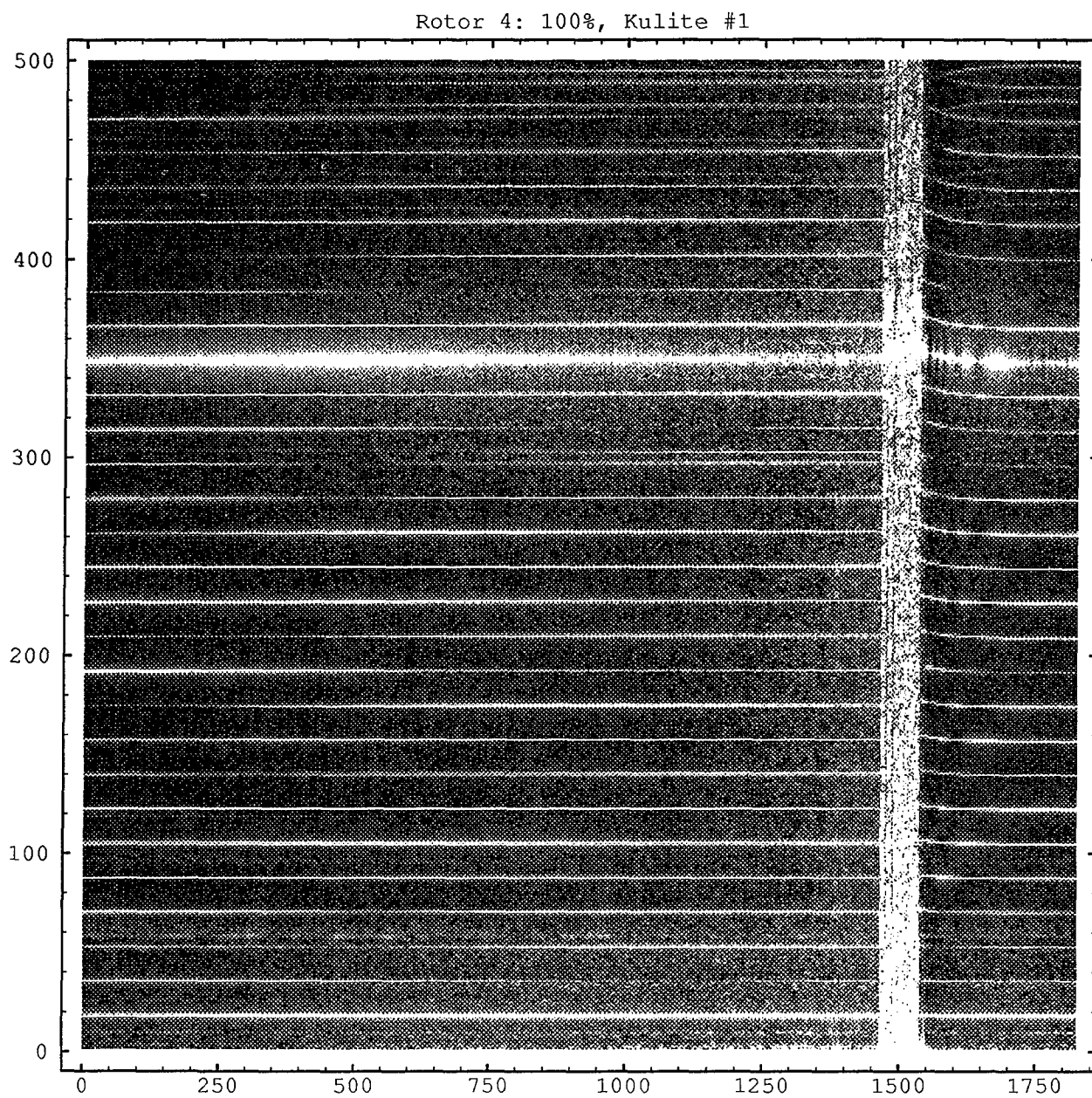


Figure A.6 Rotor 4, 100%, Kulite #1: TFM Plot

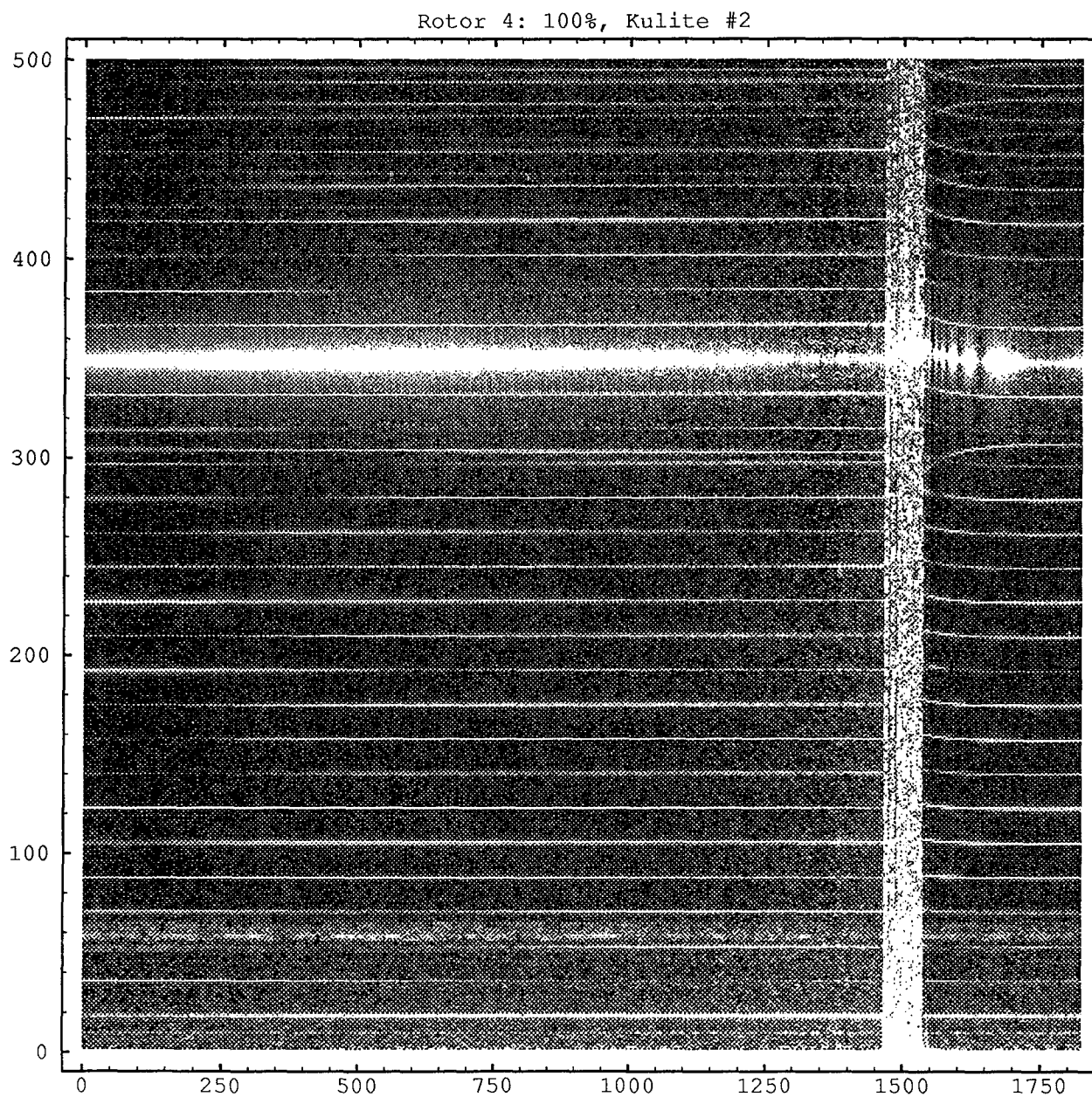


Figure A.7 Rotor 4, 100%, Kulite #2: TFM Plot

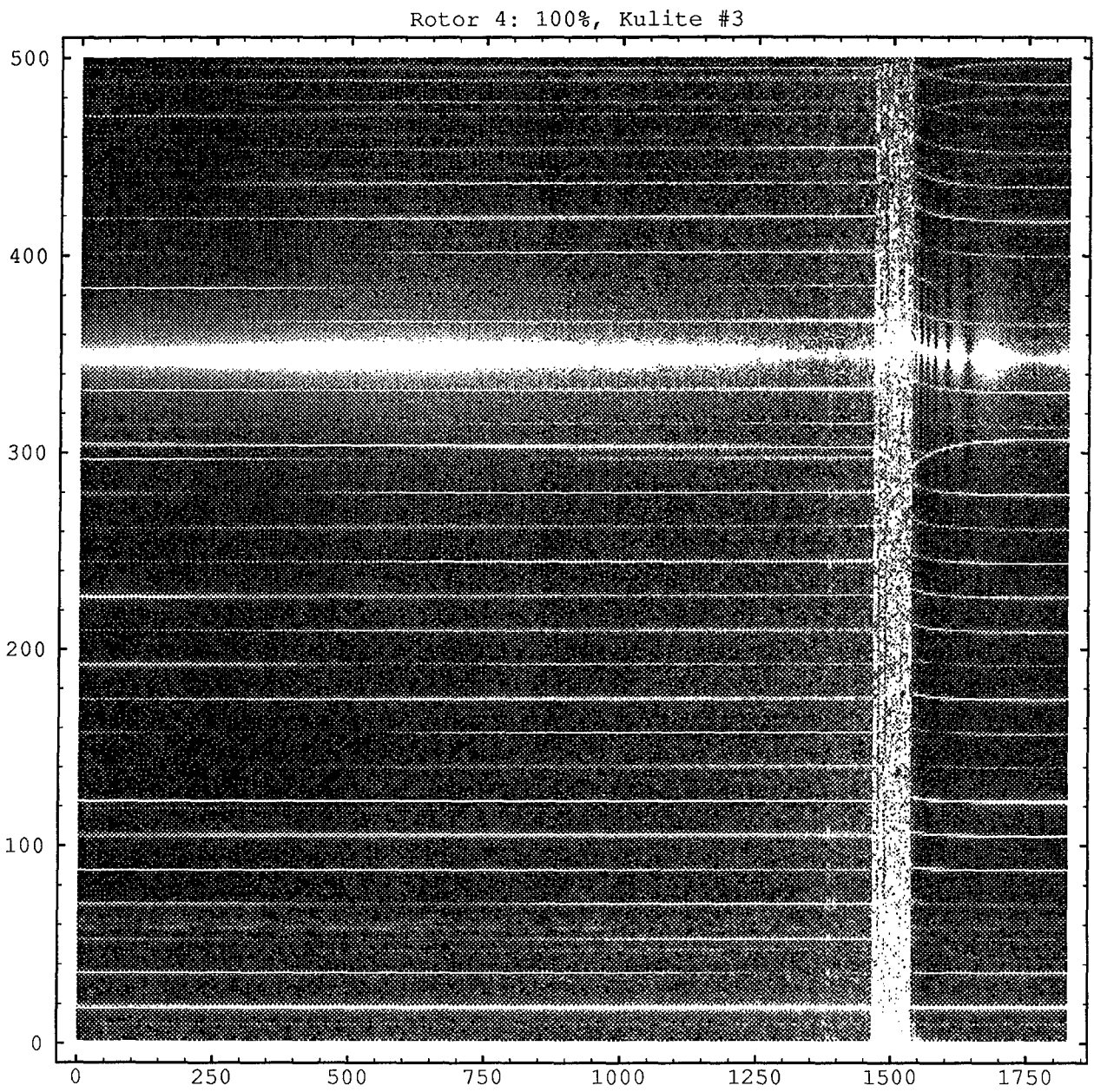


Figure A.8 Rotor 4, 100%, Kulite #3: TFM Plot

Rotor 6: 90%, Kulite #1

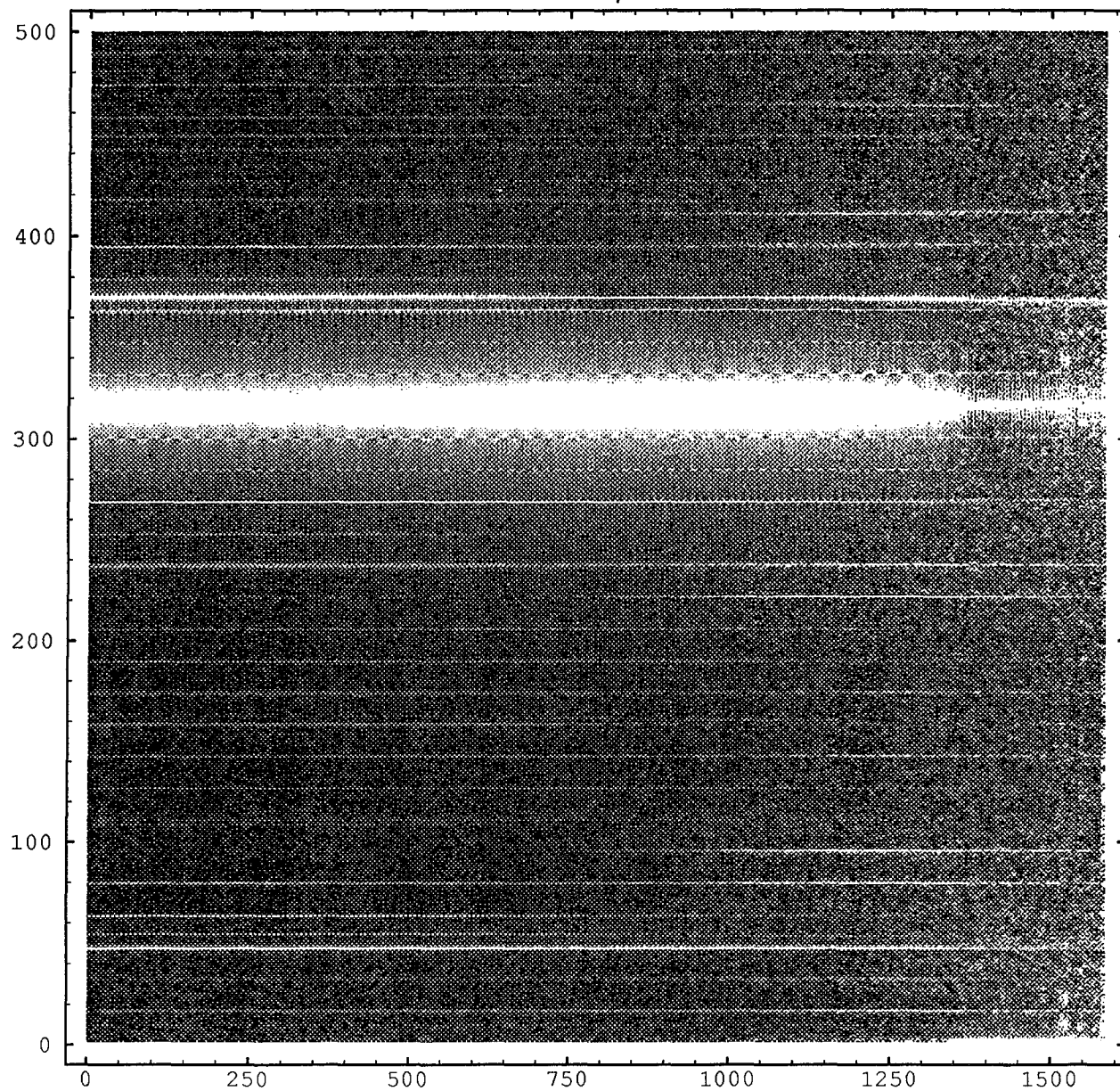


Figure A.9 Rotor 6, 90%, Kulite #1: TFM Plot

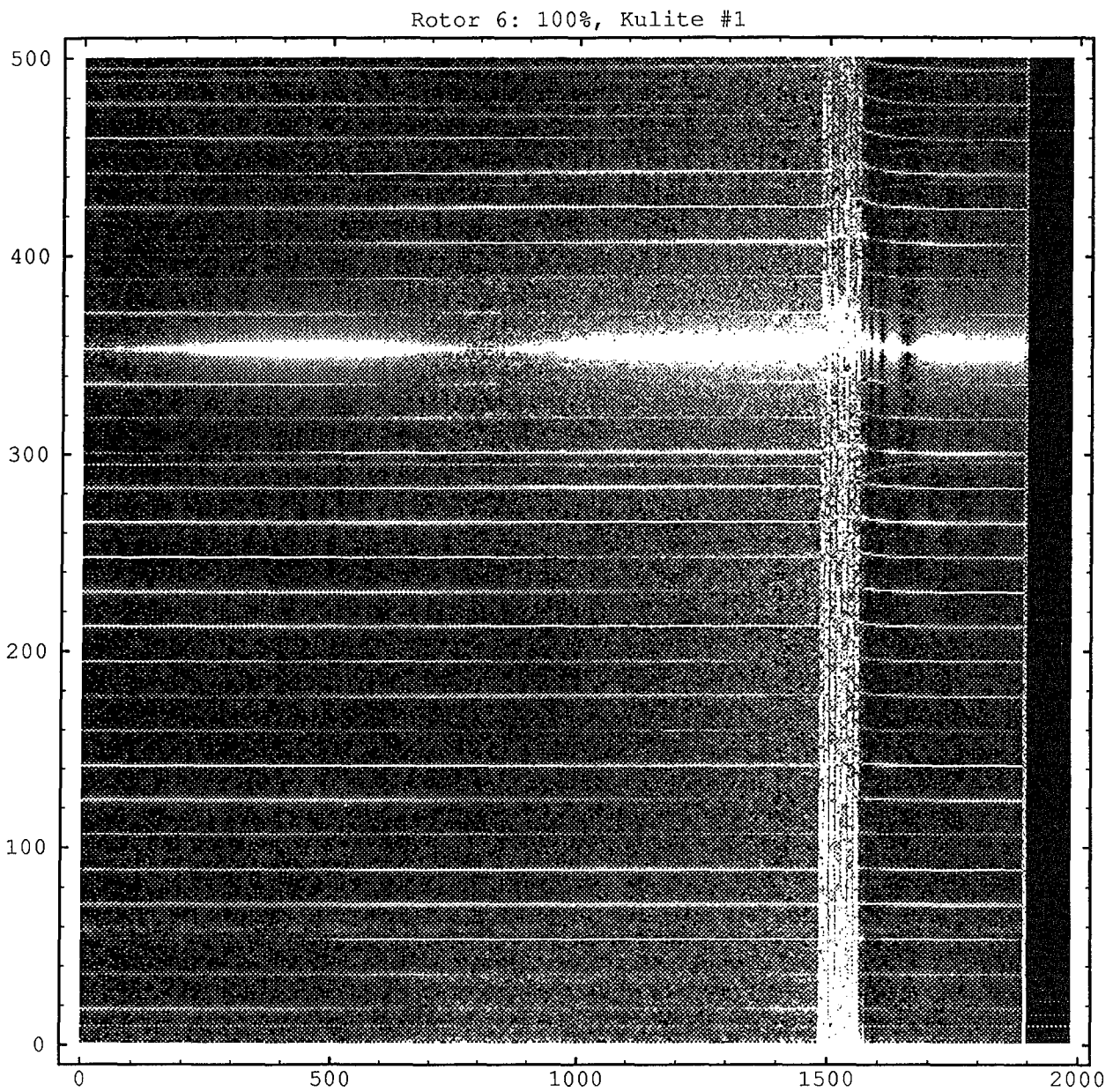


Figure A.10 Rotor 6, 100%, Kulite #1: TFM Plot

Rotor 9: 95%, Kulite #1

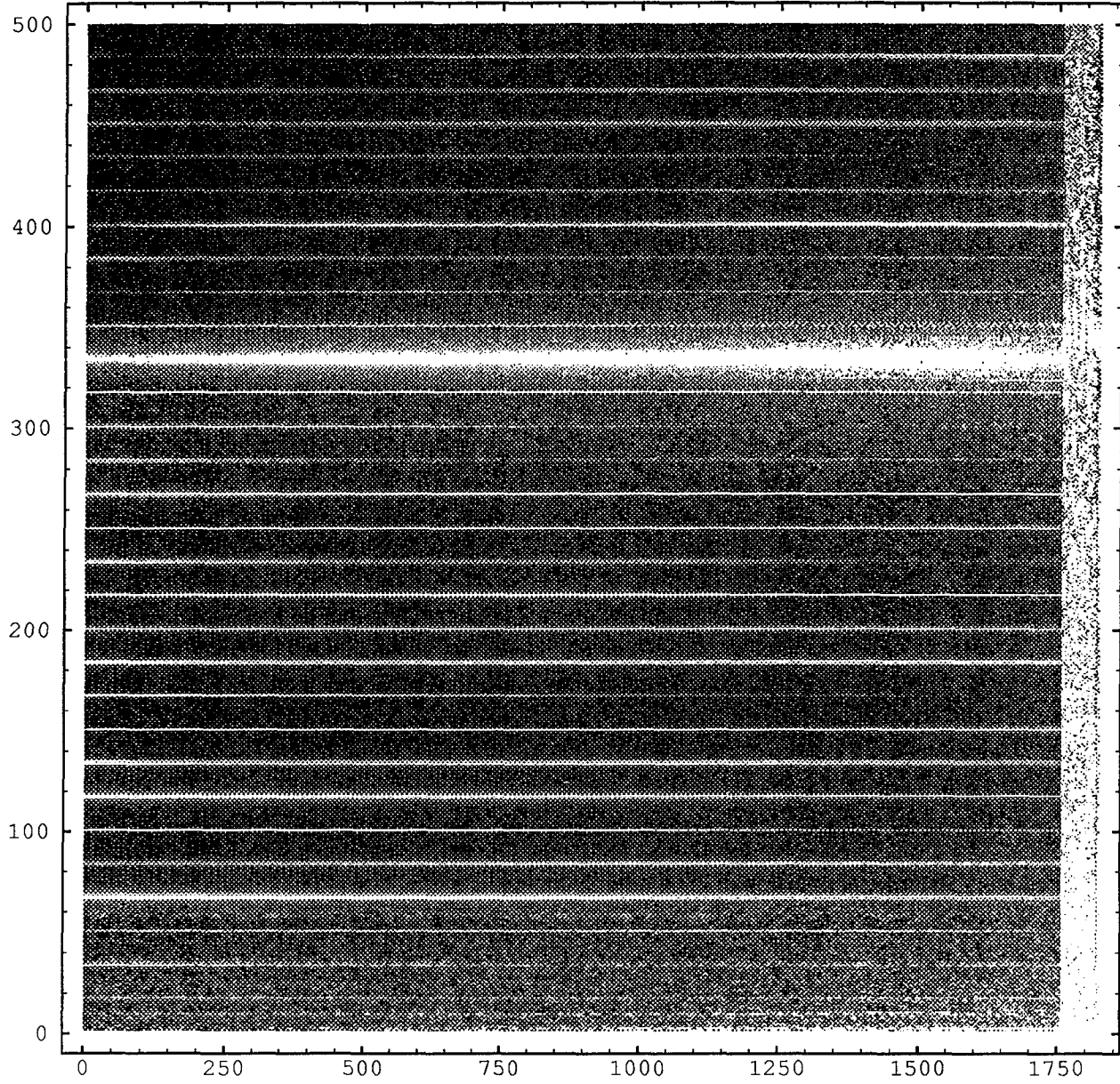


Figure A.11 Rotor 9, 95%, Kulite #1: TFM Plot

Rotor 9: 100%, Kulite #1

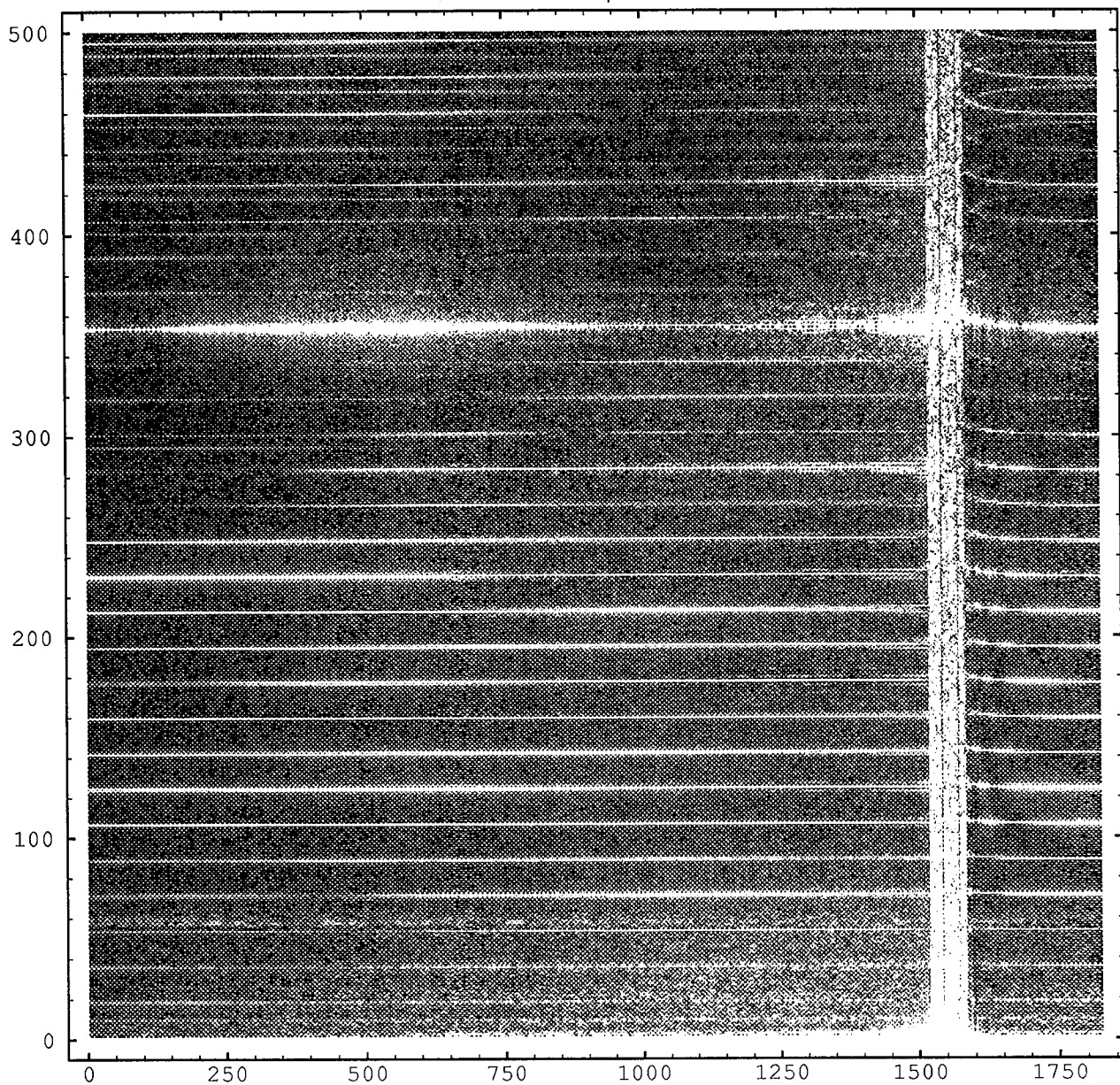


Figure A.12 Rotor 9, 100%, Kulite #1: TFM Plot

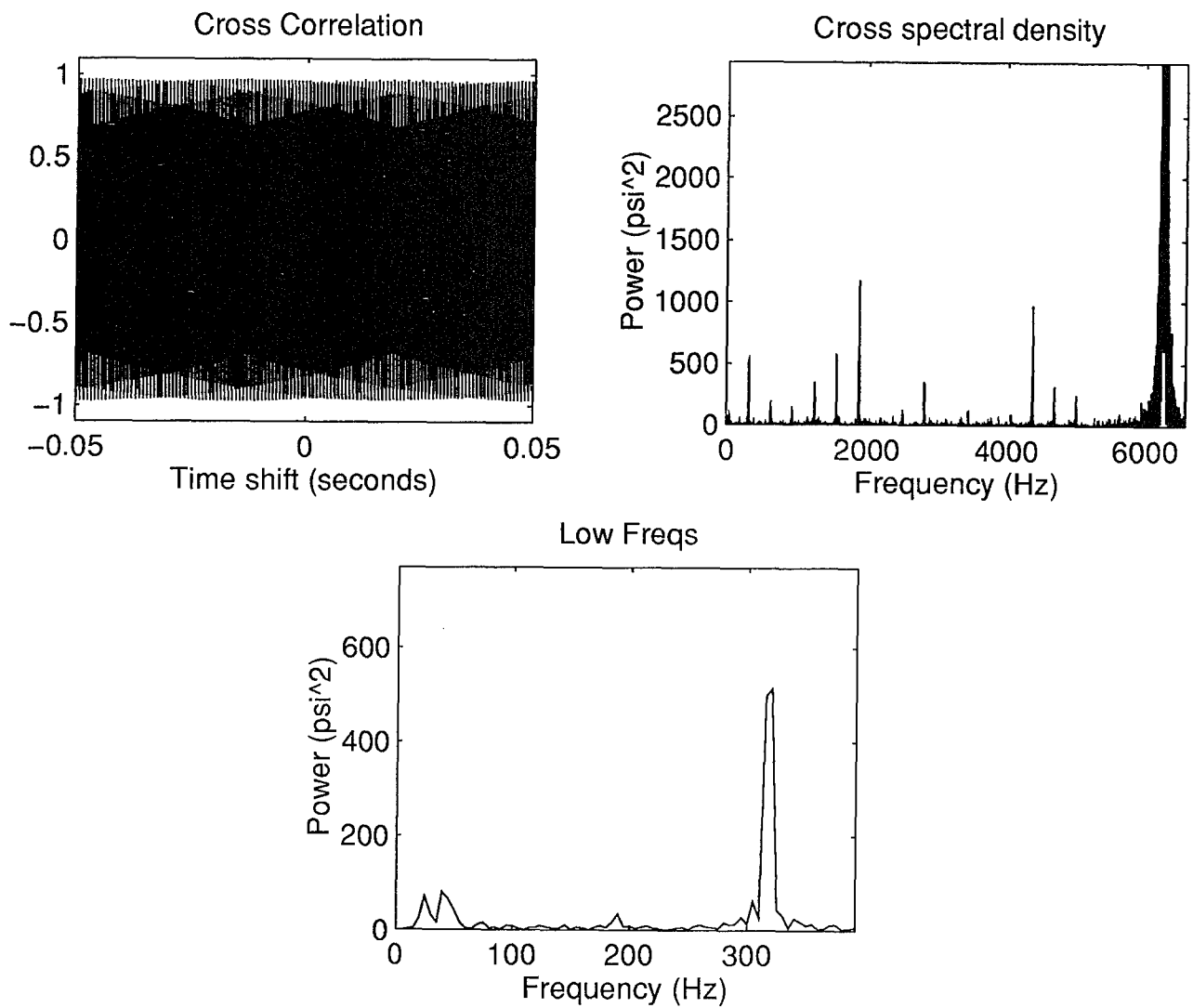


Figure A.13 Rotor 4, 90%: Cross-Correlation of Kulites #1 and #4 at $T = -0.124$

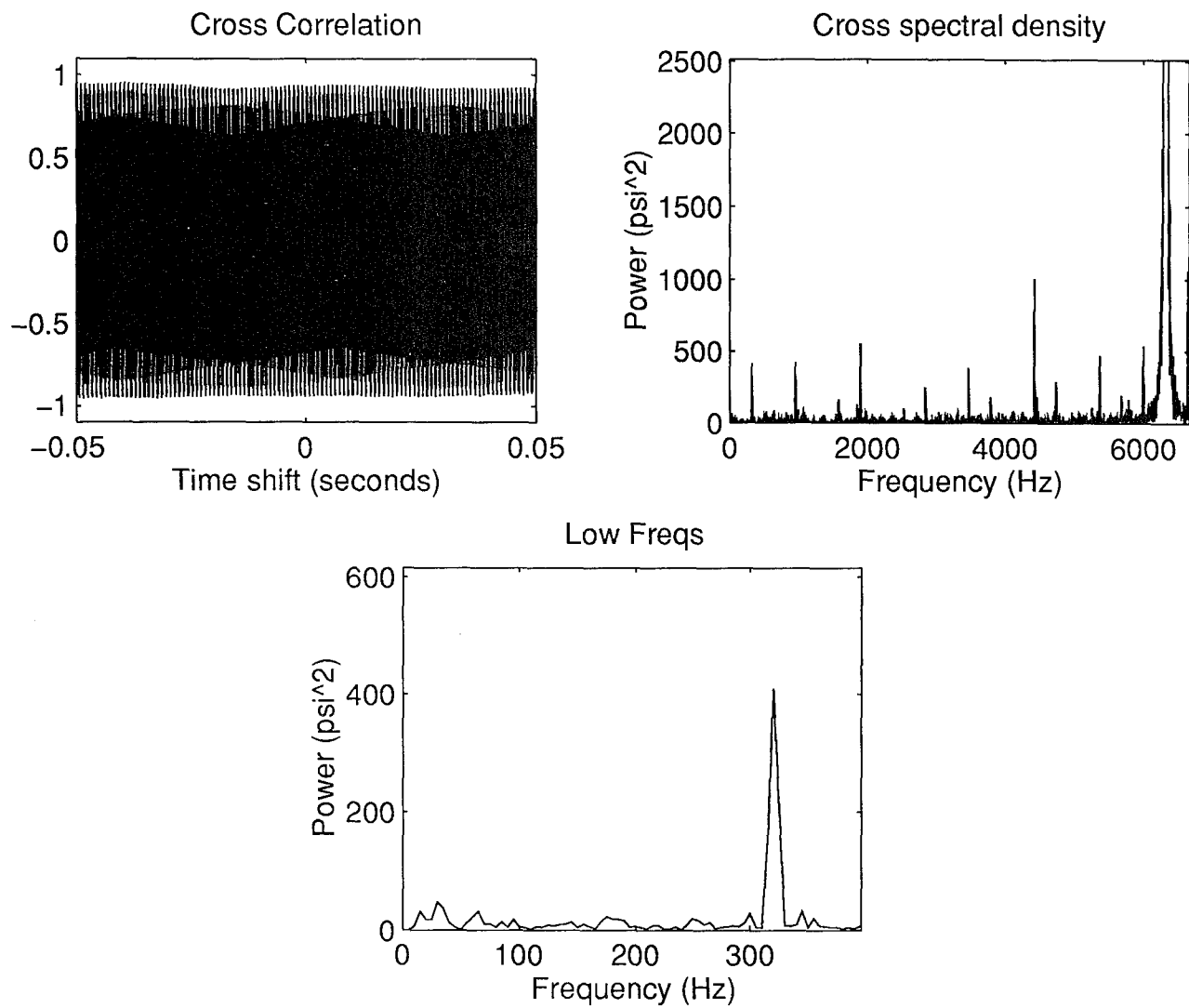


Figure A.14 Rotor 6, 90%: Cross-Correlation of Kulites #1 and #4 at T = -0.15

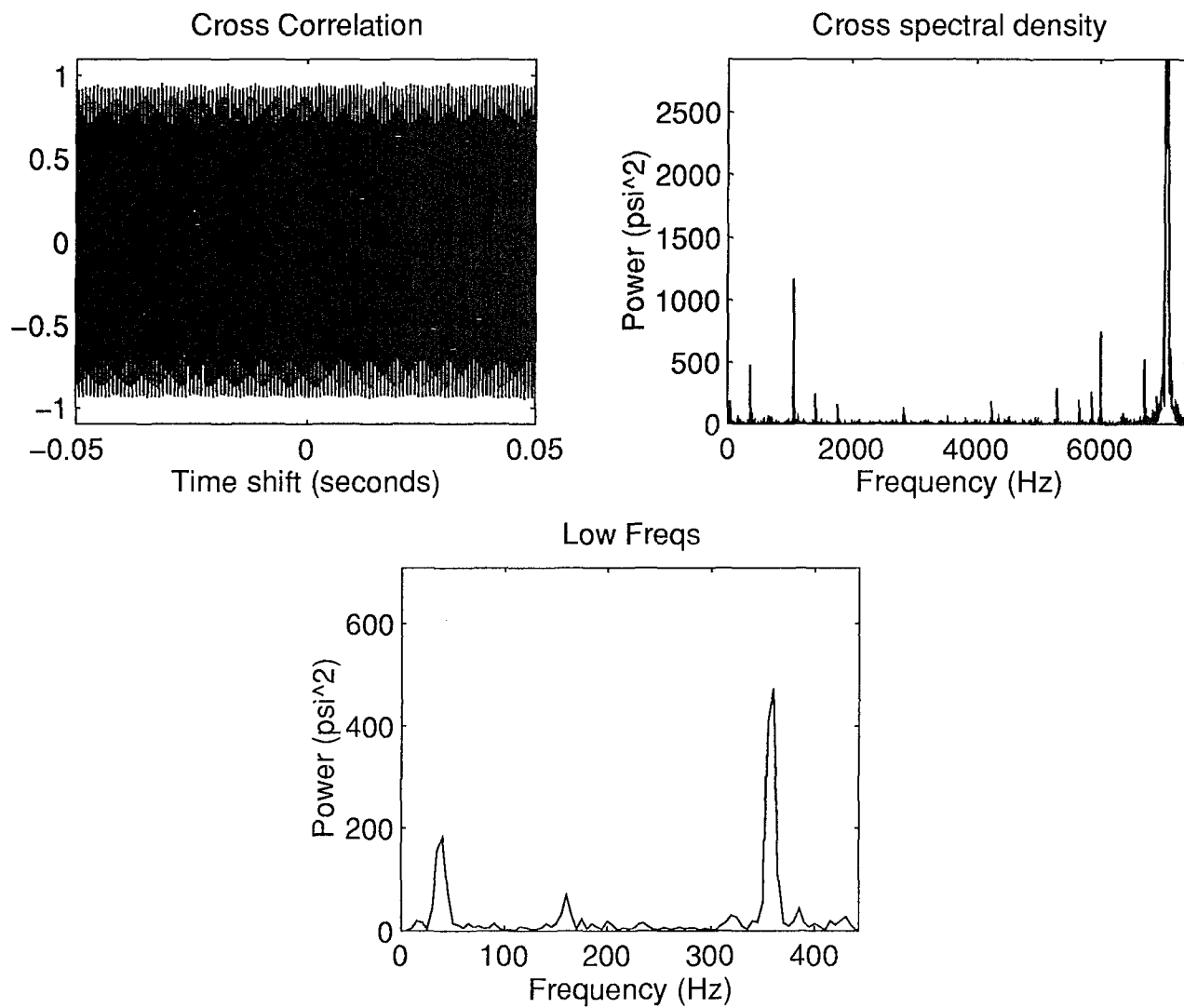


Figure A.15 Rotor 6, 100%: Cross-Correlation of Kulites #1 and #4 at $T = -0.02$

```

%This M-file plots the power of rotor frequency bands based on the matrix fftmatrix
%(supplied by user). fftmatrix is an m by n matrix containing windowed FFTs from raw
%rotor frequency data. m is the number of FFT points in a window (the first half of the
%points provided by the FFT function, i.e. without the complex conjugate FFT coefficients),
%n is the number of FFT windows used over the span of the data. FFT data consists of real
%number magnitudes obtained from the complex number FFT. lowband and hiband are
%required from the user to set the low and high ends of the frequency band of interest. To
%eliminate DC effects, the lowest value of lowband used was 2.
%
%Also required from the user was stalltime, the number of seconds from the beginning of the
%data stream corresponding to the time the rotor was determined to have stalled.

samp=20000;
window=1000;
stepsize=125;
clear x t

%x is x-axis time; xmod is required to ensure the lengths of x and t (power data) are the
%same
x=0:stepsize/samp:stepsize*length(fftmatrix)/samp;
xmod=length(x)/(length(x)-1);
%Subtracting stalltime make xaxis the number of seconds before stall
x=xmod*x(1:length(x)-1)-stalltime;

j=1;
for i=1:length(fftmatrix)
    t(j)=norm(fftmatrix(lowband:hiband,i)).^2/(window/2);
    j=j+1;
end

figure(1)
plot(x,t)
grid
xlabel('Time (seconds, 0 = stall)')
ylabel('Power (psi^2)')
%title(['Rotor ',num2str(rotor),': ',num2str(speed),'%, Kulite #',num2str(kulite),' , Power vs.
Time'])

```

```
%This file is used to construct the cross-correlation plots and cross-spectral density plots as
%used in this report.
```

```
%
%Required from user:      rotorf, the rotor frequency (Hz)
%                          k1 and k4, calibrated pressure data from Kulites #1 and #4
```

```
sample=20000;
window=2000;
```

```
%xaxis is the frequency range for the cross-spectral density plot
x=-window/sample+1/sample:1/sample>window/sample-1/sample;
xaxis=sample/2>window:sample/2>window:(window*2-1)*sample/2>window;
clear rampbias
yaxis=0;
```

```
%This section creates the ramp bias corrector
for i=1>window-1
    rampbias(i>window)=window/(window-i);
end
rampbias(1>window-1)=fliplr(rampbias(window+1:2*window-1));
rampbias(window)=1;
```

```
figure(1)
clf
```

```
%begin is the point in the data stream where correlation is desired. This used to be a loop
%with i=begin:stepsize:close but when specific times were found to be of interest, the
%program was repeatedly run with the exact values of time specified by 'begin' alone
i=begin
```

```
x1=k1(i:i>window-1)-mean(k1(i:i>window-1));
x4=k4(i:i>window-1)-mean(k4(i:i>window-1));
```

```
%This section generates the cross-spectral density data
correlate14=xcorr(x1,x4);
cpsd=abs(fft(correlate14));
if yaxis==0
    yaxis=2.5*max(cpsd(1:rotorf*16/(sample/2)*window));
end
```

```
%Data is normalized before generating the correlation curve, so that correlation is bounded by
%-1 and 1.
```

```
x1=x1/norm(x1);
x4=x4/norm(x4);
```

```
unbiased=xcorr(x1,x4).*rampbias';
```

```
subplot(2,2,1)
plot(x(window/2:1.5*window),unbiased(window/2:1.5*window))
axis([-window/(sample*2) window/(sample*2) -1.1 1.1])
%t=sprintf('Time shift (0 = %2.2f seconds)',(i+window/2)/sample);
title('Cross Correlation')
xlabel('Time shift (seconds)')
```

```
subplot(2,2,2)
plot(xaxis,cpsd)
axis([0 rotorf*21 0 yaxis])
xlabel('Frequency (Hz)')
ylabel('Power (psi^2)')
title('Cross spectral density')
```

```
subplot(2,2,3.5)
plot(xaxis,cpsd)
axis([0 rotorf*1.25 0 1.5*max(cpsd(1:rotorf*1.25/(sample/2)*window))])
title('Low Freqs')
xlabel('Frequency (Hz)')
ylabel('Power (psi^2)')
```

VITA

Captain James F. Anderton was born at Edwards AFB, CA on May 3, 1961. He graduated from Mount Vernon High School in June 1978 and entered the University of Virginia in August 1979. In June of 1980, he transferred to the United States Air Force Academy, from which he received a Bachelor of Science degree in Aerospace Engineering in June of 1983. Following Undergraduate Pilot Training at Vance Air Force Base, OK in June of 1984, he was assigned to the 9th Tactical Fighter Squadron, 49th Tactical Fighter Wing, Holloman Air Force Base, NM as an F-15 aircraft commander. In December 1988, his next assignment took him to the 57th Fighter Interceptor Squadron at Naval Air Station Keflavik, Iceland, as an F-15 flight lead and instructor pilot. In January of 1990, he transferred to the 80th Flying Training Wing (FTW) at Sheppard Air Force Base, TX, to become a T-38 instructor pilot in the Euro-NATO Joint Jet Pilot Training program. In August of 1992, he became Chief of Flight Test for the 80th FTW. He entered the School of Engineering, Air Force Institute of Technology in May 1993. His follow-on assignment will be at Robins Air Force Base, GA, in the Structures division of the F-15 maintenance depot.

Permanent Address: 8714 Gateshead Road

Alexandria, VA 22309

REPORT DOCUMENTATION PAGE

Form Approved
OMB No. 0704-0188

Public reporting burden for this collection of information is estimated to average 1 hour per response, including the time for reviewing instructions, searching existing data sources, gathering and maintaining the data needed, and completing and reviewing the collection of information. Send comments regarding this burden estimate or any other aspect of this collection of information, including suggestions for reducing this burden, to Washington Headquarters Services, Directorate for Information Operations and Reports, 1215 Jefferson Davis Highway, Suite 1204, Arlington, VA 22202-4302, and to the Office of Management and Budget, Paperwork Reduction Project (0704-0188), Washington, DC 20503.

1. AGENCY USE ONLY (Leave blank)	2. REPORT DATE December 1994	3. REPORT TYPE AND DATES COVERED Master's Thesis
----------------------------------	---------------------------------	---

4. TITLE AND SUBTITLE STALL PRECURSOR STUDY OF HIGH FREQUENCY DATA FOR THREE HIGH SPEED, SWEEP COMPRESSOR ROTORS	5. FUNDING NUMBERS
--	--------------------

6. AUTHOR(S) James F. Anderton, Captain, USAF
--

7. PERFORMING ORGANIZATION NAME(S) AND ADDRESS(ES) Air Force Institute of Technology, WPAFB OH 45433-6583	8. PERFORMING ORGANIZATION REPORT NUMBER AFIT/GAE/ENY/94D-13
--	---

9. SPONSORING/MONITORING AGENCY NAME(S) AND ADDRESS(ES) William W. Copenhaver WL/POTF 1950 5th Street Building 18 WPAFB, OH 45433-7251	10. SPONSORING/MONITORING AGENCY REPORT NUMBER
--	--

11. SUPPLEMENTARY NOTES

12a. DISTRIBUTION/AVAILABILITY STATEMENT Approved for public release; distribution unlimited	12b. DISTRIBUTION CODE
---	------------------------

13. ABSTRACT (Unannounced) Experimental data from three high speed compressors, including straight, backward-swept, and forward-swept blade designs, was examined for stall precursors. Data was acquired from four pressure transducers located on the compressor casing and arranged axially between locations 40% of blade chord upstream of the rotor face to just over the leading edge of the blades. Analyses for characteristics of impending stall included examination of integrated signal power and cross-correlations of transducer signals from the upstream and downstream-most pressure transducers. Results of the integrated signal power approach detected differences in the signal power at the two transducers in the immediate pre-stall time frame. Pre-stall warning times varied from several seconds to less than 0.5 second, with higher rotor speeds giving less warning time. Results for the forward-swept rotor, however, showed that integrated signal power did not warn of impending stall, and that surge energies played an important role in this rotor's stalling characteristics. An hypothesis for the behavior of the forward swept rotor, based on the possibility of stall development beginning in the near-hub radial region of this compressor, was developed.
--

14. SUBJECT TERMS Compressors, axial compressors, compressor stall, stall inception, stall warning, transonic compressors	15. NUMBER OF PAGES 162
	16. PRICE CODE

17. SECURITY CLASSIFICATION OF REPORT Unclassified	18. SECURITY CLASSIFICATION OF THIS PAGE Unclassified	19. SECURITY CLASSIFICATION OF ABSTRACT Unclassified	20. LIMITATION OF ABSTRACT UL
---	--	---	----------------------------------